

University of Alberta

CO₂ Rock Physics: A Laboratory Study

by

Helen Yam

A thesis submitted to the Faculty of Graduate Studies and Research
in partial fulfillment of the requirements for the degree of

Master of Science
in
Geophysics

Department of Physics

©Helen Yam
Fall 2011
Edmonton, Alberta

Permission is hereby granted to the University of Alberta Libraries to reproduce single copies of this thesis and to lend or sell such copies for private, scholarly or scientific research purposes only. Where the thesis is converted to, or otherwise made available in digital form, the University of Alberta will advise potential users of the thesis of these terms.

The author reserves all other publication and other rights in association with the copyright in the thesis and, except as herein before provided, neither the thesis nor any substantial portion thereof may be printed or otherwise reproduced in any material form whatsoever without the author's prior written permission.

To

My family and Dennis

Abstract

In any geological sequestration projects, monitoring and verification are essential components in ensuring storage integrity. Seismic methods are regarded as a feasible way to monitor the subsurface CO₂ because of their sensitivity to a rock's pore space content. Therefore understanding the effects of CO₂ and its variability on seismic response is important.

Ultrasonic pulse transmission measurements were conducted on a porous ceramic sample and on a Berea sandstone sample. P-and S-waveforms were collected under various pressures, temperatures, and fluid-type saturation. The wave velocity and attenuation under full CO₂ saturation and under a constant differential pressure were analyzed. The presence of differing phase states and some phase transitions were notable from wave velocity and wave attenuation changes. Only the observed wave velocities of the porous ceramic sample were in good agreement with Biot's modelled results. Generally, CO₂'s density plays a more dominant role than its bulk modulus on controlling the P-wave velocity.

Acknowledgements

I want to thank my supervisor, Dr. Doug Schmitt, for his guidance, his continuous encouragement and the many invaluable learning opportunities he has provided me throughout my studies, both in the laboratory and out in the field. I want to thank the U of A technicians, Lucas Duerksen and Len Tober, for their technical support in the laboratory, especially for making the CO₂ experiments vital to this thesis possible. Also, I want to thank the Experimental Geophysics Group for their assistance with my work and for their helpful discussions in the Rock Physics Laboratory. Furthermore, I am grateful to the many colleagues in the Department of Physics for their upbeat support and for the many laughs shared in the hall.

Sincerely, I want to thank my loving family, my mom, my dad, Polly and Stewart, for their never-ending care. Without their constant attentiveness to my well-being, my entire academic journey would have been far more difficult.

Finally, I want to thank Dennis for his companionship. His incredible patience and his continuous support in both my personal and academic endeavours, have made the last few years much more enjoyable.

This work was funded in part by the National Science and Engineering Research Council (NSERC) of Canada by supporting me through the CGS M.Sc. scholarship and by supporting the U of A Rock Physics Laboratory through Dr. Schmitt's Discovery grant.

Table of Contents

Chapter 1: Introduction	1
1.1 Climate Change.....	1
1.2 Aim of Research and Chapter Description	4
Chapter 2: Background on Carbon Storage	8
2.1 Types of CO ₂ sequestration.....	8
2.2 Examples of Geological Sequestration	14
2.3 Safety and Monitoring	15
2.4 Direct monitoring measurements	17
2.5 Indirect monitoring measurements (Geophysical).....	17
2.5.1 Geodetic	18
2.5.2 Electromagnetic (EM).....	19
2.5.3 Gravitational	20
2.6 Seismic	21
2.6.1 Surface Seismic.....	22
2.6.2 Vertical Seismic Profiling.....	24
2.6.3 Cross-well Imaging	26
2.7 Review of existing literature on CO ₂ laboratory measurements.....	27
2.8 Summary	32
Chapter 3: Theoretical Background	34
3.1 Carbon dioxide	35
3.1.1 Introduction to Thermodynamics.....	35
3.1.2 CO ₂ Phase States.....	36
3.1.3 Geological Sequestration Approximate Physical Conditions ...	
.....	38
3.2 Seismic Theory	40
3.2.1 Theory of Elasticity.....	41
3.2.2 Wave propagation in an isotropic linear elastic medium.....	45

3.2.3 Viscoelasticity	47
3.3 Rock Physics	50
3.3.1 Gassmann's Equation.....	51
3.3.2 Biot's Formulation	57
3.4 Introduction to Elastic Wave Velocity and Attenuation Determination in the laboratory	64
3.4.1 Laboratory Measurement Method.....	65
3.4.2 Attenuation.....	67
3.4.3 The Attenuation of Ultrasonic Waves through Acrylic	72
3.5 Summary	77
Chapter 4: Experimental Setup and Procedure	79
4.1 Piezoelectric Transducers	79
4.2 Sample Preparation	82
4.3 Experimental Apparatus.....	84
4.4 Experimental Procedure	87
4.5 Velocity and Attenuation Analysis Methodology.....	91
4.5.1 Velocity and Error Analysis.....	92
4.5.2 Attenuation and Error Analysis.....	96
4.6 Chapter Summary	100
Chapter 5: Sample Characterization	102
5.1 Samples	102
5.2 Density and Porosity	103
5.2.1 Grain Volume and Density	104
5.2.2 Bulk Density and Porosity	105
5.2.3 Pore Size Distribution	106
5.3 Permeability	110
5.4 Tortuosity	112
5.5 Scanning Electron Microscope Imaging (SEM)	114
5.6 Summary	118
Chapter 6: Results and Discussion: Synthetic sample	119
6.1 Dry	119

6.1.1 Dry Waveforms.....	120
6.1.2 Dry Wave Velocities.....	121
6.2 CO ₂	122
6.2.1 CO ₂ Saturated Waveforms	123
6.2.2 Observed CO ₂ Saturated Wave Velocity	125
6.2.3 Modelled CO ₂ Saturated Wave Velocity	129
6.2.4 Observed CO ₂ Saturated Wave Attenuation	134
6.2.5 Modelled CO ₂ Saturated Wave Attenuation	138
6.3 Water.....	143
6.3.1 Water Saturated Waveforms	143
6.3.2 Observed Water Saturated Wave Velocities.....	144
6.3.3 Modelled Water Saturated Wave Velocities.....	144
6.4 Results and Discussion	146
6.4.1 CO ₂	146
6.4.2 Water.....	148
6.5 Summary	149
Chapter 7: Results and Discussion: Non-synthetic sample	152
7.1 Dry	152
7.1.1 Dry Waveforms.....	153
7.1.2 Dry Wave Velocities	153
7.2 CO ₂	154
7.2.1 CO ₂ Saturated Waveforms	155
7.2.2 Observed CO ₂ Saturated Wave Velocity	157
7.2.3 Modelled CO ₂ Saturated Wave Velocity	162
7.2.4 Observed CO ₂ Saturated Wave Attenuation	167
7.2.5 Modelled CO ₂ Saturated Wave Attenuation	171
7.3 Water.....	175
7.3.1 Water Saturated Waveforms	175
7.3.2 Observed Water Saturated Wave Velocities.....	176
7.3.3 Modelled Water Saturated Wave Velocities.....	176
7.4 Results and Discussion	179

7.5 Summary	184
Chapter 8: Conclusion	187
8.1 Summary of Work.....	187
8.2 Contributions of this Work	190
8.3 Future Work	191
References	194
Appendix A: Observed and modelled Results.....	208
A.1 Porous Ceramic Rod	208
A.1.1 Dry Condition Results.....	209
A.1.2 CO ₂ Saturated Results	213
A.1.3 Water Saturated Results	233
A.2 Berea Sandstone	235
A.2.1 Dry Condition Results.....	235
A.2.2 CO ₂ Saturated Results	239
A.2.3 Water Saturated Results	263

List of Tables

3.1	Relationships among the elastic constants for a homogeneous isotropic material	45
4.1	The measurements carried out for a sample during ultrasonic pulse transmission experiments.....	91
5.1	The measured envelope volume of the samples	106
5.2	Petrophysical properties characterized of the samples	115
A.1	Petrophysical properties determined of the porous ceramic rod.....	208
A.2	Dry P-and S-wave velocities of the porous ceramic rod at $T = 23^\circ\text{C}$ under various confining pressures.....	212
A.3	Dry P-and S-wave velocities of the porous ceramic rod at $P_c = 10 \text{ MPa}$ while under various temperatures	213
A.4	CO_2 saturated P-and S-wave velocities of the porous ceramic rod for the $T= 23^\circ\text{C}$ constant temperature run.....	216
A.5	CO_2 saturated P-and S-wave velocities of the porous ceramic rod for the $T= 28^\circ\text{C}$ constant temperature run	216
A.6	CO_2 saturated P-and S-wave velocities of the porous ceramic rod for the $T= 40^\circ\text{C}$ constant temperature run	217
A.7	CO_2 saturated P-and S-wave velocities of the porous ceramic rod for the $T= 45^\circ\text{C}$ constant temperature run	217
A.8	CO_2 saturated P-and S-wave velocities of the porous ceramic rod for the $P_p= 7 \text{ MPa}$ constant pore pressure run	224
A.9	CO_2 saturated P-and S-wave velocities of the porous ceramic rod for the $P_p= 10 \text{ MPa}$ constant pore pressure run	225
A.10	CO_2 saturated P-and S-wave velocities of the porous ceramic rod for the $P_p= 25 \text{ MPa}$ constant pore pressure run	226

A.11	Water saturated P-and S-wave velocities of the porous ceramic rod at T=23°C for varying pore pressures.....	235
A.12	Petrophysical properties determined of the Berea sandstone.....	235
A.13	Dry P-and S-wave velocities of the Berea sandstone at T = 23°C under various confining pressures of the first measurement run	238
A.14	Dry P-and S-wave velocities of the Berea sandstone at T = 23°C under various confining pressures of the second measurement run.....	239
A.15	CO ₂ saturated P-and S-wave velocities of the Berea sandstone for the T= 23 °C constant temperature run.....	243
A.16	CO ₂ saturated P-and S-wave velocities of the Berea sandstone for the T= 28 °C constant temperature run.....	243
A.17	CO ₂ saturated P-and S-wave velocities of the Berea sandstone for the T= 40 °C constant temperature run.....	244
A.18	CO ₂ saturated P-and S-wave velocities of the Berea sandstone for the T= 45 °C constant temperature run.....	244
A.19	CO ₂ saturated P-and S-wave velocities of the Berea sandstone for the T= 55 °C constant temperature run.....	245
A.20	CO ₂ saturated P-and S-wave velocities of the Berea sandstone for the Pp= 7 MPa constant pore pressure run	255
A.21	CO ₂ saturated P-and S-wave velocities of the Berea sandstone for the Pp= 10 MPa constant pore pressure run	256
A.22	CO ₂ saturated P-and S-wave velocities of the Berea sandstone for the Pp= 25 MPa constant pore pressure run	257
A.23	Water saturated P-and S-wave velocities of the Berea sandstone at T=23°C for varying pore pressures.....	265

List of Figures

1.1	Atmospheric concentrations of CO ₂	3
2.1	CO ₂ versus sea water density	10
2.2	Time lapse seismic images of pre- and post-CO ₂ injection	23
2.3	Amplitude difference maps of the Midale-Marly horizon	23
2.4	Amplitude differenced image between pre-and post injection at SACROC	25
2.5	P-wave tomogram from cross-well survey in Frio, Texas	27
2.6	Depiction of Xue and Oshumi's transducer array.....	30
3.1	A generic phase diagram.....	38
3.2	CO ₂ phase diagrams	40
3.3	Creep and recovery response of a viscoelastic medium	48
3.4	Relaxation and recovery response of a viscoelastic medium.....	49
3.5	Stress and strain varying sinusoidally with time.....	51
3.6	The basic principle behind ultrasonic pulse transmission method.....	66
3.7	Illustration of phase velocity determination.....	71
3.8	The time series signals recorded through varying lengths of acrylic	73
3.9	The amplitude spectra of the times series signals through acrylic	74
3.10	P-wave attenuation coefficient and quality factor.....	76
3.11	S-wave attenuation coefficient and quality factor.....	76
4.1	P-and S-wave piezoelectric ceramics used	81
4.2	Cartoon and photograph of a transducer	83
4.3	A fully prepared and assembled sample ready for measurement.....	84
4.4	A simplified schematic and photograph of the laboratory equipment	86
4.5	Waveforms from buffer measurements over a confining pressure range of 5 MPa to 50 MPa	93

4.6	P-wave signals through only the buffer and through the buffer with sample under a confining pressure of 15 MPa	93
4.7	P-wave time series signals of the porous ceramic rod acquired at dry conditions under 5 MPa and 40 MPa confining pressure	99
4.8	The P-wave amplitude spectra and the resulting differential attenuation coefficient	100
5.1	Photographs of the samples used	103
5.2	Cumulative and incremental mercury porosimetry intrusion curves for the porous ceramic rod.....	108
5.3	Cumulative and incremental mercury porosimetry intrusion curves for the Berea sandstone	109
5.4	Photograph of Tiny Perm II, portable air permeameter system.....	111
5.5	Schematic diagram of the four electrode circuit	114
5.6	SEM images of the porous ceramic rod at 5 kX and 20 kX.....	116
5.7	SEM images of the Berea sandstone at 500 X and 10 kX	117
6.1	Normalized waveforms under dry conditions at room temperature for the porous ceramic rod displayed as wiggle traces and color amplitudes	120
6.2	Dry P-and S-wave wave velocities with errors as a function of confining pressure for the porous ceramic rod.....	122
6.3	CO_2 's bulk modulus and density phase diagram with the applied measurement conditions superimposed for the porous ceramic rod.....	123
6.4	Normalized CO_2 saturated P-and S-wave waveforms of $T = 28^\circ\text{C}$ and $T = 40^\circ\text{C}$ constant temperature runs	124
6.5	Normalized CO_2 saturated P-and S-wave waveforms of $P_P = 7$, $P_P = 10$, and $P_P = 25$ MPa constant pore pressure runs.....	126
6.6	Dry and CO_2 saturated P-and S-wave velocities with error for all constant temperature runs.....	127
6.7	Dry and CO_2 saturated P-and S-wave velocities with error for all constant pore pressure runs	128
6.8	Observed and Gassmann's modelled P-and S-wave velocities for $T = 28^\circ\text{C}$ and $T = 40^\circ\text{C}$ constant temperature runs	130

6.9	Observed and Gassmann's modelled P-and S-wave velocities for $P_P = 7$, $P_P=10$, and $P_P=25$ MPa constant pore pressure runs	132
6.10	Observed and Biot's modelled P-and S-wave velocities for $T = 28$ °C and $T = 40$ °C constant temperature runs	133
6.11	Observed and Biot's modelled P-and S-wave velocities for $P_P = 7$, $P_P=10$, and $P_P=25$ MPa constant pore pressure runs	134
6.12	Observed P-and S-wave differential attenuation coefficient for $T = 28$ °C and $T = 40$ °C constant temperature runs.....	135
6.13	Observed P-and S-wave differential attenuation coefficient for $P_P = 7$, $P_P =10$, and $P_P=25$ MPa constant pore pressure runs	137
6.14	Biot's modelled P-and S-wave differential attenuation coefficient for $T = 28$ °C and $T = 40$ °C constant temperature runs	139
6.15	Biot's modelled P-and S-wave differential attenuation coefficient for $P_P = 7$, $P_P=10$, and $P_P=25$ MPa constant pore pressure runs	140
6.16	Biot's critical frequency computed for the CO ₂ saturated porous ceramic rod	142
6.17	Normalized water saturated P-and S-wave waveforms as a function of pore pressure.	143
6.18	Dry and water saturated P-and S-wave velocities with error.....	144
6.19	Observed and Gassmann's modelled water saturated P-and S-wave velocities	145
6.20	Observed and Biot's modelled water saturated P-and S-wave velocities	146
7.1	Normalized waveforms under dry conditions at room temperature for the Berea sandstone displayed as color amplitudes	153
7.2	Dry P-and S-wave velocities with error as a function of confining pressure for the Berea sandstone	154
7.3	CO ₂ 's bulk modulus and density phase diagram with the applied measurement conditions superimposed for the Berea sandstone.....	155
7.4	Normalized P-and S-wave waveforms for $T = 23$ °C and $T = 55$ °C constant temperature runs	156

7.5	Normalized P-and S-wave waveforms for the $P_P = 7$, $P_P = 10$, and $P_P = 25$ MPa constant pore pressure runs	158
7.6	Dry and CO_2 saturated P-and S-wave velocities with error for all constant temperature runs.....	159
7.7	Dry P-and S-wave velocities with error as a function of confining pressure of two dry measurement runs of the Berea sandstone	160
7.8	Corrected dry and CO_2 saturated P-and S-wave velocities with error for all constant temperature runs.	161
7.9	Dry and corrected CO_2 saturated P-and S-wave velocities with error for all constant pore pressure runs	163
7.10	Observed and Gassmann's modelled P-and S-wave velocities for $T = 23$ °C and $T = 55$ °C constant temperature runs	164
7.11	Observed and Gassmann's modelled P-and S-wave velocities for $P_P = 7$, $P_P=10$, and $P_P=25$ MPa constant pore pressure runs	165
7.12	Observed and Biot's modelled P-and S-wave velocities for $T = 23$ °C and $T = 55$ °C constant temperature runs	167
7.13	Observed and Biot's modelled P-and S-wave velocities for $P_P = 7$, $P_P=10$, and $P_P=25$ MPa constant pore pressure runs	167
7.14	Observed P-and S-wave differential attenuation coefficients for $T = 23$ °C and $T = 55$ °C constant temperature runs.....	169
7.15	Observed P-and S-wave differential attenuation coefficients for $P_P = 7$, $P_P = 10$, and $P_P=25$ MPa constant pore pressure runs	170
7.16	Biot's modelled P-and S-wave differential attenuation coefficient for $T = 23$ °C and $T = 55$ °C constant temperature runs	172
7.17	Biot's modelled P-and S-wave differential attenuation coefficient for $P_P = 7$, $P_P=10$, and $P_P=25$ MPa constant pore pressure runs	173
7.18	Biot's critical frequency computed for the CO_2 saturated Berea sandstone	175
7.19	Normalized water saturated P-and S-wave waveforms as a function of pore pressure	176
7.20	Dry and water saturated P-and S-wave velocities with error.....	177

7.21	Observed and Gassmann's modelled water saturated P-and S-wave velocities	177
7.22	Observed and Biot's modelled water saturated P-and S-wave velocities	178
A.1	Normalized P-and S-wave waveforms under dry conditions at T = 23°C for the porous ceramic rod	209
A.2	Normalized P-and S-wave waveforms under heated dry conditions at a constant confining pressure of 10 MPa for the porous ceramic rod	209
A.3	Dry P-and S-wave wave velocities with errors as a function of confining pressure for the porous ceramic rod.....	210
A.4	Heated dry P-and S-wave velocities with errors as a function of temperature for the porous ceramic rod under a $P_c=10$ MPa	211
A.5	Normalized P-and S-wave waveforms of the CO ₂ saturated porous ceramic rod for all measured constant temperature runs	214
A.6	Dry and CO ₂ saturated P-and S-wave velocities with error for all constant temperature runs for the porous ceramic rod	215
A.7	Observed and Gassmann's modelled P-and S-wave velocities for all constant temperature runs for the porous ceramic rod.....	218
A.8	Observed and Biot's modelled P-and S-wave velocities for all constant temperature runs for the porous ceramic rod	219
A.9	P-and S-waves amplitude spectra for all constant temperature runs for the porous ceramic rod.....	220
A.10	Observed P-and S-wave differential attenuation coefficient for all constant temperature runs.....	221
A.11	Biot's modelled P-and S-wave differential attenuation coefficient for all constant temperature runs	222
A.12	Normalized P-and S-wave waveforms of the CO ₂ saturated porous ceramic rod for all measured constant pore pressure runs.....	223
A.13	Dry and CO ₂ saturated P-and S-wave velocities with error for all constant pore pressure runs for the porous ceramic rod.....	227
A.14	Observed and Gassmann's modelled P-and S-wave velocities for all constant pore pressure runs for the porous ceramic rod.....	228

A.15	Observed and Biot's modelled P-and S-wave velocities for all constant pore pressure runs for the porous ceramic rod.....	229
A.16	P-and S-waves amplitude spectra for all constant pore pressure runs for the porous ceramic rod.....	230
A.17	Observed P-and S-wave differential attenuation coefficient for all constant pore pressure runs of the porous ceramic rod	231
A.18	Biot's modelled P-and S-wave differential attenuation coefficient for all constant pore pressure runs of the porous ceramic rod.....	232
A.19	Normalized water saturated P-and S-wave waveforms as a function of pore pressure for the porous ceramic rod.....	233
A.20	Dry and water saturated P-and S-wave velocities with error of the porous ceramic rod.....	234
A.21	Normalized P-and S-wave waveforms under dry conditions at T = 23°C for the Berea sandstone of the first run	236
A.22	Normalized P-and S-wave waveforms under dry conditions at T = 23°C for the Berea sandstone of the second run	236
A.23	Dry P-and S-wave wave velocities with errors as a function of confining pressure for the Berea sandstone of the first and second run.....	237
A.24	Normalized P-and S-wave waveforms of the CO ₂ saturated Berea sandstone for all measured constant temperature runs.....	240
A.25	Dry and corrected CO ₂ saturated P-and S-wave velocities with error for all constant temperature runs of the Berea sandstone	242
A.26	Observed and Gassmann's modelled P-and S-wave velocities for all constant temperature runs of the Berea sandstone	246
A.27	Observed and Biot's modelled P-and S-wave velocities for all constant temperature runs of the Berea sandstone	247
A.28	P-and S-waves amplitude spectra for all constant temperature runs of the Berea sandstone	248
A.29	Observed P-and S-wave differential attenuation coefficient for all constant temperature runs of the Berea sandstone	249

A.30	Biot's modelled P-and S-wave differential attenuation coefficient for all constant temperature runs of the Berea sandstone	251
A.31	Normalized P-and S-wave waveforms of the CO ₂ saturated Berea sandstone for all measured constant pore pressure runs	253
A.32	Dry and corrected CO ₂ saturated P-and S-wave velocities with error for all constant pore pressure runs of the Berea sandstone.....	254
A.33	Observed and Gassmann's modelled P-and S-wave velocities for all constant pore pressure runs of the Berea sandstone.....	258
A.34	Observed and Biot's modelled P-and S-wave velocities for all constant pore pressure runs of the Berea sandstone.....	259
A.35	P-and S-waves amplitude spectra for all constant pore pressure runs for the Berea sandstone	260
A.36	Observed P-and S-wave differential attenuation coefficient for all constant pore pressure runs of the Berea sandstone	261
A.37	Biot's modelled P-and S-wave differential attenuation coefficient for all constant pore pressure runs of the Berea sandstone.....	262
A.38	Normalized water saturated P-and S-wave waveforms as a function of pore pressure for the Berea sandstone.....	263
A.39	Dry and water saturated P-and S-wave velocities with error of the Berea sandstone	264

List of Symbols

Symbol	Description
A_0	Initial wave amplitude
A	Wave amplitude, Surface area
$A(\omega)$	Amplitude spectrum of a signal
A, Q, R	Biot parameters
ber	Real part of Kelvin function
bei	Imaginary part of Kelvin function
C	Elastic stiffness constant
C'	Storage modulus
C''	Loss modulus
D_{pore}	Pore throat diameter
$D(\omega)$	Amplitude spectrum of receiver
d	Grain diameter
E	Young's modulus
E_{stored}	Stored energy
ΔE	Energy dissipated in a cycle
f	Frequency
f_C	Critical frequency
$F(\omega)$	Viscosity correction factor
G	Geothermal gradient
$G(\omega)$	Geometric effects
g	Gravity, pore size parameter
J_n	Bessel functions of order n
K	Bulk modulus

K_{dry}	Bulk modulus of dry sample
K_f	Bulk modulus of pore fluid
K_s	Bulk modulus of mineral grains
K_{sat}	Bulk modulus of saturated sample
k	Real wavenumber
k^*	Complex wavenumber
L, L_s	Sample length
L_C	Actual path through network of pores
L_0	Straight path through sample
ΔL	Amount of sample shortening
l	Path traveled by electrical current
M	P-wave modulus
m	Mass of sample
P	Pressure
P_c	Confining Pressure
P_d	Differential Pressure
P_p	Pore Pressure
ΔP	Change in pressure
Q	Quality factor
q	Darcy velocity
R	Electrical Resistance, Reflection coefficient
R_{saline}	Resistance of saline
R_{sample}	Resistance of saturated sample
$S(\omega)$	Amplitude spectrum of outgoing pulse
T	Temperature, period, response function
ΔT	Change in temperature
t	time
t_b	Travel time through buffer
t_{bs}	Travel time through buffer and sample

t_s	Travel time through sample
Δt_{phase}	Phase lag in time between signals
u	Displacement
V	volume
V_e	Envelope volume
V_g	Grain volume
V_{group}	Group velocity
V_{HG}	Volume of mercury
V_p	P-wave velocity
V_{phase}	Phase velocity
V_s	S-wave velocity, Volume of sample cell
V_R	Volume of reference cell
x	Traversed distance
z	Depth
α	Attenuation coefficient, tortuosity, linear expansion coefficient
β	Biot coefficient
γ	Coefficient of fluid content, surface tension of mercury
δ	Delayed response, error
ϵ	strain
η	Fluid viscosity
θ	Volumetric strain, contact angle of mercury
κ	Permeability
λ	Lamé first parameter
μ	Lamé second parameter Shear modulus
μ_{dry}	Shear modulus of dry saturated
μ_{sat}	Shear modulus of saturated sample
ν	Poisson's ratio

ϕ	Porosity
ϕ_c	Critical Porosity
$\Delta\phi$	Phase difference of two waveforms
ρ	Density, Electrical Resistivity
ρ_b	Bulk density
ρ_g	Grain density
ρ_{12}	Coupling mass density
σ	Stress
τ	Tortuosity
ω	Angular frequency

Chapter 1

Introduction

1.1 Climate Change

Scientists have long announced the observed increase of the overall Earth's surface temperature in the last century. According to the Fourth Assessment Report (AR4) released in 2007, the Intergovernmental Panel on Climate Change (IPCC) concluded that the average global surface temperatures have increased by $0.74 \pm 0.18^{\circ}\text{C}$ in the last century, with accelerated warming during the last two decades. Increases in sea levels are consistent with the warming; global sea levels have risen at an average rate of 1.8 mm/yr from 1961 to 2003, with the average rate accelerating to 3.1 mm/yr from 1993 to 2003. It has been estimated that thermal expansion accounts for 57% of the sea level increase and the remaining 43% is from the melting of glaciers, ice caps, and polar ice sheets. In addition to the average temperature rise, evaporation increase has caused winds and ocean currents to shift impacting global weather systems. Precipitation has significantly increased in eastern parts of North and South America, northern Europe, and northern and central Asia while precipitation has decreased in the Sahel, the Mediterranean, southern Africa and southern Asia over the last century. Severe weather events such as storms, floods, hurricanes, tornadoes, and blizzards have been more frequent and more intensive in the last few decades. Changes in ecosystems have also been documented with the warming. More evidence are showing an earlier arrival of spring events (bird migration, leaf unfolding), a poleward shifts of plants and animals, changes in the abundance of algal, plankton, and fish in high latitude oceans, and an earlier migration of fish in rivers.

The Earth's climate depends on a balance of energy from the amount received from the sun and the amount radiated back out to space. The most favoured explanation for this climate change concerns greenhouse gases (GHG) such as carbon dioxide (CO_2), methane (CH_4), nitrous oxide (N_2O), and halocarbons (gases containing fluorine, chlorine, or bromine). Greenhouse gases tend to trap heat in the atmosphere, and therefore increased concentrations of GHG in the atmosphere would consequently yield a warmer surface on the Earth.

Some of these GHG are released into the atmosphere naturally but human activities have significantly increased the emissions. CO_2 is the most important anthropogenic GHG by contributing 77% of the total anthropogenic GHG emissions in 2004. CO_2 emissions have dramatically increased since the start of the industrial revolution in 1750. Preindustrial levels of atmospheric CO_2 were 270 parts per million (ppm) compared to current date concentrations of 390 ppm, and levels are currently increasing at 2 ppm per year (figure 1.1). This increase is blamed on anthropogenic releases through the combination of fossil fuel usage and land practices, with the former holding a more dominant role. The annual emission in 2004 was 38 gigatonnes of CO_2 , mainly coming from electricity production, transportation, heating buildings and industrial processes. Energy demand is expected to rise as global population grows and developing nations expand their economies. Energy consumption is predicted in some scenarios to double between 2010 and 2050. Fossil fuels (oil, natural gas, and coal) are currently the primary source for power generation and account for 85% the world's energy needs. With such substantial energy usage predicted for the future, the current dependence on using fossil fuels to drive the world economies, and the growing evidence linking atmospheric CO_2 concentrations to climate change, methods to mitigate CO_2 emission are direly needed to avoid catastrophic environmental effects.

The different CO_2 mitigation methods can be classified as either reducing CO_2 sources or increasing CO_2 sinks. Increased energy efficiency, energy conservation, low- or zero- carbon alternatives for energy generation, and carbon capture and storage (CCS) are all ways to mitigate CO_2 emissions. As research

Changes in GHGs from ice core and modern data

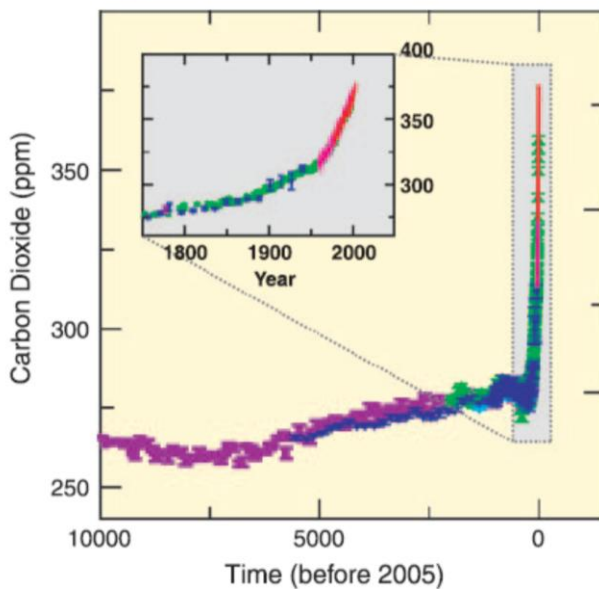


Figure 1.1: (Figure reproduced from IPCC (2007))* Atmospheric concentrations of CO₂ inferred from ice core measurements (different colored symbols for different core studies) and from atmospheric measurements (red line).

and development continues on increasing the supply of alternative energy to a level that can support the world's growing population and economies, CCS methods are deemed as the next most effective way, albeit stopgap, to combat the issue at hand. A variety of CCS techniques exist; each utilizing a different component of the Earth's natural system and each with their own problems to overcome to be effective. The different carbon sequestration methods available will be briefly described in the next chapter. Geologic sequestration is the most practiced storage technique to date and involves the injection of concentrated CO₂ into a subsurface rock formation for containment. Given the range of temperature and pressure conditions possible in the upper sedimentary basin, CO₂ can exist as a gas, liquid, or a supercritical fluid when in the subsurface. The largest factor controlling the acceptance of geological storage is the safe and secured containment of the injected CO₂. Therefore the ability to monitor, to verify, and

*Climate Change 2007: Synthesis Report. Contribution of Working Groups I, II, and III to the Fourth Assessment Report of the Intergovernmental Panel on Climate Change, Figure 2.3. IPCC, Geneva, Switzerland.

to account for the injected CO₂, is very important. Geophysics will play a key role in site selection through reservoir characterization and, in the monitoring and verification of the injected CO₂ in deep geologic formations over time.

1.2 Aim of Research and Chapter Description

Time lapse seismic surveys are an integral component of any monitoring and verification program in a geological sequestration projects. Seismic methods are used because the seismic behavior of a rock formation is not only sensitive to its mineralogical composition and porosity, but also its pore fluid content. Using seismic methods for subsurface monitoring has two aims in geological sequestration: 1.) qualitatively locate and track the movement of the CO₂ plume, and 2.) quantitatively determine the amount of CO₂ in place. CO₂'s seismic properties, bulk modulus and bulk density, are considerably different than those of other in-situ pore fluids such as oil and brine. Therefore introduction of CO₂ into the pore space would yield a change in the overall seismic signature allowing the movement of the subsurface CO₂ to be qualitatively tracked from seismic surveys. Quantitatively tracking by determining the amount of CO₂ from the changes in a seismic signal however is a much harder issue to deal with; seismic velocity change has been demonstrated to be very slight for CO₂ saturations past ~20%. Furthermore, unlike typical pore fluids encountered in-situ, CO₂ can exist as three different phase state which adds complexity to the accurate interpretation of seismic. Using other seismic attributes to accurately determine the saturation levels of CO₂ and thus quantifying CO₂ currently are subjects of ongoing research.

Understanding the effects of fluid saturation and its variability on seismic responses is crucial to the improvement of monitoring the movement and to the quantification of CO₂. CO₂ rock physics will undoubtedly play an essential part in accurate seismic interpretation over geological sequestration fields. Rock physics will enable us to relate the geological properties (e.g. porosity, lithology, saturation) of a rock at certain physical conditions (e.g. pressure, temperature) with its the corresponding elastic and seismic properties (e.g. elastic modulus,

velocity, impedance). The earliest systematic measurements of variations in the acoustic properties of rocks appeared in the 1950/1960 period and in the last 30 years, many studies have been made to understand and relate the physical properties of rocks to geophysical observations. Relationships between seismic wave velocities (P- and S- wave) and porosity, saturation, and effective pressure have been largely investigated, especially on sandstones. Some of these relationships involve the effects of pore pressure, temperature, lithology, pore structure, and fluid type. Studies on the subject of intrinsic attenuation have also been investigated, but to a lesser extent than wave velocities. The fluids used in rock physics studies typically involve water/brine or oil, and sometimes glycerol. The first known rock physics study using CO₂ as a pore fluid was inspired by its role in enhanced oil recovery processes and was not conducted until 1989 by Wang and Nur. Only recently have more CO₂ rock physics studies appeared but fundamental studies on the effects of CO₂ fluids under in-situ pressure and temperature conditions are still lacking. All related studies to date involve the injection of CO₂ into a porous media pre-saturated with another in-situ fluid and the acoustic variations observed are usually from a combination of pore pressure and fluid substitution effect. Problems with these studies are the partial saturation of CO₂ is usually unknown and the observed changes solely due to CO₂ cannot be quantitatively determined.

To differ from previous studies, my work involves full CO₂ saturation and pore fluid effects will be separated from pore pressure effects. Here, a systematic study is conducted on P- and S-wave velocities and attenuations in synthetic and real rock samples under in-situ conditions when fully saturated with CO₂ in the gas, liquid, or supercritical fluid phase states. Realistically, full saturation is unlikely in geological sequestration projects, but it is important to have an end member study in order to constraint the more complex and more probable cases of partial saturation.

Chapter 2 provides background information on carbon storage. A brief overview is provided on the types of carbon storage available with special emphasis given to geological CO₂ sequestration. The concerns of safety and

monitoring associated with geological sequestration are discussed, along with the monitoring methods that are currently available. Examples of the various seismic methods that have been employed in geological sequestration projects around the world are given. This chapter concludes with a literature review on previous laboratory rock physics work that have been conducted with CO₂.

Chapter 3 discusses the theoretical background that is relevant to the work conducted in this thesis. To begin with, CO₂'s thermodynamic behavior is introduced and the plausible phase states that can occur in a sequestration project are discussed. Following this brief introduction on CO₂, the basic concepts behind the theory of elasticity, wave propagation, and the effect of viscoelasticity on a material's behavior are provided. The theoretical fluid substitution formulations of Gassmann and Biot, their assumptions, and their applicability are reviewed and contrasted. Finally, an introduction to the foundation of the ultrasonic pulse transmission laboratory technique, an introduction to the analysis of the resulting wave velocity and wave attenuation, and an example to demonstrate attenuation analyzes conclude the chapter.

Chapter 4 focuses on the experimental setup and the laboratory procedures followed to obtain the laboratory results for this thesis. The construction of piezoelectric transducers, the required sample preparation, and the experimental configuration for the measurements are presented. A detailed description of the experimental procedure and of the data analysis followed in this study is also provided. The errors associated wave velocity and differential attenuation coefficient are assessed in this chapter.

Chapter 5 examines the petrophysical properties of the samples used for measurements. The bulk density, grain density, porosity, pore size distribution, air permeability, and tortuosity were addressed using a variety of laboratory techniques. In addition, scanning electron microscope images were used to reveal the microstructure of the samples.

Chapter 6 and chapter 7 presents the laboratory results and discuss the findings of the synthetic and non-synthetic sample, respectively. The wave velocity's dependencies on pressure, temperature and fluid-type saturation are

highlighted. In addition, the laboratory results are compared to the theoretical predictions of Gassmann and Biot. The similarities and differences between the observed results of the two samples are given in chapter 7.

Chapter 8 is the concluding chapter of this thesis where an overview of the work is provided, the contributions of the findings are discussed, and directions for future work are suggested.

Chapter 2

Background on Carbon Storage

In the previous chapter, a brief introduction on climate change was made. Increasing energy efficiency, energy conservation, alternative energy development and usage, and carbon capture and storage are ways to help reduce greenhouse gas emissions. Carbon capture and storage involves capturing anthropogenic CO₂ (usually from a large nearby point source) and storing such that it does not enter the atmosphere. In this chapter issues related to CO₂ storage, monitoring options and studies pertaining to CO₂ laboratory velocity measurements in porous media will be briefly reviewed. The material presented here in this chapter related to geological sequestration is the underlying motivation for my work.

2.1 Types of CO₂ sequestration

The scientific community has suggested various methods to store the captured CO₂ in response to mitigating global warming associated with increased anthropogenically induced CO₂. The feasibility of each proposed method depends on its scale of implementation, costs, additional research and development, and permanence. The more promising methods are oceanic, terrestrial, mineral carbonation, and geological sequestration.

1. Oceanic

Atmospheric CO₂ is regularly taken up in the ocean waters naturally through dissolution and it is estimated that 500 gigatons (Gt) of the 1300 Gt of emitted anthropogenic CO₂ have been naturally taken up by the world's ocean in the last

two centuries. It is also estimated that the world's ocean has a capacity to hold 39,000 Gt-C (gigatons of carbon) and is therefore considered a prime candidate because of this large storage potential (Rackley, 2010). Storage options in the ocean consist of injecting CO₂ into the ocean, from a fixed pipeline or from a moving ship in waters greater than 1000 m depth, and storage is attained by direct dissolution in the seawater.

One alternative to direct dissolution, storage in the ocean can be attained by injecting CO₂ at depths greater than 3000 m where the CO₂ can pool and form a lake in the deep waters of the ocean. Under the pressure and temperature conditions of very deep waters, CO₂ is denser than the surrounding saline seawater and therefore by the effects of gravity the injected CO₂ is presumed to stay on the ocean floor (Figure 2.1). Over time the CO₂ will dissolve and disperse in the surrounding waters.

Both methods of oceanic disposal of CO₂ are not permanent because the ocean plays a major part in the global carbon cycle. The surface of the ocean is in continual exchange with the atmosphere for CO₂ and therefore the dissolved CO₂ in the ocean will eventually equilibrate with the atmospheric CO₂. Furthermore, critics of this method argue that the injection of large amounts of CO₂ into the ocean will cause major negative ecological impact such as the increased acidification of the oceans from the dissociation of CO₂ in water and the extent of biological impact is unknown (Seibel and Walsh, 2001, Fabry et al, 2008). Oceanic disposal, therefore may create additional environmental problems while only temporary solving the original issue.

2. Terrestrial ecosystem:

CO₂ is naturally taken up from the atmosphere by photosynthesis. Some of this "captured" CO₂ will be released to the atmosphere through respiration while some may reside longer in the soils and biomass. A rough estimate of the net retention of CO₂ due to terrestrial processes is 2.8 Gt-C per year (Rackley, 2010). Terrestrial sequestration of CO₂ can be achieved by increasing the transfer of CO₂ from the atmosphere into soils and vegetation, and by limiting CO₂ emissions

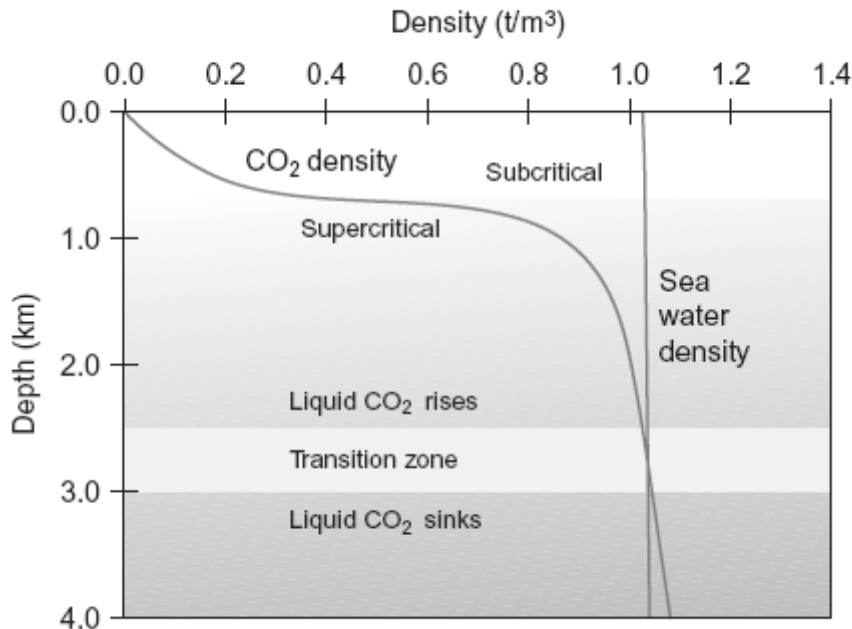


Figure 2.1: (Figure reproduced from Rackley (2010))* CO₂ versus sea water density over a range of ocean depth.

from terrestrial ecosystems into the atmosphere.

To be effective, CO₂ needs to be held in long-lived terrestrial carbon pools such as above- and below ground biomass (large capacity vegetations such as trees), long-lived products from biomass (from wood), and stabilized organic carbon fractions in soils. Practices in minimizing soil disturbance (no-till farming and soil erosion control), increase return of crop residues to soils, afforestation on degraded and marginal agricultural soils, growing plants with a large capacity for carbon storage, and refined logging techniques to reduce forest disturbances are ways to enhance carbon sequestration.

Current problems associated with this type of sequestration are determining the storage permanence and quantifying the global impact from the ecosystem on climate change with confidence. The interactions and feedbacks between ecosystems and the atmosphere is complex, and the current understanding of the factors that may interrupt and affect intermediate processes is limited.

*This figure was published in Carbon Capture and Storage, Stephen A. Rackley, Copyright Elsevier (2010).

3. Mineral carbonation:

In mineral carbonation, CO₂ is locked away by reacting it with naturally occurring Mg and Ca minerals from highly abundant silicates and oxides in the Earth's crust to form stable carbonates. The conversion process is an exothermic reaction and therefore is thermodynamically favorable because the formed carbonates are in a lower energy state than free CO₂. Geologically, this is a naturally occurring process in respect of weathering and formation of rocks and occurs on a scale of a hundred thousand years. For the purpose of CO₂ sequestration, this process can be accelerated from geological time scales by exposing the materials to an optimal reaction temperature and pressure conditions. Also, pre-treatment (heat treatment, grinding, etc) and additives or catalysts (aqueous solutions with Na₂CO₃, molten MgCl₂ salts, hydrochloric acid) can be applied to the raw materials and have been shown to facilitate the reaction time in producing carbonates. The stable carbonates formed can be stored in the mines where the original silicates or oxides were extracted. The new products are volumetrically larger than the original minerals, therefore terrain profile change maybe expected. Mineral carbonation is the only storage method where leakage is not a concern because the produced carbonates are in an inert, stable, solid form.

4. Geological Sequestration:

Geological sequestration is any means of injecting CO₂ into the subsurface and containing it in a rock formation. Suitable rock formations for storage are ones with high pore volume, located at depths greater than 1000 m, and are capped by a layer of non-porous rock above. A typical working scheme for geological storage involves capturing CO₂ at a point source (e.g. coal plant, drilling rig platform), processing for near pure CO₂, shipping to injection site via pipeline, pressurizing into liquid or supercritical form and injecting into suitable subsurface formations. Depleting oil and gas reservoirs, coal beds, and saline aquifers are all suitable sites for sequestering CO₂, each with a suite of trapping mechanisms.

Globally, depleted oil and gas reservoirs have an estimated storage capacity between 675 to 900 Gt-C (IPCC, 2005). The estimated storage in

western Canada (British Columbia, Alberta, Saskatchewan, and Manitoba) is 1.04 Gt-CO₂, with Alberta contributing 75% to this total (Bachu and Shaw, 2004). Depleted oil and gas reservoirs are favorable sites since they have been highly characterized by the hydrocarbon industry, and the sealing cap has proved to be effective from housing hydrocarbons for millions of years before oil or gas production.

Also, some oil reservoirs considered as ‘depleted’ in the past, usually still contain a significant amount of residual oil for production. This residual oil can be recovered by injecting fluids such as CO₂ into the reservoir to build up in situ pressure and to reduce the viscosity of the residual oil for easier mobilization. Some of this injected CO₂ will be produced along with oil, while some will be permanently stored from this process. Enhanced oil recovery using CO₂ has been in use since the 1970’s and its impact as a carbon storage option is currently the main focus of the IEA GHG Weyburn-Midale EOR project in Saskatchewan, Canada. It is argued that the usual high cost of geological CO₂ sequestration can be offset from the profits of the recovered oil. The trapping mechanism for depleted oil and gas reservoirs initially consists of structural trapping via impermeable cap rock as the injected CO₂ buoyantly rises in the geologic formation, followed by solubility trapping from the dissolution of the trapped CO₂ with the in-situ pore fluids. Given time, mineral trapping will be the ultimate carbon locking mechanism for carbon storage where new and stable minerals will form from the chemical reactions between the dissolved CO₂ and surrounding minerals.

Saline aquifers hold un-potable waters unsuitable for consumption and irrigation, but these aquifers could also become important for carbon storage with an estimated capacity to sequester between 1000 and 10,000 Gt-C. The trapping mechanisms of CO₂ in saline aquifers are essentially the same as in depleted oil and gas reservoirs except saline aquifers have an additional trapping mechanism called residual-phase trapping. Residual-phase trapping is also known as capillary trapping and this process involves the imbibition of water into the CO₂ plume.

This mechanism will immobilize the trailing edges of CO₂ and will slow up-dip migration.

Since they did not contain hydrocarbons, saline aquifers are not as well characterized as to hydrocarbon reservoirs due to the lack of obvious financial benefits. However saline aquifers have the advantages of vastly larger reservoir capacity, lower risk of leak paths from the fewer penetrations wells, and are more widespread in occurrences. The probability that a suitable saline aquifer sequestration site is close to a large CO₂ producer is also higher leading to reduced transportation cost. For example, at Statoil's Sleipner field sequestration project, the saline aquifer used for CO₂ injection is in the same geographic location as the natural gas reservoir that produces the CO₂, but located above the reservoir. The CO₂ is produced, removed from the natural gas, and injected into the saline aquifer from the same rig, on adjacent platforms (Kongsjorden et al, 1998).

Deep un-mineable coal beds or coal beds used for methane production are also suitable geologic options for sequestration. In coal beds, the retention of CO₂ is accomplished by adsorption trapping from the preferential adsorption of CO₂ onto coal than that of the natural occurring methane on coal. It has been shown that CO₂'s affinity to coal is at least twice that of methane due to its larger heat of adsorption (Liang, 2003; Rackley, 2010). Natural occurring methane on coal will then be desorbed and displaced by the inject CO₂ thereby allowing for coal bed methane recovery to occur while sequestering CO₂. Similar to EOR, enhanced coal bed methane (ECBMR) has financial benefits to help offset the costs for sequestration. A notable problem with ECBMR using CO₂ is that the permeability of the coal beds may decline due to the swelling of the coal matrix from the absorption of CO₂. This will restrict the flow of CO₂ for sequestering and impede the recovery of the displaced methane. The carbon sequestering capacity of un-mineable coal beds is up to 200 Gt-C (IPCC, 2005).

2.2 Examples of Geological Sequestration

Currently, geological sequestration appears to be the most economically and technically feasible long term storage for achieving significant reductions in atmospheric CO₂ emissions. It is the only carbon storage method applied on a commercial scale to date. Worldwide there are numerous geologic storage projects varying on small and large scales, mostly involving oil fields for EOR or saline aquifers. Currently there are 4 commercial scale storage projects operating around the world aimed at greenhouse gas mitigation.

Sleipner:

The Sleipner project is the world's first industrial-scale CO₂ injection project, operated by StatOil and partners offshore in the North Sea. In 1996 CO₂ injections began in the Sleipner field into a major saline aquifer, the Utsira formation. The Utsira formation is a 200 m thick sandstone formation located 800 m below the seafloor and is capped by a thick shale layer while containing multiple thin intra-reservoir shale layers. The CO₂ used for injection is produced from a natural gas reservoir in the Heimdal formation that is located in the same field but 1200 m deeper. The CO₂ is stripped from the natural gas produced and processed on the same platform for injection. Today, about 12 Mt-CO₂ have been injected at a maximum rate of 1 Mt per year. The injections are expected to proceed for 20 years.

Weyburn:

The IEA GHG Weyburn-Midale CO₂ Monitoring and Storage Project is an international collaboration with Cenovus Energy's and Apache Corporation's enhanced oil recovery operations in Saskatchewan, Canada. CO₂ injections started in late 2000 in the Weyburn and the Midale oil fields. Injections at both fields are in carbonates at depths of about 1500 m with general thickness less than 30 m. The reservoirs have caprocks composed of anhydrites from the Midale Evaporite and of anhydritized dolostones, which in turn are overlain by aquitards. Currently over 15 million tons have been stored between the two fields at a rate of

more than 2 million tons per year. The CO₂ for the injection comes from a synfuel plant located in north Dakota that supplies 2.7 million cubic meters of CO₂ per day to the Weyburn-Midale fields via a 325 km pipeline. It is estimated that approximately 35 Mt of anthropogenic CO₂ will have been stored in the reservoir by the end of the operations.

In Salah:

The In Salah CO₂ storage project began operations in 2004 and is a joint venture between BP, Sonatrach, and StatOil located in Algeria. CO₂ is injected into a 20 m thick saline formation located 1900 m below the ground, and is positioned down dip from the producing gas horizon. The storage formation, the Krechba reservoir, is composed of Carboniferous sandstone and is overlain by 950 m of impermeable mudstone, the same caprock that keeps the up dip natural gas in place. The CO₂ used for injection is produced from surrounding gas fields, processed at nearby gas plants and transported to the injection site. By 2008, 2.5 Mt-CO₂ have been stored with a future rate anticipated of 1.2 Mt per annum.

Snohvit:

Operated by StatOil, the first CO₂ injection at Snohvit in the Barent Sea was in April 2008. The CO₂ is stored in a sandstone layer can the Tubaen formation that is located 2500 m beneath the seabed and is underneath the gas containing formations where the CO₂ is produced from. The Tubaen formation is between 45 m to 75 m thick and is sealed by an overlying shale formation. It is estimated that 0.7 Mt-CO₂ will be stored annually.

2.3 Safety and Monitoring

The definition of storage permanence or successful sequestration is one that retains 99% of the injected CO₂ over 1000 years (IPCC, 2005). Understanding the geologic, hydrologic, geomechanical and geochemical processes in the subsurface are the keys to a successful and secure sequestration, as these are important factors that will influence the fate of the sequestered CO₂.

But nonetheless, monitoring will be required and will always be an essential component to any CO₂ sequestration project. The greatest resistance for a widespread implementation of geological sequestration is the public acceptance of the associated risks. Concerns with geological sequestration involve the safety of the practice for both the public and nearby natural resources, and its effectiveness in mitigating CO₂ levels in the atmosphere.

Carbon dioxide's effect on human health at low concentration is benign, composing 0.039% of the atmosphere, which is approximately 390 ppm and is currently increasing at a rate of 2ppm/yr. At an increase to 1000 ppm, health symptoms including headaches, nausea, and drowsiness can appear in some people. The Occupational Safety and Health Administration maximum acceptable level for long exposures is 5000 ppm. Exposures at levels surpassing 5000 ppm can lead to oxygen deprivation resulting in brain damage, coma or death.

Another concern with the leakage of geologically sequestered CO₂ is the impact on local environments. CO₂ seepage to the surface, will affect all living organisms apart from just humans. Local ecologies, habitats such as plant health and plant species distributions can drastically change with an influx of CO₂. Tree kills and tree plant stress caused by elevated CO₂ soil concentration levels, caused by subsurface magma interactions in Mammoth Mountain, CA, demonstrate the possible environmental catastrophic effect if CO₂ were to escape to the surface through hidden faults. In the subsurface, migration of CO₂ to a fresh water aquifer can contaminate the potable groundwater resource by creating an acidic solution when CO₂ dissociates in water.

If in an environment where both human and natural resources are not in harm, monitoring the subsurface is still essential. If a storage project is failing, this needs to be known so the injection process could be stopped immediately to avoid wasting resources and effort. For governments, policy makers, and businesses, knowing how much CO₂ have been injected and retained in the subsurface will allow for inventory verification for national accounting, carbon fines and taxes assessments, and carbon credit trading.

Monitoring CO₂ sequestration projects will then serve a few purposes in this regard. Successful monitoring will detect and allow for advance action in response to a leakage that may put human health or natural resources in jeopardy, and in otherwise successful containment, serve the purpose of inventory verification and the assurance of the storage integrity.

There are various measurement technologies that can be applied for monitoring in the case of leakage. Essentially they can be split between direct and indirect measurement methods.

2.4 Direct monitoring measurements

For direct measurements, CO₂ can be sampled in the air, water, or soil. In the air at the storage sites, sensors similar to ones found in occupational settings such as infrared gas analyzers are used that can allow for continuous and real time monitoring of the level of CO₂. Gas sampling bags, gas chromatography, and mass spectrometry are also used in checking air quality (Benson and Myer, 2002). In water, monitoring can occur from geochemical sampling from the surface or at observational wells. In observation wells, fluid samples can be collected and analyzed for changes in brine composition and for the presence of natural and injected tracers. By using pH levels, gas compositions, and tracers, CO₂ breakthrough at the well location can be determined as well as the possible chemical reactions that have taken place in the subsurface from the CO₂-water-rock interaction (Gunter et al., 2001, Blencoe et al., 2001). For soil monitoring gas surveying, probes or accumulation chambers are placed in or on the soil, and samples are analyzed periodically to determine gas composition and fluxes. Seasonal and local variations of CO₂ flux need to be accounted for.

2.5 Indirect monitoring measurements (Geophysical)

The methods listed above are only effective if there is a CO₂ leak or there is access to an observational well. Therefore direct methods limit advance preparation in the case of a leakage and their application is inadequate for providing information on the subsurface movement of the CO₂ away from the

wells. To remedy these shortcomings, indirect monitoring techniques, namely geophysical methods, can be applied in conjunction with direct measurements. The various geophysical methods that can be applied to detect underground CO₂ from the surface are land surface deformation, electromagnetic, gravitational, and seismic.

Geophysical methods are the most favored and applied monitoring techniques in geologic sequestration because of the widespread use and experience from their application in the hydrocarbon industry. The feasibility of any geophysical technique depends on the inherent resolution of the technique and the magnitude of change in the measured geophysical properties produced by increasing the CO₂ concentration.

2.5.1 Geodetic

Subsurface pore pressure changes causing land surface deformation can occur when injecting CO₂ underground. This displacement of the Earth's surface can be used to infer the migration of CO₂ and can be monitored using tiltmeters, global positioning system (GPS) and satellite/airborne interferometric synthetic aperture radar (InSAR).

Tiltmeters can be placed on the ground surface or in boreholes and have the potential to measure very small tilts, as small as one nanoradian (Sweatman and McColpin, 2009). Modern day tiltmeters use a highly sensitive electrolytic bubble level where an arrangement of electrodes senses the precise position of the bubble in the electrolytic solution. In 2010, tiltmeters were employed for the first time in a commercial scale injection project where 71 tiltmeters were deployed in the In Salah project over one of the CO₂ injectors.

GPS, a satellite-based positioning system, is well-known for providing reliable position coordinates when 4 or more satellites are accessible. To achieve higher precision than the conventional GPS, differential GPS (DGPS) is being utilized in CO₂ sequestration projects. In DGPS more than one GPS receiver is used. One of the receivers is placed in an area with minimal displacement while the other receiver(s) is/are placed where displacement is expected. DGPS allows

for compensation of atmospheric variations and errors, permitting millimeter horizontal and vertical readings to be achieved.

InSAR can produce high spatial resolution surface deformation maps (a typical coverage is 10, 000 km²) and is capable of detecting up to millimeter-scale changes on Earth. A beam of microwave energy is projected to the surface of the earth and when this energy is reflected back, images of the surface can be generated. The tilt of a surface caused by volumetric change can be measured by the phase shift between reflected pulses recorded at two different times. InSAR is currently used for monitoring at the In Salah CO₂ injection project, and have detected uplifts centered on the injection wells up to 21 mm after 3 years of injection (Falorni et al, 2010).

2.5.2 Electromagnetic (EM)

Electromagnetic techniques are responsive to the electrical resistivity of earth materials where the electrical resistivity of a rock formation is affected by its porosity, fluid saturation, and pore fluid resistivity. Therefore monitoring CO₂ in saline aquifers based on electrical methods is feasible, because changes in brine saturation would be notable due to the highly-resistive electrical nature of CO₂ with respect to the surrounding brine. In petroleum reservoirs however, both hydrocarbons and CO₂ are electrically resistive. As a result of this small electrical contrast between the original and the new pore fluid, the detection of CO₂ would be less sensitive in a hydrocarbon-bearing reservoir than in a saline aquifer. Using EM as a monitoring method is the most optimal in saline aquifers.

Electromagnetic methods involve measuring an induced or secondary electric and magnetic field from the subsurface generated by a time varying source or primary electric field. The measured fields hold information about the electrical distribution of the subsurface. A commonly exercised electromagnetic method in geologic sequestration is the cross well survey which consist of two adjacent wells, one containing transmitters and the other containing receivers. The tomography of the conductive structure between the transmitting and receiving wells can be mapped, and the ongoing replacement of original pore fluid

with CO₂ can then be monitored. Cross well EM imaging have been successful in measuring subsurface distribution of CO₂ in Frio brine formation in south Texas (Hovorka et al., 2005) and the migration of CO₂ during an EOR flood in Lost Hills oil field in southern California (Hoversten et al, 2003). In west Texas' Vacuum Oil field CO₂ flood, Wilt et al (2003) used EM to map CO₂ floods and they have shown good correlation between porosity distribution and resistivity variation.

2.5.3 Gravitational

Gravity measurements detect variations in the subsurface rock and pore fluid density from gravitational acceleration changes. CO₂ for most of the depth interval of interest for sequestration is less dense than that of oil or water. So an introduction of CO₂ into a brine or oil filled reservoir will decrease the overall bulk density which in turn will produce a change in the gravitational attraction from the reservoir. For optimal detection and the success of surface gravity, large material contrasts such as high porosity, shallow reservoir and high temperatures causing low densities would be ideal. From the size of the gravity variations, subsurface mass changes can be inferred allowing quantification of the amount of CO₂ in place. From spatial gravity variations, the lateral movement and distribution of CO₂ can be reflected.

Gravity stations are easily deployable at the surface and are relatively cheap for large spatial coverage. However, because gravity anomalies decay with the inverse square of the distance from the source, measured responses at the ground surface from the changes in gravitational attraction of the reservoir would yield weak response and could quite possibly be in the background noise level (Gasperikova et al., 2008, Hare et al., 1999). Alternatively, gravity stations can be placed inside boreholes in existing wells, thereby reducing the distance to the reservoir allowing for larger magnitude of change to be detected. However this is feasible only at the cost of substantially reduced data coverage due to the limited distribution of existing borehole.

Modelled time lapse results using Schrader Bluff oil field in Alaska by Gasperikova and Hoversten (2006) over a time interval of 20 years show direct correlation of spatial pattern change in the vertical component of gravity with net change in reservoir density. In the offshore sequestration project the Sleipner field, gravimetric measurements were conducted on the seafloor in 2002 and 2005. Notable gravimetric change is observed from the time lapse measurements and is being used to constrain the *in situ* CO₂ density estimates (Nooner et al, 2007).

2.6 Seismic

Of these geophysical methods, seismic imaging is by far the most highly developed and extensively applied. Seismic resolution is generally recognized to be higher than gravity and electromagnetic methods and is deemed as a feasible time-lapse method for monitoring (Arts et al. 2002, Newmark et al. 2002, Hoversten et al 2003, Gritto et al, 2004, Saito et al 2006, Shi et al 2007). Seismic waves depend on both the density and the elastic stiffness of the medium of propagation where the pore space content can have a large effect on these parameters. Varying pore space content can lead to sharp contrasts in acoustic impedance, consequently generating distinct high amplitude reflections. CO₂ is generally more compressible and, as stated earlier, is less dense than oil or brine. Seismic methods offer the potential to identify migration or leakage from the storage reservoir and the potential to quantify the amount of CO₂ in place based on reflected amplitudes and velocity pushdown effects. This quantitative capability of seismic methods is currently under ongoing research.

The variations of seismic methods that can be used for monitoring are surface seismic, vertical seismic profiling (VSP), and cross well seismic. For surface seismic, the source and the receivers are placed along the surface and 2D or 3D data can be acquired. In terms of lateral coverage, surface seismic can provide the most amount of spatial and geometric information for the CO₂ plume, the reservoir and the overburden. However, surface seismic when compared to the other two wellbore seismic methods, is the lowest in resolution. In vertical

seismic profiling, the source is located on the surface while the receivers are placed along the wellbore and higher resolution of the near borehole environment can be obtained. Even higher resolution can be obtained by cross well seismic. Cross well seismic, similar to cross well EM, requires a pair of boreholes close to or in the reservoir with a string of sources placed in one and a string of receivers are in the other.

2.6.1 Surface seismic

Time lapse surface seismic is the most commonly used monitoring technique in CO₂ sequestration or CO₂ enhanced oil recovery projects. All four commercial scale CO₂ sequestration projects, Sleipner, Weyburn, In Salah, and Snohvit have a time lapse surface seismic component in their monitoring program. In Sleipner, surface seismic was acquired in 1994 for pre-injection and then repeated in 1999, 2001, 2002, 2004, 2006, and 2008 for post-injection (figure 2.2). Significant differences can be noted between the pre and post injection surveys by the presence of bright reflections and their growth with time. The horizontal reflectors are interpreted to be thin layers of CO₂ accumulating underneath the many thin mudstone layers inside the reservoir and the reservoir caprock. Underneath the interpreted CO₂ plume, velocity push-down effect is apparent due to the slower wave travel through the CO₂. The plume is interpreted to be roughly 200 m thick, and in plan view the plume is elongated with a major axis of 3000 m from the 2008 seismic survey.

In Weyburn, pre-injection surveys were acquired in 1999 and subsequent post-injection surveys were acquired in 2001, 2002, 2004, and 2007 to monitor the movement of the CO₂ flood as brine and oil are produced (figure 2.3). In plan view, the negative amplitude differences in the sequential 3D surveys are clearly visible. The largest reflection amplitude changes are around the horizontal injecting wells. Generally, there is a good agreement between injection volumes and the areal extent and intensity of the amplitude and travel time anomalies. Rostron et al (2009) suggest the observed seismic response is mainly from CO₂ saturation effects rather than from pressure induced effects. They argue that, first,

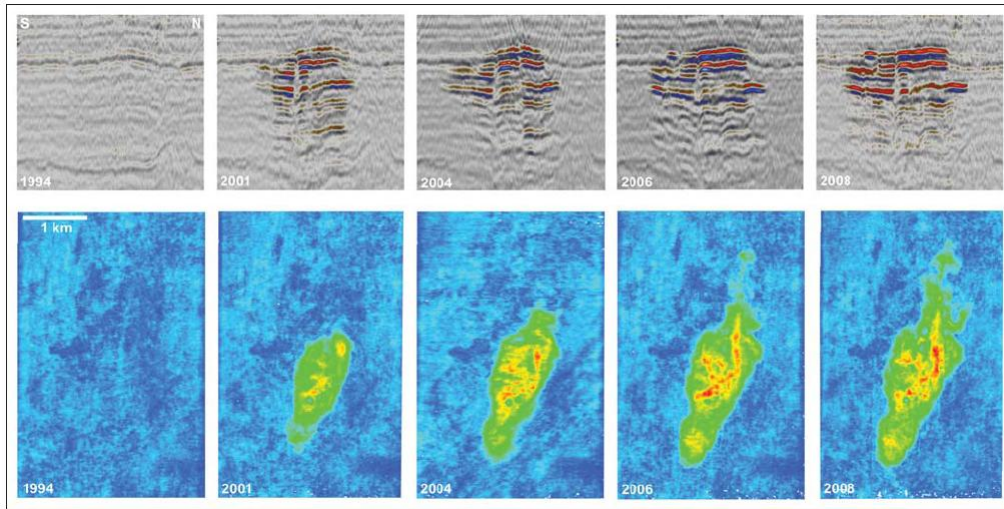


Figure 2.2: (Figure reproduced from Chadwick et al (2010))^{*} Time lapse seismic images of pre- and post-CO₂ injection: (top) North-south inline through plume; (bottom) Plan view of total reflection amplitude in plume.

there is a weak correlation between the P-wave amplitude anomalies and monitored or predicted pressure changes, second, time-travel delays can be modelled from saturation effects by using the reservoir thickness and velocity variation, and last, there is no correlation between the P-wave and S-wave time lapse anomalies suggesting the P-wave anomalies are primarily saturation related because S-waves are relatively insensitive to fluids.

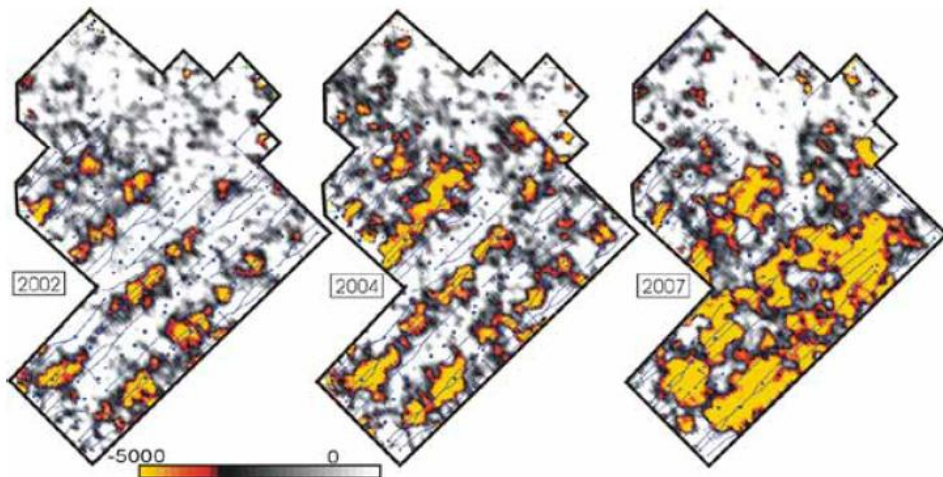


Figure 2.3: (Figure reproduced from White (2009))^{*} Amplitude difference maps of the Midale-Marly horizon. Only negative amplitude differences are shown.

*Reprinted with permission from the Society of Exploration Geophysicists.

The In Salah and Snohvit storage project in relation to Sleipner or Weyburn is a relatively much younger and the monitoring to date is still in its early stages. For In Salah, the first time lapse 3D seismic survey to monitor pore saturation and pressure changes was conducted in 2009. So far there has been little published on the results.

2.6.2 Vertical Seismic Profiling:

VSP generally provides higher frequency (higher resolution of 10-30 m) data than surface seismic methods. In comparison, VSP waves travel shorter distances and the sensors are placed below the near surface, therefore leading to a less attenuated signal.

The repeatability of VSP is also higher than surface seismic because the receivers' exact location in the borehole is known and can be replicated accurately for each survey. From these advantages of VSP, smaller scale plumes could be detected which would otherwise not be seen with surface seismic. Moreover, the VSP method can be useful for interpreting surface seismic by aiding the tie of surface seismic to borehole measurements. Since VSP allows measurements of both direct and reflected waves, the reflected waves are from the same interfaces that also produces the reflected waves for surface seismic. Application of VSP in imaging CO₂ has succeeded at various sites:

In 2001, a CO₂ EOR pilot project was launched by Anadarko Petroleum at the Patrick Draw Field in Wyoming, U.S in the Monell sandstone unit. A baseline VSP survey was acquired in 2002 and another VSP survey was recorded at the end of the project in 2003 with 430 million cubic feet of CO₂ injected in between the two surveys. From the differenced volume of the time-lapse surveys, a clear amplitude change associated with the CO₂ flood in the vicinity of the well is apparent. Apart from the change in reflection strength in the second survey, velocity push-down is also present underneath the CO₂ flood. From analyzing the amount of velocity push-down present, it has been determined that the P-wave velocity decreased between 14-19%. Also from the time-lapse surveys, it was determined that the injected CO₂ has migrated 215-275 m (700-900 ft) radially

away from the injection well, with a preferential up-dip movement. This observation is in agreement with production data.

In Frio, Texas, about 1600 tons of CO₂ were injected into an onshore saline aquifer for a small scale pilot test of CO₂ injection at a depth of 1500 m. A 70% increase in reflection amplitude and an increase of wave travel time were observed between pre- and post- CO₂ injection for the Frio horizon (Daley et al, 2008). Surveys were conducted pre-injection in July 2004 and post-injections were surveyed in November 2004.

In another project in Texas, two sets of VSP surveys were acquired in the SACROC oil field in west Texas; a baseline in 2008, and the repeated survey in 2009. CO₂ was injected at a depth of 2000 m into a reef structure and the amount injected between the two surveys was not mentioned. Figure 2.4 shows the differenced image between 2008 and 2009 surveys. A preliminary observation of the image shows an identifiable change in reflectivity at the injection zone. Further analysis is currently in progress.

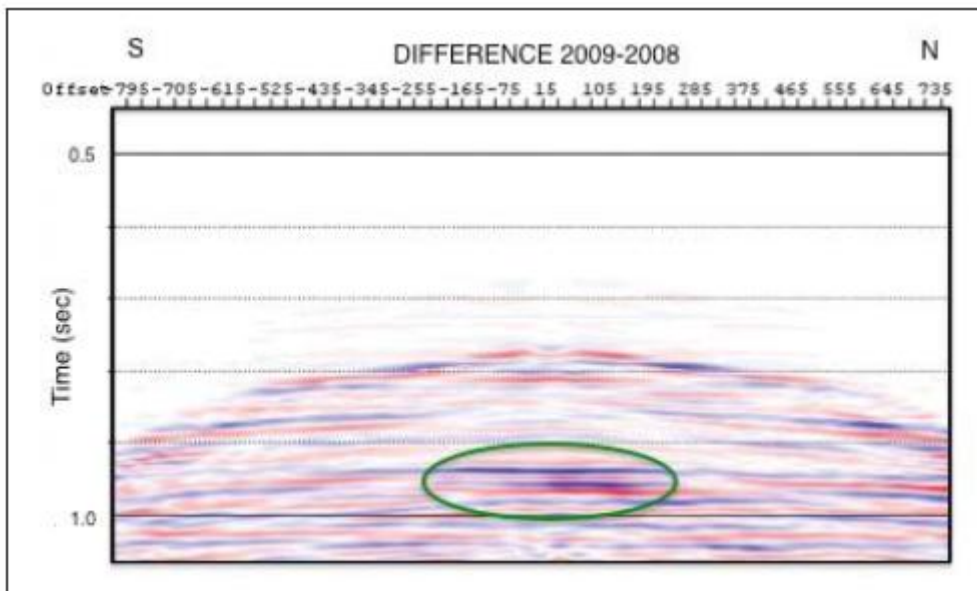


Figure 2.4: (Figure reproduced from Cheng (2010))^{*} Amplitude differenced image between pre-and post-injection at SACROC oil field. Green circle highlights the injection zone.

^{*}Reprinted with permission from the Society of Exploration Geophysicists.

2.6.3 Cross-well Imaging:

Of all three seismic methods, cross-well seismic survey has the highest resolution of 1 to 5 m, compared to 10-30 m for VSP and 30-100 m for surface seismic. The source along with the receivers is placed in the subsurface; therefore the high frequency components of a signal are preserved even more from the attenuating near surface materials. Likewise to VSP, survey repeatability is enhanced by permanently embedding the receivers and the sources (in this case) in the borehole. The purpose of using crosswell seismic surveys is to provide a spatial, high-resolution map of the subsurface CO₂ and from this attempt to estimate the CO₂ saturation between the two wells by using P- and S-wave velocity tomographic imaging. Velocity tomography between the wells is produced from the analysis of the one-way wave travel times recorded for each source-receiver pair and ray theory. A major limitation of using crosswell imaging is that only the region between the source and receiver wells is imaged. Examples of using crosswell seismic surveys in CO₂ sequestration projects are:

In Frio, Texas crosswell seismic surveying was conducted between source and receiver wells located 30 m apart. High resolution tomographic images of P-wave velocity change illustrated the CO₂ distribution between the two wells. Seismic P-wave velocity decreased up to 500 m/s and the S-wave velocity showed minimal change (Daley et al, 2008). The velocity change follows the dip of the local stratigraphy and is caused by buoyant forces acting on the injected CO₂ leading to an up-dip migration (figure 2.5). Velocity variation is not homogeneous in the injected layer with less variation near the top, which agrees with the lowered permeability observed near the top of the sands from well logs.

In Nagaoka, Japan between 2003 and 2006 multiple cross well seismic surveys were conducted during the injection of 12700 tonnes (14000 tons) of CO₂ at an onshore CO₂ sequestration pilot test in a porous sandstone reservoir at 1100 m depth. The source and receiver wells have slight deviation from the vertical where the horizontal separation between the top source and receiver wells is 92 m, while the horizontal separation of the bottom source and receiver is 200 m. Crosswell seismic data were measured before injection started and after 2902,

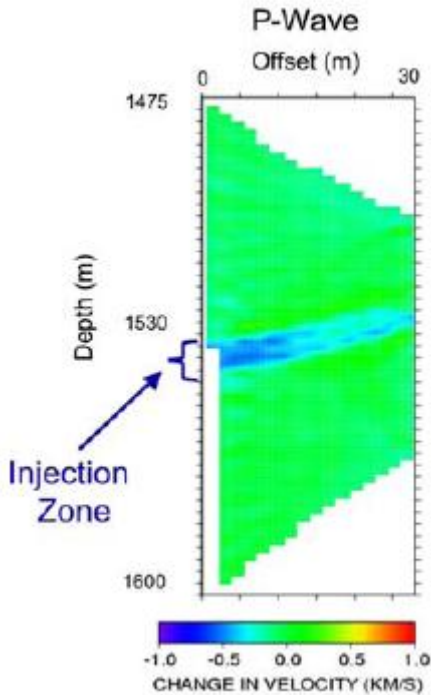


Figure 2.5: (Figure reproduced from Daley (2008))* P-wave tomogram from cross-well survey in Frio, Texas.

5623, 8072, and 9434 tonnes (3200, 6200, 8900, and 10400 tons, respectively) of CO₂ were injected. The greatest time-lapse changes occurred between pre-injection and 3200 and 6200 tons, with minor differences between the 6200 and 10400 ton injections (Spetzler et al, 2008). From the time lapse tomographic velocity images, Spetzler et al (2008) determined that there was an -18% velocity anomaly.

2.7 Review of existing literature on CO₂ laboratory measurements

As reviewed above, seismic techniques are the most promising methods in monitoring the subsurface related to CO₂ storage. Although CO₂ injections into the subsurface have been conducted for some time now, there exist a very limited number of laboratory studies on examining the elastic effects of CO₂ on pore fluid

*With kind permission from Springer Science+Business Media: Environmental Geology, Time-crosswell seismic and VSP monitoring of injected CO₂ in a brine aquifer, 54, 2008, 1662, Daley, T. M., Myer, L. R., Peterson, J. E., Majer, E.L., and Hoversten, G. M., figure 6.

seismic responses. Initial rock physics studies involving CO₂ had a focus directed to assisting EOR processes and only recently has the underlying focus of the existing studies been shifted to monitoring, verification, and accounting for carbon storage purposes. All laboratory work to date has exercised the ultrasonic pulse transmission technique and demonstrated that the presence of CO₂ in the pore space will lower seismic velocities due to its higher compressibility compared to other possible in-situ fluids. A review of existing rock physics literature on seismic velocity measurements with CO₂ will follow.

One of the first published laboratory studies involving CO₂ as a pore fluid saturant was done by Wang and Nur (1989). Their investigation was motivated by the lack of understanding of CO₂ flooding effects on the seismic properties of rocks saturated by hydrocarbons and using seismic methods in the field to assist EOR processes. P- and S-wave velocities (V_p and V_s, respectively) in seven sandstones of various porosities (6 to 29%) initially saturated with n-hexadecane C₁₆H₃₄ were measured before and after CO₂ flooding. For each sample CO₂ measurements were completed at two temperatures, 21°C and 60°C as pore pressure varied from 2 to 16 MPa while confining pressure was maintained at 20 MPa. They determined that P-wave velocities decreased greatly due to CO₂ flooding, and the extent of decrease was dependent upon porosity, temperature, and effective pressure whereas S-wave velocities were less affected. The authors concluded that the amount of decrease in P-wave velocities caused by the CO₂ flooding may be seismically resolvable so that the CO₂ zones can be mapped and tracked such that the flooding processes can be controlled to optimize EOR process.

In 1998, another rock physics study of CO₂ flooding in the laboratory was published by Wang et al. The authors were trying to understand the velocity changes observed from the crosswell seismic imaging surveys conducted at the CO₂ injection pilot project at the McElroy field in west Texas. In their experiment, 8 dolostone core samples were obtained from the reservoir,

representing the range of porosities and permeability available. The samples were initially saturated by an oil/water mixture, and then flooded with CO₂. CO₂ velocity measurements on each sample were done at a constant confining pressure of 20 MPa with the pore pressure varying from 8.3 MPa to 17.9 MPa while subjected to the reservoir temperature of 31°C. From the combined effect of CO₂ fluid substitution and pore pressure buildup, V_p reduction varied from 3 to 10.9%, while reductions in V_s varied from 3.3 to 9.5%. These magnitudes of velocity change are to the same extent as the observed velocity changes from field results using time-lapse crosswell tomographic imaging. For CO₂ accounting purposes, the authors suggested that the changes in pore fluid property effects can be semi-quantitatively separated from pore pressure buildup effects in field seismic by comparing changes in V_p with V_s. V_p is sensitive to both CO₂ saturation and pore pressure change while V_s is particularly sensitive to the latter. Consequently if a significant change in V_p is observed and is not mirrored by V_s observations, this would imply that pore pressure build up is not the main cause of the velocity change. As well, during the experiments the largest V_p and V_s changes are observed with high porosity and high permeability rocks and the authors suggested that it may be possible to distinguish high porosity and high permeability zones seismically if the size of the zones are within seismic resolution based on velocity changes.

From the Research Institute of Innovative Technology for the Earth (RITE) in Japan, in the last 10 years a suite of literature has been published as a part of the research effort for the Research and Development of Underground Storage Technology for Carbon dioxide initiative. One of the first studies was done by Xue and Oshumi (2002) where they monitored the movement of a CO₂ front during the flooding of gaseous CO₂ in a water saturated porous sandstone carried out by measurements of P-wave velocities under hydrostatic pressure. Their experiment consisted of a dense array of sixteen piezoelectric transducers arranged in a 4×4 configuration at two orthogonal directions along the axial direction of the core (figure 2.6). Two pore pressure tubes were connected to the sample, one on each end of the sample and served as either the inlet or the outlet

for the pore fluid. The outlet valve was kept opened during the CO₂ flooding to minimize velocity changes due to pore pressure build up. They demonstrated significant reduction in P-wave velocities (typically on the order of 10%) due to the displacement of water by the injected gaseous CO₂.

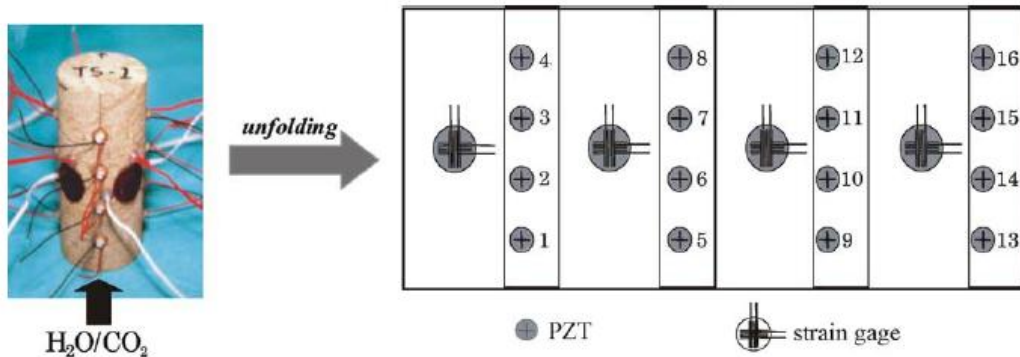


Figure 2.6: (Figure reproduced from Xue et al (2005))* Depiction of Xue and Oshumi's (2002) transducer array on their core in their experiment.

Xue and Oshumi (2004) further modified and developed their work by rearranging the configuration of their piezoelectric arrays so that the sixteen piezoelectric transducers now formed two (instead of four) parallel lines along the axial direction of the core and they conducted their tests with the injection of different phase states of CO₂. It was observed that the largest velocity reductions were recorded when using supercritical CO₂.

In another study, Xue and Lei (2006) used differential arrival time to display the velocity changes during the injection tests by P-wave velocity tomograms. Time lapse velocity images for each injection showed variations in P-wave velocity across the sample as the CO₂ swept through the core. The highest velocity decrease was observed during the supercritical CO₂ injection and the lowest velocity reduction was during gaseous CO₂ injection. They concluded that the heterogeneity of the pore distribution in the rocks and the different injected CO₂ phases contributed to observed differences in P-wave velocity images. Expanding on these preliminary results related to P-wave velocity, Lei

*Reprinted from Energy, 30, Xue, Z., Oshumi, T., and Koide, H., An experimental study on seismic monitoring of a CO₂ flooding in two sandstones, 2352-2359, 2005, with permission from Elsevier.

and Xue (2009) developed tomographic images of relative attenuation coefficient to refine their work in mapping CO₂ migration and water displacement. They reported that on average, P-wave velocity fell by 7.5, 12, 14.5% and the attenuation coefficient increased by factors of 3.3, 2.7, and 3.7 during the injection of gaseous, liquid, and supercritical CO₂ respectively.

Also from the same data set obtained, Shi et al (2007) focused on the dynamic behavior of the P-wave velocity during the supercritical CO₂ injection tests. The authors attributed the considerable variations in velocity reductions across the sample to the final state of saturation (uniform, patchy, or in between) of the two-phase fluids. Based on the amount of velocity reductions observed and from comparing them to Gassmann's modelled velocities corresponding to patchy and uniform saturation, they suggest regions of the core closest to the injection point reached uniform saturation while large patchy saturations occurred farthest from the injection point. The authors tried to integrate the laboratory data with a numerical simulation of a simplified 1D model to provide an estimation of the phase saturation changes underlying the measured P-wave velocity change observed. However, when they compared their empirically established relationship between measured P-wave velocities (corrected for velocity dispersion) and estimated CO₂ saturation to Gassmann's prediction for uniform and patchy saturation, there is a clear deviation from both velocity curves.

From the Korea Institute of Geoscience and Mineral Resources, Park et al (2009) have also carried out ultrasonic laboratory measurements on a sandstone sample to characterize the effects of CO₂ injection on seismic velocity and amplitude. They noted a reduction of 6% in velocity or more until full CO₂ saturation has been reached and the wave amplitude decreased more than the velocity decrease. In their work, they suggests that the Vs/Vp ratio is more sensitive to CO₂ saturation than the current approaches and this attribute can potentially allow quantitative assessment of CO₂.

Purcell et al (2010) performed lab-scale velocity measurements under in-situ conditions on a reservoir rock sample from the SACROC unit and on other

representative rock samples (shale and Berea sandstone). The work is intended to assist interpretation of repeated 3D reflection seismic surveys over the SACROC oil field to effectively monitor the movements of CO₂ after injection. Laboratory measurements were conducted at room temperature and reservoir temperatures (~50°C) varying pore pressure (from 0 to 30 MPa) while maintaining constant confining pressure (of 30, 40, and 50 MPa). For all 3 constant confining pressure runs at room temperature, it was shown that as pore pressure increased the velocities decreased. This observation with pore pressure change however, is a combined effect from variations in pore fluid property and the changes in differential pressure on the rock. Furthermore, their velocity results showed large fluctuations and the effects of fluid phase change on their velocities cannot be inferred from their data.

Despite the growing number of geological CO₂ sequestration projects and in view of the above laboratory studies involving CO₂, there lacks an extensive, systematic study to inspect the seismic effects from:

- 1.) CO₂ as a lone pore fluid,
- 2.) the different phase states of CO₂,
- 3.) pore fluid property changes that are definitively separated from pore pressure build-up effects.

The first effect on seismic is important for providing an end member study to constrain the possibilities with CO₂ in the pore space. The second and third effects have implications on quantifying CO₂ using seismic. These three seismic effects will be investigated in this thesis.

2.8 Summary

As concerns over climate change loom, governments, policy makers and businesses around the world strive for ways to combat increasing atmospheric CO₂. This chapter provided a brief overview on the types of carbon storage that can be exercised to mitigate CO₂ emissions and issues that can arise from the different storage options. Geological sequestration is the most practiced type of carbon storage with numerous projects on various scales around the world. A

major component of all geological sequestration projects is monitoring the subsurface movement and the behavior of the injected CO₂ for environmental/societal safety concerns and for carbon credit accounting purposes. The different monitoring techniques available were presented and the role of geophysics was discussed. Seismic techniques are deemed as an effective monitoring method and are widely exercised in geological sequestration projects. Published laboratory studies on seismic with porous media containing CO₂ were also reviewed. It was shown that upon CO₂ introduction in the pore space, ultrasonic P- and S- wave velocity reductions were always observed, regardless of the original saturation condition. However, with the minimal amount of rock physic studies to date that have been conducted with CO₂, there are some seismic effects that have yet to be addressed. This background introduction to CO₂ sequestration and the role of geophysics will lead to the next chapter in which the theories relevant to CO₂ rock physics will be discussed.

Chapter 3

Theoretical Background

Whether the motivation behind interpreting seismic data is driven by hydrocarbon/mineral exploration or is from the need to monitor subsurface containments related to safety and reservoir integrity, the behaviour of seismic waves must be well understood in order to be accurately informed about the subsurface. Seismic waves are known to be influenced by both the physical properties of the propagating medium and the ambient conditions such as pressure and temperature. Furthermore wave propagation is highly sensitive to fluids in the pore space and to their variability with changing conditions, leading to the valued use of seismic methods in CO₂ sequestration. This chapter will provide relevant background on the influences of seismic waves in geologic CO₂ sequestration and to the work conducted in this thesis. To begin, a brief introduction is given on the thermodynamics of CO₂, particularly on the elastic properties pertinent to seismic wave propagation. To follow, the basic concepts of elasticity and its relation to wave velocity is provided, along with the concept of viscoelasticity and its implication on wave travel. Next, the rock physics concept of fluid substitution is discussed by the widely used Gassmann's formulation and also the limitations of his equation. This discussion is expanded to include Biot's formulation. Finally, the foundation to the laboratory technique, ultrasonic pulse transmission, and the analysis methodologies applied in this thesis are provided.

3.1 Carbon Dioxide

Carbon dioxide (CO_2) that was first discovered in the 1750's by a Scottish chemist and physician, Joseph Black, is an odourless and colorless gas at standard temperature and pressure. In a CO_2 molecule, the carbon atom is bonded to the two oxygen atoms in a linearly symmetric form and results in a non-polar molecule. It is a commonly encountered substance that plays a major role in the process of photosynthesis for producing carbohydrates, is emitted from volcanoes, hot springs, and geysers, is an important ingredient in carbonate rocks, and as introduced in chapter 1 is a major by-product of combustion. Human uses of CO_2 include the carbonation in beverages, fire extinguishers, the decaffeination of coffee by supercritical fluid extraction, as refrigeration via dry ice, and in pneumatic systems as a compressed gas. Naturally, CO_2 is exchanged between the atmosphere, hydrosphere, biosphere, pedosphere, and lithosphere by a set of complex biogeochemical interactions, known as the carbon cycle.

As discussed in the last chapter, in order to combat the fast- rising atmospheric concentration of CO_2 , geological sequestration is conducted by injecting CO_2 into the subsurface. Concerns about the safety and the integrity of the underground containment have enlisted various methodologies for monitoring the behaviour of the injected CO_2 , where seismic methods are highly favourable. The presences of a pore fluid have been shown to have a strong impact on the elastic properties of a porous medium (Timur, 1968; De Vilbiss, 1980; Christensen and Wang, 1985; Batzle and Wang, 1992). Given the possible pressure and temperature conditions of the upper sedimentary basin, CO_2 can be in a gas, liquid, or supercritical fluid phase state, where each will yield a different effect on seismic waves from the consequent variations in density and fluid compressibility. Therefore the thorough understanding of the elastic properties of CO_2 is crucial to the accurate interpretation of a seismic response.

3.1.1 Introduction to Thermodynamics

Thermodynamics is an area of study that deals with energy transformations and of the relationships between the physical properties of

substances which are affected by these transformations. For a substance that is under a set of physical conditions, the resulting physical behaviour or its state of matter can be described by an equation of state (EOS) through the state variables of pressure, temperature, and specific volume. The simplest and most known EOS is the ideal-gas equation. However this EOS is only adequate at low pressures because the intermolecular forces that become significant at other physical conditions (particularly at higher pressures and lower temperatures) are unaccounted for. Other more accurate and well known general EOS for fluids are the Van der Waals equation, the Virial, the Redlich-Kwong, the Peng-Robinson, and the (Benedict-Webb-Rubin) BWR (Wark and Richards, 1999). At present, there is no single equation of state that accurately predicts the properties of all substances under all conditions.

A phase diagram of a generic substance is shown in figure 3.1. The triple point of a substance marks the condition of where the gaseous, liquid, and solid phase states can coexist in thermodynamic equilibrium. In contrast to the triple point, the critical point of a substance denotes the conditions above which the phase boundary between the gas and liquid phase state ceases to exist. Beyond this point, the properties of the gas and liquid phases are indistinguishable, resulting in only one phase known as the supercritical fluid phase state. A supercritical fluid has physical behaviours of both a gas and a liquid such that its density is comparable to that of liquid and it has a compressibility similar to that of a gas. Above the critical pressure for any temperature, a distinct gas cannot form and above the critical temperature for any pressure, a distinct liquid cannot form. However, for a sufficiently high enough pressure and above the critical temperature, a transition into a solid phase can occur from the supercritical fluid. Furthermore small changes in pressure or temperature near the critical point can yield large changes in density.

3.1.2 CO₂ Phase States

In the last few decades, the thermodynamic properties of CO₂ have been studied extensively and new empirical equation of state (EOS) have been

continuously proposed as more experimental data are acquired and more sophisticated correlation methods are developed (Kessel'man et al, 1965; Stein, 1972; Huang et al, 1985; Ely et al, 1989; Pitzer and Sterner, 1994; Zhang and Duan, 2005; Kim, 2007). The developed correlation equations varied in the base structure of their equation, in the data used for the correlation, and on the temperature/pressure regions of interest. Span and Wagner (1996) presented an empirical EOS for CO₂ that extended from the triple point temperature to 1100 K with pressures up to 800 MPa in the form of the fundamental equation Helmholtz free energy. Span and Wagner's empirical EOS overcame many limitations faced by previous efforts such as being descriptive over a limited physical condition range, data were not represented within their experimental uncertainty, unreasonable results near the critical point, and unstable extrapolations. The estimated uncertainty in their equation for pressures up to 30 MPa and temperatures up to 250°C ranged from 0.03 to 0.05% in density and 0.03% to 1% in the speed of sound. These errors were estimated by comparisons to experimental data and to other equations of state in regions where there were no experimental data. Their empirical EOS for CO₂ is widely used and is currently implemented by the National Institute of Standards and Technology (NIST) chemistry webBook (Lemmon et al, 2011). From their review of existing data, the triple point for CO₂ is $-56.558 \pm 0.003^\circ\text{C}$ and 0.51795 ± 0.00010 MPa, where the critical point is $30.9782 \pm 0.015^\circ\text{C}$ and 7.3773 ± 0.0030 MPa. Based on the typical temperatures and pressures encountered in the subsurface, the solid phase CO₂ is not a concern in geological sequestration. At standard temperature and pressure, CO₂ is about 1.5 times denser than air and the speed of sound is approximately 0.25 times slower than in air.

Based on the thermodynamic model of Span and Wagner, phase diagrams of CO₂'s bulk modulus, density, and fluid viscosity (figure 3.2) were created over a temperature range of 0-60°C and a pressure up to 30 MPa. The bulk modulus and the density of a fluid are the main physical properties that influence elastic wave propagation. The viscosity property of a fluid, however, is only relevant to

high frequency wave propagation in a saturated porous medium. The vapour-liquid boundary is clearly discernible by an abrupt change in all the physical

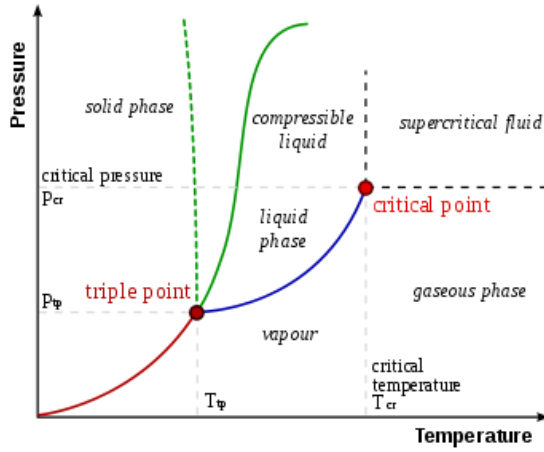


Figure 3.1: (Figure reproduced from Wikipedia)* A generic phase diagram. The dotted green line is the anomalous behaviour of water.

properties. As the critical point is approached, the properties of the gas and liquid phases converge and no distinction is apparent thereafter, yielding the supercritical fluid phase. Consequently, a phase change from a gas or a liquid state into a supercritical fluid state is a smooth transition in physical properties. Furthermore, in the supercritical region close to the critical point, large density variations are clearly seen over a small range of pressure and temperature.

3.1.3 Geological Sequestration Approximate Physical Conditions

Subsurface temperatures and pressures conditions can be influenced by a number of factors (radiogenic rocks, plate tectonic activity, or aquitards, hydrocarbon caps, and sealing faults, respectively) but are generally dependent on the depth from the surface. To provide a simple reference, the conditions that can be anticipated in a geological sequestration project could be modelled by an oversimplified situation where they are only dependent on depth. The temperature variation with depth for a constant geothermal gradient, G , is

$$T = T_o + Gz , \quad (3.1)$$

*attribution: Matthieu marelchal: <http://en.wikipedia.org/wiki/File:Phase-diag2.svg>)

where T_o is the surface temperature, z is the depth from the surface, and the geothermal gradient is typically 15-30°C/km for sedimentary basins and areas away from tectonically active zones. The pore pressure with depth can be assumed to be from the hydrostatic pressure if a fluid can freely flow from the surface to at depth without any permeability barriers (such as aquitards),

$$P_p = \rho_w g z, \quad (3.2)$$

where ρ_w is the density of water and g is the acceleration of gravity. As mentioned in the previous chapter, suitable sequestration formations are typically at depths greater than 1000 m. Using the Earth's average surface temperature of 15°C, and the average typical geothermal gradient of 22.5°C/km, a water density 1000 kg/m³, and a gravity of 9.81 m/s², the minimum temperature and pore pressure to be encountered in a geological sequestration project under the average condition is 37.5°C and 10 MPa, respectively, and is shown by the red dot in figure 3.2d. Based on this simplistic depth model relating subsurface temperature and pressure under the average condition (profile shown by the red-dashed line in figure), free CO₂ in a geologic containment is therefore nearly always expected to be in a supercritical fluid phase. If the CO₂ migrates out of its containment into a shallower formation, it can be in a liquid or a gas phase in the respect of temperature and pressure conditions. As can be seen in the figure, this simplistic profile barely traverses into the liquid regime, indicating that liquid CO₂ would only be expected within a short depth interval. The liquid phase CO₂ could be completely bypassed if a higher geothermal gradient is used, or have a greater presence if a lower geothermal gradient is applied, where the geothermal gradient changes the slope of the profile in a phase diagram plot. In figure 3.2d, the dotted lines are the resulting profiles from using the lower and upper limit of the typical geothermal gradient range, 15°C/km and 30°C/km, respectively. Furthermore, the surface temperature will also influence the position of the profile. A lower or higher surface temperature will shift the profile such that the liquid phase will have a significant presence or will be completely bypassed, respectively. For the purpose of providing a general idea of the type of pressures and temperatures

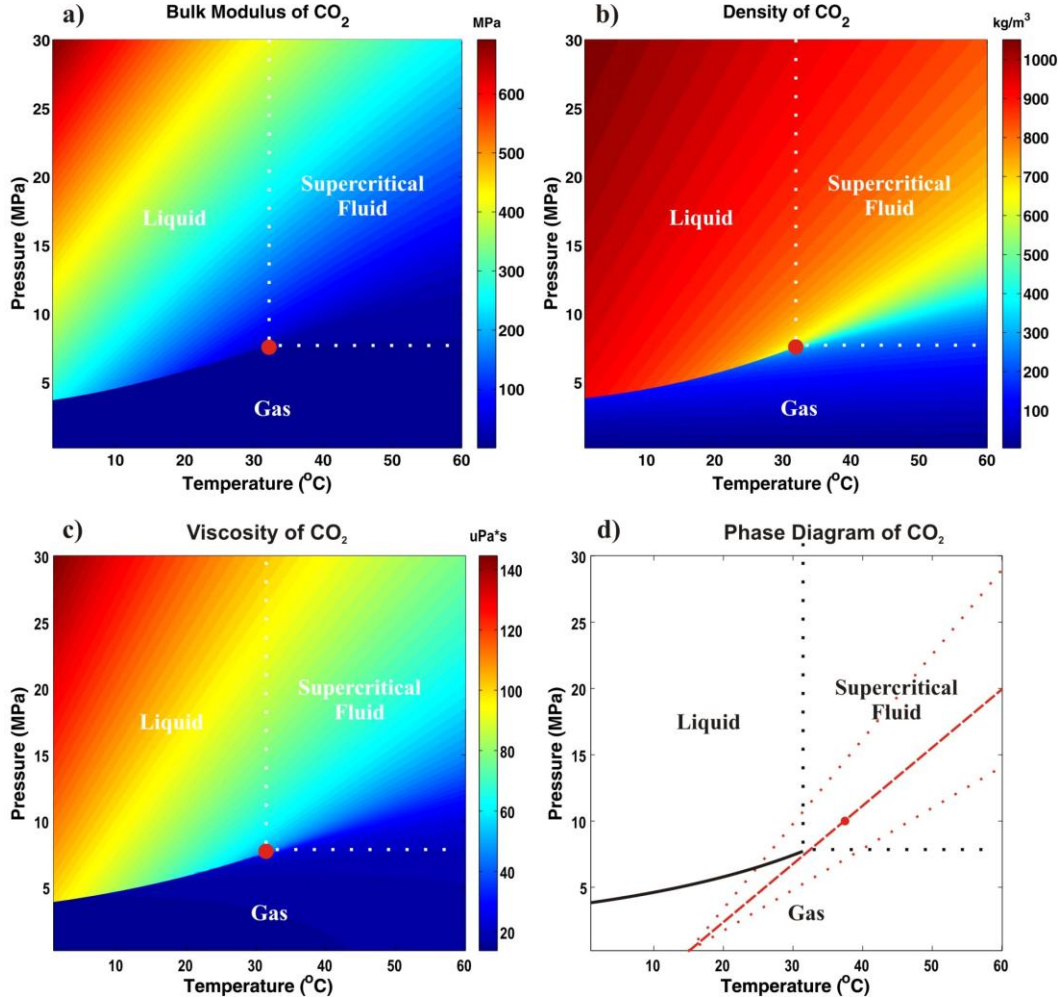


Figure 3.2: CO₂ phase diagrams of (a) bulk modulus, (b) density, (c) and viscosity. The phase boundaries of the supercritical fluid are shown by the white dotted lines. The critical point is marked by the red dot. (d) A basic CO₂ phase diagram with the possible CO₂ sequestration conditions shown by the red dashed-line, based on the simple model described.

that can occur, and consequently the type of phase states, such a simplistic view is sufficient as this is not a case study.

3.2 Seismic Theory

An elastic wave is a mechanical wave that travels in an elastic medium by displacing the particles of the medium. When an elastic wave travels through Earth materials, they are referred to as seismic waves. In this section, the theory of wave travel will be discussed by a brief introduction to the theory of elasticity by the pertinent stress-strain relationship, the resulting wave equation, and the

elastic stiffness constants for an isotropic medium. In addition, viscoelasticity and its implication on wave travel will be introduced. These sections will be briefly reviewed as the in depth discussion have been extensively presented in literature such as Aki and Richards, 1980, Bourbié et al (1987), Telford et al (1990), Lay and Wallace (1995), Lowrie (1997), Lakes (2009) and in any Rock Physics or introductory Geophysics textbooks.

3.2.1 Theory of Elasticity

When a force acts upon an elastic body, physical deformation of the elastic body will occur. This applied force can be further characterized as the applied stress, where stress is defined as the ratio of the applied force to the involved area. Fundamentally, there are two types of stresses and they are defined based on the direction of the applied force in relation to the involved area. If the direction of the force is perpendicular to the area, the stress is called a *normal* stress and if the direction of the force is tangential to the area, the stress is called a *shear* stress. The resulting physical deformation such as changes in the dimensions of the elastic body or a change in shape is described as strain; where normal stress will result in normal strain and shear stress will give shear strain. For a perfectly elastic material, an applied stress will produce in an immediate, reversible strain. The energy used to deform the material is stored so when the stress is removed, the stored energy is used to rebound the material back to its original shape. All displaced material points will resume their original positions and no energy is lost from storing to rebounding.

The mechanical behaviour for a volume of an elastic material can be described by Hooke's law, succinctly in Einstein's summation over repeated indices, as

$$\sigma_{ij} = C_{ijkl} \varepsilon_{kl} \quad i, j, k, l=1, 2, 3 \quad (3.3)$$

which relates stress, σ_{ij} , linearly to strain, ε_{kl} , by the elastic stiffness constant, C_{ijkl} . The stress and strain are second-order tensors composed of nine components that represents the three-dimensionality of a volume, where the indices, i, j, k, l , represents the three orthogonal axes. For a volume that is in static equilibrium,

the total moment is zero, thereby the stress and strain tensors are symmetrical about the main diagonal allowing

$$\sigma_{ij} = \sigma_{ji}, \quad (3.4)$$

$$\varepsilon_{kl} = \varepsilon_{lk}. \quad (3.5)$$

This symmetry reduces the nine component matrices to six independent components. The elastic stiffness constant, C_{ijkl} , is a fourth-order tensor, composed of eighty-one components. Owing to the symmetries of the stress and strain tensors and strain energy considerations, the elastic stiffness tensor has the following equivalency,

$$C_{ijkl} = C_{jikl} = C_{ijlk} = C_{jilk} = C_{klji}. \quad (3.6)$$

Consequently, the number of independent components is reduced to twenty-one. Furthermore, the representation of equation 3.3 can be simplified by employing the Voigt's notation via reducing the rank of a symmetric tensor. Using Voigt's notation, the double indices of 3.3 are transformed to only one index by:

i,j or l,k	I or J
11	= 1
22	= 2
33	= 3
23, 32	= 4
13, 31	= 5
12, 21	= 6.

As a result, equation 3.3 is simplified to

$$\sigma_I = C_{IJ} \varepsilon_J. \quad (3.7)$$

The once fourth-order elastic stiffness tensor is rewritten as a 6×6 symmetric, second-order tensor, C_{IJ} , and the once second-order stress and strain tensor are now 6×1 stress and strain vectors, σ_I and ε_J , respectively. The Hooke's law shown explicitly with these new index adaptations is,

$$\begin{bmatrix} \sigma_1 \\ \sigma_2 \\ \sigma_3 \\ \sigma_4 \\ \sigma_5 \\ \sigma_6 \end{bmatrix} = \begin{bmatrix} C_{11} & C_{12} & C_{13} & C_{14} & C_{15} & C_{16} \\ C_{21} & C_{22} & C_{23} & C_{24} & C_{25} & C_{26} \\ C_{31} & C_{32} & C_{33} & C_{34} & C_{35} & C_{36} \\ C_{41} & C_{42} & C_{43} & C_{44} & C_{45} & C_{46} \\ C_{51} & C_{52} & C_{53} & C_{54} & C_{55} & C_{56} \\ C_{61} & C_{62} & C_{63} & C_{64} & C_{65} & C_{66} \end{bmatrix} \begin{bmatrix} \varepsilon_1 \\ \varepsilon_2 \\ \varepsilon_3 \\ \varepsilon_4 \\ \varepsilon_5 \\ \varepsilon_6 \end{bmatrix} \quad (3.8)$$

For the most general elastic material, twenty-one independent constants is the maximum number of constants required for its behavioural description. Materials that require the full twenty-one elastic constants for description are the least symmetric material and are called triclinic solids. Materials of higher symmetry will contain fewer independent elastic constants. The most simplistic case is an isotropic material, where their physical properties are independent of direction such that they hold infinite symmetry. For an isotropic material only two independent elastic constants, C_{11} and C_{44} are needed and the structure of the Voigt elastic stiffness matrix has the following form:

$$C_{II} = \begin{bmatrix} C_{11} & C_{11} - 2C_{44} & C_{11} - 2C_{44} & 0 & 0 & 0 \\ C_{11} - 2C_{44} & C_{11} & C_{11} - 2C_{44} & 0 & 0 & 0 \\ C_{11} - 2C_{44} & C_{11} - 2C_{44} & C_{11} & 0 & 0 & 0 \\ 0 & 0 & 0 & C_{44} & 0 & 0 \\ 0 & 0 & 0 & 0 & C_{44} & 0 \\ 0 & 0 & 0 & 0 & 0 & C_{44} \end{bmatrix} \quad (3.9)$$

The elastic constants C_{11} and C_{44} can be related to the material's bulk modulus, K , and its shear modulus, μ , or its Lamé parameters, λ and μ by:

$$C_{11} = K + \frac{4}{3}\mu = \lambda + 2\mu, \quad (3.10)$$

$$C_{44} = \mu. \quad (3.11)$$

In rock physics and seismology, wave propagations are usually given in terms of the bulk modulus and the shear modulus. The bulk modulus is essentially a measure of the medium's resistance to uniform compression (stiffness), and is given as the ratio of the hydrostatic stress, σ_0 , to the volumetric strain, θ :

$$K = \frac{\sigma_0}{\theta}, \quad \sigma_0 = \frac{\sigma_1 + \sigma_2 + \sigma_3}{3}, \quad \text{and} \quad \theta = \varepsilon_1 + \varepsilon_2 + \varepsilon_3. \quad (3.12)$$

The reciprocal of the bulk modulus will give the compressibility of a material. The shear modulus, modulus of rigidity, or the Lamé's second parameter is a measure of the medium's resistance to shear strain, and it is the ratio of the shear stress to the shear strain:

$$\mu = \frac{\sigma_i}{2\varepsilon_i}, \quad i=4, 5, 6. \quad (3.13)$$

The Lamé's first parameter, however does not have any physical interpretation, but is useful for the simplification of the elastic stiffness matrix. If under a uniaxial stress (all stresses are zero, except in one direction), other elastic moduli can be also used to describe an isotropic material and they are Young's modulus and Poisson's ratio. The Young's modulus, E , is the ratio of the extensional stress to the extensional strain:

$$E = \frac{\sigma_i}{\varepsilon_i}, \quad i=1, 2, 3. \quad (3.14)$$

The Poisson's ratio, ν , is the negative ratio of the lateral strain to the axial strain:

$$\nu = -\frac{\varepsilon_i}{\varepsilon_j}, \quad i, j=1, 2, 3 \text{ and } i \neq j. \quad (3.15)$$

If in a uniaxial strain state (all strains are zero, except in one direction), the P-wave modulus can be used instead and it is also defined as the ratio of the axial stress to the axial strain:

$$M = \frac{\varepsilon_i}{\sigma_i}, \quad i=1, 2, 3. \quad (3.16)$$

For an isotropic, linear elastic medium any one of the isotropic constants ($K, \mu, \lambda, E, \nu, M$) can be derived in terms of the others. The relations between the given elastic moduli are listed in table 3.1.

	K	E	λ	μ	N	M
(λ, μ)	$\lambda + \frac{2\mu}{3}$	$\frac{\mu(3\lambda + 2\mu)}{\lambda + \mu}$	-	-	$\frac{\lambda}{2(\lambda + \mu)}$	$\lambda + 2\mu$
(E, μ)	$\frac{E\mu}{3(3\mu - E)}$	-	$\frac{\mu(E - 2\mu)}{3\mu - E}$	-	$\frac{E}{2\mu} - 1$	$\frac{\mu(4\mu - E)}{3\mu - E}$
(K, λ)	-	$\frac{9K(K - \lambda)}{3K - \lambda}$	-	$\frac{3(K - \lambda)}{2}$	$\frac{\lambda}{3K - \lambda}$	$3K - 2\lambda$
(K, μ)	-	$\frac{9K\mu}{3K + \mu}$	$K - \frac{2\mu}{3}$	-	$\frac{3K - 2\mu}{2(3K + \mu)}$	$K + \frac{4\mu}{3}$
(λ, ν)	$\frac{\lambda(1 + \nu)}{3\nu}$	$\frac{\lambda(1 + \nu)(1 - 2\nu)}{\nu}$	-	$\frac{\lambda(1 - 2\nu)}{2\nu}$	-	$\frac{\lambda(1 - \nu)}{\nu}$
(μ, ν)	$\mu \frac{2(1 + \nu)}{3(1 - 2\nu)}$	$2\mu(1 + \nu)$	$\frac{2\mu\nu}{1 - 2\nu}$	-	-	$\frac{2\mu(1 - \nu)}{(1 - 2\nu)}$
(E, ν)	$\frac{E}{3(1 - 2\nu)}$	-	$\frac{Ev}{(1 + \nu)(1 - 2\nu)}$	$\frac{E}{2(1 + \nu)}$	-	$\frac{E(1 - \nu)}{(1 + \nu)(1 - 2\nu)}$
(K, ν)	-	$3K(1 - 2\nu)$	$\frac{3K\nu}{1 + \nu}$	$\frac{3K(1 - 2\nu)}{2(1 + \nu)}$	-	$\frac{3K(1 - \nu)}{(1 + \nu)}$
(K, E)	-	-	$\frac{3K(3K - E)}{9K - E}$	$\frac{3KE}{9K - E}$	$\frac{3K - E}{6K}$	$\frac{3K(3K + E)}{9K - E}$
(M, μ)	$M - \frac{4\mu}{3}$	$\frac{\mu(3M - 4\mu)}{M - \mu}$	$M - 2\mu$	-	$\frac{M - 2\mu}{2(M - \mu)}$	-

Table 3.1: (After Birch (1961))* Relationships among the elastic constants for a homogeneous isotropic material

3.2.2 Wave propagation in an isotropic linear elastic medium

Detailed derivation of wave propagation in a linear elastic medium will not be presented here since this topic has been reviewed in numerous textbooks. In this section, only the basic concepts required for later use and discussion are provided. For a more in depth discussion and derivation, the reader is referred to the literature listed in the introduction of section 3.2.

From the previous section, the material dependent relationship between the applied stress and the immediate resulting strain has been established by

*Reproduced with permission from the American Geophysical Union

Hooke's law. However, Hooke's law on its own does not give the variation in the displacement of material points with time. Instead, the propagation of a wave with space and time can be described if the volume of material considered is not in static equilibrium, so that there is a non-zero net force (unbalanced) on the volume. Newton's second law of motion states that a non-zero net force on a body is equal to the product of the mass and the acceleration of the body. By substituting Hooke's law into the equation of motion and expressing the strains in terms of displacement, the scalar one-dimensional wave equation in an elastic medium for a displacement, u , is

$$\rho \frac{\partial^2 u}{\partial t^2} = C \nabla^2 u . \quad (3.17)$$

where u is given in terms of position and time, $u(x,t)$, ρ is the bulk density of the elastic medium, and C is the elastic stiffness constant or 'elastic modulus' pertaining to the type of wave in consideration. The wave velocity for the most general case in equation 3.17 is,

$$V = \sqrt{\frac{C}{\rho}} . \quad (3.18)$$

Essentially, the wave equation relates a time derivative of a displacement to spatial derivatives through the proportionality constant of V^2 .

In a homogeneous isotropic medium, there are two types of waves that can propagate, a P-wave (also known as primary, dilatational, longitudinal, irrotational, or compressional wave) and a S-wave (also known as secondary, transverse, rotational, or shear wave). Because P- and S-waves travel in the interior of a medium, they are also referred to as body waves. For the velocity of P-and S-waves, equation 3.18 would be

$$V_p = \sqrt{\frac{C_{11}}{\rho}} = \sqrt{\frac{\lambda + 2\mu}{\rho}} = \sqrt{\frac{K + \frac{4}{3}\mu}{\rho}} = \sqrt{\frac{M}{\rho}}, \quad (3.19)$$

$$V_s = \sqrt{\frac{C_{44}}{\rho}} = \sqrt{\frac{\mu}{\rho}}, \quad (3.20)$$

respectively. Since fluids cannot sustain shear forces such that the shear moduli of fluids are zero, only P-waves can travel in fluids where the wave velocity is

$$V_p = \sqrt{\frac{K}{\rho}}. \quad (3.21)$$

3.2.3 Viscoelasticity

So far discussed, the material under stress is perfectly elastic meaning when the applied stress is removed the strain is completely recovered, and no energy is lost. In contrast, there are some materials when under stress will deform by flow and the deformation is permanent. Unlike an elastic material, the energy used to strain the material is completely dissipated to the surroundings without any storage. With no energy to recover the original shape, the material stays permanently deformed when the stress is removed. This type of material has a viscous behaviour and is exhibited by fluids under shear stress. For a viscous fluid under shear stress the resulting behaviour is

$$\sigma_{ij} = \eta \frac{\delta \epsilon_{ij}}{\delta t}, \quad i \neq j \quad (3.22)$$

where the applied stress is linearly related by the fluid viscosity, η , to the strain rate, $\delta \epsilon_{ij} / \delta t$, and there is now a time dependency on the stress-strain relationship.

Between the two end member cases of elasticity, in reality materials usually exhibit both an elastic and a viscous response and they are called viscoelastic materials. Some phenomena in viscoelastic materials are (Lakes, 2009):

- 1.) *If the stress is held constant, the strain increases with time and is called a creep response:* Figure 3.3 displays the creep and recovery of a material experiencing a step stress. While under a constant stress, the deformation of a viscoelastic material will continually progress with time. On the strain plot, from examining the behaviours of all material responses, it is obvious that the viscoelastic response is the combined response between a perfectly elastic and a purely viscous material. The non-zero intercept of the strain curve is a result of the elastic behaviour of the material, where for a given stress there will be an instantaneous strain. Thereafter, the effect of a viscous deformation is evident by the increasing strain with time. When the stress is removed the strain

immediately drops a substantial amount due to the elastic rebound of the material and then tapers off without ever fully recovering the full strain, as governed by the viscous response of the material.

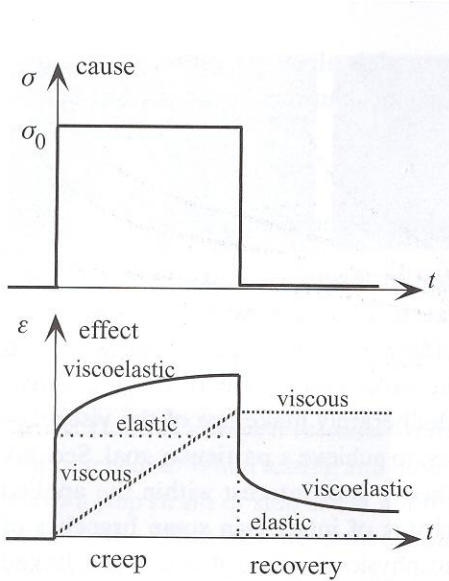


Figure 3.3: (Figure reproduced from Lakes (2009))* Creep and recovery response of a viscoelastic medium. Top plot is a step stress over time, bottom plot is the resulting strain with time. Superimposed on the bottom plot in dotted lines are the elastic and viscous responses to a step stress.

2.) If the strain is held constant, the stress decreases with time and is referred to as relaxation: Figure 3.4 displays the relaxation and recovery of a material experiencing a step strain. Since time is increasing, stress must decrease to keep strain constant. When the step strain ends at zero, implying this material has recovered its full deformation, the applied stress must need to reverse directions to attain this. Otherwise due to the viscous response, there would be residual strain.

3.) If cyclic loading is applied, hysteresis occurs, leading to dissipation of mechanical energy: In one dimension, for an applied stress that varies sinusoidally with time, t , and angular frequency, ω , given by,

$$\sigma(t) = \sigma_0 e^{i\omega t}, \quad (3.23)$$

*Reprinted with the permission of Cambridge University Press.

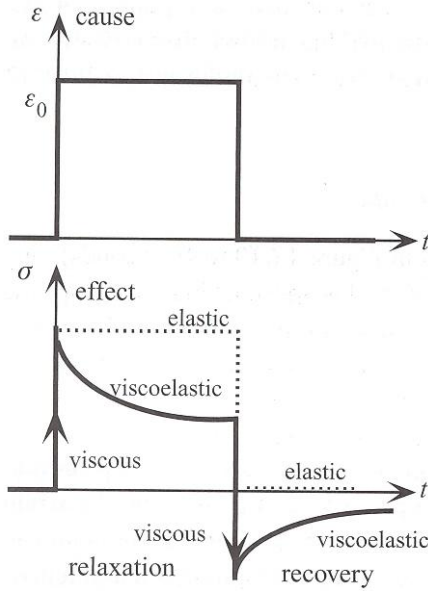


Figure 3.4: (Figure reproduced from Lakes (2009))* Relaxation and recovery response of a viscoelastic medium. Top plot is step strain over time, bottom plot is the resulting stress with time. The dotted line is elastic response to the step strain.

the responding strain in a viscoelastic material will also vary sinusoidally at the same frequency but not immediately,

$$\varepsilon(t) = \varepsilon_0 e^{i(\omega t - \delta)}. \quad (3.24)$$

The delayed strain response to the applied stress gives rise to the phase lag, δ . Figure 3.5 displays the relation between the sinusoid varying stress and strain of a viscoelastic material. With both the stress and strain functions varying at the same period T , the phase lag δ is a result of the time delay, Δt , of the strain response in respect of the stress,

$$\delta = \frac{2\pi\Delta t}{T}. \quad (3.25)$$

δ , is also referred to as the loss angle and is a measure of the internal friction and the mechanical damping of a material. It can also be given as the loss tangent where the tangent is taken of the loss angle, $\tan \delta$. If there is no phase lag between the stress and strain of a given material, $\delta=0$, this material is an elastic solid. Furthermore, the stiffness modulus, C , that relates stress and strain seen in section

*Reprinted with the permission of Cambridge University Press.

3.2.1 for a perfectly elastic material is a real number. For a viscoelastic material, as a consequence of the intrinsic phase lag between stress and strain, the stiffness modulus is now a complex number,

$$\frac{\sigma(t)}{\varepsilon(t)} = \frac{\sigma_o}{\varepsilon_o} e^{i\delta} = C^* = C' + iC'', \quad (3.26)$$

with C' and C'' being the real and imaginary parts, respectively, of the complex modulus C^* . C' is commonly called the storage modulus and it is responsible for the elastic response of the material or the preservation of energy. C'' is the loss modulus and it is responsible for the viscous response of the material or the dissipation of energy. For a propagating wave, the storage modulus supports the physical travel of a wave where the loss modulus provides the attenuation or the disappearance of the wave. Moreover, the loss tangent can be related to the storage and loss modulus by.

$$\tan \delta = \frac{C''}{C'}, \quad (3.27)$$

The physical meaning of the loss tangent is associated with the ratio of energy dissipated to the energy stored.

3.3 Rock Physics

From the last section, the background on wave propagation was given for a homogeneous medium. In geophysics, the medium of concern is usually Earth materials which are not homogeneous at a micro-scale or even at macro-scale. Earth materials or rocks are of a porous medium, consisting of a solid matrix (mineral grains) and a void volume (pores) that may be filled with fluid. The elastic properties pertaining to wave propagation in a porous medium are therefore influenced by both the solid matrix and the pore fluid constituents.

In the discipline of rock physics, the aim is to establish relations between rock properties and the observed seismic response so that predictive theories can be developed to assist seismic interpretation. Therefore the physical properties of interest are ones that will affect how seismic waves physically travel through the

Dynamic Behavior

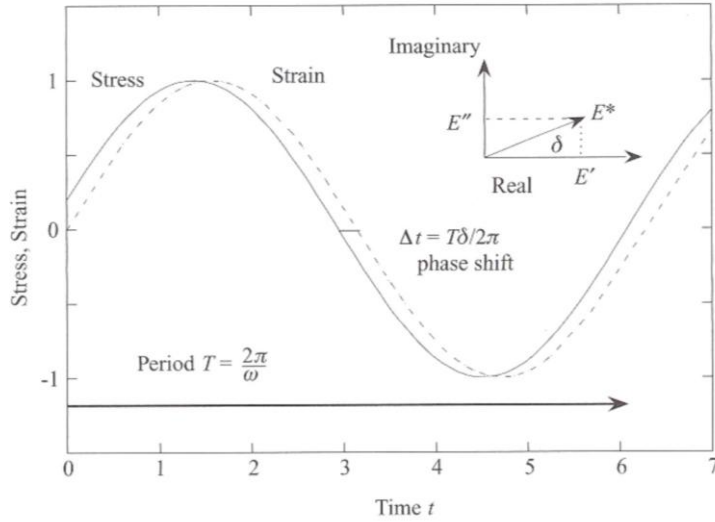


Figure 3.5: (Figure reproduced from Lakes (2009))^{*} Stress and strain varying sinusoidally with time. The time delay of the strain response in respect of the stress is given by Δt . Subpanel is a plot of complex modulus E^* , its real (E') and imaginary parts (E'') in relation to the loss angle, δ .

rocks, namely the compressibility, the rigidity, the porosity, the mass density, and the pore fluid. To establish such relation requires knowledge about the elastic properties of the rock matrix and pore fluid, and rock-fluid interaction models. Fluid substitution refers to the prediction or modeling of wave velocities in a porous medium that is saturated with a fluid from the information obtained of the dry porous medium or from the saturated porous medium with a different fluid. Two theoretical rock-fluid interaction models will be discussed in this section.

3.3.1 Gassmann's equation

In rock physics, Gassmann's equation is the most widely used fluid substitution relation due to its simplicity and presumed applicability in the seismic frequency range (~ 100 Hz). His theoretical equation was derived by considerations of elementary elasticity of the pore fluid and the mineral grains of a saturated rock sample. In his formulation, Gassmann (1951) assumed:

^{*}Reprinted with the permission of Cambridge University Press

- 1) The rock is macroscopically homogeneous and isotropic;
- 2) The rock's minerals all have the same bulk and shear moduli;
- 3) The fluids can freely move about in the pore space where pores are interconnected or communicating and the fluid viscosity is zero;
- 4) The pore space is fully saturated at all times;
- 5) The pore fluid does not interact with the rock minerals thereby changing the rock frame's stiffness.
- 6) Quasi-static conditions where the frequencies are sufficiently low such that the induced pore pressures can be equilibrated through the pore space.

Gassmann's equation will be presented here without derivation; detailed discussion on the origin of Gassmann's equation can be found in Bourbié et al (1987) and Berryman (1999).

By Gassmann's formulation, the bulk modulus of a saturated rock, K_{sat} , is related to the rock frame's bulk modulus (frame modulus), K_{dry} , the mineral grains' bulk modulus (solid constituent of the rock), K_s , the pore fluid's bulk modulus (fluid constituent of the rock), K_f , and the porosity, ϕ , of the rock through:

$$\frac{K_{sat}}{K_s - K_{sat}} = \frac{K_{dry}}{K_s - K_{dry}} + \frac{K_f}{\phi(K_s - K_f)}, \quad (3.28)$$

where rearranging gives the predicted saturated bulk modulus of the rock as,

$$K_{sat} = K_{dry} + \frac{\left(1 - \frac{K_{dry}}{K_s}\right)^2}{\frac{\phi}{K_f} + \frac{1-\phi}{K_s} + \frac{K_{dry}}{K_s^2}}. \quad (3.29)$$

If the rock frame's bulk modulus is unavailable (usually the case for in-situ measurements), the bulk modulus of a rock saturated with a fluid, K_{sat} , can instead be related to the bulk modulus of the rock saturated with a different fluid, K_{sat2} :

$$\frac{K_{sat}}{K_s - K_{sat}} - \frac{K_{f1}}{\phi(K_s - K_{f1})} = \frac{K_{sat2}}{K_s - K_{sat2}} - \frac{K_{f2}}{\phi(K_s - K_{f2})}. \quad (3.30)$$

For the shear modulus of a saturated rock, μ_{sat} , the computation is even simpler. In the Gassmann formulation, the shear modulus is regarded to be independent of

the pore fluid because fluids are incapable of sustaining shear forces. Therefore, the shear modulus of the saturated rock is the same as the shear modulus of the dry rock or, of the saturated rock with another fluid:

$$\mu_{sat} = \mu_{dry} = \mu_{sat2}. \quad (3.31)$$

From the determined saturated bulk or shear moduli, the corresponding saturated P-or S-wave velocity can be found from using equation 3.19 or 3.20 in section 3.2.2, where the bulk density of the saturated rock is given by:

$$\rho_{sat} = (1 - \phi)\rho_s + \phi\rho_f \quad (3.32)$$

In order to predict the bulk modulus of a saturated rock, 1) the mineral grain's bulk modulus, 2) the pore fluid's bulk modulus, 3) the rock frame's bulk modulus, and 4) the rock's porosity needs to be known. The determination of a sample's porosity will be given in Chapter 5 on Sample Characterization and the determination of the different bulk moduli will be given below.

1.) Estimating Mineral Grain Elastic Moduli

The mineral grain refers to the rock-forming minerals constituting the rock matrix or simply the solid component of a rock. To determine the mineral grain's bulk modulus, the minerals making up the rock need to be identified. Once identified, the bulk modulus of the constituting minerals can be determined by referring to literature on mineral and material properties such as Bass (1995). For samples whose composition is of one or is largely dominated by one mineralogy (>95%), determining K_s is straightforward and suffice. Otherwise for samples consisting of more than one mineral, the volume fraction of the various mineral constituents of the matrix needs to be identified. The mineral type and volume fractions can be determined from microscopic imaging such as thin-sections or X-ray diffraction/fluorescence (XRD/XRF) methods. With the mineral compositions known, the bulk modulus of the sample's matrix that is composed of a mixed mineral composition can be estimated by using Hill's average (1952),

$$K_s = \frac{1}{2}(K_V + K_R) \quad (3.33)$$

where the K_V is Voigt's average (1928) and K_R is Reuss' average (1929). These two averages respectively give the maximum and minimum values possible for a mixture:

$$K_V = \sum_{i=1}^n f_i K_i \quad (3.34)$$

$$\frac{1}{K_R} = \sum_{i=1}^n \frac{f_i}{K_i}. \quad (3.35)$$

where f_i is the fraction amount of the i^{th} mineral, and K_i is the bulk modulus of that corresponding mineral.

Alternatively, the mineral grain's bulk modulus can be determined without knowing the exact mineral composition of the rock matrix. Biot and Willis (1957) introduced a method of determining the mineral grain's bulk modulus in the laboratory and it is commonly referred to as the unjacketed test. This method is only appropriate if there are no occluded pores. Briefly, a sample is immersed in a fluid without being sealed such that the surrounding fluid can enter the pore space. With raised fluid pressure, the sample's pore space will be fully saturated and the pressure inside the sample is equal to the pressure on the outside. Any volumetric change (strain) of the sample from increased fluid pressure is due to the compression of the grains. Such unjacketed quasi-static strain tests were conducted by Bakhorji (2010) on carbonate rocks and Schmitt and Zoback (1989) on low porosity metamorphic gneisses. However, recently Hart and Wang (2010) have questioned this assumption.

2.) Estimating Pore Fluid Elastic Moduli

The pore fluid refers to any fluid that resides in the void space of the rock. It can be a gas, a liquid, a supercritical fluid, of hydrocarbons, of water, of CO₂, of a mixture of fluids, or even of a vacuum. The bulk modulus of the pore fluid, K_f , can be theoretically calculated from equation 3.21 if auxiliary thermodynamic properties (from EOS, or empirical relations such as Batzle and Wang, 1992) are available to provide the fluid density, ρ_f , and the speed of sound through the fluid, V_{Pf} .

$$K_f = \rho_f V_{pf}^2. \quad (3.36)$$

In the case of fluid mixtures, the overall pore fluid bulk modulus can be calculated from averaging the contribution of the individual fluids using Voigt's or Reuss' average equation. If the bulk modulus from Reuss' average is used this is also known as Wood's relation. In addition, the overall fluid bulk density from the mixture is

$$\rho_f = \sum_{i=1}^n f_i \rho_{fi}. \quad (3.37)$$

3.) Estimating Dry Frame Elastic Moduli

The term frame refers to the rock sample with empty pores or alternatively, the dry rock. The bulk and shear modulus of the dry rock, K_{dry} and μ_{dry} , can be determined from wireline log data, from a theoretical or an empirical relationship or from laboratory measurements.

In using wireline data, K_{dry} can be determined if K_{sat} is measured for a different fluid. If the parameters ϕ , K_f , K_s are known before hand, K_{dry} can be determined by rewriting the Gassmann equation for K_{dry} ,

$$K_{dry} = \frac{K_{sat} \left(\phi \frac{K_s}{K_f} + 1 - \phi \right) - K_s}{\phi \frac{K_s}{K_f} + \frac{K_{sat}}{K_s - 1 - \phi}}. \quad (3.38)$$

This back calculation for K_{dry} is an intermediate step that was skipped when applying fluid substitution of two fluids in equation 3.30.

To determine K_{dry} from using theoretical and empirical relations, there are a variety of equations that can be employed. From a theoretical standpoint, by considering the stress and strain under dry conditions, the dry rock modulus is (Bourbié et al, 1987; Mavko et al, 2009):

$$K_{dry} = K_s (1 - \beta). \quad (3.39)$$

β is formally defined as the ratio of the pore volume change to the bulk rock volume change while under constant pore pressure and is sometimes called the Biot coefficient.

In terms of using an empirical relation, Nur et al (1995) suggested that between low porosity and critical porosity (the limiting cases for rocks), there is a linear trend for the dry moduli as a function of porosity. The critical porosity separates whether the rock is in a grain- load bearing ($\phi < \phi_c$) or a fluid-load bearing ($\phi > \phi_c$) domain. For most reservoir rocks, the grains are load bearing and the critical porosity serves as a limiting case. The bulk and shear moduli for dry rocks are:

$$K_{dry} = K_s \left(1 - \frac{\phi}{\phi_c} \right), \quad (3.40)$$

$$\mu_{dry} = \mu_s \left(1 - \frac{\phi}{\phi_c} \right). \quad (3.41)$$

An alternative empirical relation to estimate the bulk modulus in dry rocks is

$$\frac{1}{K_{dry}} = \frac{1}{K_s} (1 + 50\phi), \quad (3.42)$$

developed by Geertsma (1961) for porosities $0 < \phi < 0.3$.

Lastly the dry bulk and shear moduli can be determined in the laboratory. In the laboratory, ultrasonic P- and S-wave velocities through the dry rock and the dry bulk density are measured. From rearranging equation 3.19 and 3.20, the dry bulk and shear modulus can be found:

$$K = \rho(V_p^2 - \frac{4}{3}V_s^2) \quad (3.43)$$

$$\mu = \rho V_s^2. \quad (3.44)$$

For a more in depth discussion on laboratory determination of ultrasonic P-and S-wave velocities and dry bulk density, the reader is referred to Chapter 4 and Chapter 5, respectively.

Gassmann's equation as mentioned is widely used due to its ease and also because it works reasonably well when compared to certain data. However it should be noted that for rocks with low-aspect ratio pores (cracks or fractures), or is saturated by high viscosity pore fluids, Gassmann's prediction will be lower than what is actually observed (Dewar, 2001). The overall rock sample will appear to be stiffer than assumed in the formulation because the pore shape and

viscosity of the fluid make it harder for the pore fluid to equalibrate within the appropriate time frame. Also as noted before, Gassmann's relation is only valid for low frequencies such that the motion of the pore fluid and the rock matrix are perfectly coupled when responding to a passing wave. Comparison to high frequency data such as sonic log data (~KHz) or laboratory data (~MHz) where differential movement can arise between the fluid and the solid constituents of a rock during the passing of a wave would yield a discrepancy in values. If higher frequency analysis is of interest, then Biot's equation should be employed.

3.3.2 Biot's Formulation

In contrast to Gassmann, Biot predicted the frequency-dependence of wave velocities for saturated rocks. In 1956, Biot presented the theory of propagation of elastic waves in a fluid saturated porous solid in the low frequency range and the higher frequency range in two publications (Biot, 1956a; Biot 1956b). For his low frequency limit, Biot's formulation reduces to Gassmann's relation and the equation is sometimes referred to as the Gassmann-Biot's equation. For the higher frequency range, his formulation is valid up to the limit where grain scattering becomes important and the rocks can no longer be viewed as homogeneous. In his formulation, Biot assumed:

- 1) The rock is macroscopically homogeneous and isotropic;
- 2) The rock's minerals all have the same bulk and shear moduli;
- 3) The fluids can freely move about in the pore space where pores are interconnected or communicating;
- 4) The pore space is fully saturated at all times;
- 5) The pore fluid is Newtonian;
- 6) The pore fluid does not react with the rock minerals which otherwise could change the stiffness of the rock frame.

In his derivation Biot accounted for the frequency dependence of wave behaviours by incorporating viscous and inertial interactions between the pore fluid and the solid matrix of the rock. At low frequencies, the slow rate of the oscillating stress from a passing seismic wave allows for a sufficient amount of

time for pore fluids to react to the change in stress and reach equilibrium with the solid matrix. Substantial coupling exists between the pore fluid and the pore wall and no differential motion will occur between them. The controlling factor on the pore fluid motion then is the internal resistance of the fluid to flow, namely its viscosity. Therefore, fluid motion in the low frequency regime of Biot's theory is dominated by viscous effects.

On the other hand at higher frequencies, pore fluids will not have enough time to react and relax to the passing stress or, rather the pore fluids are resisting the sudden change to its current state of motion. Therefore, fluid motion in the higher frequency regime of Biot's theory is dominated by inertial effects. The pore fluid and the pore wall will be decoupled from one another, therefore giving rise to relative motion between them. As a consequence of the resistance of fluid flow in the pore space, the overall saturated rock will appear to be stiffer at higher frequencies compared to at lower frequencies and this phenomenon is called velocity dispersion. Furthermore, the resulting relative motion between the pore fluid and pore wall will give rise to wave attenuation.

The low and high frequency range of a saturated porous medium is determined by a reference frequency, or more commonly known as the Biot's critical frequency, f_c , given by,

$$f_c = \frac{\phi\eta}{2\pi\rho_f\kappa} . \quad (3.45)$$

η is the viscosity of the pore fluid and κ is the absolute permeability of the rock. For a wave that propagates with a frequency, f , it is in the low frequency regime if $f < f_c$ and it is in the high frequency regime if $f > f_c$. A physical interpretation of the critical frequency defines it as the frequency where the viscous force equals the inertial forces acting on the pore fluid (Mavko et al, 2009).

Moreover, as a result of relative motion of the pore fluid and the pore wall Biot predicted that there are three different body waves generated inside a porous medium; one shear wave and two compressional waves where the two compressional waves are called the 'fast' P-wave and the 'slow' P-wave. The fast and slow P-waves correspond to the overall in-phase or out of phase motion,

respectively, between the rock frame and the pore fluid. The fast P-wave is the most easily observed in the laboratory and in the field. The slow P-wave, sometimes referred to as Biot's slow wave, is highly attenuating and has only been observed in the laboratory (e.g., Johnson and Plona, 1982; Bouzidi and Schmitt, 2009). In our study, the slow P-wave is not of importance because only the fast compressional wave and shear wave will be considered.

Here, a brief overview of the Biot's formulation is given; a more extensive derivation can be found in Bouzidi (2003). The equations of motion governing wave propagation in porous materials saturated with a single fluid were derived by considering the total force due to stress acting on the solid constituent and that acting on the fluid constituent, and incorporating:

- 1.) the stress-strain relations from considering potential energy effects;
- 2.) the kinetic energy of the solid, of the fluid, and of the induced mass from the solid-fluid coupling;
- 3.) and the dissipation function.

The resulting general wave equations of motion in terms of the displacement vector for the solid and fluid constituents, \vec{u}_s and \vec{u}_f respectively, are (Bouzidi, 2003):

$$(1-\phi)\rho_s \frac{\partial^2}{\partial t^2} \vec{u}_s - \rho_{12} \frac{\partial^2}{\partial t^2} (\vec{u}_s - \vec{u}_f) + F(\omega) \frac{\eta\phi^2}{\kappa} \frac{\partial}{\partial t} (\vec{u}_s - \vec{u}_f) = \mu_{dry} \nabla^2 \vec{u}_s + (A + \mu_{dry}) \vec{\nabla}(\vec{\nabla} \cdot \vec{u}_s) + Q \vec{\nabla}(\vec{\nabla} \cdot \vec{u}_f) \quad (3.46)$$

$$\phi \rho_f \frac{\partial^2}{\partial t^2} \vec{u}_f + \rho_{12} \frac{\partial^2}{\partial t^2} (\vec{u}_s - \vec{u}_f) - F(\omega) \frac{\eta\phi^2}{\kappa} \frac{\partial}{\partial t} (\vec{u}_s - \vec{u}_f) = Q \vec{\nabla}(\vec{\nabla} \cdot \vec{u}_s) + R \vec{\nabla}(\vec{\nabla} \cdot \vec{u}_f) \quad (3.47)$$

where η is the viscosity of fluid, κ is the permeability of the sample, ρ_{12} is the coupling mass density, $F(\omega)$ is a viscosity correction factor that is dependent on frequency, ω , and A , Q , and R are the Biot parameters. The coupling mass density, the viscosity correction factor and the Biot parameters will be further defined later. The solid and fluid displacement vectors can also be expressed through Helmholtz decomposition in terms of the scalar potential, $\vec{\sigma}$, and the

vector potential, $\vec{\psi}$, to simplify the equations of motion (Bouzidi, 2003). The displacement vector for the solid and fluid constituents respectively are:

$$\vec{u}_s = \vec{\nabla} \sigma_s + \vec{\nabla} \times \vec{\psi}_s \quad (3.48)$$

$$\vec{u}_f = \vec{\nabla} \sigma_f + \vec{\nabla} \times \vec{\psi}_f. \quad (3.49)$$

For only compressional waves to occur the divergence operator is applied to equation 3.46 and 3.47. In terms of the potential fields defined in equation 3.48 and 3.49, the longitudinal wave equation of motion is then

$$(1-\phi)\rho_s \frac{\partial^2}{\partial t^2} \sigma_s - \rho_{12} \frac{\partial^2}{\partial t^2} (\sigma_s - \sigma_f) + F(\omega) \frac{\eta\phi^2}{\kappa} \frac{\partial}{\partial t} (\sigma_s - \sigma_f) = \nabla^2 [(A + 2\mu_{dry})\sigma_s + Q\sigma_f] \quad (3.50)$$

$$\phi\rho_f \frac{\partial^2}{\partial t^2} \sigma_f + \rho_{12} \frac{\partial^2}{\partial t^2} (\sigma_s - \sigma_f) - F(\omega) \frac{\eta\phi^2}{\kappa} \frac{\partial}{\partial t} (\sigma_s - \sigma_f) = \nabla^2 [Q\sigma_s + R\sigma_f]. \quad (3.51)$$

If a regular plane wave solution is applied to both partial differential equations, the following results

$$\left[k^2 (A + 2\mu_{dry}) - \omega^2 (1-\phi)\rho_s + \omega^2 \rho_{12} + i\omega F(\omega) \frac{\eta\phi^2}{\kappa} \right] \sigma_s + \left[k^2 Q - \omega^2 \rho_{12} - i\omega F(\omega) \frac{\eta\phi^2}{\kappa} \right] \sigma_f = 0, \quad (3.52)$$

$$\left[k^2 Q - \omega^2 \rho_{12} - i\omega F(\omega) \frac{\eta\phi^2}{\kappa} \right] \sigma_s + \left[k^2 R + \omega^2 \rho_{12} - \omega^2 \phi\rho_f + i\omega F(\omega) \frac{\eta\phi^2}{\kappa} \right] \sigma_f = 0. \quad (3.53)$$

In the equations k is the wavenumber and ω is the angular wave frequency, where both are obtained from the plane wave solution. If a ratio of the solid to fluid scalar potential is defined,

$$\zeta_l = \frac{\sigma_s}{\sigma_f}, \quad (3.54)$$

then by combining equation 3.52 and 3.53, and eliminating k , a quadratic equation can be then obtained in terms of ζ_l

$$a\zeta_l^2 + b\zeta_l + c = 0 \quad (3.55)$$

where the coefficients a , b , and c are:

$$a = -(A + 2\mu_{dry} + Q) \left(\rho_{12} + iF(\omega) \frac{\eta\phi^2}{\kappa\omega} \right) + Q(1-\phi)\rho_s \quad (3.56)$$

$$b = (A + 2\mu_{dry} - R) \left(\rho_{12} + iF(\omega) \frac{\eta\phi^2}{\kappa\omega} \right), \\ - (A + 2\mu_d)\phi\rho_f + R(1-\phi)\rho_s \quad (3.57)$$

$$c = (Q + R) \left(\rho_{12} + iF(\omega) \frac{\eta\phi^2}{\kappa\omega} \right) - Q\phi\rho_f. \quad (3.58)$$

Equation 3.55 is a polynomial of the second degree and therefore yields two solutions by

$$\zeta_l = \frac{-b \pm \sqrt{b^2 - 4ac}}{2a}. \quad l=1, 2 \quad (3.59)$$

Furthermore, if equation 3.52 and 3.53 were combined without eliminating the wavenumber, then the wavenumber can then be defined as

$$k_l = \omega \left[\frac{\zeta_l(1-\phi)\rho_s + \phi\rho_f}{\zeta_l(A+2\mu_{dry}) + R + Q} \right]^{\frac{1}{2}} \quad l=1, 2. \quad (3.60)$$

The wavenumber is complex and has two possibilities as a result of the two ζ_l solutions of equation 3.59. The two possible complex wavenumbers corresponds to the ‘fast’ and ‘slow’ compressional waves, as introduced earlier. The real part of $k_{l,2}$ allows the determination of the phase velocity via

$$V_{p1,2} = \frac{\omega}{k_{1,2}}, \quad (3.61)$$

while the imaginary part directly provides the attenuation coefficient of which will be discussed in the next section.

For rotational waves to occur, the curl operator is applied to the general equation of 3.46 and 3.47. In terms of the potential fields defined in equation 3.48 and 3.49, the shear wave equation of motion is then,

$$(1-\phi)\rho_s \frac{\partial^2}{\partial t^2} \vec{\psi}_s - \rho_{12} \frac{\partial^2}{\partial t^2} (\vec{\psi}_s - \vec{\psi}_f) + F(\omega) \frac{\eta\phi^2}{\kappa} \frac{\partial}{\partial t} (\vec{\psi}_s - \vec{\psi}_f) = \mu_{dry} \nabla^2 \vec{\psi}_s, \quad (3.62)$$

$$\phi\rho_f \frac{\partial^2}{\partial t^2} \vec{\psi}_f + \rho_{12} \frac{\partial^2}{\partial t^2} (\vec{\psi}_s - \vec{\psi}_f) - F(\omega) \frac{\eta\phi^2}{\kappa} \frac{\partial}{\partial t} (\vec{\psi}_s - \vec{\psi}_f) = 0 \quad (3.63)$$

Applying a plane wave solution to both partial differential equations, the following results:

$$\left[k^2 \mu_{dry} - \omega^2 (1-\phi)\rho_s + \omega^2 \rho_{12} + i\omega F(\omega) \frac{\eta\phi^2}{\kappa} \right] \vec{\psi}_s - \left[\omega^2 \rho_{12} + i\omega F(\omega) \frac{\eta\phi^2}{\kappa} \right] \vec{\psi}_f = 0 \quad (3.64)$$

$$\left[\rho_{12} + iF(\omega) \frac{\eta\phi^2}{\kappa\omega} \right] \vec{\psi}_s + \left[\phi\rho_f - \rho_{12} - iF(\omega) \frac{\eta\phi^2}{\kappa\omega} \right] \vec{\psi}_f = 0 \quad (3.65)$$

Using equation 3.65 and the defining ratio of the solid to fluid vector potential as,

$$\zeta_3 = \frac{\vec{\psi}_s}{\vec{\psi}_f}, \quad (3.66)$$

the following can be obtained

$$\zeta_3 = -\frac{\phi\rho_f - \rho_{12} - iF(\omega) \frac{\eta\phi^2}{\kappa\omega}}{\rho_{12} + iF(\omega) \frac{\eta\phi^2}{\kappa\omega}}. \quad (3.67)$$

Similar to compressional waves, if equation 3.64 and 3.65 are combined, the wavenumber can be defined as

$$k_3 = \omega \left[\frac{\zeta_3(1-\phi)\rho_s + \phi\rho_f}{\zeta_3\mu_{dry}} \right]^{\frac{1}{2}}. \quad (3.68)$$

The wavenumber is also complex and has only one possibility as a result of the singular solution of ζ_l for rotational waves (where subscript $l=3$). Similar to

compressional waves, the real part of the complex wavenumber, k_3 , allows the phase velocity of the shear wave to be determined, while the imaginary part directly gives the attenuation coefficient.

From the general wave equation of motion, equation 3.46 and 3.47, the coupling mass density, ρ_{12} , the viscosity correction factor, $F(\omega)$, and the Biot parameters, A , Q , and R were introduced but were not defined. The coupling mass density describes the induced mass resulting from inertial drag caused by the relative motion between the solid frame and the pore fluid and is given by

$$\rho_{12} = (1 - \alpha)\phi\rho_f \quad (3.69)$$

where α is tortuosity and is a geometrical factor that describes the structure of the pore space.

The viscosity correction factor or also known as the viscodynamic operator accounts for the fluid flow that deviates from Poiseuille type flow that occurs at really high frequencies. At these high frequencies however, the wavelength is still larger than the pore size. The viscosity correction factor is

$$F(\omega) = \frac{1}{4} \left(\frac{\xi T(\xi)}{1 + 2i \frac{T(\xi)}{\xi}} \right), \quad (3.70)$$

where ξ is given by

$$\xi = \left(\frac{\omega g^2 \rho_f}{\eta} \right)^{\frac{1}{2}} \quad (3.71)$$

and $T(\xi)$ is

$$T(\xi) = \frac{ber'(\xi) + ibei'(\xi)}{ber(\xi) + ibei(\xi)} = \frac{e^{i3\pi/4} J_1(\xi e^{-i\pi/4})}{J_0(\xi e^{-i\pi/4})}. \quad (3.72)$$

The parameter g is a pore-size parameter that is a characteristic of the dimensions and the geometry of the pore space. For spherical pores with a grain diameter given by d , Hovem and Ingram (1979) obtained

$$g = \frac{\phi d}{3(1 - \phi)}. \quad (3.73)$$

The *ber* and *bei* are the real and imaginary parts of the Kelvin function, respectively, and ' denotes the first derivative with respect to ξ . $J_0(\cdot)$ and $J_1(\cdot)$ are the Bessel functions of order 0 and 1, respectively.

Finally, to link the stresses in the solid and fluid constituents together Biot parameters were introduced and they are:

$$A = \frac{(K_s - K_s \phi - K_{dry})^2}{K_s + \gamma K_s^2 - K_{dry}} + K_{dry} - \frac{2}{3} \mu_{dry}, \quad (3.74)$$

$$Q = \frac{\phi K_s (K_s - K_s \phi - K_{dry})}{K_s + \gamma K_s^2 - K_{dry}}, \quad (3.75)$$

$$R = \frac{\phi^2 K_{dry}^2}{K_s + \gamma K_s^2 - K_{dry}}, \quad (3.76)$$

where γ is called the coefficient of fluid content and is given by

$$\gamma = \phi \left(\frac{1}{K_f} - \frac{1}{K_s} \right). \quad (3.77)$$

The parameters in the above equations, K_s , K_f , K_{dry} , μ_{dry} , ϕ and ρ_f , are of the same nomenclature as in Gassmann's equation. Therefore they can be determined through the methods outlined earlier. In addition, Biot's formulation requires the permeability and the tortuosity of the porous sample, and the viscosity of the fluid to be known. Similar to porosity, the determination of permeability and of tortuosity will be given in Chapter 5 on Sample Characterization. For fluid viscosity, just like fluid bulk modulus and fluid density, it can be found from auxiliary thermodynamic information.

3.4 Introduction to Elastic Wave Velocity and Attenuation Determination in the Laboratory

The laboratory method employed in this thesis to study elastic wave properties and a brief background on wave attenuation will be given in this section. The ultrasonic pulse transmission is the technique used for obtaining the waveforms through our samples, from which wave velocity and wave attenuation can be estimated. The wave velocity is calculated from the arrival time of the

propagated signal and wave attenuation is determined by using the log spectral ratio method. Concluding this section is an experimental study on the wave attenuation of acrylic that demonstrates the use of the log spectral ratio method.

3.4.1 Laboratory Measurement Method

There are a variety of laboratory methods that can be used to determine the elastic properties in a rock sample such as stress-strain curves (Gordon and Davis, 1968; Mckavanagh and Stacey, 1974; Bakhorji, 2010), forced oscillations/resonant bar (Winkler, 1979; Murphy, 1982, O’Hara, 1985; Yin et al, 1992; Zadler et al, 2004), pulse echo (Winkler and Plona, 1982; McCann and Sothcott, 1992; Mashinskii, 2005), and pulse transmission. The bases of these investigative methods vary from cyclic loading and unloading to standing and traveling waves. The pulse transmission method is one of the most widely used ultrasonic methods in rock physics (Wyllie et al, 1958; Mobarek, 1971; Nur, 1971; Timur, 1977; Toksöz et al, 1979; De Vilbiss, 1980; Tosaya and Nur, 1982; Blair, 1990; Wang et al, 1991; Cadoret et al, 1995; Thurman et al, 2002; Adam et al, 2006; Verwer et al, 2008; Fujimoto et al, 2010; Wolf, 2010) and is the only known method applied to date for CO₂ laboratory studies on elastic waves. The large usage of the pulse transmission technique in laboratory experiments is associated with its relatively easy and straightforward application in comparison to the other techniques. Variables such as pressure, temperature, and saturation can be easily and are commonly manipulated to examine their effects on seismic responses. Thereby, this technique is employed in this study.

The basic premise of a pulse transmission measurement requires the sample to be placed in between a source and a receiver (figure 3.6). The source and receiver are usually piezoelectric ceramic transducers. When the source is excited, a wave is produced and propagates through the sample. The arrival of the wave at the receiver is detected and recorded where the required transit time of the elastic wave to travel between the source and the receiver through the sample is determined. With knowledge of the length of the sample, that can be measured, the wave velocity through the sample can be calculated.

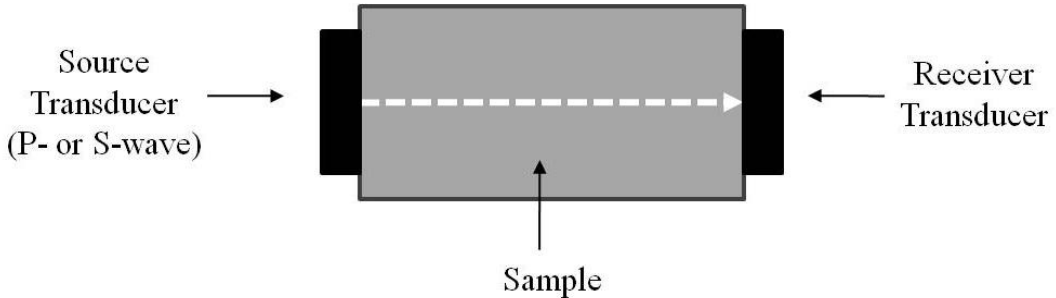


Figure 3.6: The basic principle behind ultrasonic pulse transmission method. The white-dashed arrow denotes the wave path through the sample, traveling from the source to the receiver.

The wave velocities associated with Section 3.2 and 3.3 are the phase velocities and are fundamentally different from group velocities. The phase velocity of a wave is the velocity at which a given phase in a wave propagates,

$$V_{phase} = \frac{\omega}{k} \quad (3.78)$$

where ω is the angular frequency and k is the wave number. The group velocity is the velocity of the envelope of a group of interfering waves having different frequencies and phase velocities.

$$V_{group} = \frac{d\omega}{dk}. \quad (3.79)$$

In a non-attenuating medium where the waveform shape does not evolve with time, the two velocities would be the same. However, realistically this is usually not the case. The type of wave velocity determined from pulse transmission is debatable and dependent on the method used to determine the first arrival of a signal. Molyneux and Schmitt (2000) experimentally determined the phase and group velocities in highly attenuating glycerol-saturated, unconsolidated packs of glass beads (of two different sizes) and quartz sand. They compared these fundamental velocities to the velocities estimated from the more common and simpler methods of determining the first arrival from picking the first amplitude extremum, the first peak of the Hilbert Transform amplitude envelope, cross-correlation lags, and the first onset of energy. The authors concluded that the

velocities determined from picking the signal's first amplitude extremum, the peak of the amplitude envelope, and from cross-correlation, appear to provide reasonable estimates of the group velocities. However they also showed that the velocity determined from using a signal's first amplitude extremum compared to the phase velocity agreed to better than 1% for the two glass beads packs, but differed by 15% for the quartz sand. If the wave's velocity determined from using a signal's first amplitude extremum is actually the wave's group velocity, it should be noted that the propagating medium in their study is highly attenuating; for a less attenuating medium, the separation between group and phase velocity would be minimal. The estimate quality factors of the different packs ranged from 2 to 6 over a frequency range of 400 kHz, with the quartz sand being more attenuating than the two glass bead packs at any given frequency. Therefore the large difference between the quartz sand pack's phase velocity and the determined 'group' velocity from using the signal's first extremum may be caused by the higher attenuation of the quartz sand pack. Typical Earth materials would exhibit less attenuation than that observed in this study. Therefore the wave velocities determined in the laboratory from pulse transmission by using the signal's first extremum can be a reasonable measure of the wave's phase velocity.

3.4.2 Attenuation

When a seismic signal propagates through Earth materials, the amplitude of the seismic signature decreases as it temporally broadens. This phenomenon is referred to as physical attenuation. As already introduced, an attenuating medium will cause a distinction between phase and group velocities. Quantifying physical attenuation is of great interest because of its implication on seismic analysis and imaging. Quantitative amplitude studies such as amplitude versus offset (AVO) requires the effects from attenuation on the amplitude and the phase of signal to be mitigated or modelled for proper amplitude analysis. In vertical seismic profiling (VSP), quantifying attenuation can help improve the interpretation of seismograms by serving as another seismic parameter available for petrological interpretation. Apart from signal analysis, knowledge of seismic attenuation is

also valuable in seismic acquisition. Survey planning can be optimized by understanding how much signal can be preserved in the designed geometry. In CO₂ sequestration projects, in addition to the already listed benefits, knowledge of the attenuation will assist with the identification and quantification of the subsurface CO₂ plume.

The causes of attenuation can generally be classified as either extrinsic or intrinsic. Extrinsic attenuation is caused by geometrical effects and material heterogeneities. The resulting wave dampening is not due to the loss of mechanical energy, but is instead caused by the defocusing of wavefront energy. Examples of extrinsic attenuation are wave scattering, internal multiples (multipathing), and geometric divergence. Intrinsic attenuation on the other hand is from the anelasticity of the propagating medium and results in a loss of wave energy. It is related to the interaction between a passing wave, the traversed porous medium, and its saturating fluids. Intrinsic attenuation is thus a function of the propagating medium and can be used as an additional seismic property in characterizing Earth materials.

There are a number of factors that can give rise to intrinsic attenuation, and a few proposed mechanisms for saturated rocks will be briefly mentioned. Walsh (1966) proposed inter-granular friction or frictional dissipation as a mechanism and is related to the relative grain-grain boundary slip motion. This mechanism is amplified in the presence of pore fluid from the lubrication effect between the grains. Another favoured explanation for intrinsic attenuation is global flow, the mechanism associated with Biot's theory (1956a, b). It accounts for the differential movements between the fluid and solid constituents in a saturated porous medium as a wave passes through, therefore causing energy dissipation. Local flow or squirt flow is another possible mechanism of intrinsic attenuation and it involves the local motion of the fluid in the pores (O'Connell and Budiansky, 1977; Mavko and Nur, 1979; Palmer and Traviolia, 1981). This is a result from the compression of grains and consequently the capillary tubes from a passing wave, thereby inducing pore pressure gradients and causing fluid inside the heterogeneous pore cavities to squirt.

For a harmonic plane wave propagating through an attenuating medium, the decay of the wave amplitude $A(x,t)$ with space and time can be written as

$$A(x,t) = A_0 e^{-\alpha x} e^{i(\omega t - kx)}. \quad (3.80)$$

A_0 is the initial wave amplitude before traversing a distance, x , and α is the frequency dependent attenuation coefficient (given in units of m^{-1} or *nepers-m⁻¹*), where the frequency of the wave is given by, ω , and k is the wavenumber. By this representation, the elastic travel of the wave with space and time is given by the cyclic nature of the second exponential power where the effective damping of the wave amplitude is governed by the first exponential containing the negative product of the attenuation coefficient and the traversed distance. Equation (3.80) can be, instead, rewritten under a single exponential by using a complex wavenumber, k^* ,

$$k^* = k - i\alpha, \quad (3.81)$$

so that in a simpler form, the wave amplitude can be represented by

$$A(x,t) = A_0 e^{i(\omega t - k^* x)}. \quad (3.82)$$

From equation 3.81, the attenuation coefficient is essentially the imaginary wavenumber.

Alternatively, instead of describing the attenuation of a waveform by the attenuation coefficient, the quality factor is used more commonly. The quality factor, Q , characterizes the dissipation of a medium by a dimensionless quantity that generally compares the elastic to the inelastic behaviour of a seismic wave. A large quality factor value indicates low attenuation or loss, whereas a small quality factor indicates the material is very dissipative. The quality factor can be defined in a number of ways (Lakes, 2009).

Rheologically, for a linear viscoelastic medium, the modulus relating stress and strain is mathematically complex due to a phase lag between them (refer to equation 3.26). The real and the imaginary parts of the complex modulus are the storage modulus, C' , and the loss modulus, C'' , respectively, and are related to the quality factor as a ratio,

$$Q = \frac{C'}{C''}. \quad (3.83)$$

In terms of energy, the quality factor can be expressed as the amount of energy dissipated in a cycle, ΔE , for a given amount of stored energy in the system, E_{stored} ,

$$Q = \frac{2\pi E_{stored}}{\Delta E}. \quad (3.84)$$

Harmonically, in terms of wave propagation, the quality factor is

$$Q = \frac{\omega}{2\alpha(\omega)V} \left(1 - \frac{\alpha^2 V(\omega)^2}{\omega^2} \right) \quad (3.85)$$

which can be simplified to

$$Q = \frac{\omega}{2\alpha(\omega)V(\omega)}, \quad (3.86)$$

for $Q \gg 1$, where $V(\omega)$ is the frequency dependent phase velocity of the wave.

The log spectral ratio method is a common technique employed to determine wave attenuation in both field and laboratory seismic by analyzing the times series of two signals in the frequency domain (Gladwin and Stacey, 1974; Toksöz et al, 1979; Tonn, 1991; Wepfer and Christensen, 1991; Tutuncu et al, 1994; Sarma and Ravikumar, 2000; Diallo et al, 2003; Rickett, 2006; ; Santos et al, 2009; Jaya et al, 2010). For a signal acquired in the laboratory via the ultrasonic pulse transmission technique, the Fourier amplitude spectrum of a pulse through a sample length x_i can be expressed as (after Yin, 1993):

$$A(\omega, x_i) = S(\omega)D(\omega)e^{-\alpha(\omega)x_i}(1-R^2)G(\omega, x_i). \quad (3.87)$$

$S(\omega)$ is the amplitude spectrum of the outgoing pulse, $D(\omega)$ is the amplitude spectrum of the receiver, $G(\omega, x_i)$ is geometric effects, and R is the reflection coefficient from the aluminum end cap of the transducer to the sample interface. The spectra of two signals corresponding to different traveling distances of the same viscoelastic medium can be related by

$$A(\omega, x_2) = A(\omega, x_1)e^{-\alpha(\omega)(x_2-x_1)} \frac{G(\omega, x_2)}{G(\omega, x_1)} \quad (3.88)$$

if the same signal transmitting and receiving equipment is used. Therefore if the amplitude spectra can be determined, the attenuation coefficient of a viscoelastic medium for a range of frequencies can be calculated by

$$\alpha(\omega) = -\frac{\ln\left(\frac{A(\omega, x_2)G(\omega, x_1)}{A(\omega, x_1)G(\omega, x_2)}\right)}{(x_2 - x_1)}, \quad (3.89)$$

as hinted by the name of the method. Additionally, the quality factor can be found from the attenuation coefficient if the phase velocity, $V_p(\omega)$, of the propagated signal is known,

$$Q = \frac{\omega}{2\alpha(\omega)V_p(\omega)}. \quad (3.90)$$

The phase velocity at a given frequency is

$$V_p(\omega) = \frac{(x_2 - x_1)}{\Delta t_{phase}}, \quad (3.91)$$

where Δt_{phase} is the phase lag in time between the two signals found by differencing their corresponding phase spectra over frequency (figure 3.7)

$$\Delta t_{phase}(\omega) = \frac{\Delta\phi}{\omega}. \quad (3.92)$$

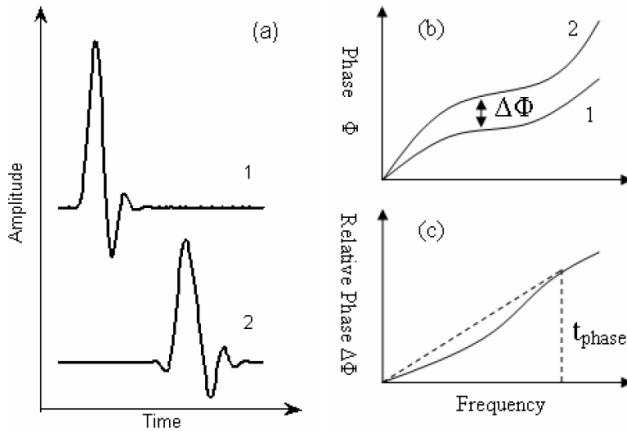


Figure 3.7: Illustration of phase velocity determination (Figure reproduced from Qi (2008) after Molyneux and Schmitt (2000)). a) Elastic wave pulses through two different sample lengths. b) Unwrapped phase of the Fourier transforms of the times series pulses. c) Determination of the frequency-dependent time phase.

* Reprinted with permission from the Society of Exploration Geophysicists.

In attenuation measurements, large errors are quite common (Bourbie et al, 1987, White, 1992; Molyneux and Schmitt, 2000) due to uncertainties in the spectral decomposition of a signal. From the conventional log spectral ratio method, the associated errors can be estimated statistically from redundant attenuation measurements if multiple (more than 2) lengths of the same samples are used (Molyneux and Schmitt, 2000; Qi, 2008). An example for demonstrating the analysis of waveform attenuation with errors using the log spectral ratio method will be shown in the next section.

3.4.3 The Attenuation of Ultrasonic Waves through Acrylic

A series of ultrasonic pulse transmission measurements were performed on four different lengths of acrylic. Acrylic is a soft, viscoelastic, synthetic polymer of methyl methacrylate that is commonly known as Plexiglass. For each sample length, the acrylic sample was placed in between a pair of transmitting and receiving transducer composed of 1 MHz P- and S-wave piezoelectric ceramics. The time series of the transmitted signal through a sample is received by an oscilloscope at a sampling interval of 10 nanoseconds. During data acquisition, the sample with the pair of transducers was subjected to a confining pressure to improve the transducer-sample coupling, thereby enhancing a received signal's quality. Further details on the transducers, the experimental set up, and data acquisition system used in these measurements can be found in Chapter 4.

P- and S-wave time series signals were acquired under a confining pressure of 20 MPa for acrylic lengths of 2.00, 3.00, 4.00, and 5.00 cm. The recorded P- and S-wave traces are shown in figure 3.8 where the dampening of wave strength with increasing sample length is apparent. However, temporal broadening of the waveform is less obvious. The times series signals were windowed and the Fast Fourier transform (FFT) was applied to obtain their equivalent in the frequency domain. The corresponding amplitude spectra of the signals are shown in figure 3.9. As expected, the strength of the Fourier amplitude spectrum is reflective of their signal strength and decreases with longer acrylic sample lengths. The peak of all P-wave spectra is centered at 0.70 MHz, while

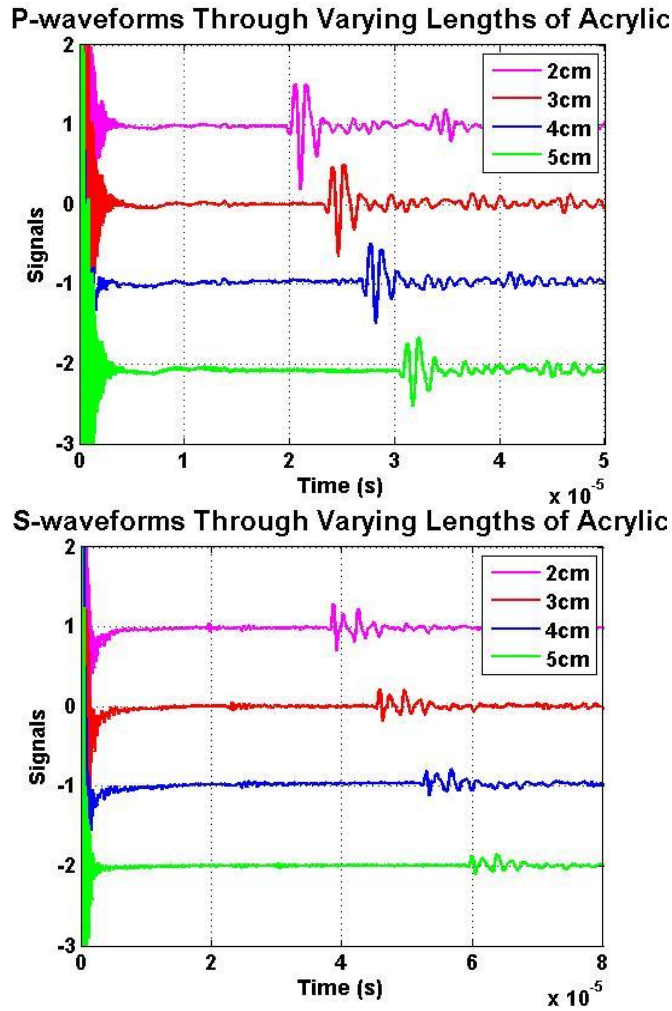


Figure 3.8: The time series signals recorded through varying lengths of acrylic: P-waves (top) and S-waves (bottom).

for the S-wave spectra the peak frequency generally shifts to a lower frequency with increasing sample length. The peak frequency is 0.59, 0.56, 0.52, and 0.54 MHz for the 2.00, 3.00, 4.00, and 5.00 cm sample, respectively. A detailed examination of the S-wave signal corresponding to the 4.00 cm long acrylic shows a slightly different morphology than the rest of the acquired S-wave signals. Thereby a skewed amplitude spectrum from this signal is evident through comparison to the rest of the S-wave signals. This variation can be attributed to misalignment of the pair of transducers (the S-wave transducer is orientation-sensitive) or to the poor connection of electrical wires in the experiment. For both the P- and S-wave amplitude spectra the majority of the energy is spread between

0.4 to 1.4 MHz. To avoid large errors, only the data in this useful frequency range is analyzed.

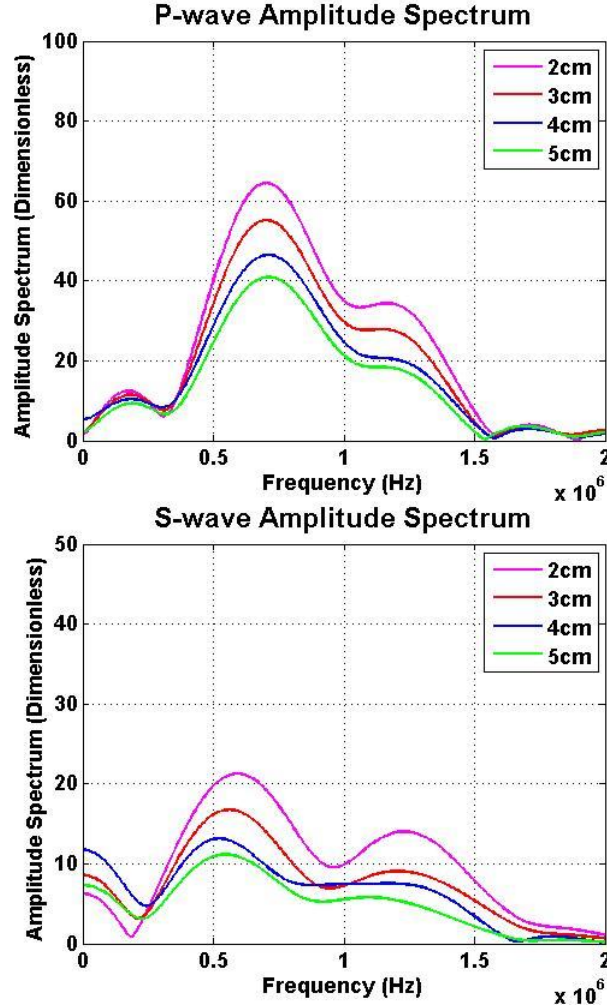


Figure 3.9: The amplitude spectra determined of the time series signals shown in figure 3.8: P-waves (top) and S-waves (bottom).

For all the possible combinations of a pair of samples with different lengths, the natural logarithm was taken of their signal's amplitude spectra ratio at each frequency, and plotted against their respective length difference, independently for P-and S-waves. The P- or S-wave attenuation coefficient of acrylic was determined from the plot based on the slope of the best fit line, as a function of frequency. In this study, the diffraction loss from the geometry of the samples was ignored. The corresponding attenuation coefficient error was

estimated by finding the maximum absolute difference between the slope of the best fit line and the slopes of all the possible lines that can fit through any two data points. The computed P-wave attenuation coefficient as a function of the frequency is shown in figure 3.10 (top plot). From 0.4 MHz to 1.4 MHz, the P-wave attenuation coefficient varies from 14.4 m^{-1} to 24.9 m^{-1} , and at the peak frequency of 0.70 MHz it has a value of 15.3 m^{-1} . The largest P-wave attenuation coefficient error estimated is 12.1 m^{-1} . The S-wave attenuation coefficient varies from 16.6 m^{-1} to 38.3 m^{-1} , and at the averaged peak frequency of 0.55 MHz it has a value of 21.5 m^{-1} . The largest S-wave attenuation coefficient error estimated is 18.2 m^{-1} (figure 3.11, top plot). With increasing frequency, both the P-wave and S-wave attenuation coefficient generally increases.

The phase velocity was found using the procedure outlined in section 3.4.2 for all the possible length combination pairs, and the averaged value was used to find the quality factor. The phase velocity for both P-and S-wave varied minimally ($\sim 10 \text{ m/s}$) over the range of frequencies analyzed. The P-wave quality factor, Q_p , with errors propagated from the attenuation coefficient and phase velocity is displayed in figure 3.10 (bottom plot). Over the useful frequency range, the quality factor varies from 21.4 to 65.4, and at 0.70 MHz the quality factor is 45.2. The largest error of the P-wave quality factor estimated is 26.6. The computed S-wave quality factor, Q_s , is shown on bottom plot of figure 3.11. The S-wave quality factor varies from 49.7 to 131.4, and at the averaged peak frequency of 0.55 MHz, it is 57.3. The largest S-wave quality factor error is 118.7.

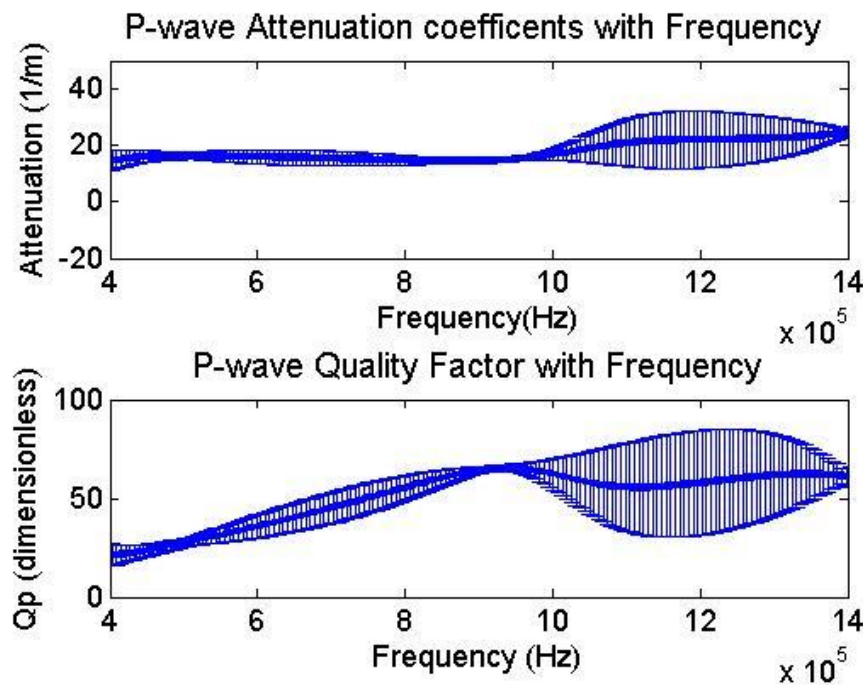


Figure 3.10: P-wave: (top) Attenuation coefficient and (bottom) quality factor, as a function of frequency.

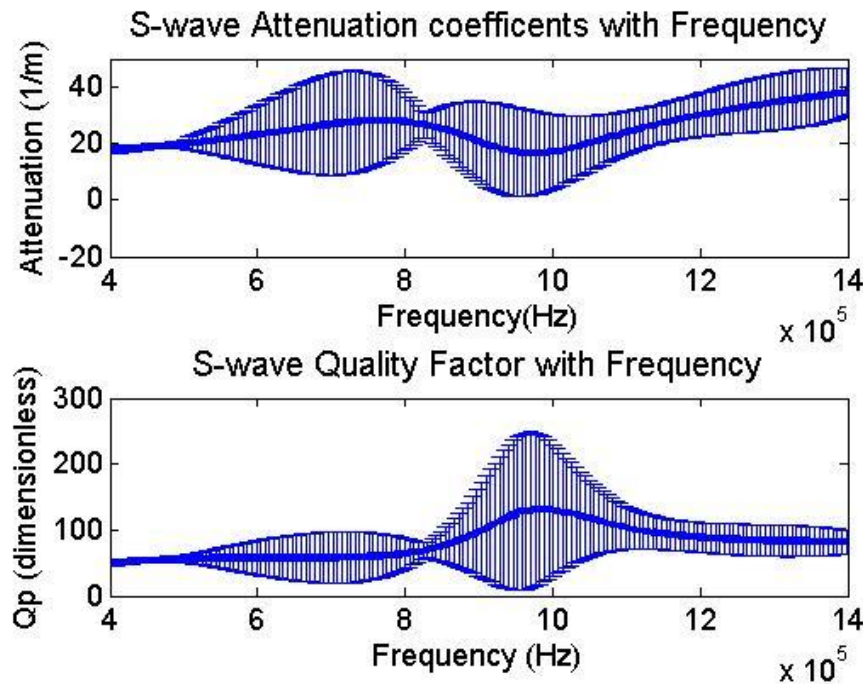


Figure 3.11: S-wave: (top) Attenuation coefficient and (bottom) quality factor, as a function of frequency.

3.5 Summary

In order to understand seismic wave behaviour pertaining to geologic CO₂ sequestration, factors that will influence subsurface wave propagation were reviewed. From reviewing the thermodynamics of CO₂ and from using a simplified temperature and pore pressure model of the upper section of the sedimentary basin, CO₂ can exist as a gas, a liquid, or a supercritical fluid for a geological sequestration project. The physical properties of these phase states relevant to wave travel were obtained from Span and Wagner's (1996) empirical equation of state and phase diagrams of these properties were generated. The behavioural variations of the bulk modulus, density, and viscosity of CO₂ with the corresponding phase state were consistent; a large change in properties for a gas-liquid transition and a subtle change for a gas- or liquid-supercritical fluid transition.

To describe the basic behaviour of elastic wave travel, the theory of elasticity was first reviewed. When a volume of perfectly elastic material is subjected to a force or is stressed, deformation will result and it is fully recoverable when the force is removed. Stress and strain relations were reviewed through Hooke's law where the elastic stiffness constant was established for a linearly elastic isotropic medium. Starting from 81 elastic constants, the tensor was reduced to 2 independent constant for an isotropic medium. From incorporating Hooke's law into Newton's second law of motion, the wave equation for an isotropic medium was shown. P- and S-wave velocities in terms of the elastic constants and the density of the material were defined. Furthermore, in contrast to a perfectly elastic material the basic concept of viscoelasticity along with its implication on wave travel was discussed. The viscous behaviour component of a viscoelastic material will give rise to the attenuation of a propagating wave.

Rock physics, the branch of geophysics that relates geophysical observation to their physical cause, was reviewed by the fluid substitution formulations of Gassmann (1951) and Biot (1956a, b). Gassmann's equation is easy to apply in relation to Biot's equation; however Gassmann's formulation has

limitations that are particularly concerning for our application, namely the restriction to low frequencies. In contrast Biot's formulation is valid for a wide frequency range and differentiates the pore fluid behaviour with respect to the mineral grain, i.e. decoupling motion. Physical velocity dispersion, wave attenuation, and two compressional waves corresponding to the in and out of phase motion between the rock frame and pore fluid, are the distinct results produced from Biot's formulation.

Lastly, an introduction to the foundation of ultrasonic pulse transmission was given. Phase and group velocity of transmitted signal was discussed. Based on Molyneux and Schmitt's (2000) work, it was determined that from picking the first arrival of a signal, the resulting velocity is a reasonable approximation for phase velocity. In addition to analyzing wave velocities from ultrasonic pulse transmission, the attenuation of an ultrasonic wave was discussed. The complex wave number, the attenuation coefficient and the quality factor used for characterizing wave dampening were formally defined. The actual application of the ultrasonic pulse transmission method and the analysis of wave attenuation experimentally were carried out by using varying lengths of acrylic. The amplitude dampening of waves through longer sample lengths is clearly evident in both the time and frequency domain of the signals. The log spectral ratio method was applied, and the attenuation coefficient and the quality factor of acrylic were determined. The typically large uncertainties associated with attenuation measurements are observed here, where the largest the errors observed with our determined P-and S-wave attenuation coefficients are 12.1 m^{-1} and 18.2 m^{-1} , respectively.

Chapter 4

Experimental Setup and Procedure

As previously discussed in Chapter 3, ultrasonic pulse transmission is the underlying methodology in our study applied to determine the wave velocity and attenuation in CO₂ saturated samples. The application of this method allows the recording of a P- or S-wave after propagation through a sample. Ultrasonic pulse transmission is a commonly applied technique to determine the dynamic elastic properties in rocks and to the best of our knowledge, has been the only laboratory method applied to date concerning CO₂ rock physics. In this chapter, the working application of this method will be introduced through a description of the experimental setup and the procedures for the laboratory measurements. First, the construction and the workings of a piezoelectric transducer will be discussed. Then the sample preparation, assemblage and the experimental apparatus will follow. Next, the experimental procedure and the acquisition of data will be given. Finally, examples of waveforms will be shown and a discussion on the determination of wave velocities, wave attenuation, and associated errors will ensue.

4.1 Piezoelectric Transducers

Transducers are the main component of pulse transmission measurements. In order to transmit and receive an elastic wave in the laboratory, ultrasonic transducers to accommodate cylindrical core samples with 2.54 cm diameter were made. In this section, the materials and construction of the transducers used in this study are reviewed. The main components of our ultrasonic transducer are

the aluminum buffer caps, P- and S-wave piezoelectric ceramics, copper foil electrodes, and the damping material.

To generate P- and S-waves in ultrasonic pulse transmission experiments, piezoelectric ceramics are typically employed. Piezoelectric materials are materials that are capable of producing an electrical potential when experiencing an applied stress such as a mechanical vibration, and this effect is linear and reversible such that when an electrical potential is applied the material will exhibit mechanical strain or a mechanical vibration. Piezoelectricity is based on the internal structures of the material and is caused by the linear interaction between the electrical and mechanical behaviour of the medium. This phenomenon can only be exhibited in materials whose crystal structure has no center of symmetry (Zhu and Meng, 2002). The type of vibration generated is determined by the polarization of the piezoelectric crystal. Longitudinal waves (P-waves) are generated if the material is axially polarized such that axial compression and expansion can occur. Transverse waves (S-waves) are generated if the material is laterally polarized allowing for shear motion to occur. The piezoelectric material used in this study (shown in figure 4.1) is a ceramic made from lead zirconate titanate with a resonant frequency of 1 MHz, manufactured by Omega Piezo Technologies Inc.

From the direct and reversible characteristic of piezoelectricity mentioned above, both the transmitting and receiving ultrasonic transducers were built in the same way by using the same materials and arrangements. On an aluminum buffer end cap, the different vibration mode ceramics were mounted in a stacked configuration to allow for the simultaneous measurement of P-and S-waves. Before construction, the surface of the aluminum buffers was polished for a smooth and flat surface to prevent scattering of the generated waves. The S-wave piezoelectric ceramic was placed directly on the surface of an aluminum buffer cap and then the P-wave piezoelectric ceramic was placed on top of the S-wave ceramic. Separating the P- and S-wave ceramics is a piece of copper foil which acts as a common electrode between the two piezoelectric

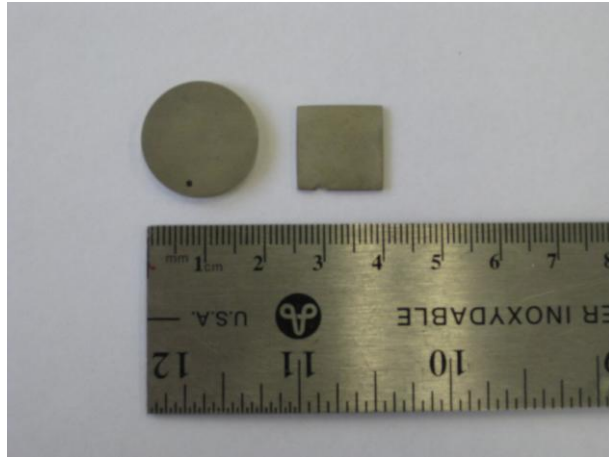


Figure 4.1: P-(circle) and S-wave (square) piezoelectric ceramics used in our transducers.
The larger increments on the topside of the ruler are in centimetres.

ceramics. It serves as the positive terminal for the S-wave ceramic and acts as the negative terminal for the P-wave ceramic. The negative terminal for the S-wave ceramic will come from the contact with the buffer cap, while the positive terminal for the P-wave ceramic comes from another piece of copper fixed onto the top of the ceramic. Each piece mentioned above in this assembly was attached to one another using CircuitWorks® CW2400 silver conductive epoxy. To prevent any short-circuiting of the positive and negative terminals, excess conductive epoxy was removed from the edges of the ceramics and tested for conductivity between each mounting. The copper foils attached only extended a short amount past the stacked ceramics and insulated electrical wires were soldered onto the exposed copper foils for extension. In addition, after the silver epoxy from the last attachment has dried, a thin film of non-conductive, general purpose epoxy was applied to the surface of the P- and S-wave ceramics and the exposed copper.

After this applied epoxy has dried, damping material made from a mixture of urethane rubber (Flexane® 80 Liquid) and tungsten filings were placed on top of the transducer arrangement in a cylindrical mould. To prevent the quick deterioration of the transducers from hydraulic oil intrusion during the lab measurements, the hardened damping material, the exposed ceramics, and parts of

the aluminum buffer were set in liquid urethane rubber for sealing. Hydraulic oil is the confining medium in the pressure vessel.

The construction of the transducers were completed at least a week prior to use because the urethane rubber requires at least 7 days to cure to its full strength. A cartoon depicting the different components and a photograph of a completed source and receiver transducer pair are shown in figure 4.2. One of the transducers in the pair contains a stainless steel tube that extends from the top of the aluminum buffer cap. The end of the tube that is not shown in the figures is connected to a hole that traverses the full, vertical length of the buffer and allows pore pressure control and fluid saturation of the sample.

4.2 Sample Preparation

Ultrasonic pulse transmission measurements were conducted on a synthetic and a non-synthetic sample, a porous ceramic rod and a Berea sandstone, respectively. Cylindrically shaped samples of 2.54 cm in diameter and of lengths greater than 4 cm were obtained for the measurements. The non-synthetic sample was cored under wet conditions using a 2.54 cm diameter diamond encrusted bit. Water was continually flushed through the drill bit and the sample during the coring process for cooling and lubrication. Afterwards, the end faces of the core sample were made parallel with first using a wet saw to achieve approximate parallelism, and then the end faces were fine tuned and smoothed with the use of a wet grinder. The parallelism for the cored sample was measured using a dial gauge and was only deemed acceptable if it was within 2 thousandths of an inch (within ± 0.025 mm). Smooth and parallel end faces are important for enhanced signal transmission and to minimize velocity measurement inaccuracy. The synthetic sample was purchased and came in a cylindrical dimension of 2.54 cm in diameter and 5 cm in length. The end faces were flat and parallel, and no additional work was required for the synthetic sample. Prior to any lab measurements, both samples were dried in an oven at 70°C under vacuum for at least 48 hours and kept in a desiccator jar afterwards until in use.

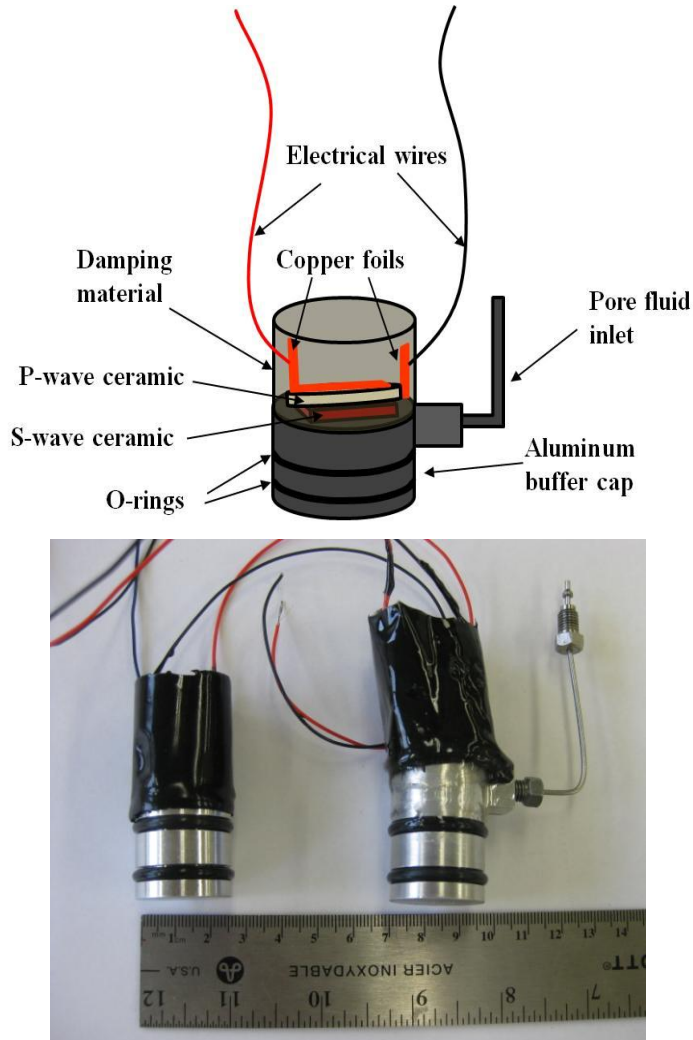


Figure 4.2: (top) Cartoon depiction of the various components in a transducer. (bottom) A photography of a completed pair of transducers (pulser and receiver). The transducer on the right has the pore pressure inlet.

The final preparation for ultrasonic pulse transmission measurements involves assembling the sample with the transducers and pieces that will provide sealing of the sample from hydraulic oil inside the pressure vessel. The sample was placed inside a flexible, 2.54 cm wide Tygon® tubing and a piezoelectric transducer was placed on each end of the sample, with a part of the transducer underneath the Tygon tubing. Since S-waves are polarized, the transducers on the ends of the sample were aligned with care to achieve proper polarization of the S-wave ceramics. Improper alignment of the shear ceramics would lead to a weak

S-wave signal and even an absent signal if the two shear ceramics were positioned 90° to each other. To prevent hydraulic oil from contaminating the sample by seeping in from between the transducer and the overlapping Tygon tubing, rubber O-rings were slipped around the aluminum buffers and underneath the tubing. In addition, metal hose clamps were placed around the outside of the Tygon tubing, positioned directly above the underlying rubber O-rings, and were tightened to maximum. A fully assembled sample ready to be placed inside the pressure vessel for ultrasonic measurements are shown in figure 4.3. The workings of the rest of the experimental apparatus will be discussed in the next section.

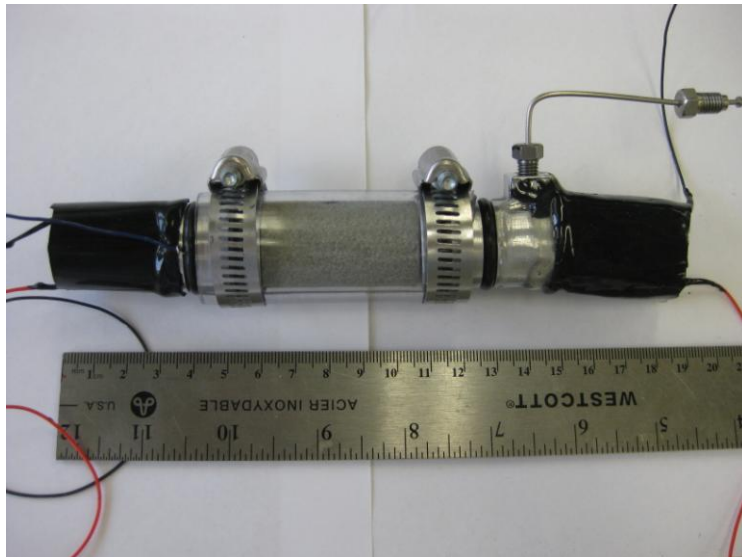


Figure 4.3: A fully prepared and assembled sample ready for measurement. The sample is placed in between a pair of transducers and is jacketed in a clear Tygon® tubing. Iron hose clamps are tightened against the tube and the rubber o-rings that surrounds the aluminum buffer.

4.3 Experimental Apparatus

Aside from the sample and transducer assemblage, the main components of the experimental set up consists of the pressure vessel, the pore fluid source, pressure gauges, a thermocouple, an electrical resistance tape, a pulse generator, and a digital oscilloscope. Figure 4.4 shows the schematic and the photograph of the pressure vessel and the rest of the experimental setup. The sample and transducer assemblage is placed inside the pressure vessel, in a 10 cm wide and 40

cm deep cylindrical cavity filled with hydraulic oil. As mentioned earlier, the hydraulic oil serves as the pressurizing medium for providing hydrostatic confining pressure on the sample.

The desired pore fluid is introduced into the sample via stainless steel tubing that connects the pore space of the sample to the pore fluid reservoir located outside of the vessel through the vessel lid. The confining and pore systems are independent of each other such that different pressure conditions can be applied in irrespective of each other by using different pumps located outside of the pressure vessel. A Quizix™ Q5000 pump system was used to control both pressure systems. Both the confining pressure (pressure vessel) and the pore pressure system are capable of reaching a maximum pressure of 70 MPa from this pump system. Higher confining pressures, up to 200 MPa, could also be achieved by using a separate air pump connected to the pressure vessel.

For CO₂ saturated measurements, a CO₂ cylinder of 99.9% purity was used. The pressure inside the tank is essentially buffered at the vapour-liquid transition pressure at the given room temperature; normally the CO₂ leaving the tank is gaseous. To generate pore pressures higher than the pressure in the tank, theoretically the pump can be used to pressurize gaseous CO₂ into a liquid phase state at room temperature. However practically this requires a lot of pumping and time. Since at room temperature the CO₂ in the tanks are partly in the gaseous phase and partly in the liquid phase state, the denser liquid state can be obtained directly by simply inverting the tank thereby allowing liquid CO₂ to be the first to leave the nozzle of the tank.

The ambient temperature of the pressure vessel can be raised from room temperature from the heating of an electrical resistance tape that is wrapped around the outside of the pressure vessel. Desired temperature of the pressure vessel is controlled by the turning on and off of the power supply to the electrical resistance tape. The actual temperature inside of the pressure vessel is determined from a K-type thermocouple and is located immediately next to the sample.

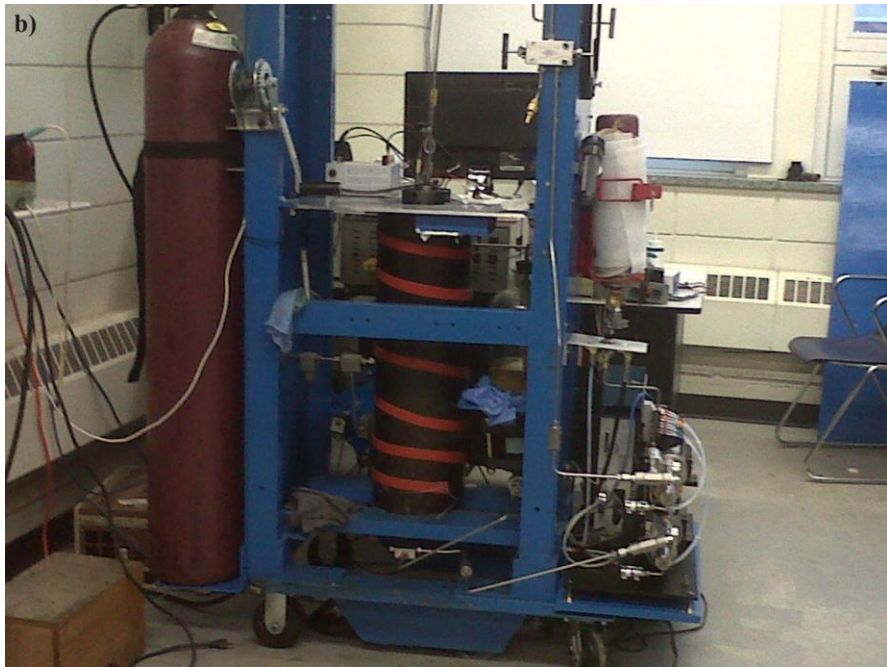
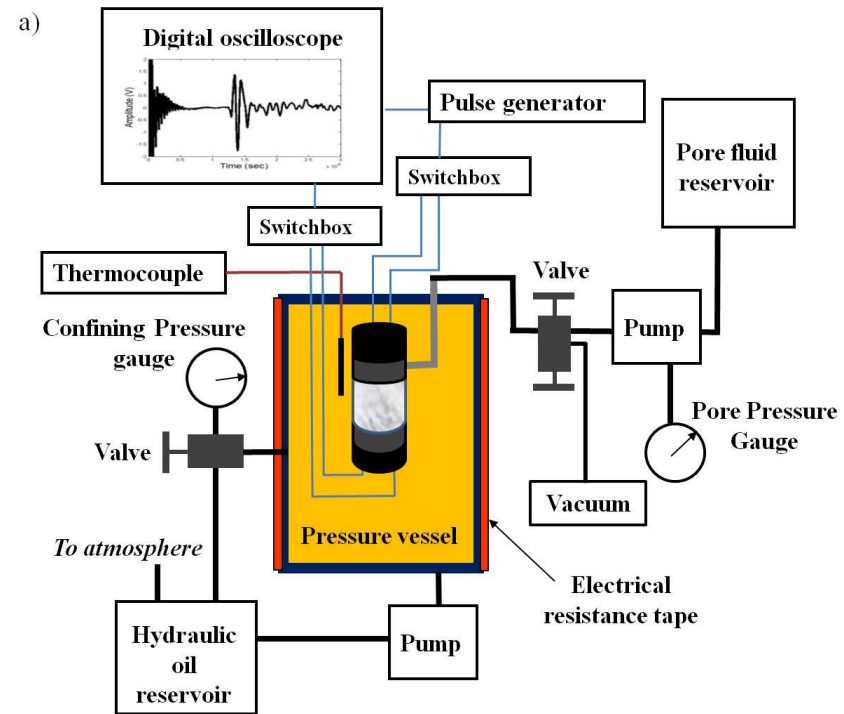


Figure 4.4: a) A simplified schematic of the experimental set up. b) Photograph of the laboratory equipment used. The acquisition system behind the pressure vessel and is not captured in the photograph.

The experimental set up pertaining to generating and recording the elastic waves consists of a pulse generator, a digital oscilloscope, a switchbox and electrical wire feed-throughs. The electrical wire feed-throughs are soldered onto the electrical wires of the transmitting and receiving transducers and are fed through the lid of the pressure vessel to allow for the external excitation and recording of the pulsed signal. The transmitted signal is generated by triggering the transmitting transducer with a fast rising 200 V square wave using a JSR-PR35 pulse generator. The propagated signal is recorded by a digital oscilloscope made by National Instrument, at a sampling rate of 10 nanoseconds. To reduce random noise effects, the final waveform recorded is a stack of over 500 traces. The switchbox was used to facilitate the switch between exciting and recording of the P- and S-waves at a given condition.

4.4 Experimental procedure

The samples were subjected to a series of measurements including measurements made under dry conditions, various CO₂ saturated conditions, and a water saturated condition. Before describing the different temperature, pressure, and fluid-type saturation conditions undertaken during this study, it is important to define the different types of pressures that can be applied to a sample during a measurement. As mentioned in the previous section, the pressurizing system controls two types, confining pressure and pore pressure. Confining pressure is the external pressure applied onto the surface of the sample. Pore pressure is the pressure of the fluids inside the pore space of a sample. These two types of pressures are exerted in opposite directions in relation to each other, where the confining pressure pushes the grains of sample together and the pore pressure pushes the grains out. The net effect of these two pressures applied on a sample is the differential pressure, P_d , and is defined as

$$P_d = P_c - P_p, \quad (4.1)$$

where P_c is the confining pressure and is usually larger, in-situ, than the pore pressure, P_p . Indeed, P_p in excess of P_c will lead to hydraulic fracturing of the rock mass.

During the measurements for a given sample or between the two samples, the conditions applied differed slightly, but fundamentally the measurements were the same and the intended conclusions could be still drawn even with the slight differences. These differences in applied procedure are due to unexpected circumstances that have arisen during the measurements and to new learning along the way that have resulted in procedural tuning between the different measurement runs to increase more relevant data and reduce less useful data. Re-measurement of the samples for perfect procedural consistency was not done due the time intensity required for a complete set of measurements for a sample and the high demand for the use of the pressure vessel and system. To follow are the set of measurements and procedures attempted for a given sample. Both the synthetic and non-synthetic samples have slight measurement deviations from this list and their deviations are mentioned.

The first set of ultrasonic measurements conducted on the samples was the dry measurements. For dry conditions, the pore space is ideally empty and the pore pressure is consequently zero. Air inside the pore space of the sample and inside the pore tubings of the pressure vessel system are pumped out over a duration of 12 hours by attaching a vacuum to the pore pressure system. When applying the vacuum to the pore pressure system, the drop in pressure follows an exponential curve with a rapid drop in the first hour followed by a slower and steady drop in the second hour and remains unchanged for the next 10 hours. The final pressure reading on the pressure gauge is usually about 0.0024 KPa. Compared to the initial pressure of about 101.3 KPa, the final pressure is only 0.002% of the original atmospheric pressure. Even though after 12 hours of vacuuming the pore pressure is not zero but, the pore space is essentially empty for the purposes of these experiments, as the mass and the gaseous compressibility are negligible. These ‘dry’ measurements were first conducted at room temperature as confining pressure was varied between 5 MPa and 40 MPa at 2.5 MPa intervals during both pressurization and depressurization cycles, while the pore pressure was under vacuum. Afterwards, heated dry measurements were conducted at a constant confining pressure of 10 MPa while the temperature of the

pressure vessel was raised. During the heated attempt for the non-synthetic sample, the connector of the thermocouple to the pressure vessel malfunctioned and this was not realized until the vessel reached 55°C. Therefore the changes in the waveform as the sample warmed were not mapped, instead only the waveforms at two temperatures, 23°C and 55°C, were recorded. Nonetheless, the temperature dependency of the sample is still exhibited by these two measurements.

Following the dry measurements, a large set of CO₂ saturated measurements were made under various pressure and temperature conditions. The samples were saturated with CO₂ by connecting the pore pressure system under vacuum to the CO₂ tank, and left overnight at a pore pressure of 10 MPa for the sample to be fully saturated. For both samples, 5 different constant temperature runs were attempted while pore pressure varied from 2 MPa to 25 MPa. The constant temperature runs were done at 23° C, 28° C, 40° C, 45° C, and 55° C. As pore pressure increased for the 2 lower temperature runs (23°C and 28°C), CO₂ changed from a gas phase to a liquid phase while for the higher temperature runs (40°C ,45°C, and 55° C), CO₂ changed from a gas phase to the supercritical fluid phase. For the synthetic sample's 55°C run, it was only partially completed because there was a lack of CO₂ in the tank to build higher pressures during the measurements. Unfortunately, the sample was later contaminated by hydraulic oil leakage and the measurements could not be repeated.

To reach the higher temperatures from room temperature (~23°C), the heating typically required 2 or more hours. To use time effectively, velocity measurements were also conducted as the temperature changed during heating while holding both confining and pore pressure constant for the synthetic sample. Constant pressure runs were conducted at 7 MPa, 10 MPa, and 25 MPa as the pressure vessel was heated from room temperature (~23°C) to the desired end temperature for the constant temperature run. For the non-synthetic sample, constant pressure runs were conducted separately from the heating up of the vessel for constant high temperature runs so that a final temperature of 50°C could

be reached for consistency. At 7 MPa, the CO₂ changed phase states from liquid to gas, while for the 10 MPa and 25 MPa the CO₂ underwent a liquid to supercritical phase transition. For both constant temperature and constant pore pressure runs, a constant differential pressure of 15 MPa was maintained by varying the confining pressure accordingly to the pore pressure.

After the series of CO₂ saturated measurement runs were completed and prior to water saturated measurements, the pore system along with the pore space of the samples was vacuumed for 12 hours and dry measurements at room temperature were repeated under the same conditions as before. The purpose of this second dry run was to verify if the nature of the sample has changed. This second dry run for the synthetic sample was done after the partial completion of the CO₂ measurements at T = 55°C, as we waited for the arrival of a new CO₂ tank.

The final run for the samples were water saturated measurements. Distilled water was introduced into the vacuumed system from a water reservoir. The sample was left overnight at a pore pressure of 10 MPa to reach full saturation. Water saturated measurements were conducted the next day at room temperature with the pore pressure varying from 2 MPa to 25 MPa while maintaining constant differential pressure of 15 MPa. As mentioned above due to oil contamination of the synthetic sample, water saturated measurements were not conducted. However, water saturated measurements on the sample were conducted in an earlier set of measurements. The conditions applied were different than the ones listed above. They were done at room temperature with a constant differential pressure of 5 MPa while pore pressure varied from 5 to 50 MPa.

All measurements listed above involved the acquisition of both P- and S-waveforms. For the measurements that involved changing pressures, 15 minutes were allowed before recording the waveform to allow conditions inside the pressure vessel to equilibrate. To summarize, the measurements conducted for a sample in terms of the type of saturation, temperature, and pressure conditions applied are given in table 4.1.

Type of Measurement (saturation)	Temperature (°C)	Pressure		
		Confining (MPa)	Pore (MPa)	Differential (MPa)
Dry	23 ^a	5-40	0	5-40
	23-50 ^b	10	0	10
CO ₂	23	17-40	2-25	15
	28	17-40	2-25	15
	40	17-40	2-25	15
	45	17-40	2-25	15
	55 ^c	17-40	2-25	15
	23-50	23	7	15
	23-50 ^d	25	10	15
	23-50 ^e	40	25	15
Water	23 ^f	17-40	2-25	15
	23 ^g	10-50	5-45	5

Table 4.1: The measurements carried out for a sample during ultrasonic pulse transmission experiments. ^a measurement run conducted twice, prior and after CO₂ saturated measurements. ^b Porous ceramic rod's end temperature was 40°C and only the beginning and end temperature waveforms were recorded for the Berea sandstone. ^c For the porous ceramic rod, the maximum pore pressure reached was 7 MPa for this measurement run. ^d Porous ceramic rod's end temperature is 40°C. ^e Porous ceramic rod's end temperature is 45°C. ^f measurement run for the Berea sandstone. ^g measurement run for the Porous ceramic rod.

4.5 Velocity and Attenuation Analysis Methodology

As per the experimental procedure reviewed above, a large suite of P- and S-waveforms was acquired under various saturation, pressure, and temperature conditions for each sample. From these collected waveforms the P-and S-wave velocities and attenuations can be analyzed as a function of the applied conditions. The method behind wave velocity and wave attenuation analysis from the acquired signals will be described in this section.

4.5.1 Velocity and Error Analysis

Before determining the P- and S-wave velocities from the acquired waveforms, the time axis of the waveforms first need to be calibrated. The arrival time of a P- or S-wave determined from the recorded waveforms is a combination of the time required for the signal to travel through both the sample and the aluminum buffer caps. To determine the actual velocity through just the sample, the time effects from the aluminum buffer caps therefore need to be eliminated and are referred to as the delay time. To determine this delay time for a transducer set, calibration measurements were conducted by performing ultrasonic pulse transmission through just the pair of buffers prior to conducting the suite of measurements on the sample. The delay time is affected by pressure, therefore the calibration measurements were done over the range of pressures that would be encountered during the measurements using a sample. Figure 4.5 is a plot of the normalized traces collected during the buffer measurements under confining pressures of 5 MPa to 50 MPa at room temperature. Each waveform is normalized with respect to the largest amplitude of the trace. At first glance, the arrival times of the signals show little pressure dependency over this pressure range. A closer and more detailed look reveals a slight linear dependence on pressure with the signals at higher pressures arriving earlier than at lower pressures. If this arrival time pressure dependency is ignored, this can translate to an incorrect velocity determination of ~50 m/s for the samples. Therefore care must be taken in applying the correct calibration measurements to the measurements made under the corresponding pressure on the samples. Figure 4.6a shows a signal through just the buffers under a confining pressure of 15 MPa and figure 4.6b shows the signal at the same confining pressure traveling through the buffer and the dry sample. The delay time of the signal in plot b is determined from the arrival time of the signal in plot a.

The arrival times of the signals were picked using the first extremum and are indicated by the red circle in figure 4.6. By determining the difference in arrival times of the signal through the buffers with sample (t_{bs}) and the signal through just the pair of buffer (t_b), the travel time of the signal through the sample

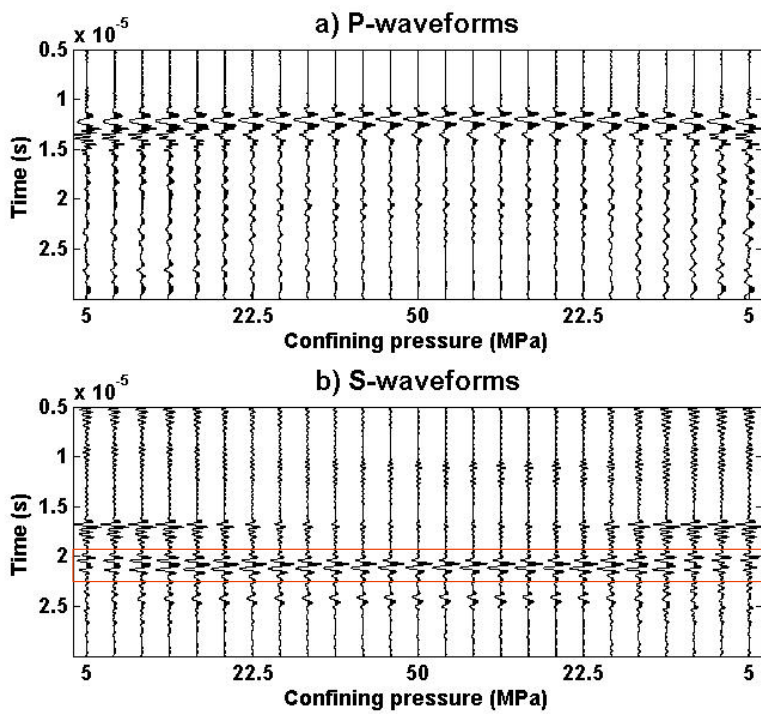


Figure 4.5: Buffer measurements over a confining pressure range of 5 MPa to 50 MPa: (a) normalized P-waveforms, (b) normalized S-waveforms. The actual S-wave arrivals are marked by the red box.

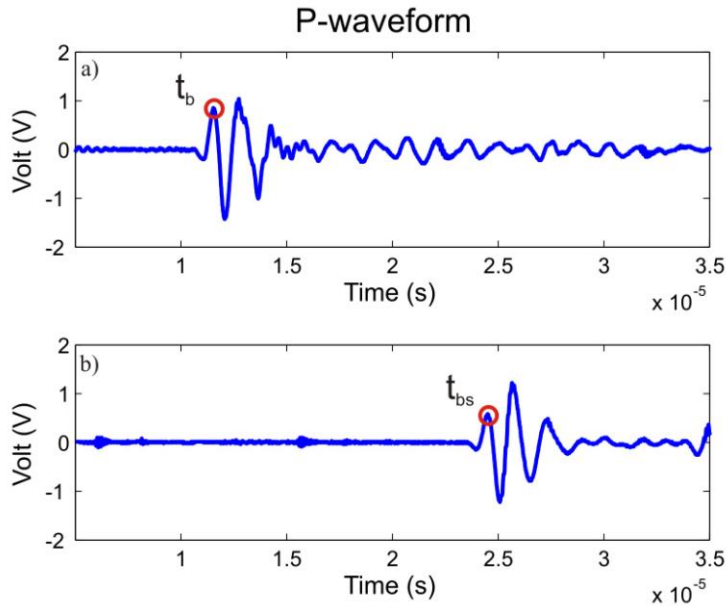


Figure 4.6: P-waves under a confining pressure of 15 MPa (a) through only the aluminum buffer cap (b) through both the aluminum buffer and synthetic sample. The red circle marks the extremum picked for the arrival time of the signal.

can be determined (t_s). Consequently, the signal's velocity, v , through a sample is determined from this travel time in conjunction with the sample's length, L_s , via the simple relation:

$$v = \frac{L_s}{t_s} = \frac{L_s}{t_{bs} - t_b} \quad (4.2)$$

In any type of work involving measurements, error will always be present. This error is associated with imprecision and uncertainties of the measurement. In order to calculate the velocity in equation 4.2, three variables had to be measured and therefore three sources for error exist in contributing to the error in velocity. The obvious uncertainties in the variables of equation 4.2 are determining the sample length and picking a signal's arrival time for both the buffer calibration measurements and the sample measurements. For the former source of error, the end faces of the samples were ground until a parallelism was within a thousandth of an inch, therefore the error in sample length is 2×10^{-5} m. For the latter source of error, the error is variable depending on the quality of signal. There is a minimum error of 10 ns (10×10^{-9} s) for high quality signals (the sampling rate is 10×10^9 s in our data acquisition system) and a maximum error of 30×10^{-9} s for low quality signals (the time window where the largest peak or trough value is certainly within for the poorest quality signals).

Apart from these 3 obvious sources of errors, other less apparent factors and errors also need to be addressed that may be significant and will contribute to the total velocity error. Additional error to length determination could be sample shortening under pressure. Hemsing (2007) suggested that sample shortening is not a great concern as he estimated a 0.1-0.2% velocity change over the range of pressures he subject his rock samples to in his measurements. The amount of sample shortening, ΔL , under a certain change in pressure, ΔP , can be estimated from the sample's Young's modulus, E , and the sample length measured at room conditions, L , by

$$\frac{\Delta L}{L} = \frac{\Delta P}{E} . \quad (4.3)$$

Using equation 4.3, a sample shortening of 1.3×10^{-4} m was estimated for the least stiff sample under a pressure of 50 MPa for our study. Furthermore, during calibration measurements the temperature dependency of the buffer delay time was not considered. All materials will experience thermal expansion when heated, with our aluminum buffer caps expanding more readily than our porous medium samples which are consisted of either alumina or quartz grains. For measurements conducted at 50°C, using the calibration measurements conducted at room temperature (~23°C) is therefore inaccurate. The linear expansion of a material can be calculated using:

$$\frac{\Delta L}{L} = \alpha \Delta T \quad (4.4)$$

where ΔL is expanded length, L is the original length of the sample, α is the linear expansion coefficient, and ΔT is the temperature change. The linear expansion coefficient for aluminum is $2.34 \times 10^{-5}/^\circ\text{C}$. A temperature change from 23°C to 50°C then translates to a 4.3×10^{-5} m lengthening of the aluminum buffer caps. If it is assumed that the elastic wave velocities through aluminum stays relatively constant over this 27°C temperature change, then the lengthening of the aluminum buffers at 50°C would increase the delay time by 7×10^{-9} s for P-waves and 1×10^{-8} s for S-waves, compared to the delay times measured at 23°C. The thermal expansivity of alumina and quartz is $4 \times 10^{-6}/^\circ\text{C}$ and $0.55 \times 10^{-6}/^\circ\text{C}$, respectively, therefore the lengthening of our samples in this study is considered negligible from the effects of heat.

After considering these different possibilities for error, the error in velocity can be calculated by the propagation of error using equation 4.2:

$$\frac{\delta V}{V} = \sqrt{\left(\frac{\delta L_s}{L_s}\right)^2 + \left(\frac{\delta t_s}{t_s}\right)^2} \quad (4.5)$$

where δ is the error of the particular parameter. The largest velocity error possible for a measurement involves the shortest sample length and the shortest travel time. The non-synthetic sample, Berea, has the shortest length of 43.45 mm and it has the shortest travel time under dry conditions and the highest confining pressure. The error for length is 2×10^{-5} m from parallelism and 1.3×10^{-4} m from

sample shortening, totalling an error in length of 1.5×10^{-4} m. The maximum error in picking arrival times for buffer calibration and sample measurements due to poor signal quality is 3×10^{-8} s for each, and the error in the arrival time for buffer calibration due to thermal expansion of the buffer caps is 7.0×10^{-9} s for P-waves and 1.0×10^{-8} s for S-waves. This totals an error in time of 6.7×10^{-8} s and 7×10^{-8} s for P-and S-waves, respectively. Using equations 4.5, the largest percentage error in P-wave velocity is 0.7% and in S-wave velocity is 0.5% for this study. These percentage errors were used in determining all P-and S-wave velocity uncertainties in chapter 6 and 7.

4.5.2 Attenuation and Error Analysis

In our study, measurements were conducted only for one length of each sample. In order to study waveform attenuation, a modified approach to the conventional log spectral ratio method was developed. The conventional log spectral ratio described in Chapter 3 is based on comparing two waveforms obtained from two different sample lengths and all other factors are held constant including the viscoelastic behaviour of the samples. Therefore the attenuation between waveforms is investigated through the absolute attenuation coefficient via differential sample lengths. However, absolute measurements of any kind are always problematic and here a ‘differential’ measure technique was developed. In our study, when using only one sample length but subjecting the sample to different conditions (saturation, pressure and temperature), various viscoelastic behaviours will arise and hence different waveforms will result. The varying factor is the viscoelasticity of the overall propagating medium while the sample length is held constant. By using equation 3.87 to describe the amplitude spectrum of a signal due to attenuation, the attenuation of two waveforms corresponding to traveling in two different viscoelastic media but of the same distance, x , can be related by their differential attenuation coefficient, [$\alpha_2(\omega)$ - $\alpha_1(\omega)$],

$$[\alpha_2(\omega) - \alpha_1(\omega)] = -\frac{\ln\left(\frac{A_2(\omega)}{A_1(\omega)}\right)}{x}. \quad (4.6)$$

Therefore the attenuation between waveforms in our study is investigated via differential attenuation coefficient, and not the absolute attenuation coefficient.

In using only one sample length and analyzing attenuation from determining the differential attenuation coefficient, multiple advantages arise over the conventional log spectral ratio method. First, the geometric diffraction loss does not need to be determined in equation 3.87 because the sample length is invariant between the two signals and geometric effects are therefore eliminated in equation 4.6. Second, carrying out the complete set of measurements listed in section 4.4 is quite time intensive, therefore running the full set of measurements just once, in our approach, will save at least half the time. Third, the integrity of the sample over the course of the measurements will be altered due to saturation and hysteresis effects, which will be discussed in chapter 7. In the conventional log spectral ratio method, the same viscoelastic behaviour may not be repeatable for the varying lengths and therefore can lead to inaccurate attenuation analysis. Fourth, the signal strength through a sample is also affected by how the sample is assembled in the experimental setup prior to measurements. Minor inconsistencies during set up such as slight S-wave misalignments and the connection in the soldered joints of the electrical wires will cause signal strength variations among the different sample lengths that is not caused by viscoelastic attenuation. Therefore by using only one sample length, these inconsistencies are not a concern. Finally, any systematic errors that are inherent to determining the absolute attenuation coefficient will be cancelled out when the difference is taken in differential attenuation coefficient.

To analyze the attenuation of waveforms, all of the waveforms acquired were first windowed and then the Fast Fourier Transform (FFT) was applied to get the amplitude spectra of the windowed signals. Figure 4.7 shows an example of two windowed P-wave time series signal recorded under dry conditions at room temperature and experiencing a confining pressure of 5 MPa and 40 MPa. The

amplitude spectra of the windowed signals from FFT are shown in figure 4.8a. Applying the natural logarithm to their spectral ratio and dividing by the length of the sample yields the differential attenuation coefficient as a function of frequency for the pair of signals (figure 4.8b). From the amplitude spectra of the signals, the peak frequency of the signals have shifted from the nominal 1 MHz resonant frequency of the piezoelectric ceramics and only a limited frequency band carries most of the energy (0.4-1.4 MHz). This shift in peak frequency is likely attributed to the construction of the transducers from the compilation and mounting of multiple pieces with the piezoelectric ceramics, therefore shifting the energy from higher frequencies. Outside of this high energy band of frequencies, the spectrum is weak and is considered unreliable due to noise contamination. Consequently, the differential attenuation coefficient outside of this range behaves erratically and this information should be disregarded, or if it must be analyzed it should proceed with great caution.

Since analyzing waveform attenuation was conducted from using only one sample length, statistical error analysis was not possible for our set of measurements. In addition, applying the propagation of errors for equation 4.6 was met with difficulty from the inability to accurately assess the error in determining the amplitude spectrum of a signal. Therefore the exact errors of the differential attenuation coefficients could not be estimated. However, as mentioned in chapter 3, the errors in attenuation measurements are usually quite large so interpreting just the differential attenuation coefficient values without any guidance on the possible amount of error is inadequate. Since the experimental method and setup applied in the acrylic attenuation measurements introduced in chapter 3 is the same as the measurements described in this chapter, the errors estimated statistically for the acrylic measurements would be an appropriate estimate for our differential attenuation coefficients errors. The attenuation of waveforms in the acrylic measurements was analyzed using the conventional log spectral ratio method and the errors found were for the absolute attenuation coefficients. The maximum errors found of the attenuation coefficient were 12 m^{-1} for P-waves and 18 m^{-1} for S-waves. For the errors in the differential

attenuation coefficients, they can be taken directly from the errors determined for the absolute attenuation coefficient and do not need to be propagated for the subtraction in its definition. This is because the computations for these two different quantities are actually exactly the same. To recap, the absolute attenuation coefficient is determined from two different sample lengths of the same viscoelastic medium by

$$\alpha(\omega) = -\frac{\ln\left(\frac{A(\omega, x_2)}{A(\omega, x_1)}\right)}{\Delta x},$$

which has the same format to equation 4.6 for the differential attenuation coefficient. Furthermore from the reasons stated earlier, the error associated with absolute attenuation coefficient is greater than the errors in differential attenuation coefficient. Therefore these approximated errors should be more than suffice to account for the actual error in determining the differential attenuation coefficient.

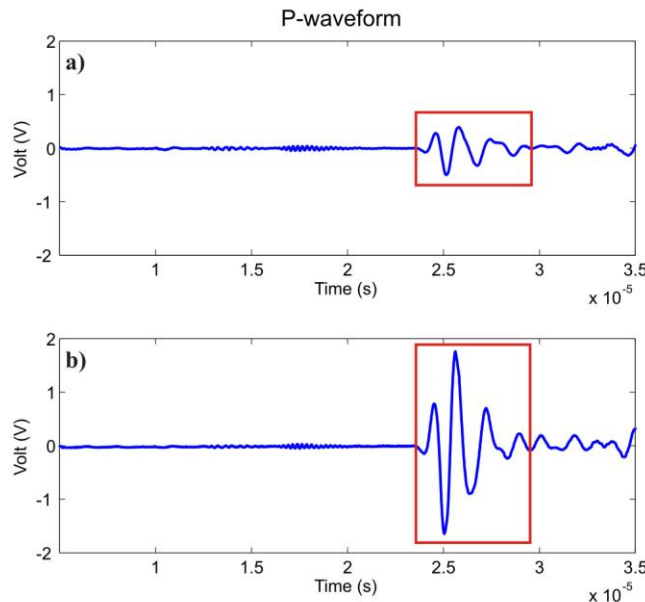


Figure 4.7: The P-wave time series signals of the porous ceramic rod at dry conditions under two confining pressures: a) at 5 MPa b) at 40 MPa. The red box is shows the windowed signal used for the FFT.

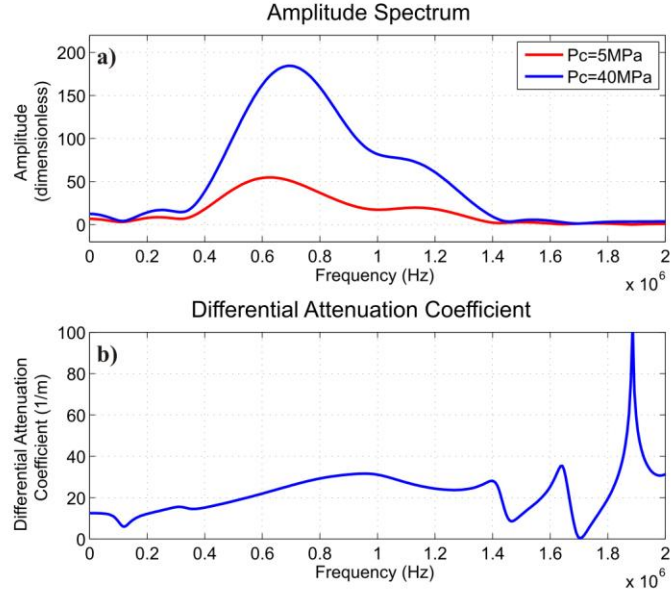


Figure 4.8: (a) The amplitude spectra of the windowed-part of the two signals shown in figure 4.7. (b) The resulting differential attenuation coefficient.

4.6 Chapter Summary

This chapter gave a detailed description of the experimental setup, the procedures that were used to obtain waveforms and the methods that were applied to analyze the data for the results reported in chapter 6. Ultrasonic pulse transmission is the technique applied to acquire P-and S-waveforms for velocity and attenuation analysis. This chapter provided the details behind building a set of transducers for ultrasonic pulse transmission, the procedure used to prepare and assemble the samples prior to measurement, a description of the experimental apparatus, and a description of the different measurements conducted. Under a variety of pressure and temperature conditions, measurements were carried out on all samples for three saturation conditions: dry, CO_2 saturated, and water saturated. Examples of the waveforms acquired during the measurements were introduced, and the methods for analyzing them for signal velocity and the attenuation were discussed. Signal velocity was determined from picking the time of the first extremum and applying a delay time correction. The error in the signal velocity was calculated from the propagation of errors and a maximum error of 0.7% and 0.5% were estimated for P-waves and S-waves, respectively. In order

to study waveform attenuation, a modified approach to the conventional log spectral ratio method was applied, where the differential attenuation coefficient between waveforms is analyzed instead of the absolute attenuation coefficient. Analyzing waveform attenuation with this new approach provides many advantages over the conventional log spectral ratio method, from reducing laboratory time to minimizing measurement errors. The errors in differential attenuation coefficients were not determined directly but were adopted from the statistically estimated errors in the acrylic attenuation measurements from chapter 3. The adopted errors for the P- and S-wave differential attenuation coefficient are 12 m^{-1} and 18 m^{-1} , respectively.

Chapter 5

Sample Characterization

In this chapter the porous media used in this thesis will be introduced and characterized, mainly through petrophysical parameters. The petrophysical parameters measured are density (grain and bulk), porosity, pore throat size, air permeability, and tortuosity. Furthermore, images of the micro-structure of the samples were examined. All sample characterizations were conducted at the University of Alberta and their characterization methodologies will be reviewed. The samples were dried under vacuum in an oven at 70°C for more than 48 hours before the various characterizations were performed. The main petrophysical properties determined will be reported in table 5.2 at the end of the chapter.

5.1 Samples

In this thesis laboratory measurements were focused on two samples, a synthetic sample and a natural rock. The synthetic sample is a porous ceramic rod purchased from Hoskin Scientific Ltd. and was manufactured by Soilmoisture Equipment Corporation. The porous ceramic rod is developed from a high fired, alumina (aluminum oxide- Al_2O_3) body. It is consisted of open pore structure thereby permitting fluid to move from one end of the sample to the other through interconnected network of channels. The porous ceramic rod is white coloured, appears to be very homogeneous, and composed of very fine grains. The pores or the grains are not readily visible to the naked eye.

The natural sample is a porous sandstone from the Berea formation in Ohio. This sample was obtained by material provided for a round-robin physical testing campaign associated with the San Andrea's Fault Observatory at Depth

(SAFOD) project. The Berea sandstone is predominantly composed of quartz with minor traces of clay minerals for holding the quartz grains together. The porosity and permeability of Berea sandstone is known to be relatively high, and consequently it has been extensively used in petrophysical testing (Wyllie et al, 1958; Timur, 1968; Mobarek, 1971; De Vilbiss, 1980; Johnston and Toksoz, 1980; Nur and Murphy, 1981; Winkler and Nur, 1982; Winkler, 1985; Jones and Nur, 1983, Shankland and Johnson, 1993; Hart and Wang, 1995; Zhan et al, 2010). The Berea sandstone appears as a light grey, homogeneous coloring with no layering or noticeable features in macro-view, and is composed mainly of sand-sized grains. Photographs of the two samples are shown in figure 5.1.

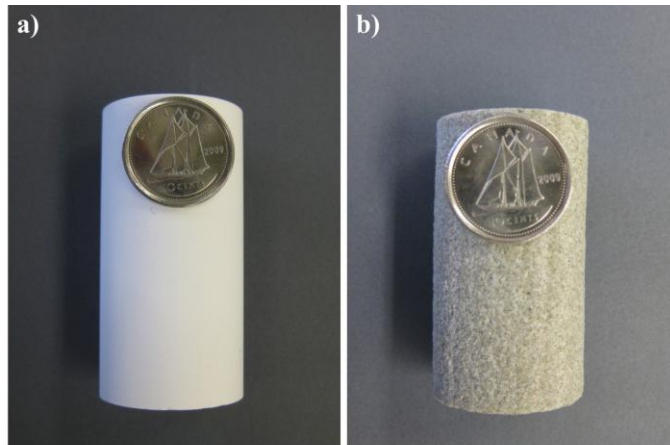


Figure 5.1: Photographs of a) Porous ceramic rod and b) Berea sandstone.

5.2 Density and Porosity

The grain volume, grain density, bulk density, porosity, and pore size of the samples will be examined in this section. From helium porosimetry the grain volume of the samples is determined, and consequently the grain density and the porosity can be inferred. Bulk density is simply determined from the weighed mass of the dry sample and measured dimensions of the sample. Mercury porosimetry will also be discussed and it is used to describe the pore size distribution.

5.2.1 Grain Volume and Density

Helium porosimetry is used to determine the grain volume of the samples. The grain volume is the volume of the solid constituents of the porous sample (i.e. rock matrix). The governing principal behind determining grain volume from helium porosimetry is Boyles's gas law. This ideal gas law states that under conditions of fixed gas quantity and constant temperature, the product of the pressure and volume stays constant and is expressed as

$$P_1V_1 = P_2V_2 \quad (5.1)$$

where P_1 and V_1 are the original gas pressure and volume, respectively, and P_2 and V_2 are the new gas pressure and volume, respectively.

A helium pycnometer, Quantachrome Instruments MVP- D160-E, was used to perform the porosimetry measurements. The machine essentially consists of a sample cell compartment and a reference cell compartment, which are connected by a valve. To commence the measurement, a sample is placed in the sample cell compartment and the entire pycnometer system is vacuumed, flushed through with helium gas, and vented to the atmosphere. Then the reference compartment is closed off from the sample compartment and only the reference cell is filled with helium. The resulting pressure from this compartment is logged (P_1). Next, the valve to the sample cell from the reference cell is switched open, allowing the helium that was originally in the reference cell to expand to the new available volume and the resulting new pressure is then logged (P_2). A helium gas of 99.995% purity was used for these porosimetry measurements.

Based on the above Boyle's gas law, a more descriptive equation of the different volumes involved in our measurement can be written and equation 5.1 becomes,

$$P_1V_R = P_2(V_R + V_s - V_g) \quad (5.2)$$

V_R is the volume of the reference cell, V_s is the volume of the sample cell, and V_g is the grain volume. The volumes of the reference and sample cells are

predetermined; the sample cell compartment used in our measurement has a volume of 147.903 cm^3 , while the reference cell compartment has a volume of 88.52 cm^3 . From this known information and with the original and new pressures recorded, the grain volumes of our samples were calculated from equation 5.2. From the determined grain volume and knowing the mass of the dry sample, m , the grain density can be consequently calculated,

$$\rho_g = \frac{m}{V_g} . \quad (5.3)$$

The dry mass of a sample was found from weighing the sample prior to helium porosimetry measurements and is reported in table 5.2.

5.2.2 Bulk Density and Porosity

The bulk density of a sample can be determined relatively easily and does not require the use of the helium pycnometer. The bulk density of the sample is simply the ratio of the sample's dry mass to the sample's envelope volume, V_e ,

$$\rho_b = \frac{m}{V_e} . \quad (5.4)$$

The envelope volume of the sample is found from measuring the length and diameter of the sample using a Vernier caliper and is reported in table 5.1. However, this seemingly simple measurement is often not that accurate due to even relatively small variations in sample shape.

To determine the porosity of a sample, the information on grain volume found from helium porosimetry is used. Porosity is usually the most important characteristic used to describe a porous medium. The porosity of a sample is defined as the ratio of the total void volume of a porous medium to the envelope volume of the sample, or the ratio left over if the ratio of the grain volume to envelope volume is subtracted from unity,

$$\phi = 1 - \frac{V_g}{V_e} . \quad (5.5)$$

Sample	Diameter (cm)	Length (cm)	Envelope Volume (cm ³)
Porous Ceramic Rod	2.54	5.061	25.64
Berea Sandstone	2.54	4.345	22.02

Table 5.1: The measured envelope volume of the samples.

5.2.3 Pore Size Distribution

To determine the distribution of pore size in our samples, mercury injection porosimetry is used. This method operates by injecting liquid mercury into the pore space of the porous medium. Liquid mercury is a non-wetting fluid, with a contact angle, θ , of about 140° . Unlike wetting fluids, without external pressure liquid mercury would not enter the pore space of a porous medium. The smaller the pore size, the larger the pressure is required to force the liquid mercury in. Therefore by monitoring the amount of mercury that is injected into the sample as the applied pressure increases, the pore sizes of the sample can be inferred. The relationship relating pressure and pore size from the penetration of mercury is given by the Washburn equation,

$$D_{pore} = -\frac{4\gamma \cos \theta}{P} \quad (5.6)$$

where D_{pore} is the pore throat diameter, P is the exerted pressure, γ is the surface tension of mercury which is 0.485 Nm^{-1} at 25°C , and θ is the contact angle of mercury. The maximum applied pressure on the mercury in our measurements is 413 MPa, therefore the smallest pore that can be investigated is about 3.5 nm. It should be noted that mercury porosimetry measurements measures the largest entrance into a pore, and not the actual inner size of a pore. So the determination of the pore size distribution is more accurately the pore *throat* size distribution, if the access to the larger pore is through a smaller pore. Also, closed pores cannot be analyzed by this method because mercury has no way of entering the pore space.

To conduct these measurements, the mercury porosimeter, Autopore IV 9500 from Micromeritics, was used. A small piece of sample is placed into the

sample cell of the penetrometer which has a long hollow stem connected to the sample cell. The long hollow stem is coated with a metal sheet. Initially, the penetrometer with the sample is placed into the low pressure cycle part of the porosimeter. The penetrometer is evacuated to remove air and then it is filled with mercury under low pressure. In this low pressure cycle, mercury will penetrate the largest pores and fill the spaces between the pieces of the sample, if more than one piece is used. At the completion of the low pressure cycle, the penetrometer is removed and placed into the high pressure cycle part of the porosimeter where the actual intrusion measurements begin. In this cycle as the exerted pressure increases, the total amount of pore space intruded with mercury also increases while the size of the pore spaces being progressively invaded decreases. The amount of mercury used up from intrusion into the pore space of the sample is monitored throughout pressurization by the capacitances changes between the mercury in the stem and the metal coating on the stem of the penetrometer. Therefore the cumulative volume of mercury injected into the sample is recorded as a function of pressure. Incremental intrusion as a function of pressure can also be determined from the recorded cumulative volume data by taking the derivative,

$$\partial V_{Hg} = \frac{dV_{Hg}}{dP} \Delta P . \quad (5.7)$$

It basically represents the change in volume of mercury that has intruded into the pore space from the last pressure to the new pressure. This quantity reveals the relative distribution of the samples' porosity among the pore sizes, and at which pressure the contribution of mercury is the greatest. Consequently, a peak in the incremental intrusion curve would coincide with the steepest increase in the cumulative intrusion curve. Figure 5.2a and 5.3a shows the cumulative and incremental intrusion with pressure for the porous ceramic rod and Berea sandstone respectively. Converting pressure to pore size via Washburn's equation, Figure 5.2b and 5.3b shows the incremental intrusion with pore size, instead. Any large peaks in incremental intrusion indicate a dominant pore size. For both samples, the incremental curve exhibits a modal behaviour indicating

that majority of the pores is of one size. The modal pore size of porous ceramic rod is 2 μm while for the Berea is 11 μm . Contrasting the morphology of the two

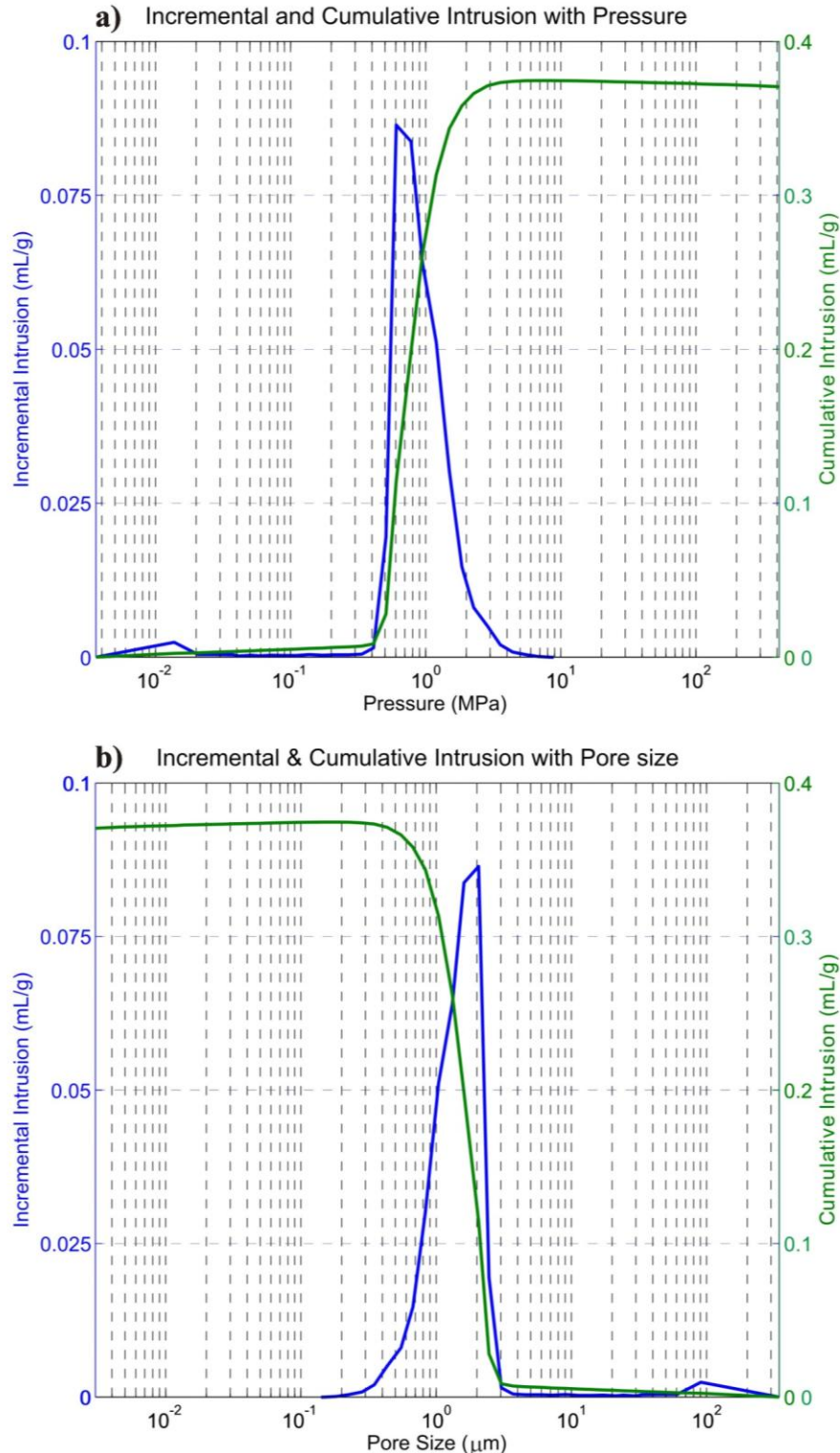


Figure 5.2 Cumulative and incremental intrusion curves for the porous ceramic rod **a)** with pressure **b)** with pore size

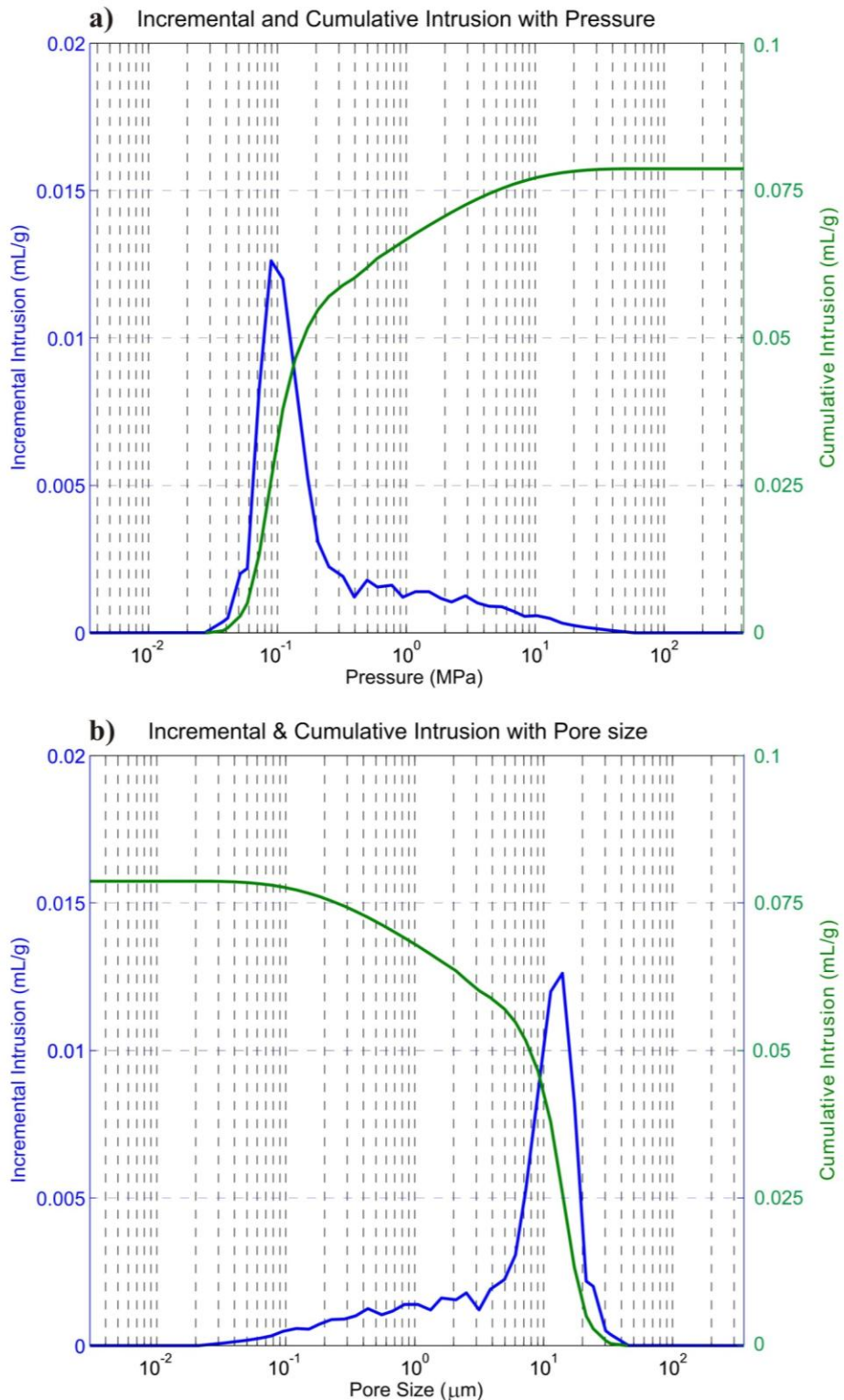


Figure 5.3 Cumulative and incremental intrusion curves for the Berea sandstone a) with pressure b) with pore size

incremental intrusion curves, the porous ceramic rod exhibits a smoother and cleaner curve compared to the Berea sandstone, especially at pores smaller than the dominant pore size. This signifies that the Berea sandstone pore size distribution has more variability than the porous ceramic rod. In particular, the Berea's pore size distribution extends to quite small dimensions; and this is likely indicative of the small aspect ratio (i.e. microcrack) porosity that leads to highly nonlinear elastic behaviour.

5.3 Permeability

Another important characteristic used often to assess the nature of a porous medium is permeability. This petrophysical property describes how easily fluid can flow through the voids of the medium, where open and interconnected pores make a medium more permeable. Permeability, k , is physically defined by relating the fluid volume flow per second and per area (Darcy velocity), q , of fluid flow to pressure gradient, dP/dx , experienced by the fluid and the viscosity of the fluid, η ,

$$q = -\frac{k}{\eta} \frac{dP}{dx}. \quad (5.8)$$

To measure the permeability of our samples a portable air permeameter, Tiny Perm II made by New England Research Inc. and courtesy of Professor David Potter at the University of Alberta, was used. This measuring system is consisted of a plunger connected to a vacuum cylinder with an attached pressure transducer, and this transducer is connected to a microprocessor and control unit by an electrical cable. Figure 5.4 shows a photograph of the Tiny Perm II used. Prior to measurement with the plunger withdrawn and no vacuum is indicated on the control unit, the rubber nozzle on the tip of the vacuum cylinder is pressed up against the sample. The measurement begins by depressing the plunger and the control unit shows a reading on the current vacuum in the cylinder and the measurement status. When the plunger is completely depressed and the reading indicates that there is no vacuum, a response function result will appear. The manufacturer indicates that the micro-processor unit computes the response

function from monitoring the syringe volume and transient vacuum pulse created as the plunger is depressed. The permeability of the sample in millidarcies is related to the response function, T , by the following calibration relationship,

$$T = -0.8206 \times \log_{10}(k) + 12.8737. \quad (5.9)$$



Figure 5.4: Tiny Perm II, the portable air permeameter system used in measuring the air permeability of our samples. The two arrows are pointing out the connection between the pressure transducer in the black box to the yellow microprocessor and control unit.

Photograph from NER Tiny Perm II user's manual.

Several readings were taken for each sample, and the average permeability value was taken and is shown in table 5.2. The permeability values fluctuated within 5% of the average permeability value for both samples.

Strictly speaking the permeability value determined this way of a sample is its air permeability, and it is generally known to be higher than its liquid permeability (Klinkenberg, 1941; Kilmer et al, 1987; Springer, 1998; Wu, 1998), especially in low-permeable rocks. This difference in value of gas permeability to liquid permeability for the same medium is caused by gas slippage at the walls of the pores, known as the Klinkenberg effect. Liquid flow and gas flow at high pressure is laminar, following Darcy's Law, with a zero flow velocity at the pore

walls. Gas flow at low pressures on the other hand moves in a non-Darcy fashion where the flow at the pore walls is not zero. Klinkenberg (1941) developed an equation to correct for this slippage effect so that gas permeability can be converted to its equivalent liquid permeability if the gas pressures are known during the permeability measurements. No correction for the Klinkenberg effect was carried out on our air permeability values because the permeameter unit used in our study, strangely, does not provide this required information. However, in the manual of the equipment, the permeability values determined from the calibration curves are referred to as absolute permeability. The term ‘absolute’ permeability is a bit ambiguous as it can be referred to the permeability measured when there is only one type of fluid present in the pore space, or it can be synonymous to liquid permeability. Nonetheless, if the Klinkenberg effect correction is not applied by the air permeameter, this effect on our samples would only cause a slight difference between the two permeability values. As mentioned earlier this effect is only significant for a low-permeable sample and as a result, a large majority of its correction in scientific studies are performed on tight samples (<0.0001 mD). Klinkenberg (1941) states for samples of moderately high permeability, the discrepancies gas and liquid permeability are not of first importance for practical purposes. He showed the differences in permeabilities are about ~10% for samples with liquid permeabilities greater than 100 mD.

5.4 Tortuosity

Tortuosity in a porous medium is a measure that describes how twisted, crooked, and convoluted the shortest passage is between two points taken through only the voids in the medium. It is defined as the ratio of distances of the actual path taken, L_C , through the network of channels to that of the straight path, L_0 , between the same starting and ending points,

$$\tau = \frac{L_C}{L_0} \geq 1. \quad (5.10)$$

This parameter of a porous medium impacts how easily a fluid can move within the void space; the less tortuous the path, the less resistant in the movement of the

fluid. The tortuosity of a sample in our study was measured using an electrical method with an experimental set up similar to that described by Garrouch et al (2001). Essentially, by comparing the resistance of a sample saturated with a saline solution to the resistance of only the saline solution over the same distance and knowing what the porosity of our sample is, the tortuosity of the sample can be inferred. This method can only be applied if the matrix of the sample is electrically non-conductive. The principal behind this method comes from the relationship between electrical resistance, R , and resistivity, ρ :

$$R = \frac{\rho l}{A} \quad (5.11)$$

where l is the distance of the path traveled by a current in a conductive medium, and A is the surface area of the conductive medium subjected to an applied current.

For the measurements, the sample was vacuumed and then saturated with a saline solution of 15,000 ppm. The four electrode technique was adopted to avoid contact resistance from developing between the sample and the electrodes. The four electrodes consist of two current electrodes and two voltage probes. The sample is placed between the two current electrodes that covers the parallel end surfaces exactly and the two needle voltage probes are placed on the surface of the sample. A 60 Hz AC source was connected to the current electrodes and an ammeter was used to determine the current following through this circuit. From measuring the voltage drop across the two probes and knowing the current in the circuit, the resistance of the saturated sample, R_{sample} , is determined by Ohm's law. The same electrical measurement was repeated with only saline solution and the resulting resistance, R_{saline} , was found. Figure 5.5 depicts the electric circuit and electrical current path taken in each measurement. Care was taken to ensure the distances between the four electrodes were the same for both measurements. From these measured resistances and using equation 5.11 to describe each measurement scenario, the tortuosity of a sample is simply

$$\tau = \frac{R_{sample}}{R_{saline}} \phi. \quad (5.12)$$

Due to the need of this parameter for the analysis of the porous ceramic rod's ultrasonic pulse transmission measurement results, tortuosity was only measured of the porous ceramic rod.

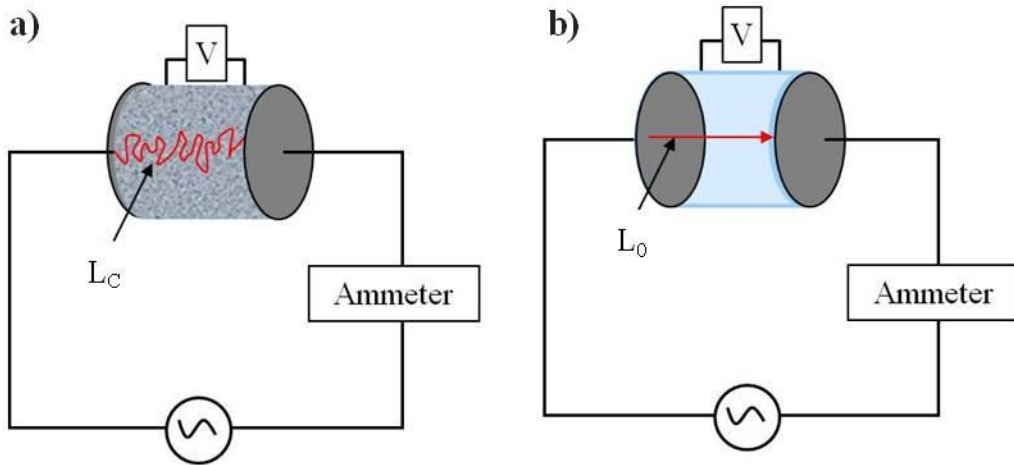


Figure 5.5: Schematic diagram of the four electrode circuit. The red line denotes the path taken by the electrical current. a) Electrical measurement with the sample saturated with saline solution, b) electrical measurement with only saline solution.

5.5 Scanning Electron Microscope Imaging (SEM)

A scanning electron microscope (SEM) was used to obtain images of our samples to examine their grain structures and micro-features qualitatively. SEM is a microscope that can produce highly magnified and resolved microscopic images of the surface of an object through scanning the object with a beam of electrons. The Zeiss EVO MA 15 SEM used in imaging our samples had a magnification up to 100 000 X. During an SEM imaging, a beam of electrons is emitted from an electron gun fitted with a filament and is accelerated by attractive forces towards an anode. This electron beam is focused on a small area of the sample by a magnetic field. When this beam interacts with the surface of the sample, secondary electrons are created from ionization and scatters. These secondary electrons are recognized and accounted by a detector, and an image is produced from the number of electrons scattered from each spot on the sample's surface. The electron beam is moved across the sample by a set of scanning coils. Prior to imaging, the sample specimen is prepared by coating the surface with gold powder. This gold powder is to provide conductivity to the surface of the

sample to prevent electrons from being trapped, thereby creating an overly bright image. SEM imaging was carried out at the Earth and Atmospheric Science department at the University of Alberta.

Figure 5.6 and figure 5.7 are the SEM images for the porous ceramic rod and Berea sandstone, respectively, for two different magnifications. The 5 kX magnification image of the porous ceramic rod shows that the overall sample is fairly uniform. At a magnification of 20 kX, the image reveals the aluminum oxide grains and some secondary material attached to them. This secondary material is believed to be a binder material used in the making of the sample during firing. For the Berea sandstone SEM image at 500 X magnification, the image shows a generally uniform rock sample. The large grains are quartz and they are surrounded by another mineral. At 3.5 kX magnification, the surface of the quartz grains reveals evidence of dissolution and sheet-like minerals. These sheet-like minerals have been identified as kaolinite, a type of clay.

From these SEM images of the two samples, the grains and pore throats of the porous ceramic rod are evidently smaller than that of the Berea sandstone. Also despite the irregular shape of the alumina grains, the pores of the porous ceramic rod appear more open, in contrast to the large amounts of crack-like pores of the Berea sandstone. These images are in qualitative agreement with the mercury porosimetry curves of Figs. 5.3 above.

Sample	Porous ceramic Rod	Berea Sandstone
Mass (g)	39.6	43.24
Bulk Volume (cm ³)	25.33	22.02
Bulk Density (g/cm ³)	1.55	2.15
Grain Volume (cm ³)	10.63	17.79
Grain Density (g/cm ³)	3.70	2.64
Porosity (%)	58.4	19.0
Modal Pore Size (μm)	2.06	11.33
Air Permeability (mD)	96.94	237.65
Tortuosity (dimensionless)	1.73	3.9 ^a

Table 5.2: Petrophysical properties characterized of the samples. ^a tortuosity value taken from Garrouch et al (2001)

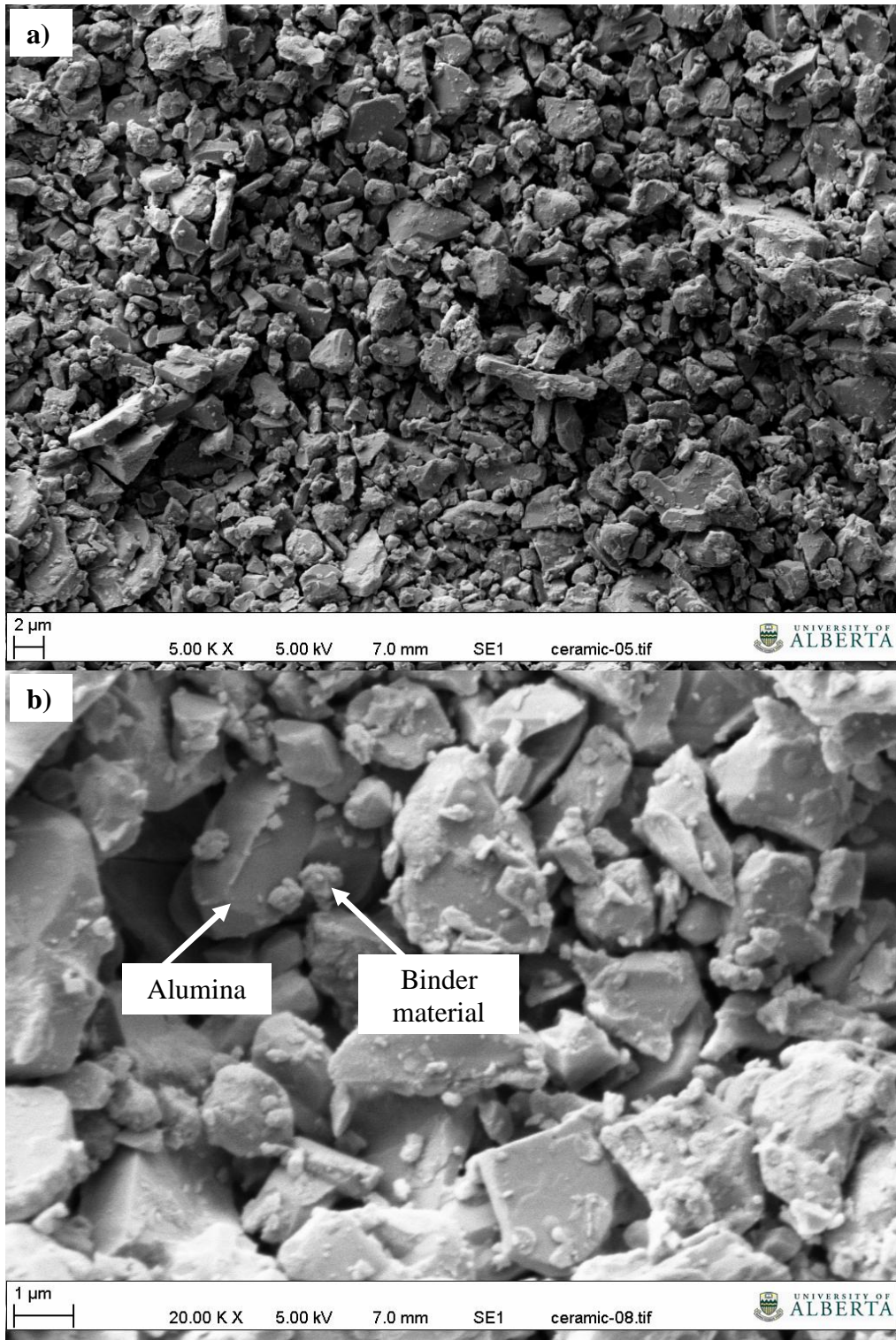


Figure 5.6: SEM images of the porous ceramic rod at two magnifications a) 5 kX b) 20 kX.

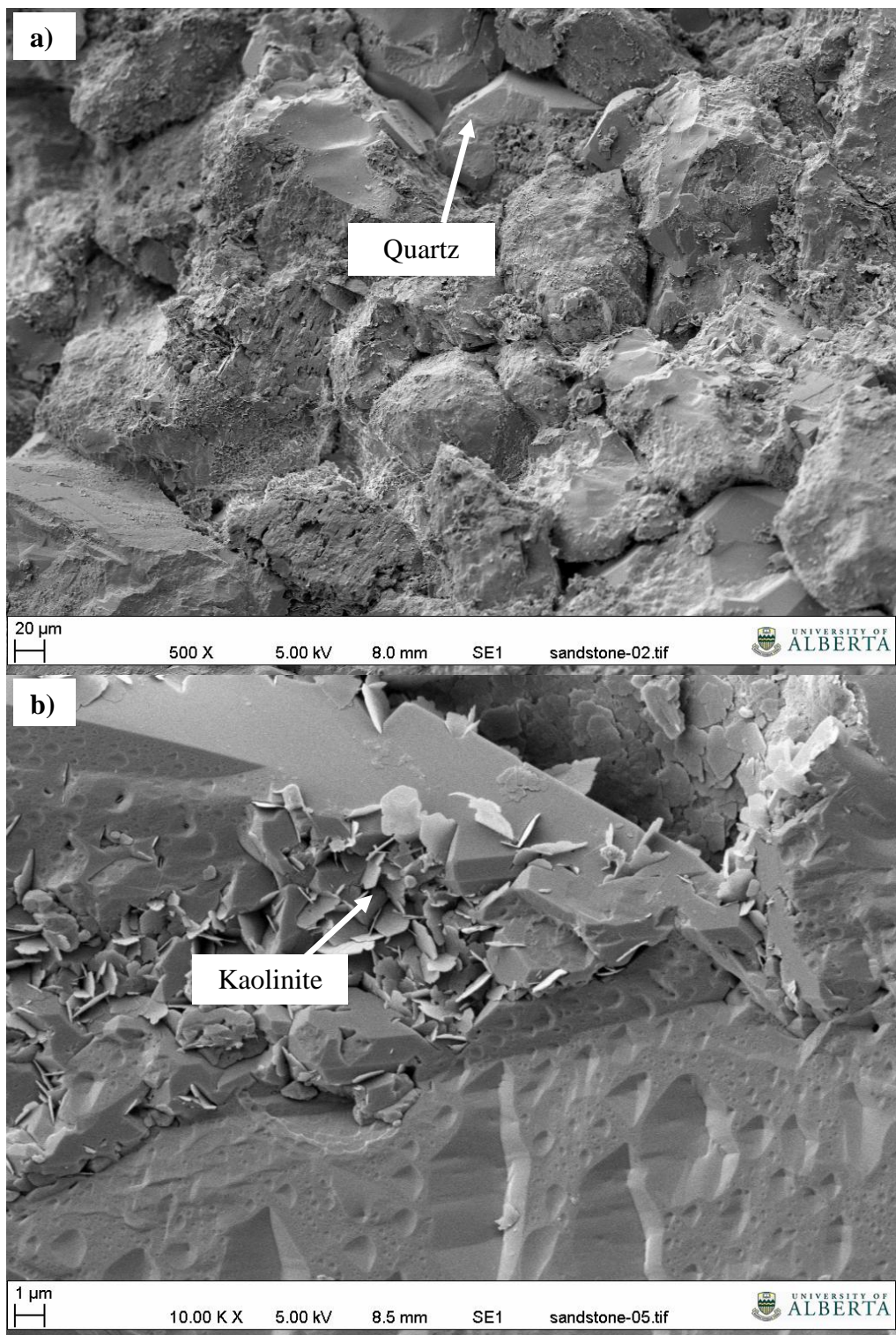


Figure 5.7: SEM images of the Berea sandstone at two magnifications a) 500 X b) 10 kX.

5.6 Summary

The synthetic sample, porous ceramic rod, and the non-synthetic sample, Berea sandstone, used in this thesis were petrophysically characterized using a variety of methods. Helium porosimetry was used to determine the bulk grain volume, grain density and porosity of the two samples. Both samples have high porosity with the porous ceramic rod being extremely porous. Mercury porosimetry was used to reveal the pore size distribution in the samples and both samples exhibits a modal pore distribution with a dominant pore diameter on the order of microns for both samples. From the variability of the mercury intrusion curves, the pore structure of the porous ceramic rod displays more uniformity than the Berea sandstone. Air permeability of the samples was determined using a portable air permeameter. Just like the dominant pore size, the permeability of the Berea sandstone is higher than the porous ceramic rod. The tortuosity was only measured of the porous ceramic rod and was done by using an electrical method. Finally, SEM images were examined for both samples at various magnifications. The Berea sandstone showed a lot of compliant pores where as the porous ceramic rod displayed only non-compliant pores.

Chapter 6

Results and Discussion: Sintered Alumina

In this chapter the laboratory results, the modeling results, and a discussion on the wave behaviours of the porous ceramic rod with the petrophysical characteristics described in table 5.2 and that was subjected to the pressure, temperature, saturation conditions outlined in table 4.1 are given. The P-and S- waveforms and their determined wave velocities will be provided for all three saturation states of dry, CO₂ saturated, and water saturated. Their comparison to modelled velocities will be conducted for only the CO₂ saturated and water saturated states. The laboratory results and the modelled predictions of the differential attenuation coefficient will be given for only the CO₂ saturated measurements.

All waveforms in this study were acquired using the ultrasonic pulse transmission method introduced in chapter 3. The methods in determining the wave velocity, the wave attenuation, and their associated errors from the acquired waveforms were discussed in chapter 4. Gassmann's and Biot's fluid substitution models, for predicting wave velocities of saturated porous medium, were introduced in chapter 3.

6.1 Dry

P-and S-waveforms were obtained of the porous ceramic rod under dry (i.e. vacuum in the pore space) conditions at room temperature (T = 23°C) while

confining pressure varied between 5 to 40 MPa, undergoing through both pressurization and depressurization cycles.

6.1.1 Dry Waveforms

The full set of normalized P-and S-waveforms are shown in figure 6.1. The signals are normalized with respect to the largest amplitude within the given set of waveforms. In the figure, the waveforms are displayed conventionally by wiggle traces and also alternatively by coloured amplitudes to highlight patterns and subtle features. All waveform plots hereafter will be only be displayed as normalized coloured amplitudes. In the waveform plot, the arrival for both the P-

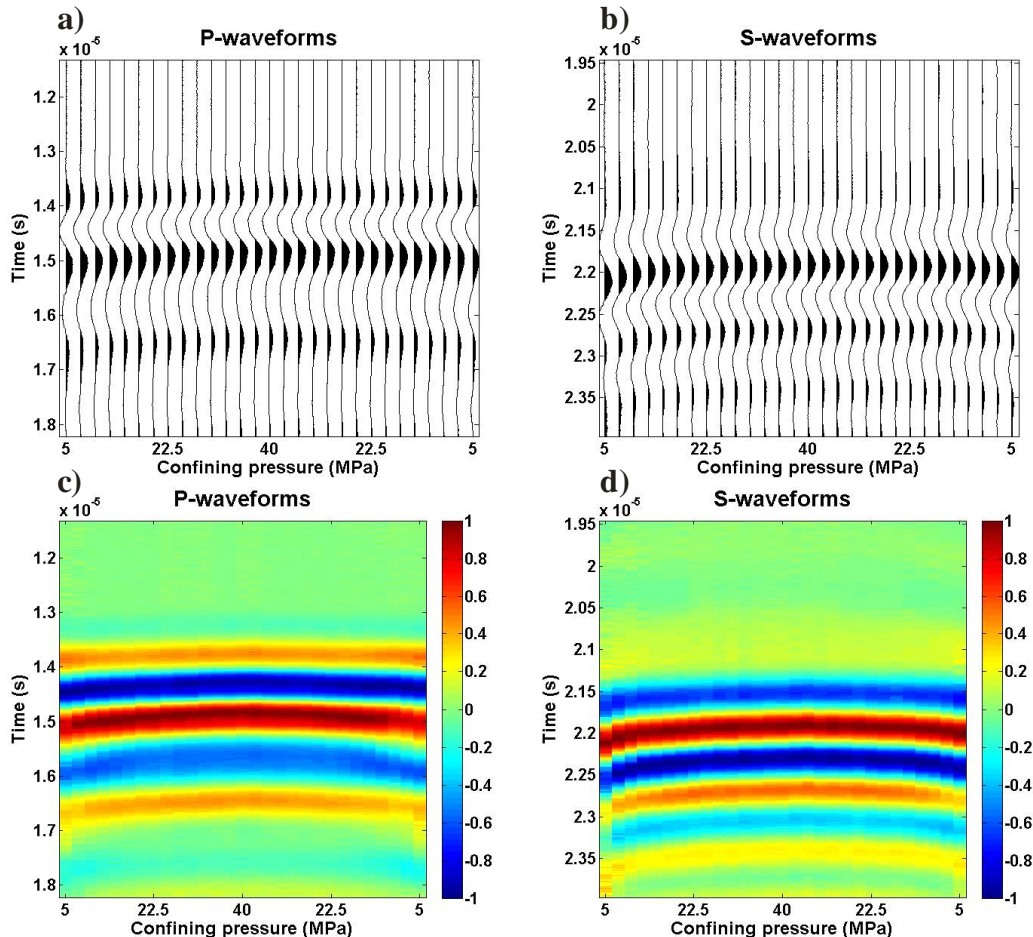


Figure 6.1: Normalized waveforms obtained under dry conditions at room temperature plotted as a function of confining pressure for the porous ceramic rod. a) and b) shows the P-and S-waves as wiggle traces. c) and d) shows the P-and S-waves as coloured amplitudes.

and S- waveforms for the dry porous ceramic rod do not vary much over this pressure interval. However, minor signal strength changes can be seen.

6.1.2 Dry Wave Velocities

The P-and S-wave velocities with their uncertainties estimated from the waveforms (method discussed in section 4.5.1) shown in figure 6.1 are plotted in figure 6.2. As applied confining pressure increases on the sample, the wave velocities increase. However over the entire 40 MPa pressure range investigated, the amount of change in wave velocities is quite insignificant, less than 1% for both P-and S-waves. Furthermore, at a given confining pressure the wave velocities during pressurization cycle (upward-pointing triangle) are always lower than the wave velocities during the depressurization cycle (downward-pointing triangle). This behavioural hysteresis can be attributed to the closing of compliant pores during pressurization that are not reopened at the same pressure during depressurization due to frictional forces. However, the differences between the wave velocities of the pressurization and depressurization cycles are minor where the velocities are well within error.

Overall the velocity changes and hysteresis observed here with pressure are insignificant and can be considered as negligible, in comparison to that of real rocks (Gardner et al, 1965). The vanishingly small changes observed are due to the lack of low-aspect ratio pores, or alternatively micro-cracks, in the sample. Low-aspect ratio pores are compliant meaning they are inclined to collapse under pressure. As pores close up in a porous sample, the overall sample will become stiffer. If the presence of micro-cracks is large, this will translate to large increases in wave velocity with pressure due to the increased sample stiffness (as will be seen with the Berea sandstone in chapter 7). Therefore from the wave velocity behaviour observed with pressure, the porous ceramic rod studied here contains mainly of high-aspect ratio, non-compliant pores. This inference is in agreement with the non-cracked nature of the sample that was first suggested from reviewing SEM images in chapter 5 and from the mercury injection porosimetry.

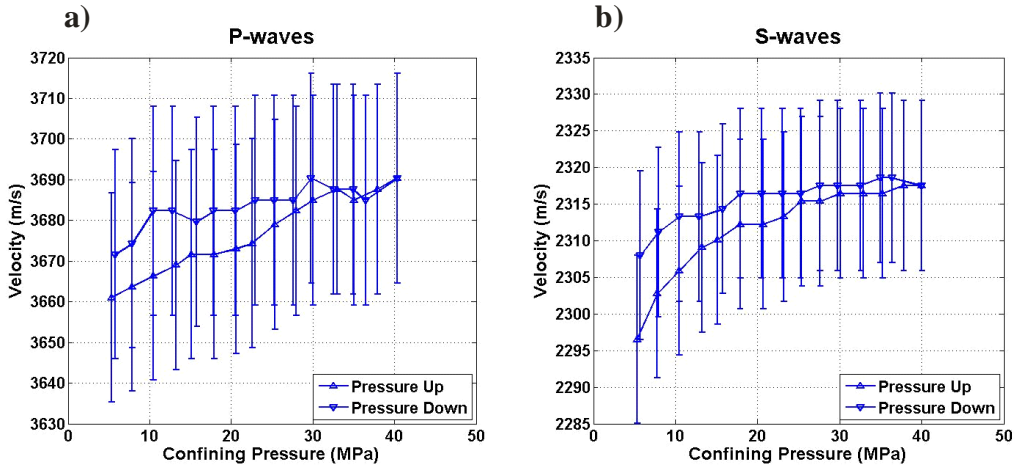


Figure 6.2: Dry P-wave (a) and S-wave (b) velocities with their respective errors as a function of confining pressure for the porous ceramic rod.

6.2 CO₂

The measurements made under a CO₂ saturated state can essentially be classified as either a constant temperature or a constant pressure run. To recapture the measurement conditions applied, figure 6.3 displays the different temperatures and pore pressures that were explored, superimposed on the bulk modulus and density phase diagram of CO₂. In the figure the vertical arrows are of constant temperature measurement runs, and the horizontal arrows are of the constant pressure (confining and pore pressure) measurement runs. Each measurement run conducted is expected to cross a phase boundary. During all CO₂ saturated measurements, a constant differential pressure of 15 MPa was maintained. Because a constant differential pressure is maintained, any waveform variations observed should solely caused by pore fluid effects. For all the constant temperature runs, the pore pressure varied from 2 MPa to 25 MPa. CO₂ is a gas at low pore pressures and is a liquid or a supercritical fluid at higher pore pressures depending on the temperature. For all the constant pressure (pore, confining, or differential) runs, the measurements began at a temperature of 23°C where CO₂ is a liquid state. As temperature increased CO₂ eventually transforms into a gaseous or a supercritical fluid state, depending on the pore pressure shown in figure 6.3.

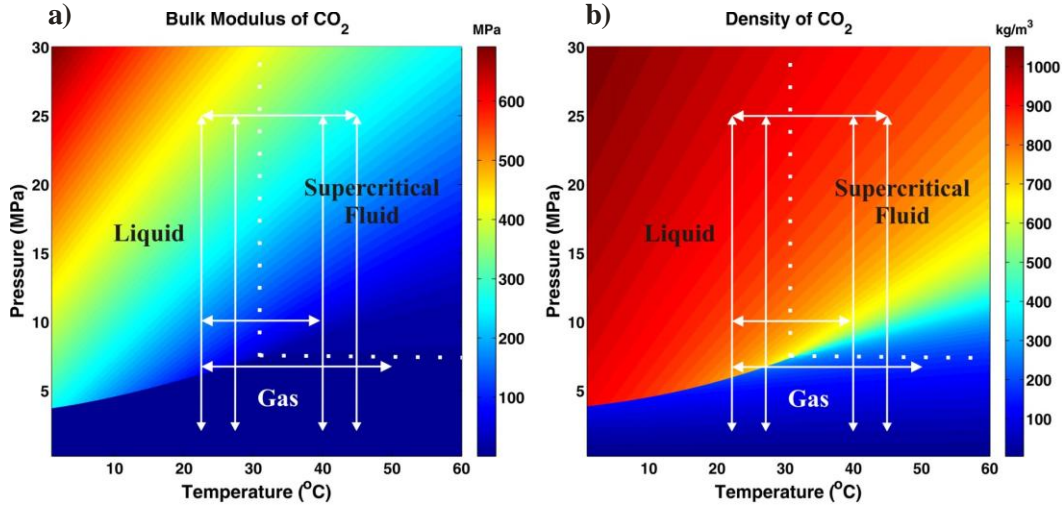


Figure 6.3: Phase diagrams of CO₂'s: (a) bulk modulus (b) and density. The temperature and pressure conditions applied to the CO₂ saturated porous ceramic rod during ultrasonic pulse transmission measurements are shown by the white arrows.

6.2.1 CO₂ Saturated Waveforms

Figure 6.4 shows the P-and S- waveforms as a function of pore pressure for the constant temperature measurements at T = 28°C and at T = 40°C. The major trends and features in waveform variations and wave attenuation with pore pressure for the T = 23°C and T = 28°C runs are quite similar, as are the T = 45°C and T = 40°C runs; therefore not all are shown to avoid redundancy. However, the laboratory results of the T = 23°C and T = 45°C measurements are available in the appendix. In all the P-and S-wave waveform plots, within a given CO₂ phase state the observed variations of the waveform such as amplitude and arrival time are minor. Between CO₂ phase states the observed differences in waveforms are significant with the phase transitioning of the CO₂ being quite obvious. Both P- and S-waves arrive earlier and more strongly in the gaseous phase (lower pore pressures) than in the liquid or supercritical phase (higher pore pressures). The large changes to the waveforms are more immediate for the T = 28°C run where as the changes to the waveforms for the T = 40°C run are less abrupt. Also the phase transition for the T = 40°C run appears to take place at a higher pore pressure, past 7 MPa, than the T = 28 °C run, under 7 MPa.

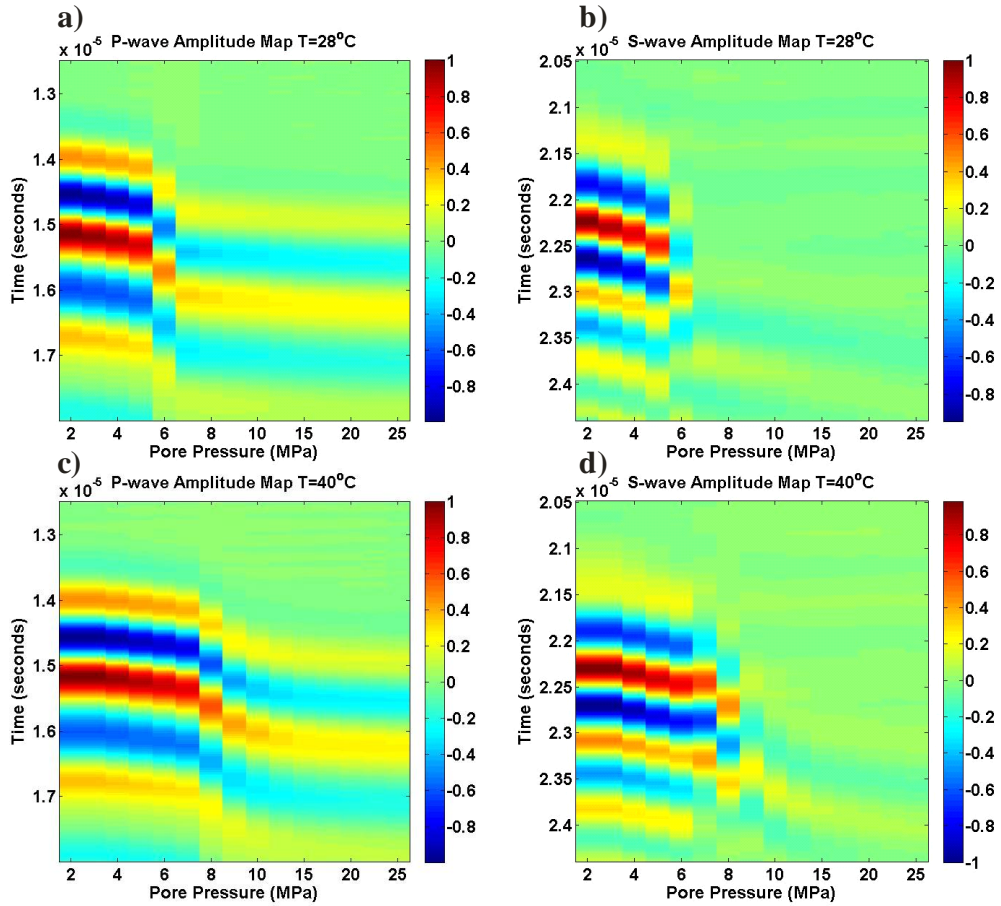


Figure 6.4: Normalized P- and S-wave waveforms as a function of pore pressures collected during the constant temperature runs of a) and b) $T = 28^\circ\text{C}$ and, c) and d) $T = 40^\circ\text{C}$. A constant differential pressure of 15 MPa was maintained throughout each measurement run.

Figure 6.5 shows the P-and S-waveforms as a function of temperature at a constant pore pressure (P_p) of 7 MPa, 10 MPa, and 25 MPa while the differential pressure was held constant at 15 MPa. The $P_p = 7$ MPa P-and S-waveform plot shows large changes with the signals arriving earlier and with greater amplitude in the gaseous phase (higher temperature) than in the liquid phase (lower temperature). In contrast, for the $P_p = 10$ MPa and $P_p = 25$ MPa waveform plots, there are no substantial changes to the waveforms even over the anticipated liquid to supercritical fluid phase transition. However for the $P_p = 10$ MPa run, the arrivals of the P-and S-waveforms do appear to arrive slightly earlier and slightly higher amplitude at the higher temperatures. For the $P_p = 25$ MPa run, the P-waves display little noticeable change over the range of temperature

change while the S-waves show slightly earlier arrivals at higher temperatures. The S-waves of the $P_p = 25$ MPa, figure 6.5f, also appear to be highly attenuated as is demonstrated by the noise overprint.

6.2.2 Observed CO₂ Saturated Wave Velocity

The P- and S-wave velocities with their estimated errors for the four constant temperature runs are shown in figure 6.6. The wave velocities of the two runs whose waveforms were not shown in the previous section are also shown here on the same velocity plot for the purpose of reinforcing the observed trends. Also, the dry wave velocities obtained under a confining pressure of 15 MPa are plotted at $P_p = 0$ MPa to provide a reference for the changes seen. With CO₂ saturating the pore space, irrespective of the phase state, both P-and S-wave velocities are lower than the dry wave velocities. The CO₂ phase transition out of the gaseous state is marked by a significant drop in wave velocity, with the drop being smaller and less immediate for the two higher temperature runs. Comparing velocities right before and right after the large drop, namely where the velocities change becomes minor, the change is about 4.5% and 5.2% for the P-and S-waves of $T = 28^\circ\text{C}$ respectively, and the change is about 4.2% and 4.8% for the P-and S-waves of $T = 40^\circ\text{C}$ respectively. Over the entire 2 to 25 MPa pore pressure interval, the overall $T = 28^\circ\text{C}$ velocity change is 6.7% and 8.1%, for P-and S-wave, respectively. The overall $T = 40^\circ\text{C}$ velocity change is 6.1% and 7.1% for P-and S-wave, respectively. Furthermore, the large drop in wave velocities for the two higher temperature runs occur at pore pressures that are higher than the pore pressures of the two lower temperature runs. The large drop in wave velocities for the two higher temperature runs occur at pressures close to the CO₂'s critical pressure of 7.4 MPa. While the large drop in wave velocities for the two lower temperature runs occur at pore pressures that approximate CO₂'s temperature dependent-vapour pressure. For both cases, the exact agreement to the vapour pressure or to the critical pressure cannot be determined due to the coarse pore pressure increments taken of the laboratory measurements.

Within a given phase state (gas, liquid, or supercritical) as pore pressure

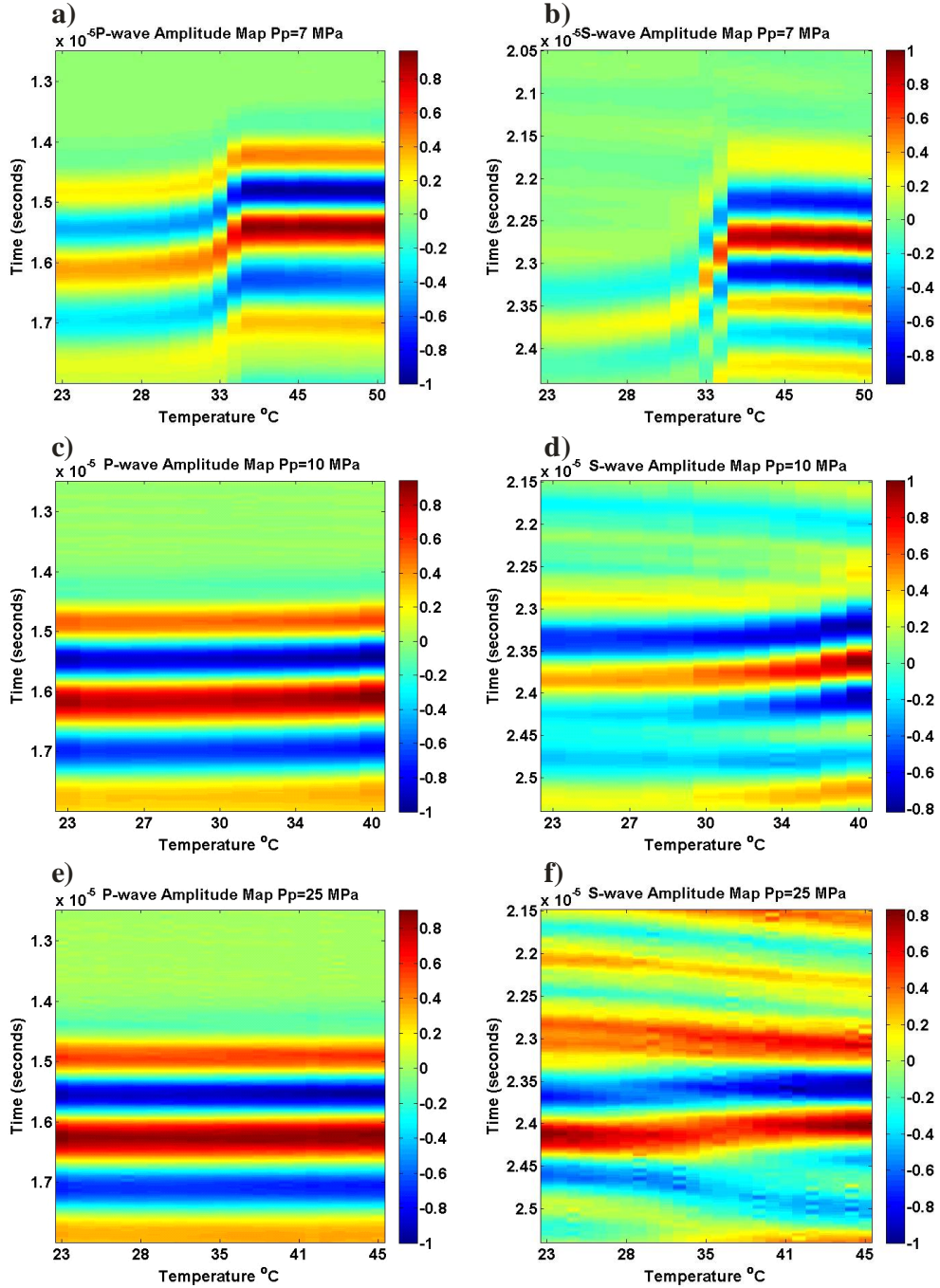


Figure 6.5: Normalized P- and S-wave waveforms as a function of temperature collected during the constant pore pressure runs of a) and b) $P_p=7$ MPa, c) and d) $P_p=10$ MPa and e) and f) $P_p=25$ MPa. A constant differential pressure of 15 MPa was maintained throughout each measurement run.

increases the elastic wave velocities decrease, even though the differential pressure is constant for all measurements. When all four constant temperature runs are compared at a high pore pressure, the velocities of the higher temperature

runs, which are in the supercritical fluid phase, are generally greater than the lower temperature runs, which are in the liquid phase. However the actual velocity differences between the liquid and supercritical fluid phase are small and are within error, in contrast to large velocity change associated with the gas to liquid or gas to supercritical phase transition.

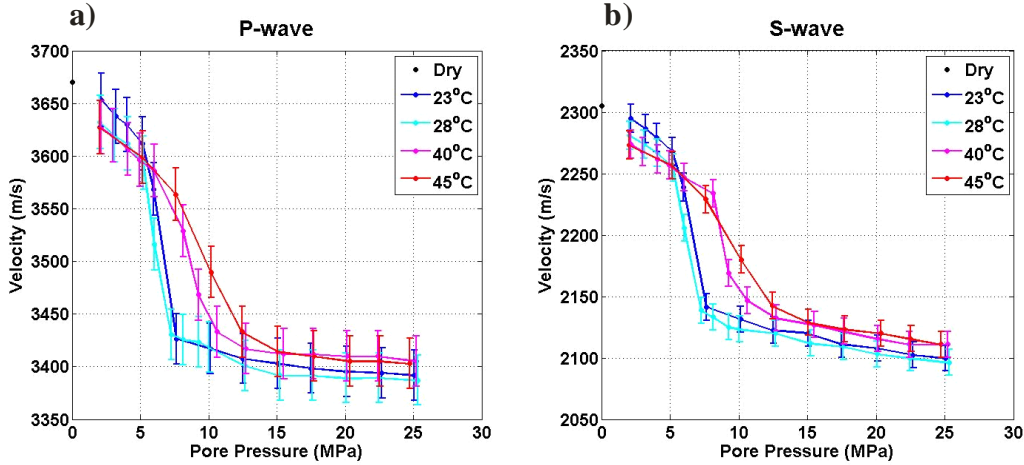


Figure 6.6: Ultrasonic P-wave (a) and S-wave (b) velocities with their respective errors measured of the porous ceramic rod saturated with CO₂ for all constant temperature runs and when the sample is not saturated (black dot at P_p = 0 MPa).

The P-and S-wave velocities with their errors for the three constant pore pressure runs are shown along with the dry wave velocities obtained under a confining pressure of 15 MPa plotted at T = 23°C, in figure 6.7. Similarly to above, with CO₂ in the pore space the wave velocities decrease with respect to the dry wave velocities. The CO₂ phase transition from liquid to gas is marked by a significant increase in wave velocity of about 3.8% and 4.3% for both P-and S-waves, respectively. The overall increase in P-and S-wave velocities over the entire temperature interval is 4.1% and 4.8%, respectively. The phase transition from liquid to supercritical fluid does not exhibit much variation on wave velocity but does show a slight overall increase in velocity with higher temperatures. The P_P = 10 MPa run exhibits a 0.4% and 0.9% overall increase in P-wave and S-wave velocity, respectively. The P_P = 25 MPa run exhibits a 0.1% and 0.4% overall increase in P-wave and S-wave velocity, respectively. When all three constant

pore pressure runs are compared at a given temperature, the velocities of a low pore pressure run are generally higher than a high pore pressure run.

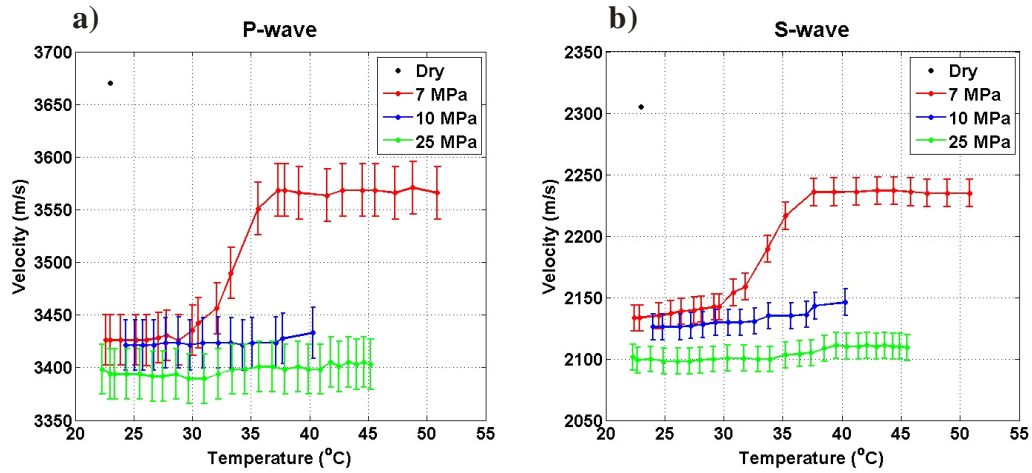


Figure 6.7 Ultrasonic P- wave (a) and S-wave (b) velocities with their respective errors measured of the sample saturated with CO₂ for all constant pore pressure runs and when the sample is not saturated (black dot at P_p = 0 MPa).

The wave velocity change observed over the vapour-liquid boundary for the constant pore pressure run is less immediate than that observed for the constant temperature runs. Also, this liquid to gas phase transition occurs at a delayed temperature in respect to the vapour temperature expected from CO₂'s phase diagram. The large P-and S-wave velocity variations occurred after 33°C in our data, while CO₂'s vapour temperature is 29°C at a fluid pressure of 7 MPa. This temperature delay maybe caused by the lack of time provide at each new temperature for the pore fluid to equilibrate during data acquisition. Alternatively, it may be related to the influence of the finite pore size on the phase transition, occurring in a porous medium due to energy cost associated with surface energy effects. It should be noted that during constant pore pressure runs, the measurements were taken as the vessel was continually heated. The thermal inertia of the system makes changing the temperature a slow and difficult to control process.

6.2.3 Modelled CO₂ Saturated Wave Velocity

In chapter 3, two fluid substitution models used for predicting wave velocities of a saturated porous medium were introduced. Gassmann's and Biot's theoretical predictions are computed here over the same pressure and temperature conditions as applied in the laboratory. In order to compute both models a series of sample and fluid properties need to be known. The bulk modulus, the density, the fluid viscosity of the pore fluid (CO₂) were determined from the thermodynamic properties obtained from NIST's online chemistry webBook, the density and the bulk modulus of the mineral grains were determined from Bass (1995), the bulk modulus of the frame was determined from ultrasonic pulse transmission measurements on the dry sample, and the bulk density, the porosity, and the tortuosity of the sample were determined in chapter 5. The bulk modulus of the frame was determined as a function of temperature to account for the softening of the sample frame with heat. Incorporating the temperature dependency of the frame will allow for the modelled results to be more accurate. The modelled results from their predictions are compared to the laboratory observed results.

Gassmann's Model

Here, the modelled P-and S-wave velocities of the CO₂ saturated porous ceramic rod are presented by applying the widely employed Gassmann's fluid substitution formulation given by equation 3.29 and 3.31. Figure 6.8 shows the modelled P-and S-wave velocities along with the observed velocities under CO₂ saturation for two of the four constant temperature runs, T = 28°C and T = 40°C. The results and comparisons for all four constant temperature runs can be found in the appendix. For both P-and S-waves, Gassmann's modelled velocities show similar behaviours with varying pore pressure, specifically: the large drop in wave velocities; where the wave velocities begin to change significantly; and the immediate or gradual nature of the velocity change over the phase transition. In terms of the absolute velocity values, the modelled velocities are almost in agreement with the observed velocities over low pore pressures. However, as

pore pressure increases the discrepancy between the modelled and observed velocities enlarges. The largest discrepancy is 6.6% and 6.0% for P-and S-waves, respectively. This discrepancy is larger than the drop in wave velocities over the phase transition of the observed laboratory data. Essentially, Gassmann's model predicts a larger change in wave velocities than that is observed. Over the phase transition interval for P-and S-waves, respectively, Gassmann predicts a 7.5% and 7.6% change for $T = 28^{\circ}\text{C}$, and a 7.4% and 7.5% change for $T = 40^{\circ}\text{C}$. For the $T = 28^{\circ}\text{C}$ run the overall change in wave velocity over the entire interval is 12.0% and 13.2% for P-and S-wave velocity, respectively. For the $T = 40^{\circ}\text{C}$ run the overall change in wave velocity over the entire interval is 11.7% and 12.7% for P-and S-wave velocity, respectively. Generally for both P-and S-waves, the modelled velocities are always lower than the observed velocities.

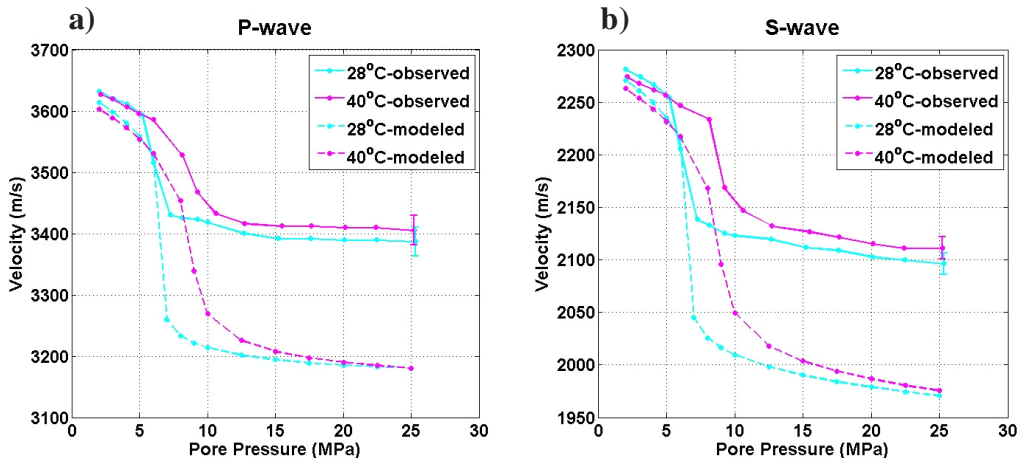


Figure 6.8: Observed and Gassmann's modelled P- wave (a) and S-wave (b) CO_2 saturated velocities for $T = 28^{\circ}\text{C}$ and $T = 40^{\circ}\text{C}$ constant temperature runs. To avoid clustering, only the error at a pore pressure of 25 MPa are shown. The errors at all other data points are approximately the same size.

Figure 6.9 shows the modelled P-and S-wave velocities with the observed velocities under CO_2 saturation for the three constant pore pressure runs. Starting with the $P_p = 7$ MPa results, Gassmann's modelled velocities do show a large change over the vapour-liquid boundary; a 6.1% and a 6.2% increase in P-and S-wave velocities, respectively. However for the modelled velocities, the large change in wave velocities in response to the phase transition appears to be more

immediate and it occurs at an earlier temperature than the observed velocities. Also there is a large discrepancy between the absolute velocity values where the discrepancy is largest with low temperatures and the discrepancy decreases with higher temperature. Unlike in the constant temperature runs, the modelled and observed velocities here are nowhere near agreement for any data point. Over the entire interval, Gassmann predicts an overall P-wave increase of 8.8% and an overall S-wave increase of 9.0%.

For the $P_P = 10$ MPa and $P_P = 25$ MPa runs in terms of behavioural trends, Gassmann's modelled results also show that there is no significant wave velocity change over the liquid to supercritical fluid phase transition. For the $P_P = 10$ MPa run, the modelled velocities show a smooth increase with temperature where the increase is more than the observed velocities are showing with temperature. A 2.0% and 2.4% increase in wave velocity is modelled for the P-and S-wave, respectively. For the $P_P = 25$ MPa run, the modelled S-waves velocities also show a smooth increase with temperature but the increase is slighter; this is consistent with the observed S-wave velocity increase. The modelled P-wave velocities however appear to be invariant with temperature where this behaviour is somewhat consistent with the observed P-wave velocities. A 0.0% and 0.5% increase in wave velocity is modelled for the P-and S-wave, respectively. In terms of absolute velocity values, there is a large discrepancy between the modelled and observed for all the temperatures explored. The discrepancy for the $P_P = 10$ MPa run does appear to decrease with higher temperatures, where as the discrepancy for the $P_P = 25$ MPa run does not show any perceivable change with temperature. For all constant pore pressure runs of both P-and S-waves the largest discrepancy in velocity values between modelled and observed is 6.3%, and the modelled velocities are always less than the observed velocities.

Overall Gassmann's predictions do not adequately describe the wave behaviour observed in the laboratory. Gassmann's formulation always under-predicts the wave velocities and it does not account for the wave attenuation observed. This is a direct consequence of applying Gassmann's formulation to the inappropriate frequency regime; Gassmann's equation is only valid for

describing wave behaviour pertaining to low frequencies and strictly only at zero-frequency (static deformation). High wave frequency effects that can give rise to differential movements between the pore fluid and pore wall leading to frequency-dependent wave attenuation that Gassmann's zero-frequency limit was never intended to account for.

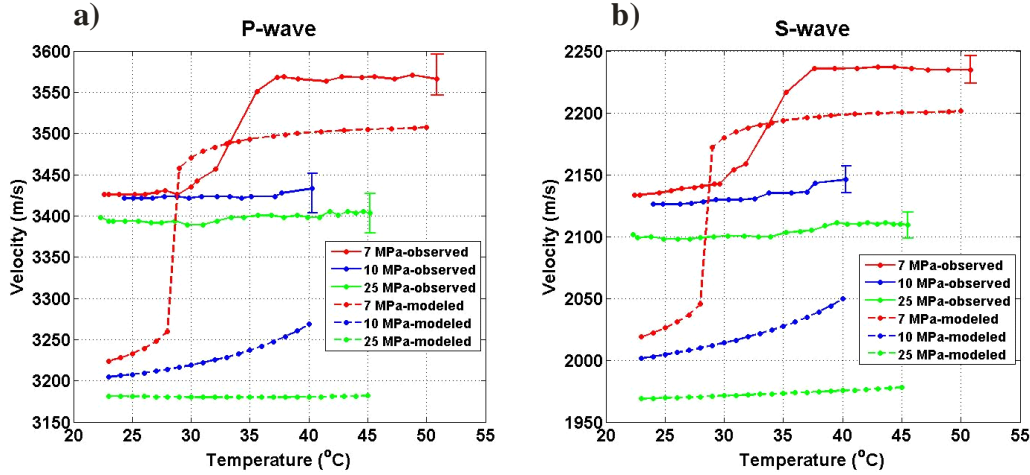


Figure 6.9: Observed and Gassmann's modelled P-wave (a) and S-wave (b) CO_2 saturated velocities for $P_p=7 \text{ MPa}$, $P_p=10 \text{ MPa}$, and $P_p=25 \text{ MPa}$ constant pore pressure runs. To avoid clustering, only the error at the highest temperature in each run is shown. The errors at all other data points are approximately the same size.

Biot Model

The P-and S-wave velocities of the CO_2 saturated porous ceramic rod are modelled by using Biot's formulation given in section 3.3.2. As a reminder, there are two advantages in using Biot's formulation over Gassmann's formulation:

- 1.) Biot's model is valid for a wide range of frequencies; for low frequencies, where Gassmann is valid, and for the high frequencies, which are encountered in our laboratory data.
- 2.) Considers wave attenuation.

Figure 6.10 shows the modelled P-and S-wave velocities along with the observed velocities under CO_2 saturation for the same two of the four constant temperature runs shown before for Gassmann's model. The results and comparisons for all four constant temperature runs again can be found in the appendix. For both the P-and S-waves the modelled velocities are generally

within the error of the observed velocities and for where there is a disagreement between results, the discrepancy is usually small (< 1%). Of all the velocity comparisons the S-wave velocities of $T = 28^{\circ}\text{C}$ show a disagreement between results the most frequent with them all occurring in the higher pore pressures. Furthermore as a result of the predominantly good agreement between Biot's modelled and observed results, Biot's modelled velocities show the same magnitude in the drop of wave velocities with the phase transition, the same pore pressures of where the wave velocities begin to change significantly, and the same immediate or gradual nature of the velocity change over the phase transition.

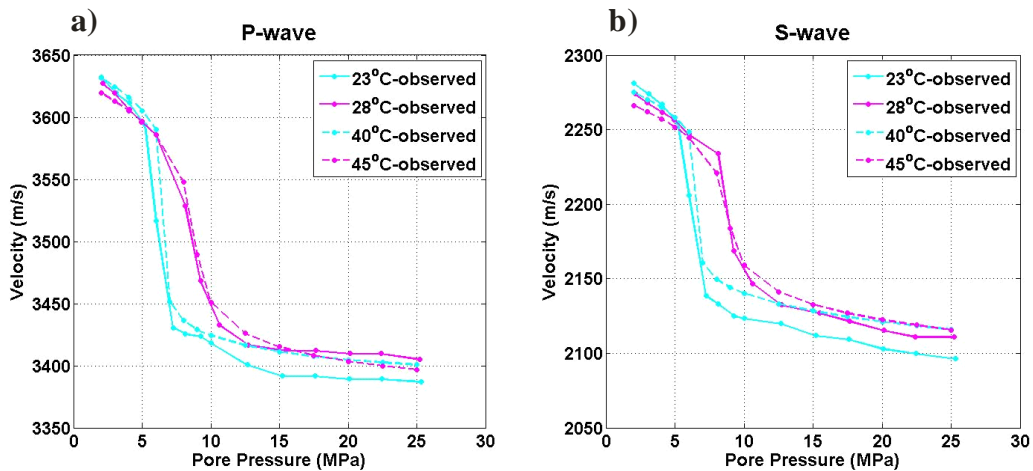


Figure 6.10: Observed and Biot's modelled P- wave (a) and S-wave (b) CO_2 saturated velocities for $T = 28^{\circ}\text{C}$ and $T = 40^{\circ}\text{C}$ constant temperature runs. No error bars are shown, however the size of errors can be referred to in figure 6.6 and 6.8.

Figure 6.11 shows the modelled P-and S-wave velocities with the observed velocities under CO_2 saturation for the three constant pore pressure runs. Starting with the P-wave velocities, for both the higher pore pressure runs the agreement between the modelled and observed is good for all temperatures explored. For the $P_p = 7 \text{ MPa}$ run, the results are only in agreement at temperatures well away from the phase transition. Near the phase transition temperatures, the discrepancy is quite large (4.2%) where the modelled response to the phase transition is again more immediate than observed response. For the S-wave velocities, the general agreement is less than that observed with P-wave velocities for all three runs. Where there is a disagreement in velocity values, for

the two higher pore pressure runs the discrepancies are not substantial ($< 1\%$). For the $P_p = 7$ MPa run the manner of the S-wave discrepancies are similar to that seen with P-waves; insignificant away from the phase transition but is quite large over the phase transition (4.8%).

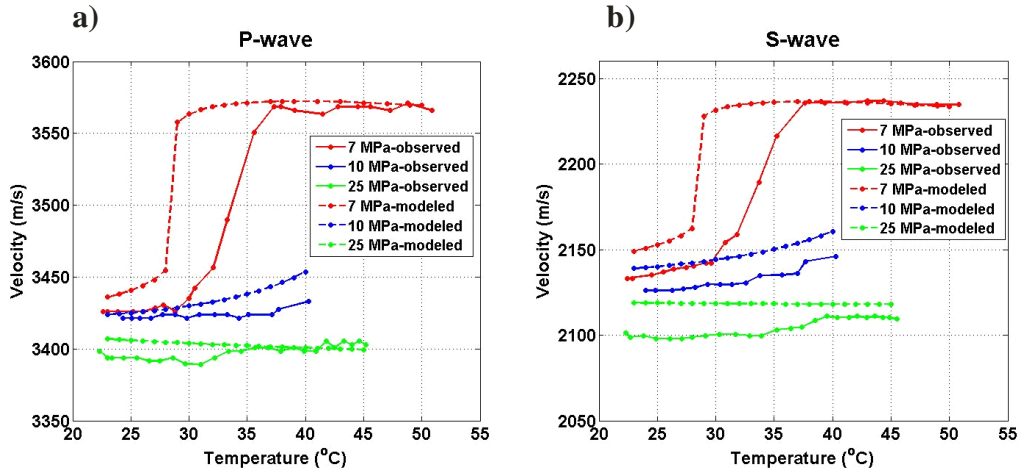


Figure 6.11: Observed and Biot's modelled P-wave (a) and S-wave (b) CO_2 saturated velocities for $P_p = 7$ MPa, $P_p = 10$ MPa, and $P_p = 25$ MPa constant pore pressure runs. No error bars are shown, however the size of errors can be referred to in figure 6.7 and 6.9.

6.2.4 Observed CO_2 Saturated Wave Attenuation-

From the waveform plots pertaining to the CO_2 saturated state, displays of large signal strength variations were observed. Here the earlier qualitative observations made on wave attenuation will be examined quantitatively. The attenuation of waveforms was studied by determining the differential attenuation coefficient as described in section 4.5.2. For all CO_2 saturated measurements, the differential attenuation coefficient of each waveform was determined with respect to the waveform acquired at 2 MPa of CO_2 and 23°C. The waveform acquired at 2 MPa and 23°C was used as the reference signal because it has the greatest signal strength of all the waveforms collected.

Figure 6.12 displays the differential attenuation coefficient for P-and S-waves for the two constant temperature runs as a function of pore pressure and of frequency. Here, only the differential attenuation coefficients for the $T = 28$ °C and $T = 40$ °C constant temperature runs are presented. The computed amplitude

spectrum of the signals used for determining the differential attenuation coefficient for all the measurement runs is given in the appendix, along with the differential attenuation coefficient results of $T = 23^{\circ}\text{C}$ and $T = 45^{\circ}\text{C}$ measurement runs. The frequency range used for analysis is limited by the band of frequencies that carries most of the energy in their amplitude spectra. The useable frequency range considered not to be contaminated by too much noise is from 0.4 to 1.4 MHz for P-waves and 0.5 to 1.7 MHz for S-waves. The peak in the spectra is at about 0.67 MHz and 1.2 MHz for P-and S-waves, respectively.

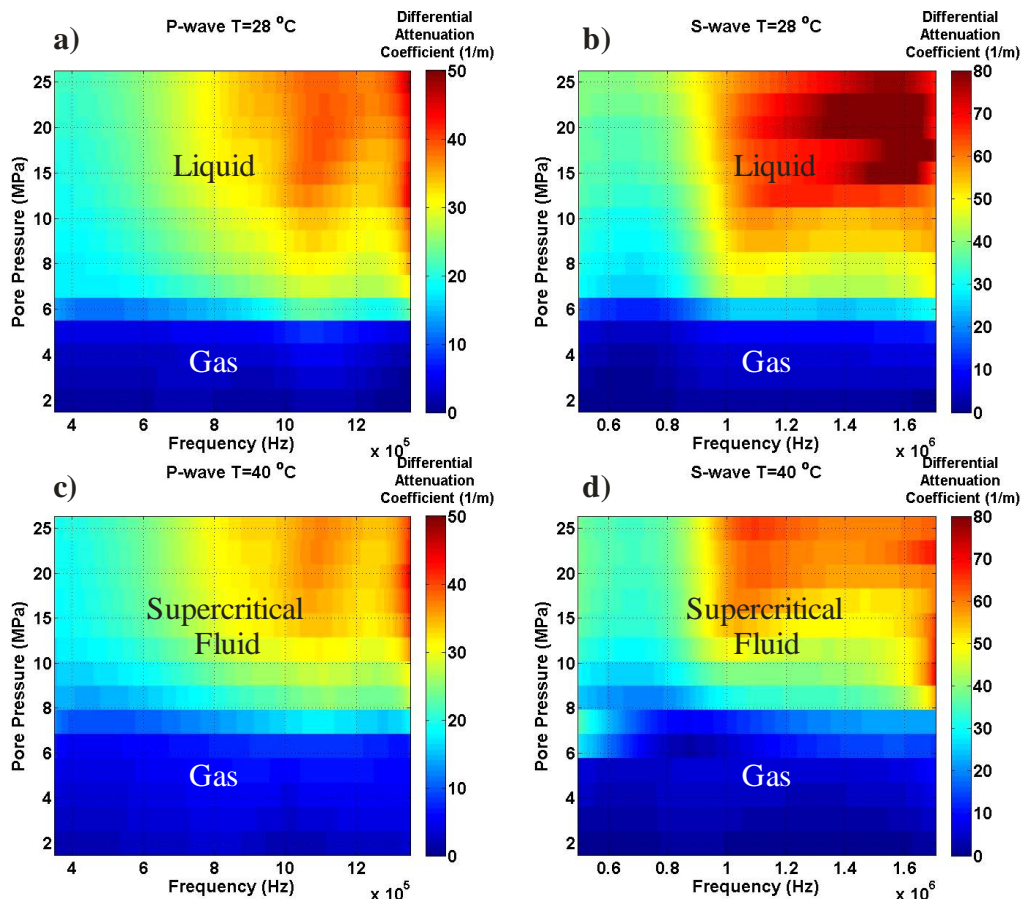


Figure 6.12: Observed P- and S-wave differential attenuation coefficient determined for a) and b) $T = 28^{\circ}\text{C}$, and c) and d) $T = 40^{\circ}\text{C}$ constant temperature runs as a function of frequency and pore pressure. The expected CO_2 phase state is indicated at the appropriate physical conditions.

The CO_2 phase transition out of the gaseous state and into the liquid or supercritical states is marked by a significant increase in wave attenuation. When

contrasting the $T = 28^{\circ}\text{C}$ to the $T = 40^{\circ}\text{C}$ plots for both P-and S-waves, especially at high pore pressure and high frequencies the attenuation is slightly greater for the $T = 28^{\circ}\text{C}$ than for the $T = 40^{\circ}\text{C}$. Furthermore, similar to that seen with wave velocities, the large changes in wave attenuation occurs at a lower pore pressure for the $T = 28^{\circ}\text{C}$ results than the $T = 40^{\circ}\text{C}$ results.

When comparing the P-wave differential attenuation coefficient to the S-wave differential attenuation coefficient under the same condition, the S-wave generally appears to be more attenuated than the P-wave. Also, the differential attenuation coefficients of S-waves appear to be more variable than the P-waves especially at high pore pressure and frequencies. This is because the S-waves are more susceptible to noise effects due to their lower amplitude strength.

From examining all the differential attenuation coefficient plots, two general attenuation trends can be established. First, the attenuation increases with pore pressure where it is the lowest in the gaseous phase state and becomes higher in the liquid or supercritical fluid phase states. Second, as would be expected the attenuation is greater at higher frequencies than at lower frequencies and is particularly more obvious at high pore pressures.

Figure 6.13 displays the differential attenuation coefficient for P-and S-waves for the constant pressure runs with pore pressure at 7 MPa, 10 MPa, and 25 MPa as a function of temperature and frequency. When the P-and S-wave plots of $P_p=7$ MPa are compared to the P- and S-wave plots of $P_p=10$ MPa and of $P_p=25$ MPa the overall character of the plots are different. The $P_p = 7$ MPa displays a sharp decrease in differential attenuation coefficients. The $P_p = 10$ MPa plots and $P_p = 25$ MPa plots, just like their wave velocity behaviours, do not exhibit any significant attenuation variations that signifies a phase transition. When all three constant pressure runs are compared at a given temperature, the attenuation of a low pore pressure run is generally lower than the attenuation for a high pore pressure run. Again, S-wave generally appears to be more attenuated than P-waves when compared at the same condition.

In general, two attenuation trends can be established from these constant pressure runs. First, however slight, the attenuation decreases with increasing

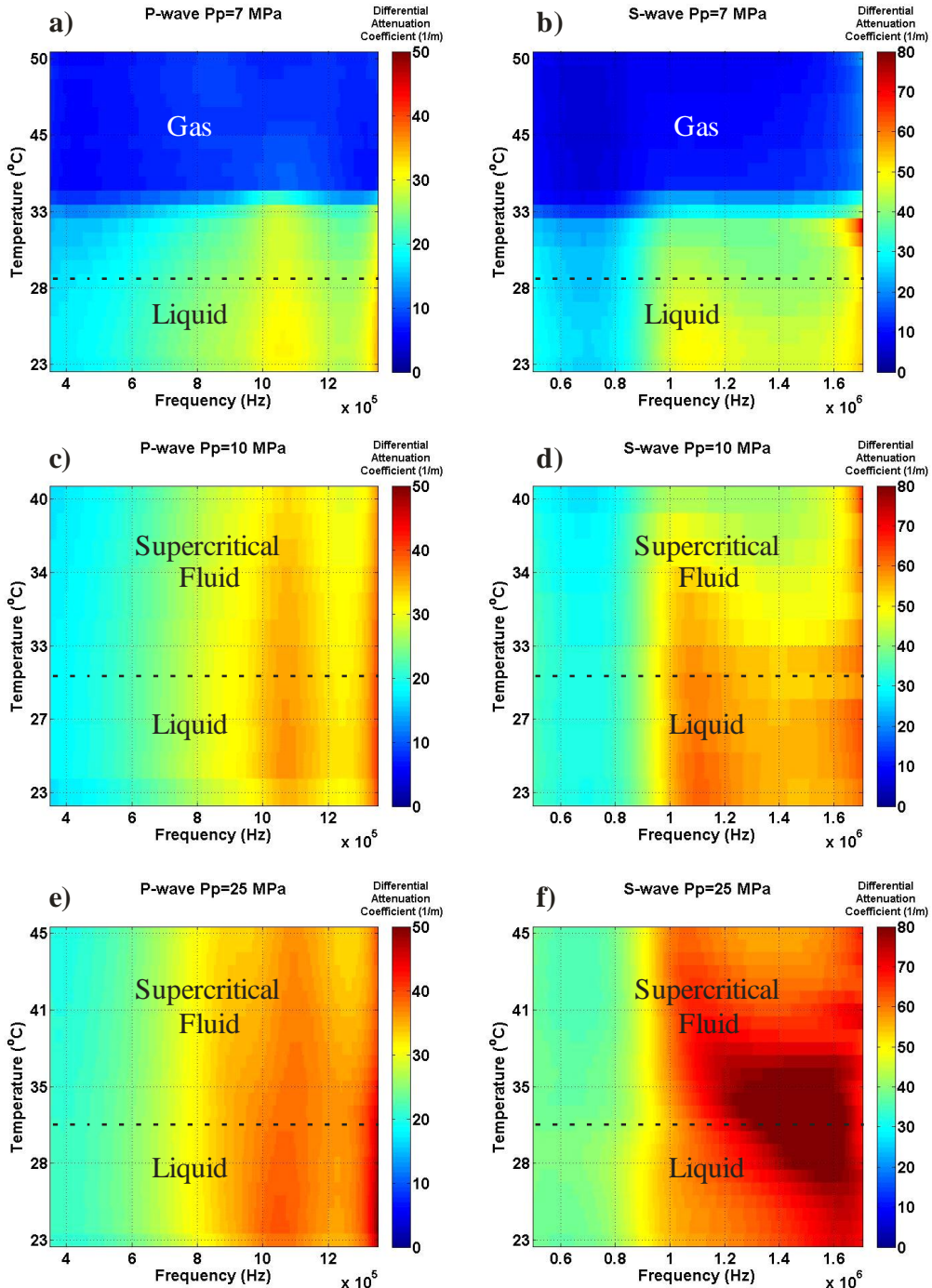


Figure 6.13: Measured P- and S-wave differential attenuation coefficient determined for a) and b) $P_p = 7 \text{ MPa}$, c) and d) $P_p = 10 \text{ MPa}$, and e) and f) $P_p = 25 \text{ MPa}$ constant temperature runs as a function of frequency and pore pressure. The expected CO_2 phase state is indicated at the appropriate physical conditions. The black dashed-line indicates where the phase transitions are suppose to occur.

temperature where it is the highest in the liquid phase and becomes lower in the gas phase or supercritical fluid phase. Second, the attenuation is frequency

dependent where attenuation is greater at high frequencies than at lower frequencies and is especially obvious at lower temperatures.

6.2.5 Modelled CO₂ Saturated Wave Attenuation

As mentioned earlier, Biot's formulation also considers wave attenuation. Figure 6.14 shows the computed differential attenuation coefficient from Biot's model for two constant temperature runs. A large change to both P-and S-wave attenuation in response to the phase transition is modelled. Comparing these two temperature runs at the same pore pressure and frequency, Biot's model shows that the attenuation is always greater for the lower temperature run than the higher temperature run. Between the P-and S-wave differential attenuation coefficients for any constant temperature runs, Biot's model shows that the S-wave results are larger than the P-wave's results when compared under the same conditions. Both of these comparisons between modelled results (low against high temperature; P-against S-waves) are consistent with the comparisons between observed results. Furthermore, the two general attenuation trends of attenuation increasing with pore pressure and with frequency seen with the observed results are also supported by Biot's modelled results. However when the absolute differential attenuation coefficient values are compared between the modelled and observed results there are some discrepancies where Biot's modelled attenuation are generally much lower than the observed attenuation. From the discussion in section 4.5.2, the errors of the observed P-and S-wave differential attenuation coefficient for this study are 12 m^{-1} and 18 m^{-1} respectively. With these errors considered, the differential attenuation coefficients are in agreement at only low pore pressures before the phase transition. At high pore pressures after the phase transition, disagreement between the results occurs for all frequencies although the discrepancy is less at lower frequencies. The largest discrepancy in differential attenuation coefficient values is 68% for P-waves and 63% for S-waves.

Figure 6.15 shows the computed differential attenuation coefficient from Biot's model for the three constant pore pressure runs. The modelled differential

attenuation coefficients do show large changes in response to the gas to liquid phase transition whereas the modelled attenuation response to the liquid to supercritical phase transition shows only a smooth variation. When the three constant pore pressure runs are contrasted with each other at a given condition

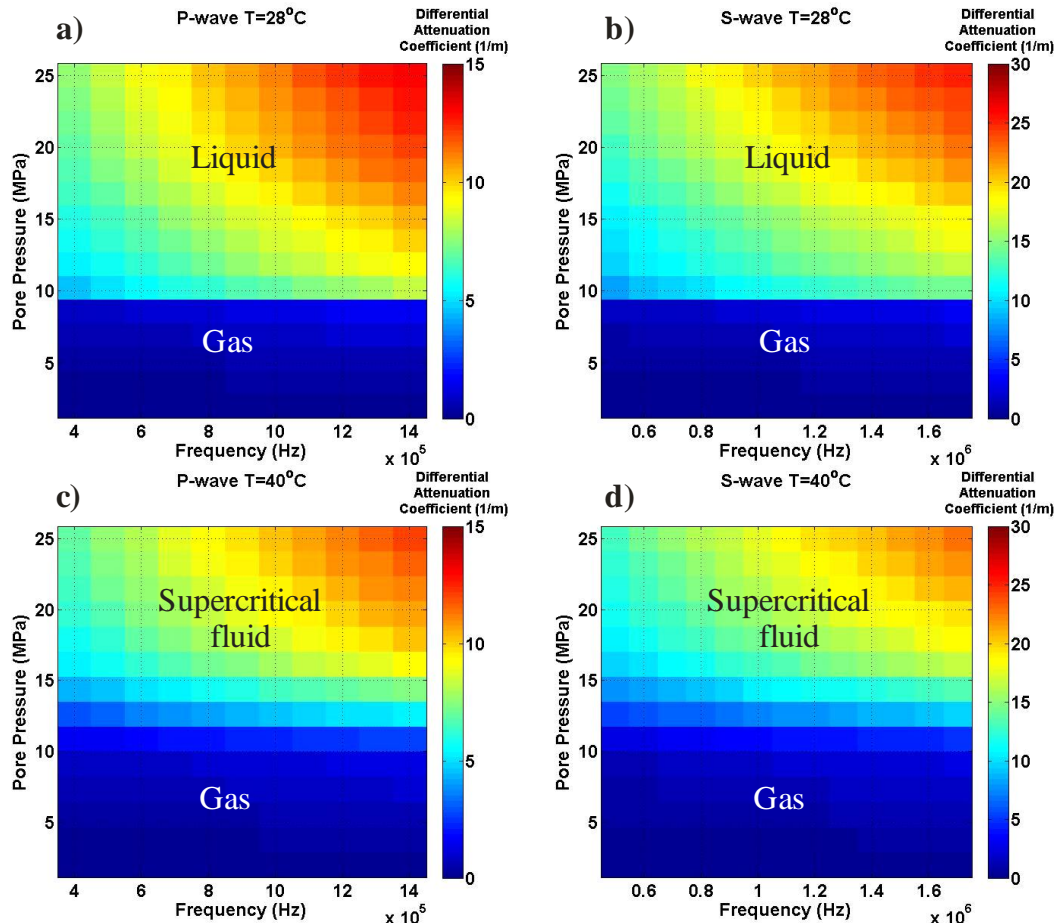


Figure 6.14: Biot's modelled P- and S-wave differential attenuation coefficient determined for a) and b) $T = 28^\circ\text{C}$, and c) and d) $T = 40^\circ\text{C}$ constant temperature runs as a function of frequency and pore pressure. The prevailing CO₂ phase state is indicated at the appropriate physical conditions.

irrespective of the wave type, the attenuation is always higher for the higher pore pressure. Again when the differential attenuation coefficient of the S-waves is compared to the P-waves at the same condition of any pore pressure run, the attenuation of S-waves is always greater than P-waves. Overall Biot's modelled results show that attenuation decreases with temperature and increases with frequency, and they are in agreement with our observed attenuation trends.

All these trends deduced from Biot's modelled differential attenuation coefficients are in qualitative agreement with the observed differential attenuation

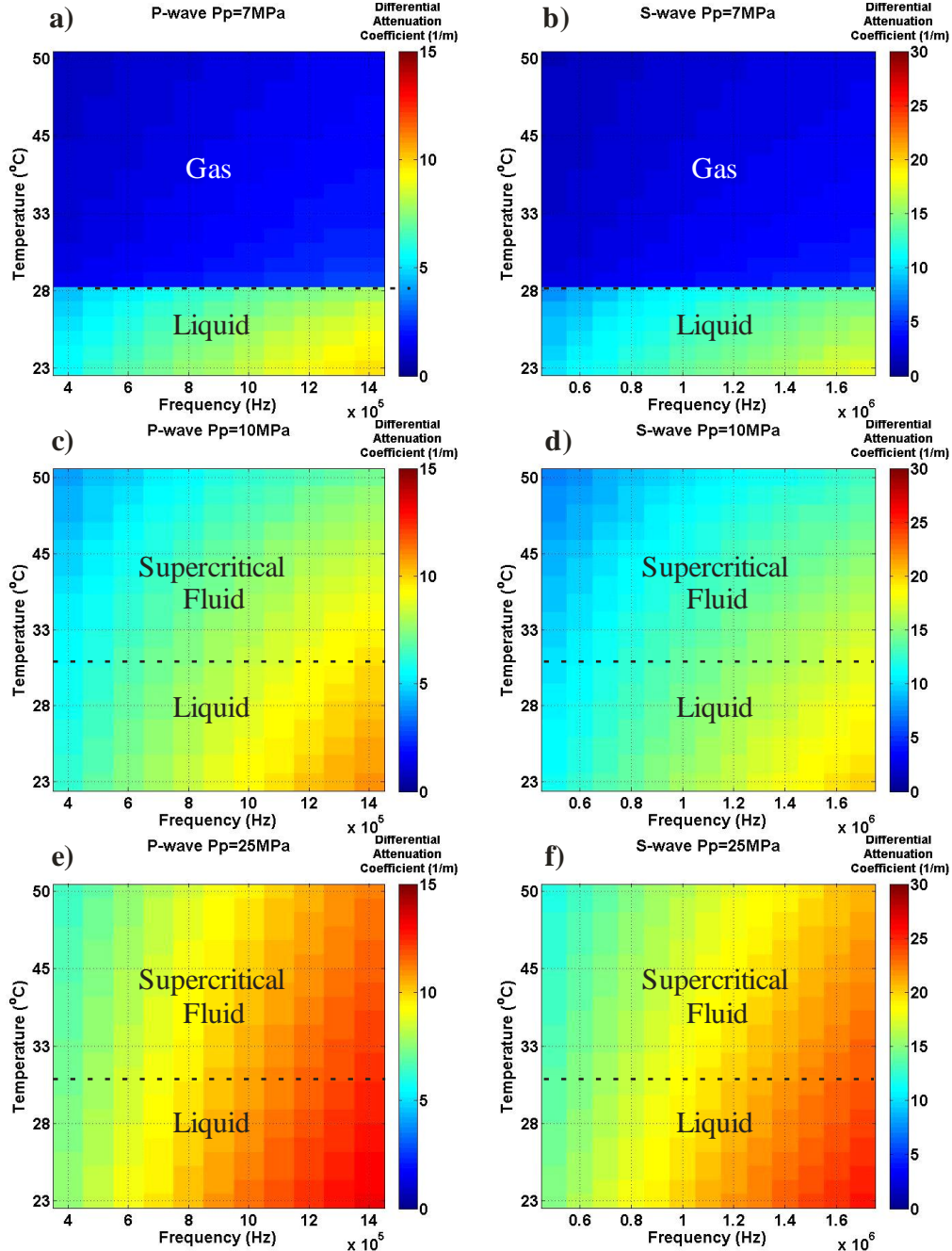


Figure 6.15 Biot's modelled P- and S-wave differential attenuation coefficient determined for a) and b) $P_p = 7 \text{ MPa}$, c) and d) $P_p = 10 \text{ MPa}$, and e) and f) $P_p = 25 \text{ MPa}$ constant temperature runs as a function of frequency and pore pressure. The expected CO_2 phase state is indicated at the appropriate physical conditions. The black dashed-line indicates where the phase transitions are suppose to occur.

coefficients. However in terms of quantitative agreement, the modelled and the observed results disagree. Similar to the constant temperature runs there is a

discrepancy of absolute differential attenuation coefficient values. Apart from gaseous region where the results are in agreement, the discrepancy between results increases with decreasing temperature and increasing frequency. The largest discrepancy in differential attenuation coefficient values is 72% for P-waves and 69% for S-waves. Also, the decrease in attenuation with increasing temperature for observed results is significantly less pronounced than that displayed by Biot's results, particularly for the two high pore pressure runs. For example from 23°C to 40°C at a frequency of 1 MHz for the $P_p = 10$ MPa run, Biot's results show a 40% change while the observed results yield only a 4% change.

Overall, Biot's modelled results show much improvement over Gassmann's modelled results. For the majority of wave velocities, Biot's results are in agreement with the observed laboratory results, whereas Gassmann's results were never in agreement. When Biot's modelled results do not agree with the observed results, the disagreement is usually substantially less than the disagreement between the observed and Gassmann's modelled values. In addition, Biot's formulation accounts for wave attenuation, which is apparent in our data and was not considered by Gassmann's formulation. The significant improvements of Biot's model over Gassmann's model are because Biot's model considers a wide range of wave frequencies.

Recall, Biot's formulation describes wave behaviour based on the prevailing frequency regime. A wave is in the low frequency regime if its frequency is less than the critical frequency and a wave is in the high frequency regime if its frequency is greater than the critical frequency, defined by equation 3.45. The critical frequency given here again is

$$f_c = \frac{\phi\eta}{2\pi\rho_f\kappa}$$

where ϕ is porosity, η is the viscosity of the pore fluid, ρ_f is pore fluid density, and κ is the absolute permeability of the porous sample. The computed critical frequency for the porous ceramic rod saturated with CO₂ over a range of pressures and temperatures are shown in figure 6.16. Over the actual CO₂ conditions

explored for the porous ceramic rod (shown by the white arrows in the diagram) the critical frequency ranges from 0.07 MHz to 0.43 MHz where a large majority of the critical frequencies are below 0.10 MHz. The higher critical frequencies are actually comparable to the wave frequencies of our data and all the higher critical frequencies occur at conditions where CO₂ is a gas. This implies that our data in the gaseous CO₂ state should also display behaviours relevant to low frequencies. From our laboratory data results, there are two observations that support low frequency behaviours. First, in the gaseous CO₂ state wave attenuation is low. Second, in the gaseous CO₂ state, when the observed wave velocities are compared with Gassmann's modelled velocities, the wave velocities are almost within error.

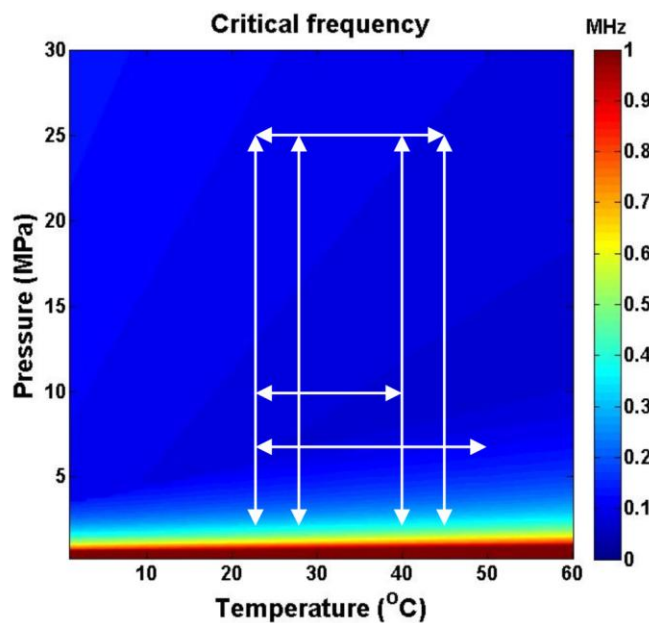


Figure 6.16: Biot's critical frequency for the CO₂ saturated porous ceramic rod. The superimposed white arrows represent the conditions investigated in the study.

In regards to wave attenuation, Biot's predictions are qualitatively in line with observed wave attenuation behaviour. Quantitatively however Biot's wave attenuation predictions are substantially less than the observed wave behaviour. The wave attenuation mechanism considered in Biot's formulation may not be the only wave attenuation mechanism occurring in the laboratory. Alternatively,

measurements of attenuation are notoriously prone to error and this may be the reason for the discrepancy (e.g., White (1992)).

6.3 Water

Water saturated measurements were conducted on the porous ceramic rod under full water saturation at $T = 23^\circ\text{C}$ with pore pressure varying from 5 to 50 MPa while differential pressure was maintained at 5 MPa. It should be noted that this water saturated measurement run was not obtained during the same series conducted for the dry and CO_2 saturated measurements (see chapter 4), but was acquired earlier on a different sample of the same material.

6.3.1 Water Saturated Waveforms

The P- and S-waveforms obtained under full water saturated conditions of the porous ceramic rod are shown in figure 6.17. In this figure, both the P-and S-waveforms do not vary significantly over this pressure interval. The signal strength appears relatively constant throughout, with very slight weakening at the lowest pore pressure. As pore pressure increases the P-waves arrive slightly earlier, but the S-wave arrival times do not appear to vary.

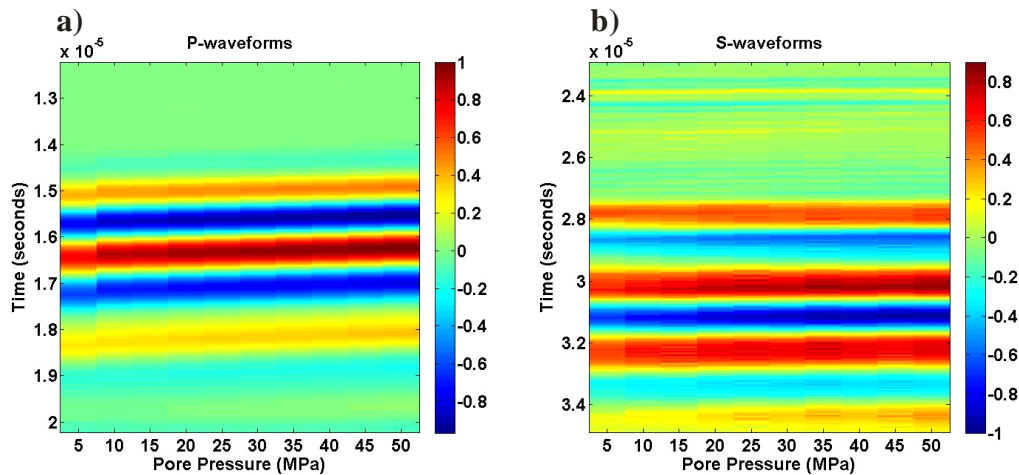


Figure 6.17: Normalized P- (a) and S-wave (b) water saturated waveforms as a function of pore pressure. These water saturated waveforms were collected from another porous ceramic rod sample instead of the one used for the dry and CO_2 saturated measurements. A constant differential pressure of 5 MPa was maintained throughout the measurement run.

6.3.2 Observed Water Saturated Wave Velocities

Figure 6.18 displays the P-and S-wave velocities with error as a function of pore pressure using the waveforms shown in figure 6.17. The dry P-and S-wave velocity obtained under a confining pressure of 5 MPa is shown at $P_p = 0$ MPa. Similar to that observed with CO₂, with water in the pore space the wave velocities decreases with respect to the wave velocities under dry conditions. The wave velocity decrease from dry to saturated is much more than that for CO₂. This could be because water is denser than CO₂ in general. However, as the pore pressure of water increases the P-wave velocities also increases. Over this 5 to 50 MPa pore pressure interval, the P-wave velocities increased linearly of about 1.2%. In contrast over the same pressure range the S-wave velocities decreased linearly, but of only 0.3%.

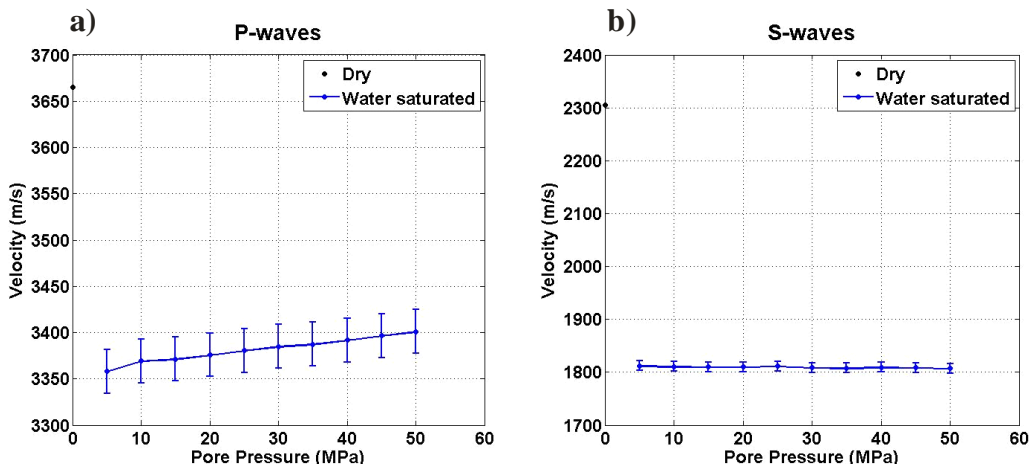


Figure 6.18: Ultrasonic P- (a) and S-wave (b) velocities with their respective errors measured of the sample saturated with water under various pore pressures at $T = 23^\circ\text{C}$ and when the sample is not saturated (black dot at $P_p = 0$ MPa).

6.3.3 Modelled Water Saturated Wave Velocities

As for the CO₂ saturated results, Gassmann's and Biot's theoretical predictions are computed here over the same pressure and temperature conditions as applied in the laboratory under water saturation. The water properties essential to the computations such as bulk modulus, density, and fluid viscosity, were also obtained from NIST's online chemistry webBook.

Gassmann Model

Figure 6.19 shows the modelled and observed P-and S-wave velocities of the water saturated state. The observed linear increase of P-wave velocities with increasing pore pressure and the observed opposite behaviour of a linear decrease of S-wave velocities with increasing pore pressure are both modelled by Gassmann's fluid substitution. The modelled increase in P-wave velocity is 0.6% and the modelled decrease in S-wave velocities is 0.3%. However neither the P- nor S-wave modelled velocities are in agreement with the observed velocities; the modelled velocities are consistently lower than the observed velocities. The discrepancy is 1.6% for P-waves and 3.6% for S-waves.

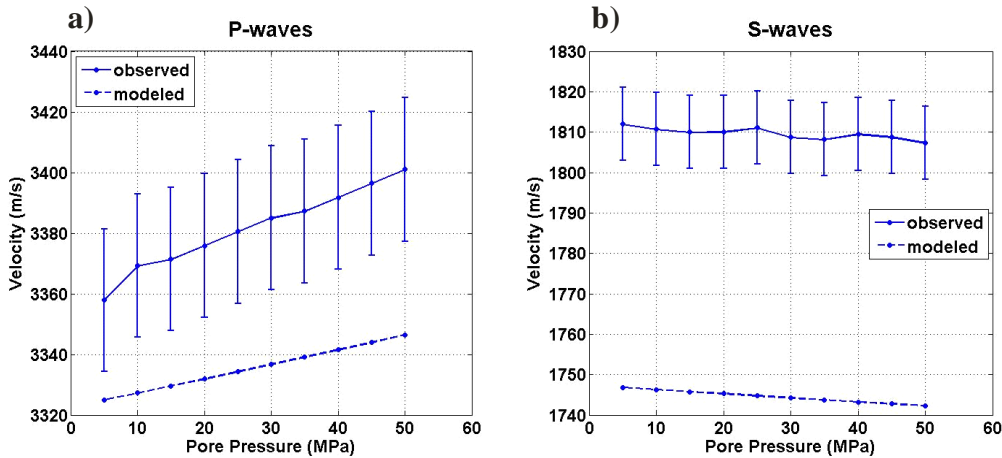


Figure 6.19: Observed and Gassmann's modelled P-waves (a) and S-wave (b) water saturated velocities.

Biot Model

Figure 6.20 displays the water saturated modelled and observed P-and S-wave velocities. The linearly increasing and decreasing trend with pore pressure for the P-and S-wave velocities respectively, are also predicted by Biot's model. The increase for P-wave velocities is 0.5% while the decrease for S-wave velocities is 0.1%. However, overall there is a disagreement between the velocity results. The modelled velocities are always higher than the observed velocities and the disagreements are greater for the S-waves than the P-waves; the largest discrepancy for P-waves is 1.3% while for S-waves the largest discrepancy is

1.4%. These are still reasonably close. Again, Biot's modelled results show a closer fit with the observed data than Gassmann's modelled results.

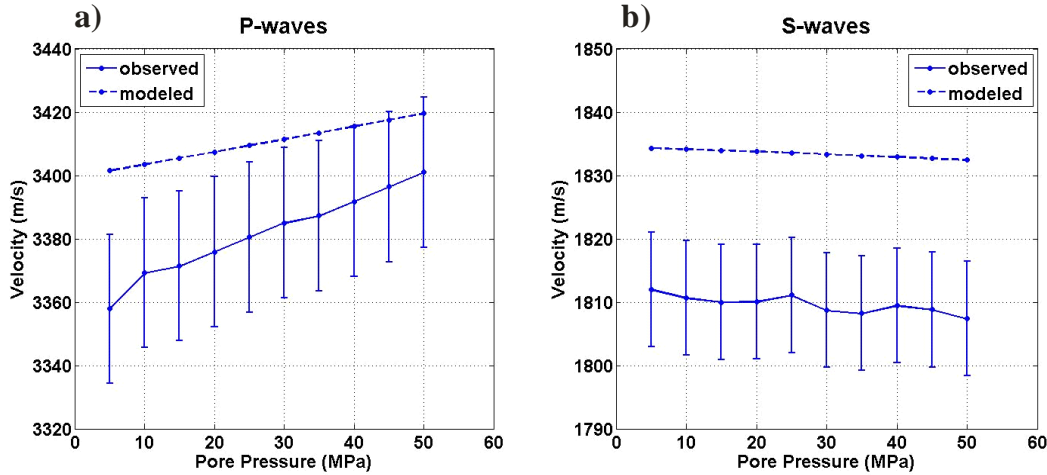


Figure 6.20: Observed and Biot's modelled P- wave (a) and S-wave (b) water saturated velocities.

6.4 Results and Discussion

In this section, the pore fluid effects of CO₂ and water on the wave behaviours observed and modelled are reviewed, generalized and discussed.

6.4.1 CO₂

In general from all the wave velocity behaviours seen in both laboratory and modelled results and from considering the simple equations of 3.19 and 3.20, it appears the controlling factor is the bulk density of the sample. For S-waves, this observation is obvious because theoretically the changes to S-wave velocities can only be caused by density changes, if the rigidity (shear modulus) of the sample remains unaffected by the fluid. As the bulk density of the sample (which is dependent on CO₂'s density) increases the S-wave velocities decreases due to the inversely proportional effect of bulk density to wave velocity. For P-waves, the changes to wave velocity are theoretically affected by the changes in both bulk modulus and bulk density of the sample. The effects of bulk modulus and bulk density on P-wave velocities oppose each other; a bulk modulus change will yield a directly proportional change to the wave velocity whereas a density change will

cause an inversely proportional change to wave velocity. From the observed and modelled results, the P-wave velocity decreases whenever the bulk modulus and bulk density of CO₂ are supposed to increase (due to increase in pore pressure or decrease in temperature, or going from a dry to CO₂ saturated state). Therefore the changes of CO₂'s density dominate those of the bulk modulus in contributing to the P-wave velocity. Furthermore, because S-waves velocity variations are only affected by the bulk density changes, the fact that all P-wave velocity variations mirror the S-wave variations under the same conditions also suggests the behaviour of P-wave velocities is largely controlled by the variation in the bulk density for the sample.

For the constant temperature runs, the wave responses (velocity and attenuation) to the gas to liquid phase transition are more immediate than the wave responses to the gas to supercritical fluid phase transition. Also as the temperature of the run increases, the levelling of the wave response from the large changes caused by the phase transition do not occur until a higher pore pressure. These responses are seen with laboratory observed results, Gassmann's modelled results, and Biot's modelled results. The immediate or gradual nature of the wave responses are related to the sharp or subdued contrast in the bulk modulus and density of the CO₂ when the phase transition boundaries are traversed. Because supercritical fluids have behaviours of both a gas and liquid, any transition from a gas or liquid will yield a smooth physical property change and consequently a smooth wave response. Furthermore, the different pore pressures where the large changes in wave responses begin to taper off are controlled by where the large changes to the density of CO₂ begins to level off. In figure 6.3 large changes to CO₂'s density are seen to occur at a higher pore pressure for a higher temperature run.

For both observed and modelled results, the P-and S-wave changes (of velocity and attenuation) are always greater for the gas-liquid phase transition than for the gas-supercritical or liquid-supercritical fluid transition, when comparing within constant temperature or constant pressure runs, respectively. The larger wave variation for the gas-liquid transition is also due to the same

reasoning above; supercritical fluids have behaviours of both a gas and a liquid. The absolute change in physical properties for the gas-supercritical or liquid-supercritical transition will always be less than the gas-liquid transition, therefore causing a smaller wave variation.

Furthermore, over the temperature and pressure conditions explored the phase transition between a gas and liquid phase or a gas and supercritical fluid phase is detectable from both P-and S-wave velocities and attenuation changes. Based on observed data, a sudden drop in velocity and large increase in attenuation is seen over the conditions close to when gas transitions into a liquid or supercritical fluid. However the phase transition between a liquid and a supercritical fluid phase state is not abrupt; there are no sudden wave changes. The undetectable liquid –supercritical phase change in wave velocities is a consequence of the more gradual CO₂ density change across this transition.

6.4.2 Water

Both the observed and modelled behaviour of the water saturated sample show a linear increase in P-wave velocities and shows a slight linear decrease in S-wave velocities. The smooth nature of the velocity variation seen is expected since water will not undergo any phase transition based on the applied conditions. From a pore pressure of 5 MPa to 50 MPa, according to NIST's online chemistry webBook the density of water increases from 999.8 kg/m³ to 1019.1 kg/m³, while the bulk modulus of water increases from 2.25 GPa to 2.52 GPa. Both the density and bulk modulus of water are greater than those for CO₂ over the pressure and temperature conditions investigated. The slight linear decrease of the S-wave velocities is due to the minor increase in water's density over the investigated pressure interval. For P-waves the increases in velocities with pressure suggests that the changes in the bulk modulus of water have a greater effect on influencing the overall wave velocity than the changes in fluid density. This is a behaviour that was not seen when the sample was saturated with CO₂. However similar to the behaviour under CO₂ saturation, both the observed and modelled results show that once water is introduced into the pore space, P-and S-waves velocity is

lowered significantly in comparison to the dry wave velocities in this highly porous material. The effect of the changes to the bulk density is greater than the effect of the changes to bulk modulus *only* as the sample goes from dry to water saturated. The reader should not take this as a general trend for all porous media as this will reverse in lower porosity materials.

The physical properties of the porous ceramic rod are not typical of real reservoir rocks. It should be remembered that the porous ceramic rod is highly porous. With a porosity greater than 58%, its high porosity have allowed the overall wave response to be more sensitive to the changes in the physical properties of CO₂ than a less porous sample would. Furthermore this synthetic sample contains a negligible amount of micro-cracks, which in a larger presence can complicate the acoustic behaviour of a sample as will shortly be seen in the next chapter. By using a sample with such physical properties, in addition to applying full CO₂ saturation, we have provided the possible wave behaviours for an extreme case of having CO₂ in the pore space. In the next chapter, a less extreme and a more realistic study on the CO₂ wave response is given.

6.5 Summary

Ultrasonic pulse transmission experiments were performed on the porous ceramic rod under dry, CO₂ saturated, and water saturated conditions. The P-and S-waveforms and the corresponding wave velocities of all three saturated states and the differential attenuation coefficient of just the CO₂ saturated state were presented for this sample. As a function of applied pressure the dry wave velocities of the porous ceramic rod showed little change. This behaviour with pressure provided further evidence, in conjunction to SEM images and mercury injection porosimetry results, indicating this material contains a lack of micro-cracks.

CO₂ saturated measurements were conducted for a variety of temperatures and pressures where the gas, liquid, and supercritical phase state of CO₂ were explored. Both the P-and S-wave velocities of the CO₂ saturated sample are always lower than the dry wave velocities. From all the observed wave velocity

changes, changes to the bulk density of the CO₂ saturated sample appear to be the controlling factor on the response of both P-and S- wave velocity. For the gas to liquid and gas to supercritical phase transition, significant drops in wave velocity and wave amplitude were observed. The porous ceramic rod displayed a wave velocity drop of 4-5% for both P-and S-waves. The differential attenuation coefficients showed a large increase over the phase transition interval and remained relatively constant thereafter. The wave changes related to the gas-liquid transition were always greater and more immediate than the gas-supercritical transition. The nature of the wave responses was reflective of the changes in CO₂'s physical properties. For the liquid to supercritical fluid phase transition, the waveforms showed minor and smooth wave velocity and wave amplitude increase. No signs of CO₂ phase transition could be detected from observing the waveforms due to the lack of distinct waveform changes. The observed smooth wave velocity change leading to an undetected liquid to supercritical phase transition is a consequence of the lack of significant CO₂ density change over the conditions investigated.

Fluid substitution using Gassmann's and Biot's equations were applied to the same CO₂ saturated conditions as conducted in the laboratory for this sample. Gassmann's modelled results show poor agreement with the observed wave velocities except at the low pore pressures. The agreement or disagreement between Gassmann's and the observed results could be understood through the critical frequency of the porous ceramic rod. Moreover the Biot's modelled wave velocities agreed well with the observed wave velocities and Biot's modelled differential attenuation coefficients agreed only qualitatively with the observed.

Water saturated measurements on the porous ceramic rod were only conducted as a function of pore pressure while under a constant differential pressure. Minor linear changes in wave velocities with pore pressure were observed. Similar to the CO₂ saturated results, the Biot's modelled wave velocities agree better than Gassmann's modelled velocities, however there is still a disagreement between modelled and observed wave velocities.

The good agreement between the observations and the Biot modeling suggests that the Biot theory reasonably predicts the wave behavior. Consequently, and perhaps paradoxically, this further suggest that the Gassmann's equations, that are the same as Biot's formulations at zero frequency, should describe the low frequency behavior of the sintered alumina.

Chapter 7

Results and Discussion: Natural Berea Sandstone

In the previous chapter, the results and discussion pertaining to a synthetic sample were given. Instead in this chapter the laboratory results, the modeling, and a discussion on the Berea sandstone are given. Similarly, the P-and S-waveforms, the determined wave velocities, and their comparison to modelled velocities will be given for all three states: dry, CO₂ saturated, and water saturated. The laboratory results and the modelled predictions of the differential attenuation coefficient will be given for only the CO₂ saturated measurements.

The methodology behind signal acquisition, wave velocity and attenuation analysis, and fluid substitution modeling applied to the Berea sandstone are the same as applied to the porous ceramic rod. The natural Berea sandstone is petrophysically quite different from the porous ceramic rod. The Berea sandstone is two-thirds less porous and contains micro-cracks (refer to chapter 5's observations). In comparison to the porous ceramic rod, this sample provides a more realistic study for geological sequestration.

7.1 Dry

P-and S-waveforms were obtained of the Berea sandstone under dry (i.e. vacuum in the pore space) conditions at room temperature (T = 23°C) while the confining pressure varied between 5 to 40 MPa. Both pressurization and depressurization were applied to the sample over this pressure interval.

7.1.1 Dry Waveforms

The full set of normalized P-and S-waveforms displayed as coloured amplitudes are shown in figure 7.1. The signals are normalized with respect to the largest amplitude within the given set of waveforms. In contrast to the waveform plots of the porous ceramic rod subject to the same conditions (figure 6.1), the Berea sandstone displays remarkable nonlinear changes in travel times with pressure as has been seen by many authors in the past (e.g. Christensen and Wang, 1985). In addition, a slight asymmetry of the wave arrivals is apparent especially in the S-wave plot; the waves arrive earlier during the depressurization cycle than the pressurization cycle for the same pressure.

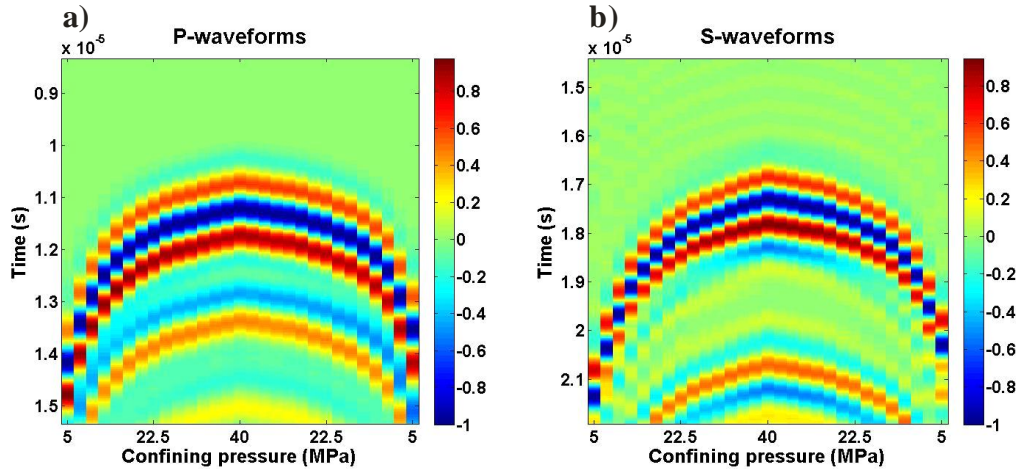


Figure 7.1: Normalized P- wave (a) and S-wave (b) waveforms obtained under dry conditions at room temperature plotted as a function of confining pressure as coloured amplitudes for the Berea sandstone.

7.1.2 Dry Wave Velocities

The P-and S-wave velocities with error of the waveforms obtained under dry conditions are shown in figure 7.2. Both P-and S- wave velocities exhibit a nonlinear increase with pressure. The wave velocities increase rapidly at low pressures that taper off with higher pressures. This behavioural increase is caused by the progressive closure of compliant pores where most of the compliant pores will close at low pressures, therefore causing a rapid velocity increase. The velocity increase diminishes at higher pressure because as the applied pressure increases, the amount of compliant pores available for collapse reduces.

Furthermore from the velocity plots the wave velocities obtained during depressurization are always higher than the velocities taken during pressurization, thereby demonstrating wave velocity hysteresis.

Due to the cracked nature of the Berea sandstone, its pressure dependent behaviour differs from that of the porous ceramic rod. The Berea sandstone exhibits large velocity variations with pressure and large velocity hysteresis in comparison to the synthetic sample where the presence of micro-cracks is minimal.

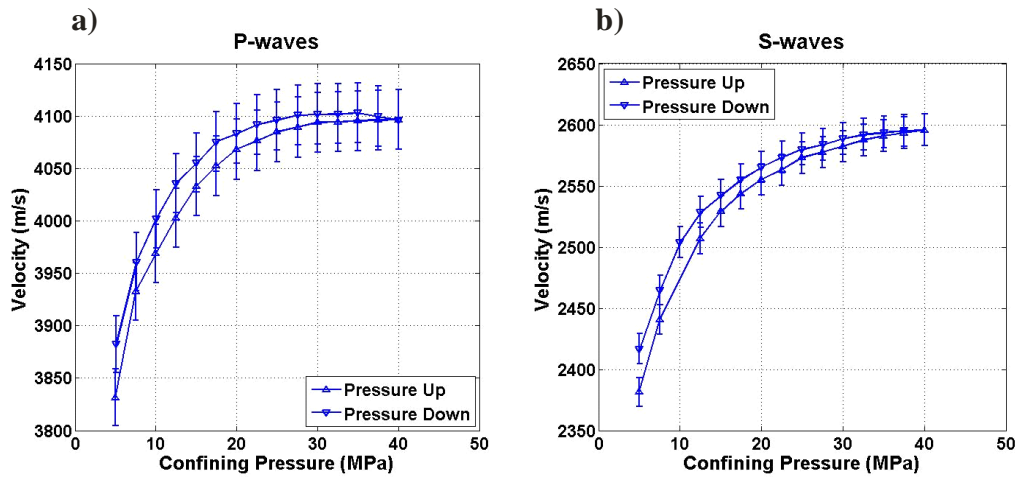


Figure 7.2: Dry P-and S-wave velocities with their respective errors as a function of confining pressure for the Berea sandstone.

7.2 CO₂

For the Berea sandstone, five constant temperature runs and three constant pore pressure runs were conducted. The measurement conditions applied to the CO₂ saturated sample are shown in figure 7.3. Each measurement run conducted is expected to cross a phase boundary. Constant temperature runs were conducted at 23°C, 28°C, 40°C, 45°C, and 55°C while pore pressure varied from 2 to 25 MPa. CO₂ is a gas at low pore pressures and is a liquid or a supercritical fluid at higher pore pressures depending on the temperature. Constant pressure runs were conducted at a pore pressure of 7 MPa, 10 MPa, and 25 MPa while temperature varied from 23°C to around 50°C. For each of the three constant pressure (pore, confining, or differential) runs, CO₂ is a liquid state at low temperatures. As

temperature increases CO_2 eventually transforms into a gaseous or a supercritical fluid state, depending on the pore pressure as shown in figure 7.3. Similar to the porous ceramic rod, during all CO_2 saturated measurements a constant differential pressure of 15 MPa was maintained for each measurement run so that any waveform variation observed is solely caused by pore fluid effects. Maintaining a constant differential pressure during CO_2 measurements for the Berea sandstone is especially important since the wave behaviours of this sample display strong pressure dependence.

To avoid redundancy, only the most representative measurement runs for this sample are shown here. Therefore for the constant temperature runs, only the waveforms and differential attenuation coefficient of $T = 23^\circ\text{C}$ and $T = 55^\circ\text{C}$ run are shown. The laboratory results for $T = 28^\circ\text{C}$, $T = 40^\circ\text{C}$, and $T = 45^\circ\text{C}$ measurement runs are available in the appendix.

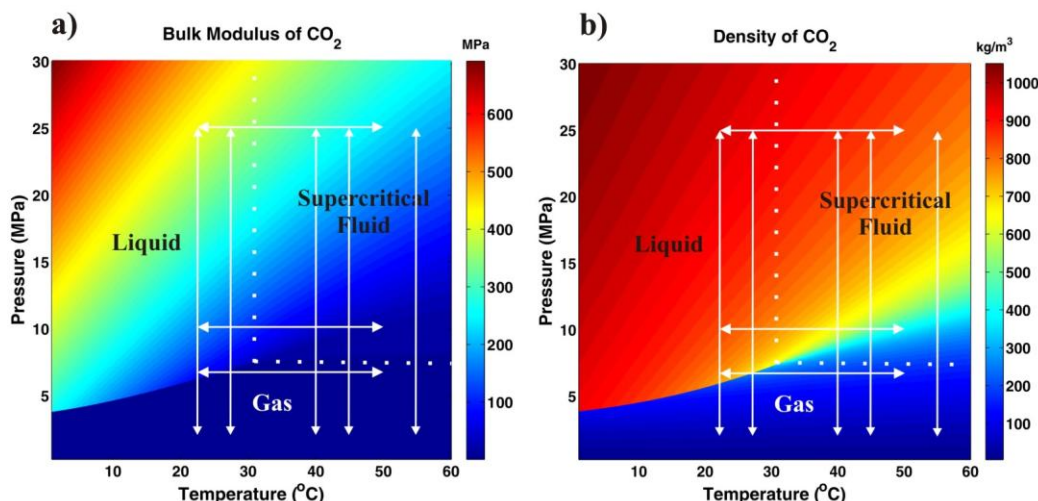


Figure 7.3: Phase diagrams of CO_2 's: (a) bulk modulus (b) and density. The temperature and pressure conditions applied to the CO_2 saturated Berea sandstone during ultrasonic pulse transmission measurements are shown by the white arrows.

7.2.1 CO_2 Saturated Waveforms

Figure 7.4 shows the P-and S-waveforms as a function of pore pressure for the lowest and highest temperature run, $T = 23^\circ\text{C}$ and $T = 55^\circ\text{C}$ respectively. In general, as pore pressure increases the signals arrive later and within a given plot, two arrival trends can be seen. Furthermore, the waveforms' signal strength

shows a slight decrease near the anticipated phase transition. For the lower temperature run ($T = 23^{\circ}\text{C}$), the elastic wave response to CO_2 's phase transition is sharp and significant. In contrast, the elastic wave responses of the higher temperature run ($T = 55^{\circ}\text{C}$) to CO_2 's phase transition are gentle and lack any abrupt change.

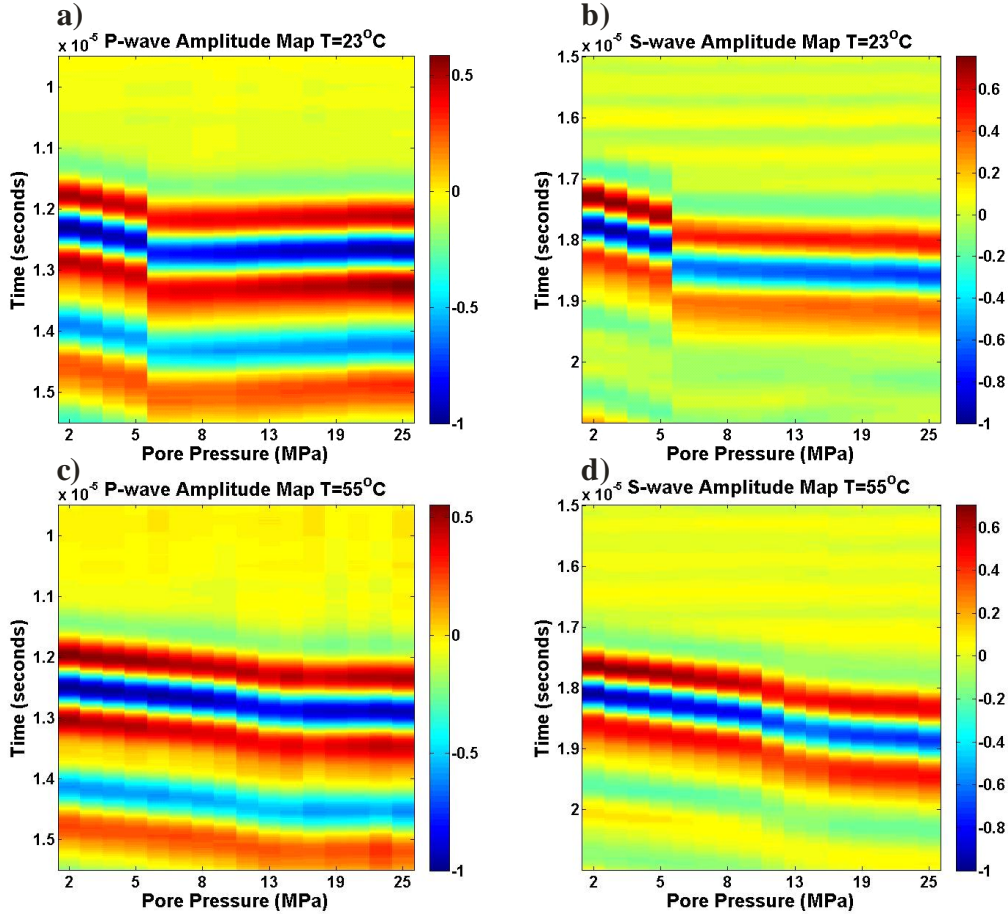


Figure 7.4: Normalized P- and S-wave waveforms as a function of pore pressures collected during the constant temperature runs of a) and b) $T = 23^{\circ}\text{C}$ and, c) and d) $T = 55^{\circ}\text{C}$. A constant differential pressure of 15 MPa was maintained throughout each measurement run.

Figure 7.5 displays the P-and S-waveforms as a function of temperature from 23°C to 50°C for all three measurement runs. The P-and S-waveform plot of $P_p = 7$ MPa exhibits a sharp change with the signals arriving earlier and stronger at higher temperatures than lower temperatures. Away from the transition, both P-and S-waveforms do not noticeably change. For both the $P_p =$

10 MPa and $P_P = 25$ MPa P-and S-waveform plots, no sharp or large changes to the waveforms occur. For the $P_P = 10$ MPa waveform plots, both travel times and signal strengths seem constant over the entire temperature range. For the $P_P = 25$ MPa waveform plots no obvious signal strength changes are seen, however the signals do arrive later with increasing temperature.

7.2.2 Observed CO₂ Saturated Wave Velocity

The P- and S-wave velocities with their estimated errors for all five constant temperature runs, and the dry wave velocities obtained at a confining pressure of 15 MPa plotted at $P_P = 0$ MPa are shown in figure 7.6. Unlike that seen before for the porous ceramic rod, the distribution of the five measurement runs with respect of each other is somewhat scattered with no reasonable relations.

Both the P-and S-wave velocities obtained under dry conditions are slower than those obtained when the sample is saturated with gaseous CO₂. For the P-wave, this response is hard to validate quickly since both bulk modulus and bulk density can affect the wave velocity and in opposite manners. However for the S-wave, the response is not expected because the change in S-wave velocity should only be affected by changes in bulk density (equation 3.20), which increases from a dry to a saturated state and has an inverse effect on velocity, if the integrity of the sample is assumed to be unchanged. Instead seen here, the dry S-wave velocity is lower than all the saturated S-wave velocities at under low pore pressures. This indicates that the material property of the sample has changed in between the measurement runs.

Further evidence for a substantial change in the properties of the Berea sandstone is found once the velocities under dry conditions are repeated. The dry wave velocity shown in figure 7.6 was obtained prior to all the CO₂ saturated measurements. A second set of dry measurements was conducted after all the CO₂ saturated measurements and the resulting wave velocities are significantly higher at all confining pressures than the initial set, see figure 7.7. The greatest

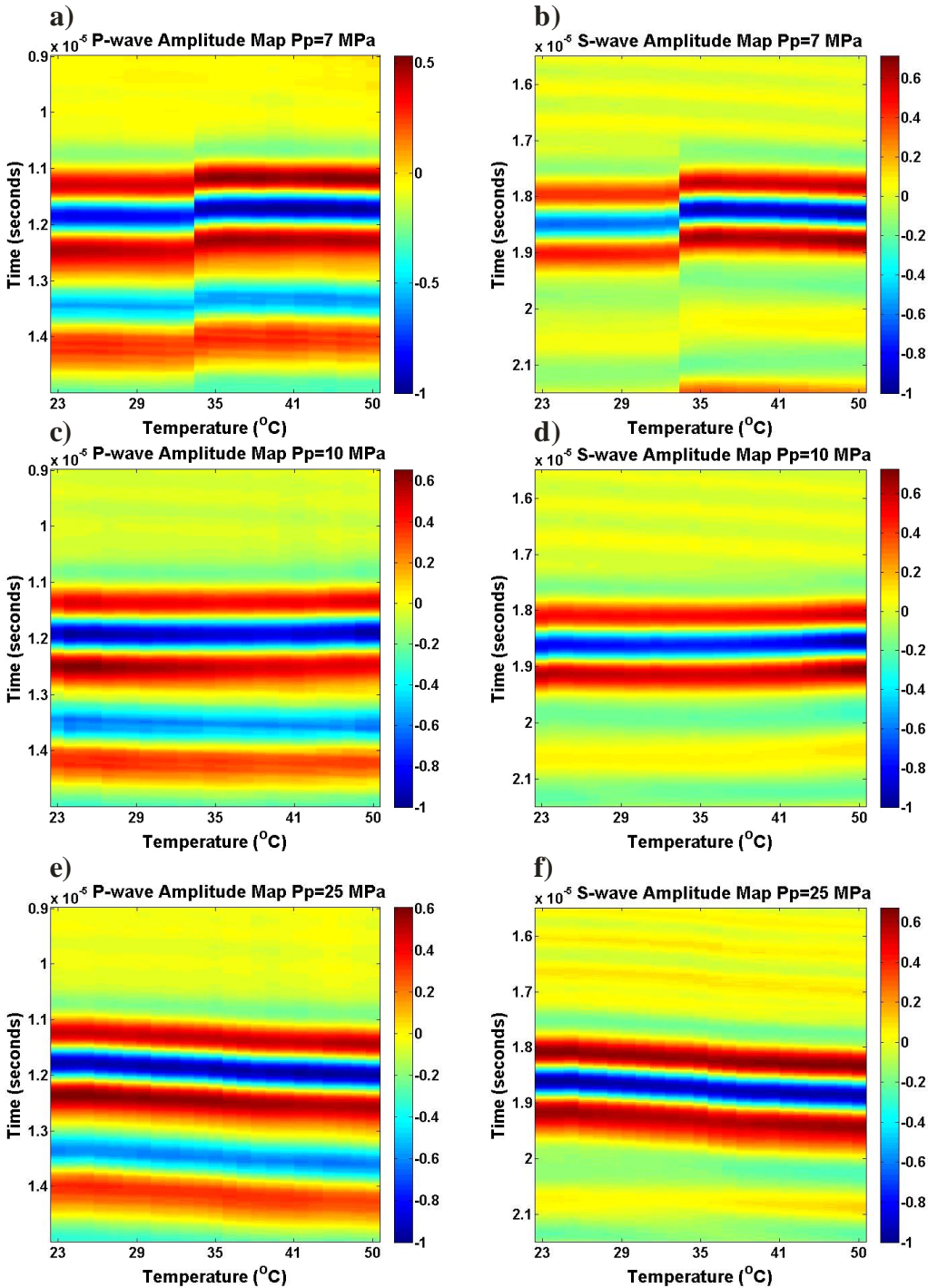


Figure 7.5: Normalized P- and S-wave waveforms as a function of temperature collected during the constant pore pressure runs of a) and b) $P_p = 7 \text{ MPa}$, c) and d) $P_p = 10 \text{ MPa}$ and e) and f) $P_p = 25 \text{ MPa}$. A constant differential pressure of 15 MPa was maintained throughout each measurement run.

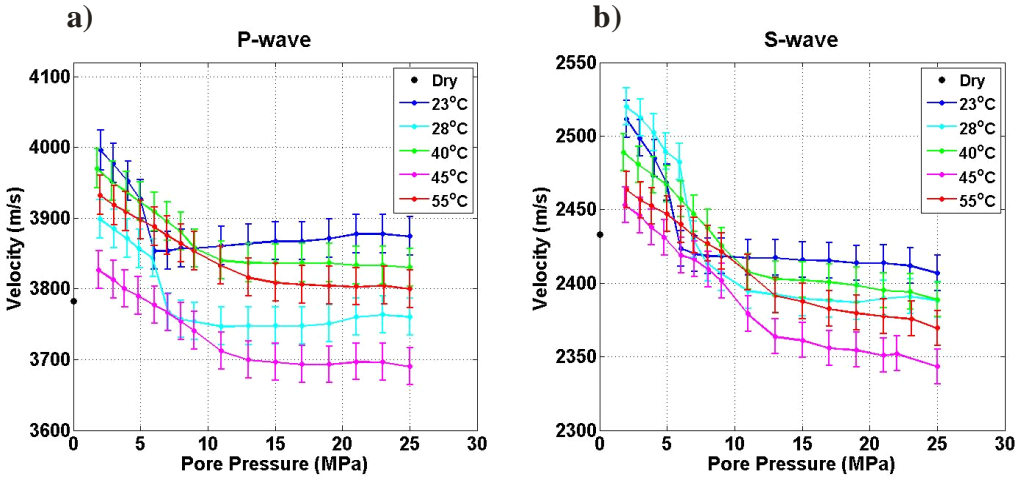


Figure 7.6: Ultrasonic P-wave (a) and S-wave (b) velocities with their respective errors measured of the Berea sandstone saturated with CO₂ for all constant temperature runs and when the sample is not saturated (black dot at P_p = 0 MPa).

difference in wave velocities occurs at low confining pressures and the velocity difference lessens with increasing confining pressure. The second set of dry wave velocities show a smaller nonlinear increase of wave velocities with pressure and displays smaller velocity hysteresis between the pressurization and depressurization cycle. These observed differences between the two dry measurement runs suggest sample consolidation, the permanent change in physical properties of the material under pressure due to the irreversible closure of micro-cracks. Sample consolidation would cause the sample undergoing the second dry measurement run to contain less collapsible pores with respect to the first dry measurement run.

In order to obtain a reasonable relation between the different measurement runs, the absolute velocities were corrected with respect of each other by considering the change to the nature of the sample. CO₂ saturated measurements for each run were also conducted at a pore pressure of 1 MPa. It is assumed that at this low pore pressure the amount of influence from the pore fluid on the overall sample behaviour is minor so if the integrity of the sample has not changed, all wave velocities at 1 MPa would be about the same. Using the wave velocity of the T = 23°C as the reference velocity, the difference in wave velocities from all constant measurement runs were determined at 1 MPa and then

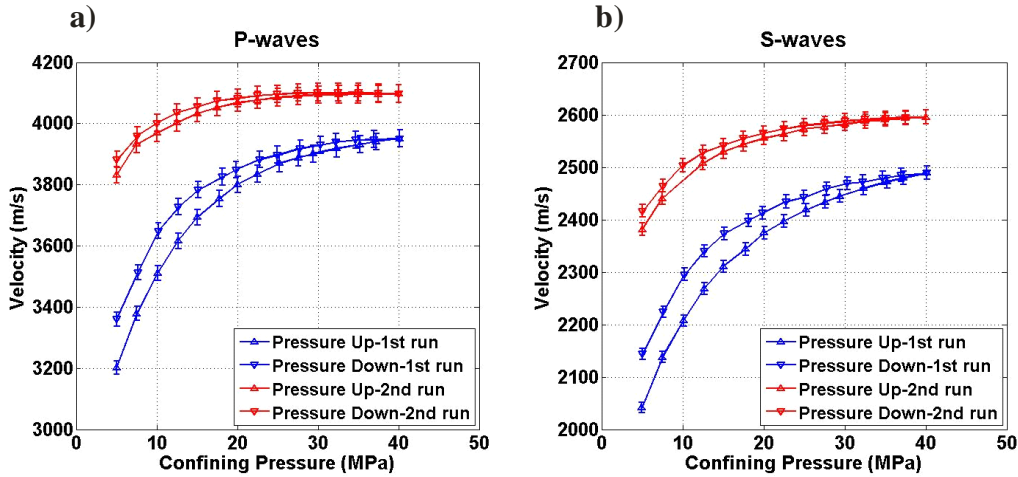


Figure 7.7: P-wave (a) and S-wave (b) velocities with their respective errors as a function of confining pressure for the two dry measurement runs of Berea sandstone at room temperature, conducted before and after the series of CO_2 saturated measurements.

applied to the rest of the wave velocities of their respective measurement runs. Figure 7.8 shows the wave velocities after applying the velocity corrections. The dry wave velocity shown at $P_p = 0$ MPa is the velocity determined from the second set of dry measurements. The reasonability of the five measurement runs' distribution in relation to each other and the dry wave velocity has improved.

Similar to that seen with porous ceramic rod, with CO_2 in the pore space irrespective of the phase state, both the new P-and S-wave velocities are lower than the dry wave velocities. In addition, the new distribution of the five measurement runs displays a positive trend with temperature, if their errors are considered. At a given pore pressure, as the temperature of the run increases the wave velocity of the run also increases. This observation generally holds except for the S-waves of the $T = 28^\circ\text{C}$ run at high pore pressures, where some of the velocities are below the velocities obtained at $T = 23^\circ\text{C}$. For P-waves, a similar discrepancy is also seen, however the discrepancy is still within error. This disagreement of wave velocities could be attributed to the deterioration of one of the transducers. The day after conducting the $T = 28^\circ\text{C}$ measurement run, it was determined that one of the transducers has failed where S-waves could not be transmitted. Therefore the data for the $T = 28^\circ\text{C}$ measurement run should be interpreted with caution.

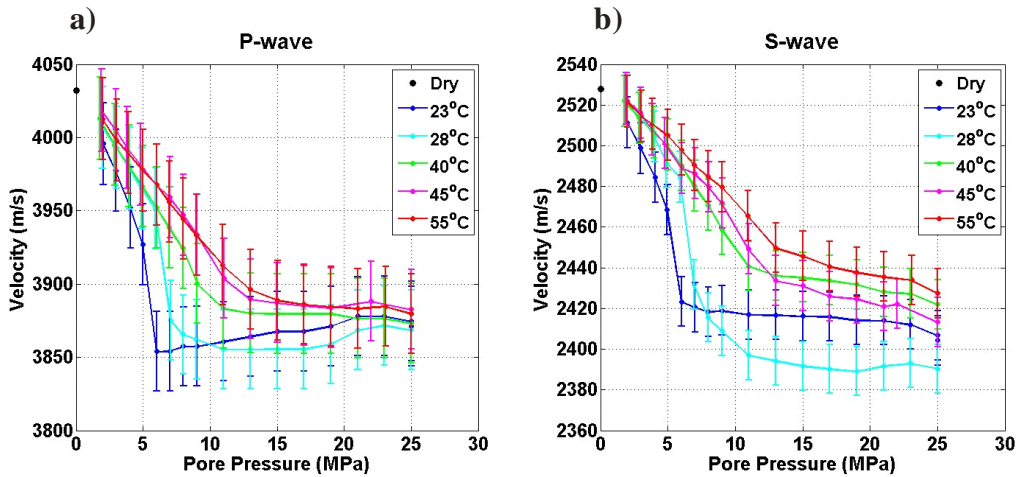


Figure 7.8: The corrected ultrasonic P-wave (a) and S-wave (b) velocities of the Berea sandstone saturated with CO_2 for all constant temperature runs.

Furthermore, as pore pressure increases, the wave velocities generally decrease with the exception of P-waves at high pore pressures of the two lower temperature runs, which display velocity increase with increasing pore pressure. The phase transition out of the gaseous state is clear for the two lower temperature runs where an immediate and large drop in wave velocities occurs near their respective vapour pressure (the pressure that marks the transition between a gas and a liquid for a given temperature). The drop in wave velocity right before and after the phase transition for $T = 23^\circ\text{C}$ run for both P-wave and S-wave is 1.8%. Over the entire investigated pore pressure interval the drop in overall wave velocity is 3.0% and 4.2% for P-and S-wave respectively. In contrast, the phase transition for the three higher temperature runs is less obvious with the wave velocities displaying a very gradual response. The exact occurrence of the phase transition cannot be identified from the velocity plot. Therefore the amount of velocity change can only be reported over the entire investigated pore pressure interval. From a pore pressure of 2 to 25 MPa, the P-wave velocities dropped 3.3% for the $T = 55^\circ\text{C}$ run and the S-wave velocities dropped 3.8%. The overall P-wave velocity change for the $T = 55^\circ\text{C}$ is greater than the $T = 23^\circ\text{C}$ because the P-wave velocities of the $T = 23^\circ\text{C}$ actually recovers after the large drop.

The three constant pore pressure measurement runs, are also affected by the varying nature of the sample due to consolidation. Unlike the constant temperature measurements, for the conditions applied to the three constant pore pressure runs there are no similar pore fluid physical properties which would have allowed similar corrections of the constant temperature runs to be employed. However, from reviewing figure 7.3 of the various conditions applied to the Berea sandstone, all three constant pore pressures do have points of overlap with four constant temperature measurements. Therefore all the wave velocities of the constant pore pressure measurements were corrected so that the wave velocities obtained under the same conditions as the constant temperature run of $T = 23^{\circ}\text{C}$ are the same.

Figure 7.9 shows the corrected P-and S-wave velocities with their errors for the three constant pore pressure runs along with the dry wave velocity obtained under a confining pressure of 15 MPa from the second set of dry measurements plotted at $T = 23^{\circ}\text{C}$. Similarly to above, with CO_2 in the pore space the wave velocities are lower with respect of the dry wave velocity. The CO_2 phase transition of the $P_p = 7 \text{ MPa}$ run from liquid to gas is evident from an obvious increase in wave velocity of 1.1% for both P-and S-wave velocities. Over the entire investigated temperature interval an overall increase of 1.0% and 0.8% for P-and S-wave, respectively is seen. For the $P_p = 10 \text{ MPa}$ and $P_p = 25 \text{ MPa}$ the phase transition is not apparent at all; the wave velocities variations are smooth and there are no changes to the velocity trend. The $P_p = 10 \text{ MPa}$ run exhibits a 0.2% overall increase with temperature for both P-wave and S-wave velocity. In contrast, the $P_p = 25 \text{ MPa}$ run exhibits a decrease in both P-and S-wave velocities with increasing temperatures; P-waves show an overall decrease of 1.7% in velocity and S-waves show an overall decrease of 1.3% in velocity.

7.2.3 Modelled CO_2 Saturated Wave Velocity

Here, the observed results for the CO_2 saturated Berea sandstone are

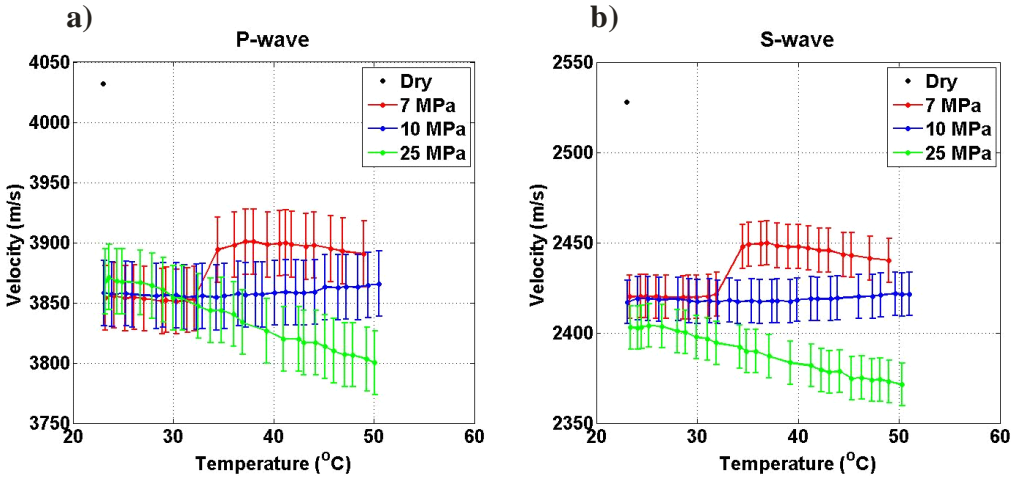


Figure 7.9: The corrected ultrasonic P- wave (a) and S-wave (b) velocities of the Berea sandstone saturated with CO_2 for all constant pore pressure runs.

compared to modelled results computed from Gassmann and Biot's formulations over the same pressure and temperature conditions. To compute the models, the series of parameters required as inputs were obtained from the same sources or by the same methods as mentioned for the porous ceramic rod. However unlike the porous ceramic rod, for the Berea sandstone the temperature dependency of the frame is not included in the modeling results. This correction was not needed as all the observed velocities shown in figure 7.8 were already corrected with respect to the $T = 23^{\circ}\text{C}$ data, thereby eliminating the temperature dependence of the frame in the observed velocities.

Gassmann Model

Using equation 3.29 and 3.31 the Gassmann's modelled P-and S-wave velocities of the CO_2 saturated Berea sandstone was calculated. Figure 7.10 shows the modelled and the observed P-and S-wave velocities under CO_2 saturation for the constant temperature runs of $T = 23^{\circ}\text{C}$ and the $T = 55^{\circ}\text{C}$. The rest of the modelled constant temperature run results can be found in the appendix. Unexpectedly slight agreements can be seen between some observed and modelled results, such as at low pore pressures of the $T = 55^{\circ}\text{C}$ for both P-and S-waves. Also, the amount of change in wave velocity with changing pore pressure is somewhat comparable between the two results for both P-and S-waves

and for both the low and high temperature runs. For $T = 23^{\circ}\text{C}$, over the phase transition Gassmann predicts a 2.5% and 2.7% drop in P-and S-wave velocity, respectively and an overall drop of 2.9% and 3.8% for P-and S-wave velocity, respectively. For $T = 55^{\circ}\text{C}$, Gassmann predicts an overall drop of 2.8% and 3.2% drop in P-and S-wave velocity. Strangely, when there is a disagreement between results, Gassmann's modelled wave velocities are always greater than the observed wave velocities. The largest discrepancy between modelled and observed results is 2.0% and 1.8% for P-and S-wave respectively. Furthermore for the $T = 23^{\circ}\text{C}$ results the observed P-wave's velocity curve overall tends to have a greater slope than the modelled velocity curve. For S-waves this only occurs at lower pressures before the phase transition. For the $T = 55^{\circ}\text{C}$ results for both P-and S-waves the shape of the observed and modelled velocity curves follow each other quite well.

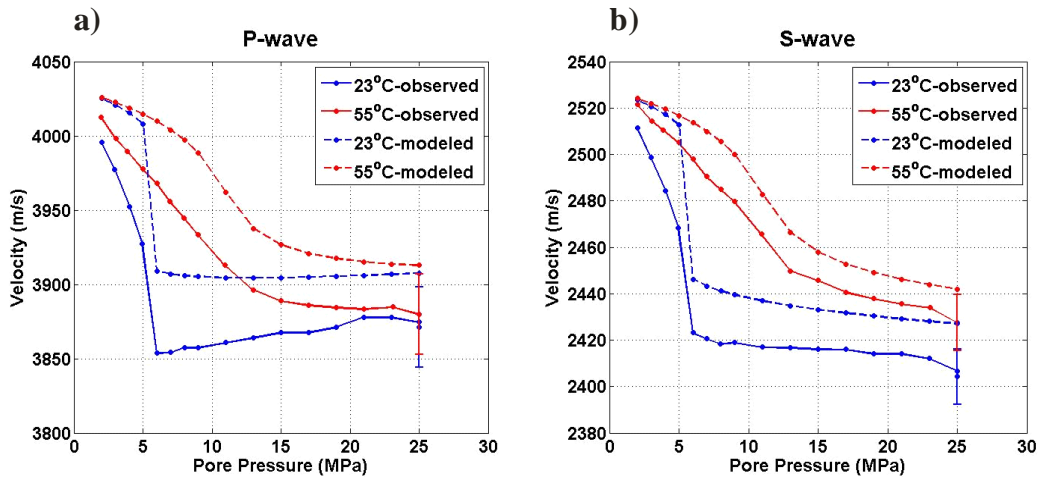


Figure 7.10: Observed and Gassmann's modelled P- wave (a) and S-wave (b) CO_2 saturated velocities for $T = 23^{\circ}\text{C}$ and $T = 55^{\circ}\text{C}$ constant temperature runs. To avoid clustering, only the error at a pore pressure of 25 MPa are shown. The errors at all other data points are approximately the same size.

Figure 7.11 displays the modelled and observed P-and S-wave velocities under CO_2 saturation for all three constant pore pressure runs. None of the observed and modelled results are in agreement with each other, where Gassmann's modelled results are always higher than the observed. As the temperature increases, the discrepancy between observed and modelled results

increases. Starting with $P_p = 7$ MPa, similar to that seen with the porous ceramic rod, the observed results have a lagged temperature response to the occurrence of the liquid to gas phase transition. The phase transition theoretically should occur around 29 °C while the observed results do not show a transition until after 33 °C. Possible reasons for this discrepancy were provided in section 6.2.2. Similar to the constant temperature runs, the amount of change in wave velocity in response to the phase transition is roughly comparable between the observed and modelled results for both P- and S-waves; Gassmann's predicts a 1.5% and 1.6% P-and S-wave velocity increase. Over the entire temperature interval, a 2.4% and a 2.6% overall increase is predicted. Aside from the region close around the phase transition, the largest discrepancy between the results is 2.8% for both P-and S-waves. Also there is a discrepancy on the slope of the velocity curves; away from the phase transition at both low and high temperatures, the observed velocity curve has a negative slope while the modelled shows a positive slope.

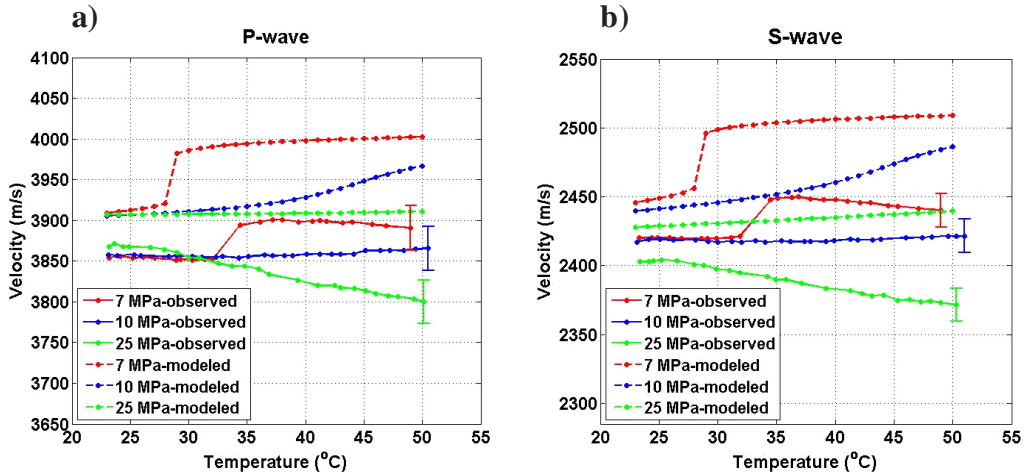


Figure 7.11: Observed and Gassmann's modeled P-wave (a) and S-wave (b) CO_2 saturated velocities for $P_p = 7$ MPa, $P_p = 10$ MPa, and $P_p = 25$ MPa constant pore pressure runs. To avoid clustering, only the error at the highest temperature in each run is shown. The errors at all other data points are approximately the same size.

For both the $P_p = 10$ MPa and $P_p = 25$ MPa runs, the modelled results show no sudden changes in wave velocities in response to the anticipated liquid to supercritical phase transition. For the $P_p = 10$ MPa results, the largest velocity discrepancy is 2.6% for both P-and S-waves. For this constant pore pressure run,

both the modelled and observed velocity curves have positive slopes, except the observed results' slope is much slighter. Over the entire temperature interval, Gassmann's model predicts a 1.5% P-wave velocity change and a 2.1% S-wave velocity change while observed results show only a 0.2% velocity change for both P-wave and S-waves. For the $P_p = 25$ MPa results, the largest discrepancy is 2.9% for both P-and S-waves. Similar to $P_p = 7$ MPa results the velocity curves of the observed and modelled results slope in opposite directions; observed results slopes negatively while modelled results slopes positively but gently, with temperature. Over the entire temperature interval the modelled results show less than 0.1% increase in P-wave velocity and a 0.5% increase in S-wave velocity while the observed results show a 1.7% and 1.3% decrease in P-and S-wave velocity, respectively.

Biot Model

Even though Gassmann formulation deals with wave frequencies that are much lower than the wave frequencies dealt with in the laboratory, surprisingly Gassmann's prediction sometimes agrees with the observed results (the constant temperature runs). Also, where there is a poor agreement in this study for the Berea sandstone, Gassmann's modelled results are usually higher than the observed results. Therefore if Biot's formulation is applied even higher wave velocities would result from the modelling. However Gassmann's theory, unlike Biot's theory, does not provide a description for wave attenuation which is present in our data. Therefore, for the completeness of applying Biot's model, here Biot's modelled wave velocity is still computed and compared for the Berea sandstone.

Biot's modelled P-and S-wave velocities of the CO_2 saturated Berea sandstone of the constant temperature and constant pore pressure runs are displayed in figure 7.12 and 7.13, respectively. All of Biot's modelled velocity curves show the same behaviour trends and variation with changing pore pressure or temperatures as that shown by Gassmann's modelled results. As expected, the modelled velocities are all higher than the observed velocities. Apart from the results at low pore pressures of the $T = 55^\circ\text{C}$ constant temperature run, all other

modelled and observed results are not in agreement. The majority of the discrepancies are greater than 2.0%.

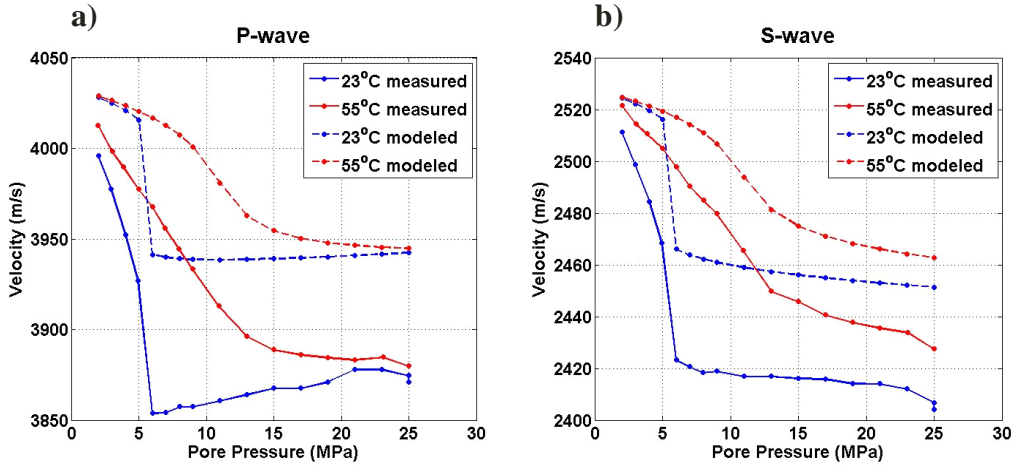


Figure 7.12: Biot's modelled and observed P- wave (a) and S-wave (b) CO_2 saturated velocities for $T = 23^\circ\text{C}$ and $T = 55^\circ\text{C}$ constant temperature runs. No error bars are shown, however the size of errors can be referred to in figure 7.8 and 7.10.

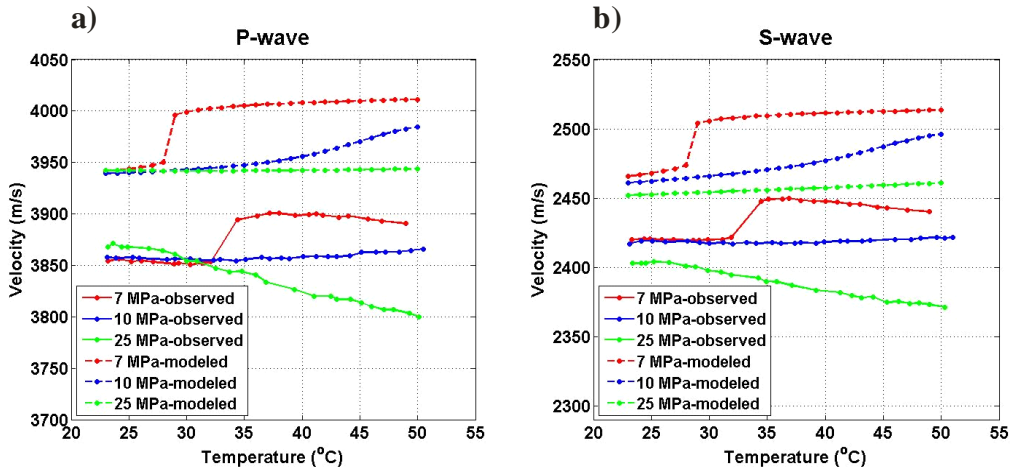


Figure 7.13: Biot's modelled and observed P-wave (a) and S-wave (b) CO_2 saturated velocities for $P_p = 7 \text{ MPa}$, $P_p = 10 \text{ MPa}$, and $P_p = 25 \text{ MPa}$ constant pore pressure runs. No error bars are shown, however the size of errors can be referred to in figure 7.9 and 7.11.

7.2.4 Observed CO_2 Saturated Wave Attenuation

As with the porous ceramic rod, the attenuation of the acquired waveforms of the Berea sandstone was studied by determining the differential attenuation coefficient as described in section 4.5.2. For all CO_2 saturated measurements, the differential attenuation coefficient of each waveform was determined with respect

to the waveform acquired at 2 MPa and 23°C. Unlike that of the porous ceramic rod, the waveform acquired at 2 MPa and 23°C does not have the greatest signal strength of all the measurement runs, especially for the S-wave. However it was still used as the reference signal for the purpose of maintaining procedural consistency with the analysis conducted for the porous ceramic rod.

Figure 7.14 display the differential attenuation coefficient for P-and S-waves for the two constant temperature runs, $T = 23^\circ\text{C}$ and $T = 55^\circ\text{C}$, as a function of pore pressure and of frequency. For the lower temperature run, the phase transition from gas to liquid is met by a sudden increase in attenuation and is especially obvious at the higher frequencies. For the higher temperature run, the phase change from gas to supercritical fluid is also marked by an increase in attenuation, and is again more pronounced at higher frequencies. In contrast to the lower temperature run, the large change in differential attenuation coefficients is less drastic. Also, large changes to attenuation do not begin until well after the critical pressure.

From examining these differential attenuation plots some general behaviour can be established for both P-and S-waves. First, wave attenuation is usually lower in the gaseous phase (low pore pressures) than the liquid phase or supercritical fluid phase (higher pore pressures). Second, wave attenuation is the greatest immediately after the phase transition into the liquid or supercritical phase state but then lessens with increasing pore pressure. Third, wave attenuation increases as the frequency increases. Four, S-waves attenuate more than P-waves. However when comparing the low and the high temperature run to each other at the same conditions, for both P- and S-waves the attenuation of the $T = 23^\circ\text{C}$ is usually higher than the $T = 55^\circ\text{C}$.

On the color bar index, the scale sometimes indicates negative differential attenuation coefficient values. This is because the reference signal is not the strongest signal of all measurement runs. In addition, for the $T = 23^\circ\text{C}$ run even though the reference signal is the strongest signal of the entire run, however the amplitude spectrum of the reference signal is not consistently the greatest for all frequencies.

Figure 7.15 displays the differential attenuation coefficient for P-and S-wave for the three constant pressure runs, with pore pressure at 7 MPa, 10 MPa, and 25 MPa as a function of temperature and frequency. The character of both the P-and S-waves of the $P_p = 7$ MPa plot is much different than the other two

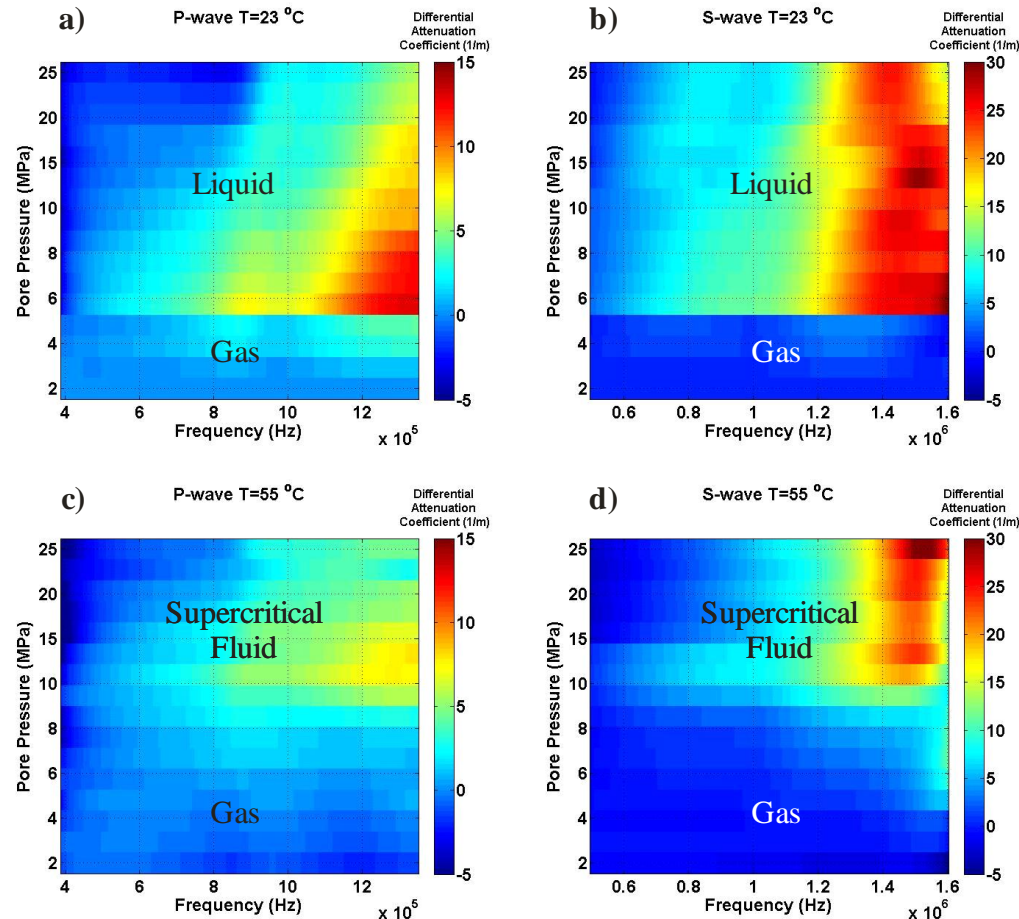


Figure 7.14: Observed P- and S-wave differential attenuation coefficient determined for a) and b) $T = 23^\circ \text{ C}$, and c) and d) $T = 55^\circ \text{ C}$ constant temperature runs as a function of frequency and pore pressure. The expected CO_2 phase state is indicated at the appropriate physical conditions.

constant pressure plots by displaying a sharp change in wave attenuation in response to the liquid to gas phase transition. The wave attenuation peaks near the phase transition and then decreases with increasing temperature thereafter. For the other two constant pressure plots there are no significant changes in attenuation with respect to the phase transition. The P-and S-wave $P_p = 10$ MPa

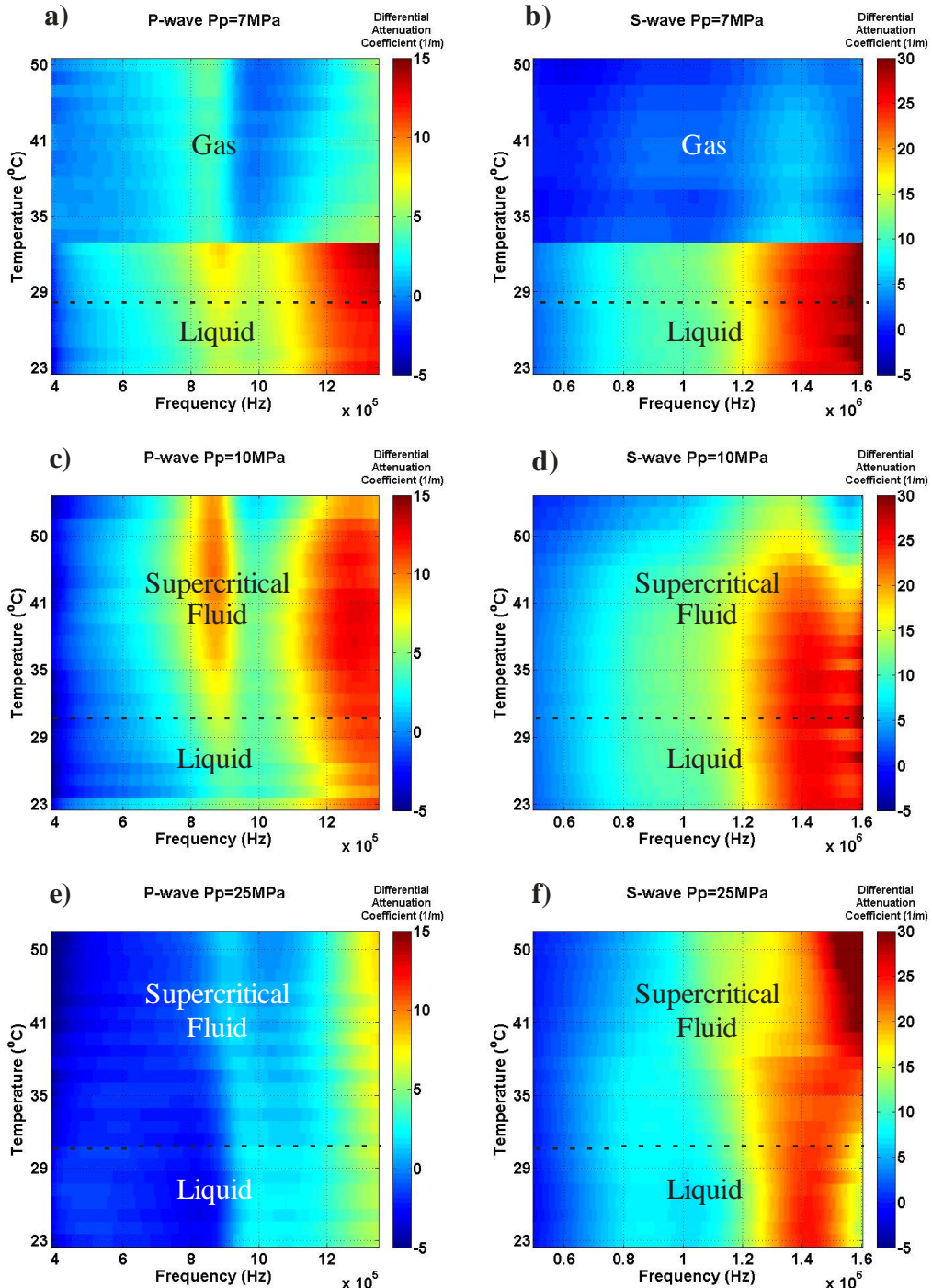


Figure 7.15: Observed P- and S-wave differential attenuation coefficient determined for a) and b) $P_p = 7 \text{ MPa}$, c) and d) $P_p = 10 \text{ MPa}$, and e) and f) $P_p = 25 \text{ MPa}$ constant temperature runs as a function of frequency and pore pressure. The expected CO_2 phase state is indicated at the appropriate physical conditions. The black dashed-line indicates where the phase transitions are supposed to occur.

plots also shows an attenuation peak, the attenuation increases with increasing temperature and then also decreases with increasing temperature, but without any sudden changes between these two trends. For the $P_p = 25$ MPa P-and S-wave plots, with increasing temperature there is no peak in attenuation. Generally in all three constant pore pressure runs, wave attenuation is higher for the higher frequencies and the S-wave attenuation is usually greater than P-wave attenuation. When comparing the three constant pore pressure runs with one another, no single general attenuation trend can be established. At low temperatures, it appears the lower the pore pressure is for the run, the higher the attenuation. At high temperatures, the $P_p = 7$ MPa run shows the lowest attenuation, the $P_p = 10$ MPa run shows the highest attenuation while the $P_p = 25$ MPa run is in between. However this observed complex trend between the different pore pressure runs is consistent with the attenuation trends observed from the constant temperature runs; wave attenuation do not vary only positively with pore pressure but instead varies positively and then negatively with pore pressure where the attenuation peaks near the phase transition.

7.2.5 Modelled CO₂ Saturated Wave Attenuation

The computed P-and S-wave differential attenuation coefficient of the two constant temperature runs, $T = 23^\circ\text{C}$ and $T = 55^\circ\text{C}$, as a function of temperature and frequency are shown in figure 7.16. Biot's modelled results do show a significant increase in attenuation in response to the phase transition of gas to liquid or gas to supercritical fluid around similar pore pressures of that seen with our observed results. However the peak in attenuation after the phase transition and its gradual decline with increasing pore pressures seen in the observed data is not modelled. Instead, Biot's modelled results shows a consistent increase in wave attenuation as pore pressure increases for all frequencies. Furthermore, a consistent increase in wave attenuation is also modelled with increasing frequencies for all pore pressures. This attenuation trend with frequency agrees with our observed attenuation results, although our observed results do show more variability. Also similar to our observed results, Biot's model shows that S-wave

attenuation is greater than P-wave attenuation under the same condition. Comparing the modelled P-and S-wave attenuation of the $T = 23^{\circ}\text{C}$ to $T = 55^{\circ}\text{C}$, the attenuation of $T = 23^{\circ}\text{C}$ runs is always greater than the attenuation of $T = 55^{\circ}\text{C}$. This is only consistent with the P-waves and not with the S-waves of the observed results. Also dissimilar is the magnitude of the differential attenuation coefficient values; the Biot modelled results are 2 orders of magnitude lower than the observed results.

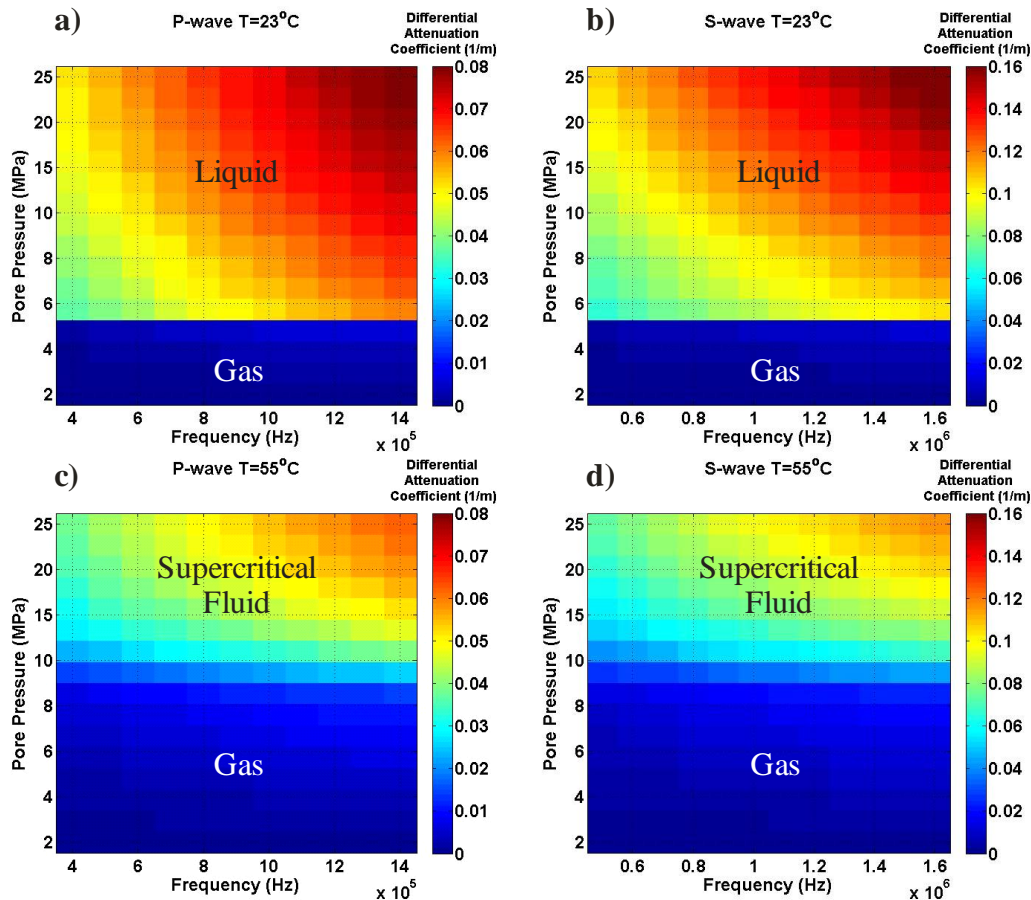


Figure 7.16: Biot's modelled P- and S-wave differential attenuation coefficient determined for a) and b) $T = 23^{\circ}\text{C}$, and c) and d) $T = 55^{\circ}\text{C}$ constant temperature runs as a function of frequency and pore pressure. The prevailing CO_2 phase state is indicated at the appropriate physical conditions.

Figure 7.17 shows the computed differential attenuation coefficient from Biot's model for the three constant pore pressure runs, as a function of temperature and frequency. The modelled differential attenuation coefficients do

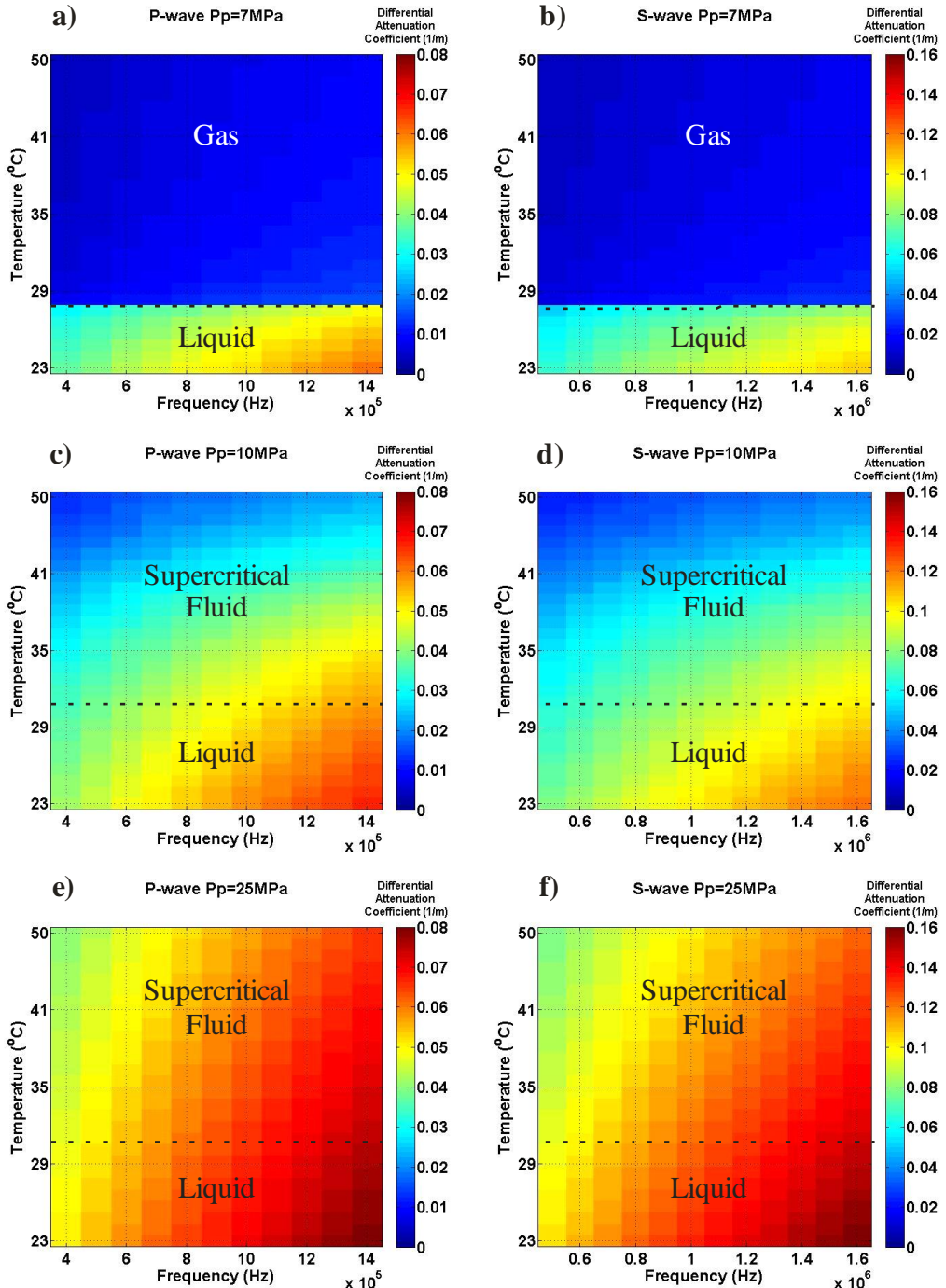


Figure 7.17: Biot's modelled P- and S-wave differential attenuation coefficient determined for a) and b) $P_p = 7 \text{ MPa}$, c) and d) $P_p = 10 \text{ MPa}$, and e) and f) $P_p = 25 \text{ MPa}$ constant temperature runs as a function of frequency and pore pressure. The expected CO_2 phase state is indicated at the appropriate physical conditions. The black dashed-line indicates where the phase transitions are supposed to occur.

show large changes in response to the liquid to gas phase transition where as the modelled attenuation response to the liquid to supercritical phase transition shows only a smooth and gentle variation, this agrees with our observed results. Within a given plot, the modelled attenuation increases with increasing frequency and decreases with increasing temperature. This modelled variation with frequency agrees with observed results, but the modelled simple decrease with increasing temperature does not agree. The observed results show a more complex behaviour between pore pressure and with temperature than that is modelled by Biot. When the three constant pore pressure runs are contrasted with each other at a given condition, a general trend can be established where the modelled attenuation is always higher for the higher pore pressure. This simple trend however is also not displayed by the observed results. At the same condition of any pore pressure run, the differential attenuation coefficient of the S-waves is always greater than that of the P-waves and this is consistent with our observed data. Similar to the constant temperature runs, the modelled results are two orders of magnitude smaller than the observed results.

The critical frequencies of Biot's theory were computed for the Berea sandstone saturated with CO₂ under a range of pressure and temperature conditions and are shown in figure 7.18. In the figure, the white arrows denote the actual experimental conditions considered in our study. For the range of conditions applied in our study, the critical frequency ranges from 0.01 to 0.05 MHz where a large majority of the critical frequencies are below 0.03 MHz. Therefore theoretically all our laboratory data are in the high frequency regime of Biot's formulation and large discrepancies with Gassmann's results should be anticipated. Instead overall Gassmann's modelled velocity results provide a much better description of the observed results than that of Biot's modelled velocity results, where Biot modelled velocities are usually significantly higher than the observed velocities. Furthermore, Biot's modelled differential attenuation coefficients are two orders of magnitude smaller than the observed results. Biot's results suggest that minimal changes in the waveform should occur over the investigated conditions for the saturated sample, which is far from what is

observed in the laboratory data. In short, Biot's modelled results do not provide an adequate description of the observed wave behaviour for the Berea sandstone.

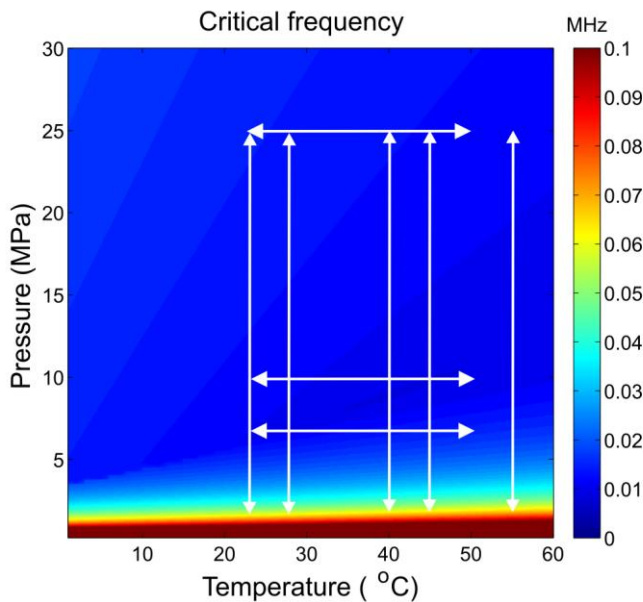


Figure 7.18: Biot's critical frequency for the CO₂ saturated Berea sandstone. The superimposed white arrows represent the conditions investigated in the study.

7.3 Water

Water saturated measurements were conducted on the Berea sandstone after the series of CO₂ saturated measurements. The sample was subjected to full water saturation at T = 23°C while pore pressure varied from 2 to 25 MPa and a constant differential pressure of 15 MPa was maintained.

7.3.1 Water Saturated Waveforms

The P- and S-waveforms obtained under full water saturated conditions of the Berea sandstone are shown in figure 7.19. Both the P-and S-waveforms' travel times and signal strength show minor changes over this pressure interval, where the P-waves show more change. With higher pore pressure, the P-waves appear to be arriving earlier and stronger in amplitude.

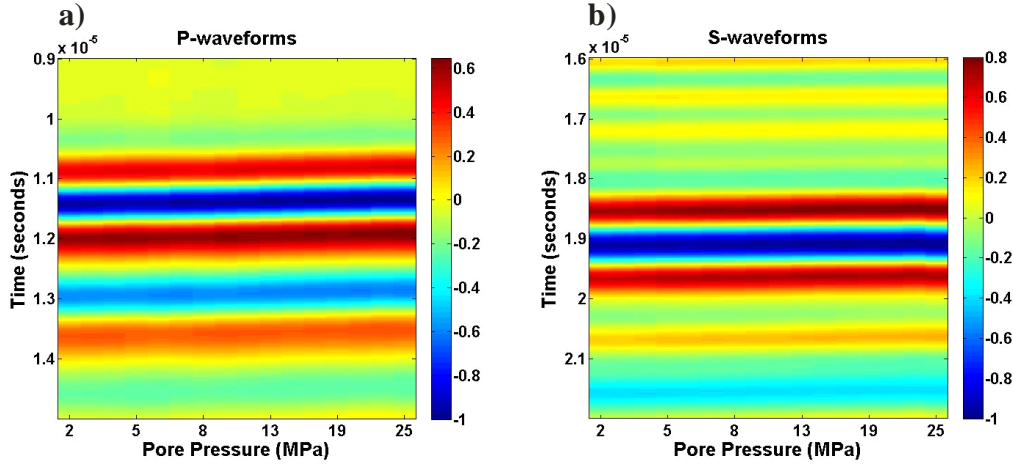


Figure 7.19: Normalized P- (a) and S-wave (b) water saturated waveforms as a function of pore pressure. A constant differential pressure of 15 MPa was maintained throughout the measurement run.

7.3.2 Observed Water Saturated Wave Velocities

Figure 7.20 displays the water saturated P-and S-wave velocities with error as a function of pore pressure determined from the waveforms shown in figure 7.19. The dry P-and S-wave velocity of the second dry run obtained under a confining pressure of 15 MPa is shown at $P_p = 0$ MPa. Similar to that observed with CO₂, with water in the pore space the P-and S-wave velocities decrease with respect to the dry wave velocities where the decrease in wave velocity is much greater for S-waves than P-waves. As pore pressure of the saturated sample increases, the P-wave velocity also increases. Over this 2 to 25 MPa pore pressure interval, the P-wave velocities increased linearly of about 0.8%. Oddly, for the S-waves as pore pressure increases the wave velocity also increases, even though the bulk density of the saturated sample should increase. However the overall increase in wave velocity is small; over the entire pore pressure interval, the velocity increase is 0.2% which is only 5 m/s.

7.3.3 Modelled Water Saturated Wave Velocities

Gassmann's and Biot's theoretical wave velocity predictions are computed here over the same pressure and temperature conditions as applied in the

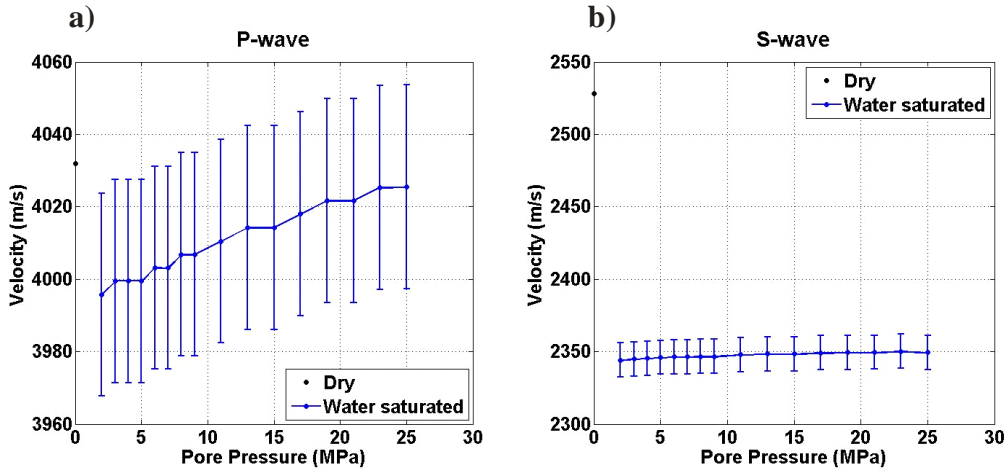


Figure 7.20: Ultrasonic P- wave (a) and S-wave (b) velocities with their respective errors measured of the sample saturated with water under various pore pressures at $T = 23^\circ\text{C}$ and when the sample is not saturated (black dot at $P_p = 0 \text{ MPa}$).

laboratory under water saturation. The fluid properties of water essential to the two models were obtained from NIST's online chemistry webBook.

Gassmann Model

Figure 7.21 shows the modelled and observed P-and S-wave water saturated velocities. Both the observed and modelled behaviour of the water saturated Berea sandstone displays a linear change in wave velocities with

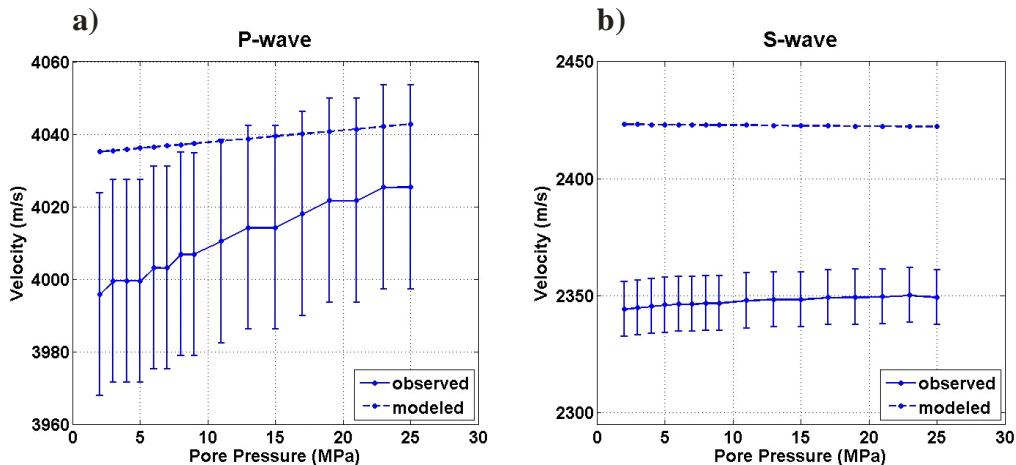


Figure 7.21: Observed and Gassmann's modeled P-wave (a) and S-wave (b) water saturated velocities.

changing pore pressure. For P-waves similar to the porous ceramic rod's results, the observed velocity increase with pore pressure is modelled by Gassmann's equation; however the rates of increase are different. As a result at high pore pressures the results are in agreement but at low pore pressures the results are in disagreement. The largest disagreement is at the lowest pore pressure, 2 MPa, where the discrepancy is 1.0%. For S-waves, dissimilar to the porous ceramic rod's results, the observed slight velocity increase with pore pressure is not modelled by Gassmann's equation; instead the modelled results show a slight decrease in wave velocity. The largest discrepancy between S-wave velocity results is 2.4% and again occurs at the lowest pore pressure. For both water saturated P-and S-wave velocities, the Gassmann modelled response is higher than the observed. Furthermore once water is introduced into the dry sample, the modelled wave velocity shows an increase in P-wave velocity and a decrease in S-wave velocity with respect to the dry wave velocities. The observed results instead show that both P-and S-wave velocity are lower with respect to the dry wave velocities.

Biot Model

Figure 7.22 displays the water saturated modelled and observed P-and S-

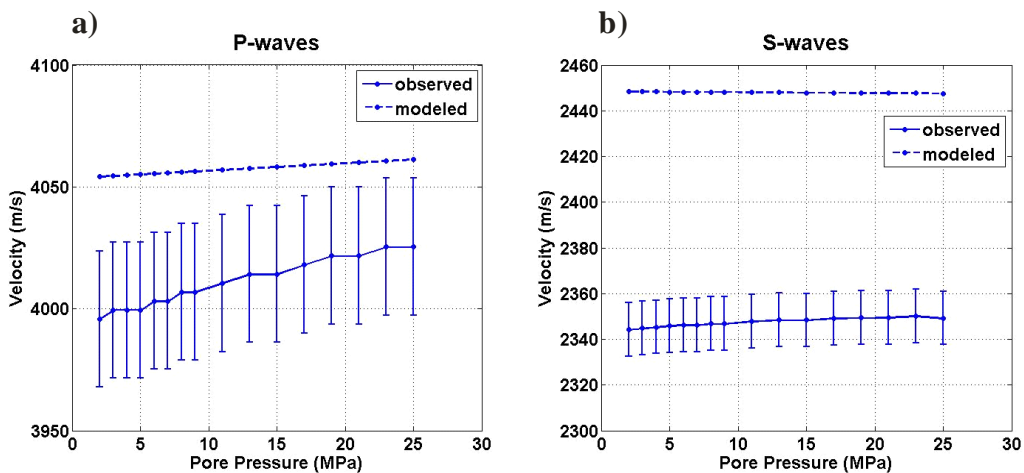


Figure 7.22: Biot's modelled and observed P- wave (a) and S-wave (b) water saturated velocities.

wave velocities. Biot's modelled velocity curves show the same trend with pore pressure as that shown by Gassmann's modelled results. Similar to that seen with the CO₂ saturated results, Biot's modelled velocities for the water saturated Berea sandstone are all higher than the observed velocities, and have a poorer fit to the observed results than Gassmann's modelled velocities.

7.4 Results and Discussion

In this section, the pore fluid effects of CO₂ and water on the wave behaviours observed and modelled are reviewed and discussed. The similarities between the results of the Berea sandstone and the porous ceramic rod are given, and also the differences between the results of these two samples will be discussed. Moreover, the unexpected behaviours and issues with the Berea sandstone will be examined.

Many of the wave behaviours and responses of the CO₂ saturated porous ceramic rod, observed and modelled, are also seen with the CO₂ saturated Berea sandstone. It is perhaps best to begin by noting these similarities:

- 1.) the dominance of the bulk density over bulk modulus in controlling the wave velocity is seen in most of the observed and modelled wave responses of the Berea sandstone. Deviations from this general wave behaviour with bulk density will be discussed later;
- 2.) for the constant temperature runs the wave responses (velocity and attenuation) to the gas to liquid phase transition is more immediate and occurs at a lower pore pressure than the wave responses to the gas to supercritical fluid phase transition. Furthermore the levelling of wave responses after the phase transition is also seen to occur at a higher pore pressure for a higher temperature run;
- 3.) the gas-liquid phase transition always results in a larger change in wave response than a gas-supercritical or liquid-supercritical phase transition;
- 4.) in this study the gas-liquid and gas-supercritical phase change is detectable from sudden changes to both wave velocity and wave

attenuation. However the liquid-supercritical phase change is less detectable due to the lack of sudden and large wave velocity and wave attenuation changes.

The reasons for all these observed and modelled wave behaviours of CO₂ saturated measurements have been given in section 6.4.1 for the discussion on the porous ceramic rod.

Although many wave behaviours of the porous ceramic rod are seen with the Berea sandstone, there are some differences between the two materials. As mentioned earlier some of the Berea sandstone observed wave velocities deviate from the general behaviour of being controlled by bulk density. An example of this exception to this general behaviour appears at high pore pressures for the P-waves of the two low constant temperature runs of T = 23°C and T = 28°C, in figure 7.8. The T = 23°C run shows an obvious increase in P-wave velocity right after the CO₂ transitions into the liquid state where as for the T = 28°C run, the overall increase is slighter. This increase in P-wave velocity for these two low constant temperature runs are also predicted by both the Gassmann and the Biot models, however their predicted P-wave velocity increase is minor in comparison to that observed. For the T = 23°C run, the observed increase from 6 MPa to 25 MPa is 0.6% (24 m/s) whereas the modelled increase is less than 0.1% (3 m/s). This increase in P-wave velocity from both observed and modelled results suggests that the change in bulk modulus' effect is greater than the change in bulk density's effect. Referring to figure 7.3 the two lower temperature runs do undergo a greater change in bulk modulus than in bulk density over this pressure interval. Only past the critical point of CO₂ does bulk density vary more than bulk modulus over the same interval. Therefore with CO₂ in the pore space, depending on the conditions the P-wave velocity may increase or decrease with increasing bulk density and bulk modulus.

Another exception to the wave velocities being controlled by bulk density is demonstrated by the observed velocities of the constant pore pressure runs. For all three constant pore pressure runs as the temperature increases the bulk density of the sample should decrease and would yield an increase in wave

velocity if the bulk density is the controlling factor. This wave response is demonstrated by both Gassmann and Biot's modelled results. For our observed results however, apart from the obvious jump in P-and S-wave velocity seen for the $P_P = 7$ MPa run in response to the liquid to gas phase transition, for the rest of the $P_P = 7$ MPa run and for the entire $P_P = 25$ MPa run, both P-and S-wave velocity decreases with decreasing bulk density. The decrease in S-wave velocity suggests that as temperature increases the bulk density is not the only changing factor, but instead the shear modulus of the sample is also changing. This implies that the nature of the sample is varying with temperature. The nature of the sample with increasing temperature changes as a result of frame softening, therefore wave velocities would decrease with increasing temperature if all other conditions were held constant. This frame weakening with increasing temperature was addressed in the velocity analysis for the porous ceramic rod but was not included for the Berea sandstone because the amount of velocity change caused by temperature's effect alone is difficult to quantify because of the hysteresis effects. For the Berea sandstone, the nature of the sample not only changes with temperature but also with the number of measurements conducted on the sample as discussed in section 6.2.2. Therefore, the velocity changes observed during the heated dry measurements cannot be used to correct for frame weakening since temperature is not the lone cause in affecting the dry wave velocities.

Furthermore, the waveform changes (velocity and attenuation) in response to the varying pressure and temperature conditions for the Berea sandstone are reduced in comparison to the porous ceramic rod. For example, the gas-liquid phase transition usually yields about a 4-5% observed wave velocity change for the porous ceramic rod, whereas for the Berea sandstone an observed wave velocity change of 1-2% is seen. Also when comparing the velocity plots of the high constant temperature runs of the Berea sandstone to the velocity plot of the porous ceramic rod under the same conditions, the velocity curves of the Berea sandstone show less curvature. These reduced wave velocity responses of the Berea sandstone is a result of its significantly lower porosity compared to the

porous ceramic rod. A lower porosity means lower pore fluid content in the sample which leads to a reduced sensitivity of the overall sample to pore fluid changes. For wave attenuation, when compared under similar conditions the observed differential attenuation coefficients of the Berea sandstone are usually a few times less than the porous ceramic rod. In fact the modelled differential attenuation coefficients suggest that the attenuation of the Berea sandstone should actually be two orders of magnitude smaller than of the porous ceramic rod. This large difference between the modelled wave attenuation of the two samples is due to the combined effect of Berea sandstone's lower porosity and higher tortuosity. When the porosity and tortuosity values of the porous ceramic rod was used instead in the modelling of the Berea sandstone, similar magnitudes in differential attenuation coefficients to that of the porous ceramic rod were computed.

The differential attenuation coefficients observed for the Berea sandstone show more variability and less consistency than the observed results for the porous ceramic rod. Theoretically the Berea sandstone should have better data than porous ceramic rod because its waveforms are less attenuated from the effects of pore fluid. However the transducer used to acquire the Berea sandstone data unfortunately is weaker, therefore the resulting signals are smaller and are more susceptible to noise.

Although the above dissimilar observed behaviours of the Berea sandstone to the porous ceramic rod can be rationalized, there are other dissimilar observed wave behaviours that are not understood. First, all the observed CO₂ and water saturated wave velocities have a closer fit with Gassmann's than Biot's predicted wave velocities, even though the computed critical frequency for the Berea sandstone suggests our data is in the high frequency regime for both pore fluids. Furthermore, the Gassmann's modelled wave velocities are actually higher than the observed wave velocities. Gassmann's formulation strictly describes low frequency waves (more accurately, zero frequency static deformation) and based on physical velocity dispersion it is expected that the observed ultrasonic wave velocities be greater than Gassmann's predicted velocities. However this is not seen.

Second, the observed water saturated P-and S-wave velocities both have behaviours that are unexpected. Starting with P-waves, the observed wave velocities compared to the dry wave velocities are lower (figure 7.20). However both Gassmann and Biot's modelled P-wave velocities do not agree with this observation (figure 7.21 and 7.22). Typically real rocks do exhibit a higher P-wave velocity in a water saturated state than in its dry state. In fact we conducted another set of dry and water saturated measurements on a different Berea sandstone sample that yielded results that agrees with this common observation. Unfortunately in the set of measurements central to this study the water saturated results are atypical. For S-waves, the common and reasonable lower water saturated wave velocity compared to its dry state is observed in the laboratory data. However, as the pore pressure increased (water density increases too) the S-wave velocities unexpectedly increased. Since the differential pressure stays constant while the pore pressure changed, this increase in S-wave velocities is not explained by the Gassmann-Biot formulations.

Third, regardless of the phase states involved the observed attenuation of the Berea sandstone tends to peak around the phase transition and usually occurs in the denser CO₂ phase state. This behaviour is not displayed in the porous ceramic rod and nor is it modelled by Biot's formulation. Furthermore on observed wave attenuation, as mentioned before negative differential attenuation coefficients are seen in the plots. This is because the signal obtained at T = 23°C and 2 MPa that is used as the reference signal is not the strongest of all signals acquired and its signal amplitude spectrum is not consistently the greatest for all frequencies. This observed behaviour deviates from that seen with the porous ceramic rod and that of Biot's modelled results for the Berea sandstone.

All these unexpected behaviours suggest the nature of the Berea sandstone sample used in this study is far more complex than the porous ceramic rod and what Gassmann and Biot's formulation can describe. The complex nature of the Berea sandstone has already been suggested based on the observed sample consolidation. Due to the presences of micro-cracks in the sample, the integrity of the sample has changed over the series of measurements where higher wave

velocities are observed for later measurements than earlier measurements under the same conditions. Also the length of the sample has changed over the course of the measurements, where a length shortening of 0.02 mm has been measured. Apart from varying the nature of the sample between and possibly during the measurements, the thorough impact and implications of using a cracked sample on the resulting wave responses are not fully understood in this study.

Another factor that may contribute to the altering of sample integrity is chemical effect. The dissolution of minerals is expected to occur when CO₂ is introduced into an environment that contains water. The mixture of CO₂ and water will form an acidic solution where this solution will dissolve rock minerals. Our CO₂ saturated measurements were conducted with full CO₂ saturation and should not have contained water. However, there may have been a reaction during the full water saturated measurements. Water saturated measurements were conducted after the CO₂ saturated measurements where the previously CO₂ saturated sample was vacuumed for 12 hours before being saturated with water. Even though the pore space is considered to be under vacuum, this ‘vacuum’ is not perfect where the lowest pressure reached was 0.0024 KPa (refer to Chapter 4). Therefore a very minor trace of CO₂ may have been left in the sample when saturated with water. The amount of impact or mineral dissolution from such a small trace of CO₂ or from full CO₂ saturation was not investigated. However the dry weight of the sample measured after the full series of measurements did show a decrease from its original starting weight of 43.70 g to 43.24 g. The porosity of 19.0% of the sample remained unchanged and could be a result of the opposing effects of sample consolidation and mineral dissolution.

7.5 Summary

Ultrasonic pulse transmission experiments were performed on the Berea sandstone under dry, CO₂ saturated, and water saturated conditions. The P-and S-waveforms and the corresponding wave velocities of all three saturated states and the differential attenuation coefficient of just the CO₂ saturated state were presented. As a function of applied pressure the dry wave velocities of the Berea

sandstone showed a substantial change. This observed wave velocity dependency on pressure is due to the presence of micro-cracks in the Berea sandstone, which have been shown to complicate wave responses.

CO_2 saturated measurements were conducted for a variety of temperatures and pressures where the gas, liquid, and supercritical phase state of CO_2 were explored. Many trends and behaviours observed for the porous ceramic rod were also observed here for the Berea sandstone. Such similarities seen are:

- the P-and S-wave velocities of the CO_2 saturated sample are always lower than the dry wave velocities;
- changes to bulk density appears to be the controlling factor on the response of the P-and S-wave velocities;
- the wave response to the gas-liquid transition is more immediate and yields larger changes than the other phase transitions;
- the liquid-supercritical fluid transition is less detectable because there are no disruption to the smooth and continuous change in wave velocity.

Despite these similarities between the two samples, there are some differences and deviations in the wave behaviours observed. Bulk density as the controlling factor on the resulting wave response was seen for most wave responses, but not for the constant temperature runs at $T = 23^\circ\text{C}$ and $T = 28^\circ\text{C}$. Over the gas to liquid and gas to supercritical phase transition, a sudden drop in wave velocity and wave amplitude was observed however the wave velocity drop was of less than 2%. Furthermore, unlike that seen with porous ceramic rod results, the observed differential attenuation coefficients tends to show a peak in attenuation around the phase transition interval and then drops off subsequently. This peak in attenuation was also observed for the constant pore pressure runs, even though there were no distinct changes to the wave velocities to signify the liquid-supercritical fluid transition.

Fluid substitution using Gassmann's and Biot's equations were applied to the same CO_2 saturated conditions as were conducted in the laboratory for the Berea sandstone. Both Gassmann and Biot's modelled wave responses generally

did not agree with the observed wave's behaviour; the observed wave velocities were always lower than both model's wave velocities, Biot's modelled differential attenuation coefficient values were two orders of magnitude larger than the observed values, and the peaks in wave attenuation near the phase transition seen in the observed data were not seen in Biot's model.

Water saturated measurements on the Berea sandstone were only conducted as a function of pore pressure while under a constant differential pressure. Minor linear changes in wave velocities with pore pressure were observed. Gassmann's predicted wave velocities showed a slightly closer fit in terms of absolute wave velocities to the observed results than Biot's predicted results. The observed S-wave velocity increase with pore pressure is unexpected in both model's results.

Overall the Berea sandstone displays wave behaviours that are less understood than the porous ceramic rod. This is due to the more complex nature of the sample. The larger presence of micro-cracks and chemical change in the sample could be possible factors in influencing and complicating the observed wave behaviour.

Chapter 8

Conclusion

8.1 Summary of Work

The important role of seismic methods in geological CO₂ sequestration is to locate the subsurface movement of the injected CO₂ and to determine the amount of CO₂ in place. Given the range of possible temperature and pressure conditions in an upper sedimentary basin, CO₂ can be a gas, liquid, or supercritical fluid. The physical properties of the pore fluid in a saturated rock can have a large impact on the overall seismic wave response. The purpose our work is to improve the understanding of the effects CO₂ has on the overall wave response of a saturated medium, under the possible geological sequestration conditions. Moreover, our work provides an end member study by conducting measurements under full CO₂ saturation to manifest the possible extreme pore fluid effects. In this thesis, a series of ultrasonic pulse transmission measurements were performed on a synthetic and a non-synthetic sample subjected to various conditions. The samples were subjected to dry, full CO₂ saturation and full water saturation. Under CO₂ saturated conditions, various pressures and temperatures were applied in order to yield a gas, liquid, or supercritical fluid phase. All measurements pertaining to fluid saturation were conducted under constant differential pressure to ensure pressure effects are eliminated and the resulting wave variations observed are solely due to pore fluid effects. The samples were also subjected to petrophysical characterization to assist the understanding and analysis of the observed wave behaviours.

In this study the synthetic sample used is a porous ceramic rod derived from an alumina body and the non-synthetic sample is a Berea sandstone that is

composed predominantly of quartz grains with minor amounts of clay. The petrophysical properties of these two samples are quite different with respect to one another. The porous ceramic rod is extremely porous, very fine-grained, and contains a small, negligible amount of micro-cracks. The Berea sandstone is two-thirds less porous than the porous ceramic rod, larger grained, and contains a significant amount of micro-cracks. The extremely high porosity of the porous ceramic rod allows for larger pore fluid effects to occur, which reinforces our intent of providing an end member CO₂ study.

The presence of CO₂ in the pore space is notable from wave velocity changes in both samples. The introduction of CO₂ into a dry sample yields a reduction in both P-and S-wave velocities regardless of the prevailing phase state. Of the three possible CO₂ phases examined over the conditions explored, the wave velocity reduction is the least for the gas phase. Furthermore, the variations in CO₂ phase states, or more specifically the variations in CO₂'s physical properties are also reflected in waveform changes. The behaviour of the wave velocity change shows a greater dependence on the change in the bulk density of the sample, which in turn is largely dependent on CO₂'s density, rather than on the change in bulk modulus. The only exception to this general behaviour is when CO₂ is in the liquid phase for the Berea sandstone where the change in bulk modulus' effect dominates. Considering the prevailing type of conditions in geological sequestration projects, the dominating effect of bulk modulus' changes on P-wave velocity is less likely because large changes in bulk modulus only occur at lower temperatures. These temperatures are still plausible in sequestration projects but are less likely to occur. Therefore, for rock samples or any porous media of similar properties as the samples used in our study, a P-wave velocity decrease indicates that both the pore fluid's density and bulk modulus has increased. Other than the wave velocity of a waveform, the wave amplitude is also responsive to the variations in CO₂'s physical properties. It appears whenever the wave velocity decreases, the wave amplitude also decreases. Therefore, the wave amplitude strength or wave attenuation is also sensitive to changes in CO₂ physical properties.

Moreover, over the range of pressure and temperature conditions investigated, the difference in waveforms (characterized by wave velocity and wave amplitude) between a gaseous-CO₂ saturated sample and a liquid/supercritical fluid-CO₂ saturated sample is larger than that displayed between a liquid-and supercritical fluid saturated sample. Furthermore, the phase transition from a gas to a liquid/supercritical fluid phase is more distinctive through greater waveform changes than the liquid to supercritical fluid phase transition. The latter transition lacks any distinguishing waveform changes to signify a phase change. These varying wave responses to the different phase transitions are dependent on the amount of density change encountered; the larger the CO₂ density change, the larger the signal variation.

For the porous ceramic rod, the comparison of observed CO₂ saturated results to Biot's modelled results shows a good agreement in P-and S-wave velocities and only a qualitative agreement in P-and S-wave differential attenuation coefficients. Biot's modelled attenuation is always lower than what is observed. In contrast, Gassmann's modelled wave velocities usually fit poorly with the observed wave velocities and the formulation does not account for wave attenuation. For the Berea sandstone the comparison between observed results and modelled results generally show large discrepancies, indicating that both models are inadequate in describing the rock behaviour. The observed wave velocities are always lower than predicted by both Biot's and Gassmann's models. Furthermore, the predicted wave attenuation by Biot's model is substantially less, two orders of magnitude smaller than observed.

Between the porous ceramic rod and the Berea sandstone results, the waveforms' response to CO₂ physical property changes pertaining to the porous ceramic rod is much greater and shows more sensitivity than the Berea sandstone. This is a consequence of the much higher porosity of the porous ceramic rod. The amount of waveform variation of the porous ceramic rod is unrealistic. However these obtained results provides an end member knowledge of what extremities can be expected with CO₂ in the pore space. The waveform variations around the amount displayed by the Berea sandstone are more realistic; however the changes

do pertain to full CO₂ saturation. Also it should be remembered that the observed wave responses of the Berea sandstone are less consistent and show more complexity than of the porous ceramic rod. The integrity or nature of the sample have changed over the series of measurement runs and maybe even during a measurement run. The mechanisms behind the observed wave behaviour are not fully understood. Therefore interpretations of the lone effect of CO₂'s physical properties on Berea sandstone's observed wave velocity or wave attenuation should be preceded with caution.

8.2 Contributions of this work

The main intent of our work is to add to the existing laboratory studies central to understanding the seismic effects CO₂ has as a pore fluid. To our knowledge, this is the first systematic laboratory study conducted to inspect the wave velocity and wave attenuation for the purpose of geological CO₂ sequestration as a result of:

- 1.) full CO₂ saturation,
- 2.) the different phase states of CO₂,
- 3.) definitively separating pore fluid property effects from pore pressure build-up effects.

The use of the porous ceramic rod sample in conjunction to full CO₂ saturation has allowed us to present possible end member wave behaviours with CO₂ in the pore space. This information will help constrain the more complex, but more probable, partially saturated cases in sequestration projects. The variations in wave velocity in response to a CO₂ phase transition between a gas and liquid/supercritical fluid is ~5% from ultrasonic frequency laboratory data and is ~8% from seismic frequency data determined from Gassmann's prediction. Further away from the phase transition intervals, the difference between a gas and liquid/supercritical fluid phase is even greater, 6-8% for ultrasonic frequency waves and more than 12% for seismic frequency waves. It should be noted that these percentage changes are solely due to pore fluid effects where pressures effects are eliminated by maintaining a constant differential pressure.

Realistically, the overburden pressure (confining pressure) would stay constant while the pore pressure of the in-situ fluid varies. Therefore as pore pressure increases with a constant overburden the differential pressure would decrease. As shown by the measurements on the dry sample, wave velocity decreases with decreasing differential pressure. Therefore the percentage changes observed and modelled for the phase transitions and for distinguishing between phase states would be even greater if pressure effects are considered as well. From these considerations, differentiating in situ CO₂ phase states from seismic, namely a gaseous CO₂ from a liquid or a supercritical fluid CO₂, should be resolvable.

The identification of the different phase states using changes in seismic reflectivity, travel times, or wave attenuation are important to the quantification of CO₂ in situ. In order to quantify the amount in place the density of the CO₂ needs to be known, where the density is dependent on the phase state. Therefore the ability to identify the existing phase state implies the ability to quantify the subsurface CO₂. Furthermore from our study, it was shown that over the conditions investigated and with the samples we used the difference in waveforms between a liquid-and a supercritical fluid-CO₂ saturated sample is minimal. This would not be a great concern to CO₂ quantification since this minor difference in waveforms is a consequence of the minor difference in the density between these two phase states.

8.3 Future Work

As mentioned, the purpose of our work is to present an end member study to observe the extreme wave behaviour possible with CO₂ in the pore space. In order for pore fluid effects to manifest in the wave responses, an extremely porous sample was used and full CO₂ saturation was applied. Due to the properties of the sample, both P-and S-wave velocity decreased with increasing pore pressure. A different extreme wave response to CO₂'s behaviour change could be attained if a less stiff sample is used. A sample with a lower bulk modulus will allow the change in the overall bulk modulus to be greater in response to the varying pore fluid properties. This change in bulk modulus could be greater than the change in

bulk density. Therefore the resulting P-wave velocity would vary directly proportionally to the variations in bulk modulus. In addition perhaps the differentiation between a liquid and supercritical fluid CO₂ phase state could occur since the difference between their respective bulk modulus is greater than their respective bulk density.

Full CO₂ saturation was applied in our study, however realistically this situation is unlikely under in situ conditions. To move away from this end member and to better represent the conditions encountered in geological sequestration, other possible in-situ fluids such as brine and oil should be considered in the pore space. Various saturations of CO₂ in various phase states should be attempted to determine if the different phases of CO₂ or phase transition can be identified through waveform changes and the resulting implications on CO₂ quantification.

The wave frequencies applied in our laboratory work are much higher than those employed in seismic surveys over geological sequestration projects. As a consequence of physical velocity dispersion, a direct comparison between laboratory results and field results should not be carried out. Instead the high frequency results need to be scaled down to low frequencies by rock physics models. The accuracy in this approach is restricted by how adequate the model is in describing the actual wave behaviours with the different frequency ranges. If low frequency laboratory measurements can be conducted then the laboratory results can be directly compared with surface seismic, VSP, and crosswell seismic. Therefore without the need of a model to mediate between results, the possibility of additional errors introduced by the model is reduced.

The same set of ultrasonic pulse transmission measurements should be conducted on the Berea sandstone again. However, prior to performing the measurements the sample should be cycled through a series of high pressures several times. By applying this procedure, the troublesome wave velocity hysteresis prevalent in our data would be reduced and the resulting data should be more consistent. Furthermore, this new and improved data should be compared to

our results to see whether the characteristic peak in wave attenuation near CO₂ phase transitions seen in our data is still observed.

References

- Adam, L., Batzle, M., and Brevik, I., 2006, Gassmann's fluid substitution and shear modulus variability in carbonates at laboratory seismic and ultrasonic frequencies: *Geophysics*, **71**, F173-F183.
- Aki, K., and Richards, P. G., 1980, Quantitative Seismology: Theory and Methods: W. H. Freeman and Co., San Francisco, USA.
- Attia, A. M., 2005, Effects of petrophysical rock properties on tortuosity factor: *Journal of Petroleum Science and Engineering*, **48**, 185-198
- Arts, R., Elsayed, R., Van Der Meer, L., Eiken, O., Ostmo, O., Chadwick, A., Kirby, G., and Zinszner, B., 2002, Estimation of the mass of injected CO₂ at Sleipner using time-lapse seismic data: EAGE 64th Annual Conference, Paper H-16.
- Bachu, S. and Shaw, J. C., 2004, CO₂ storage in oil and gas reservoirs in Western Canada: Effects of aquifers, potential for CO₂- flood enhanced oil recovery and practical capacity: Proceedings of the 7th International Conference on Greenhouse Gas Control Technologies. Volume 1: Peer-Reviewed Papers and Plenary Presentations, Vancouver, BC, September 5-9, 2004.
- Bakhorji, A. M., 2010, Laboratory Measurements of Static and Dynamic Elastic Properties in Carbonate: PhD Thesis, University of Alberta.
- Bass, J. D., 1995, Elasticity of Minerals, Glasses, and Melts, in T. J. Ahrens, ed., Mineral Physics and Crystallography: A Handbook of Physical Constants: American Geophysical Union, Washington, USA., pp 45-63.
- Batzle, M. L., and Wang, Z., 1992, Seismic properties of pore fluids: *Geophysics*, **57**, 1396-1408.
- Benson, S. M., and Myer, L., 2002, Monitoring to ensure safe and effective geologic sequestration of carbon dioxide: IPCC Workshop for Carbon Capture and Storage 2002, Regina, Canada.

- Berryman, J. G., 1999, Origin of Gassmann's equation: *Geophysics*, **64**, 1627-1629.
- Biot, M. A., 1956a, The theory of propagation of elastic waves in a fluid-saturated solid, I lower frequency range: *Journal of Acoustical Society of America*, **28**, 168-178.
- Biot, M. A., 1956b, The theory of propagation of elastic waves in a fluid-saturated solid, II higher frequency range: *Journal of Acoustical Society of America*, **28**, 179-191.
- Biot, M. A., and Willis, D. G., 1957, The elastic coefficients of the theory of consolidation, *Journal of Applied Mechanics*, **24**, 594-601.
- Birch, F., 1961, The velocity of compressional waves in rocks to 10 kilobars, Part 2: *Journal of Geophysical Research*, **66**, 2199-2224.
- Blair, D. P., 1990, Seismic pulse assessment of cracked and jointed rock: *Engineering Fracture Mechanics*, **35**, 447-455.
- Blencoe, J. G., Cole, D. R., Horita J., and Moline, G.R., 2001, Experimental Geochemical Studies Relevant to Carbon Sequestration: Proceedings of the First National Symposium on Carbon Sequestration, National Energy Technology Laboratory, Washington DC.
- Bourbie, T., Coussy, O., and Zinszner, B., 1987, Acoustics of porous media: Editions Technip, Paris, France.
- Bouzidi, Y., 2003, The Acoustic Reflectivity and Transmissivity of Liquid Saturated Porous Media: Experimental Tests of Theoretical Concepts: PhD Thesis, University of Alberta.
- Bouzidi, Y., and Schmitt, D. R., 2009, Measurement of the speed and attenuation of the Biot slow wave using a large ultrasonic transducer: *Journal of Geophysical Research*, **114**, B08201.
- Cadoret, T., Marion, D., and Zinszner, B., 1995, Influence of frequency and fluid distribution on elastic-wave velocities in partially saturated limestones: *Journal of Geophysical Research*, **100**, 9789-9803.
- Chadwick, R. A., Arts, R., Bentham, M., Eiken, O., Holloway, S., Kirby, G. A., Pearce, J. M., Williamson, J. P., and Zweigel, P., 2009, Review of monitoring

- issues and technologies associated with the long-term underground storage of carbon dioxide: Geological Society, London, Special Publications, **313**, 257-275
- Chadwick, R. A., Williams, G., Delepine, N., Clochard, V., Labat, K., Sturton, S., Buddensiek, M. L., Lima, A. L., Arts, R., Neele, F., and Rossi, G., 2010, Quantitative analysis of time-lapse seismic monitoring data at the Sleipner CO₂ storage operation: The Leading Edge, **29**, 170-177.
- Cheng, A., Huang, L., and Rutledge, J., 2010, Time-lapse VSP data processing for monitoring CO₂ injection: The Leading Edge, **29**, 196-199.
- Christensen, N. I., and Wang, H. F., 1985, The influence of pore pressure and confining pressure on dynamic elastic properties of Berea Sandstone: Geophysics, **50**, 207-213.
- Cole, D. R., Chialvo, A. A., Rother, G., Vlcek, L., and Cummings, P. T., 2010, Supercritical fluid behaviour at nanoscale interfaces: Implications for CO₂ sequestration in geologic formations: Philosophical Magazine, **90**, 2339-2363.
- Daley, T. M., Myer, L. R., Peterson, J.E., Majer, E.L., and Hoversten, G.M., 2008, Time-crosswell seismic and VSP monitoring of injected CO₂ in a brine aquifer: Environ Geol, **54**, 1657-1665.
- De Vilbess, J. W., 1980, Wave dispersion and absorption in partially saturated rocks: PhD. Thesis, Stanford University, California.
- Dewar, J., 2001, Rock Physics for the rest of us –An informal discussion: CSEG Recorder, **26**, 42-49.
- Diallo, M. S., Prasad, M., and Appel, E., 2003, Comparison between experimental results and theoretical predictions for P-wave velocity and attenuation at ultrasonic frequency: Wave Motion, **37**, 1-16.
- Ely, J. F., Haynes, W. M., and Bain, B. C., 1989, Isochoric (P, V_m, T) measurements on CO₂ and on (0.982CO₂ + 0.018N₂) from 250 to 330 K at pressures to 35 MPa: Journal of Chemical Thermodynamics, **21**, 879-894.

- Fabry, V. J., Seibel, B. A., Feely, R. A., and Orr, J. C., 2008, Impacts of ocean acidification on marine fauna and ecosystem processes: ICES Journal of Marine Science, **65**, 414-432.
- Falorni, G., Tamburini, A., Novali, F., Ferretti, A., and Young, B., 2010, Multi-interferogram InSAR Techniques for Monitoring Surface Deformation in CO₂ Sequestration, AAPG Annual Convention and Exhibition, New Orleans, Louisiana, April 11-14, 2010.
- Fujimoto, Y., Kono, Y., Hirajima, T., Kanagawa, K., Ishikawa, M., and Arima, M., 2010, P-wave velocity and anisotropy of lawsonite and epidote blueschists: Constraints on water transportation along subducting oceanic crust: Physics of the Earth and Planetary Interiors, **183**, 219-228.
- Gardner, G. H. F., Wyllie, M. R. J., and Droschak, D. M., 1965, Hysteresis in the velocity-pressure characteristics of rocks: Geophysics, **30**, 111-116.
- Garrouch, A. A., Ali, L., and Qasem, F., 2001, Using diffusion and electrical measurements to access tortuosity of porous media: Ind. Eng. Chem. Res, **40**, 4363-4369
- Gasperikova, E., and Hoversten, G.M., 2006, A feasibility study of nonseismic geophysical methods for monitoring geologic CO₂ sequestration, The Leading Edge, **25**, 1282-1288
- Gasperikova, E., and Hoversten, G.M., 2008, Gravity monitoring of CO₂ movement during sequestration: Model studies: Geophysics, **73**, WA105-WA112.
- Gassmann, F., 1951, Elasticity of porous media: Uber die Elastizitat poroser Medien: Vierteljahrsschrift der Naturforschenden Gessellschaft in Zurich, **96**, 1-23.
- Geertsma, J., 1961, Velocity-log interpretation: the effect of rock bulk compressibility: Society of Petroleum Engineers Journal, **1**, 235-248.
- Gladwin, M. T., and Stacey, F. D, 1974, Anelastic degradation of acoustic pulses in rocks: Physics of the Earth and Planetary Interiors, **8**, 332–336.
- Gordon, R. B., and Davis, L. A., 1968, Velocity and attenuation of seismic waves in imperfectly elastic rock: Journal of Geophysical Research, **73**, 3917-3935.

- Gritto, R., Daley T. M., and Myer, L.R., 2004, Joint cross-well and single-well seismic studies at Lost Hills, California: *Geophys. Prospect*, **52**, 323-339.
- Gunter, W. D., and Perking, E., 2001, Geochemical Monitoring of CO₂ Enhanced Oil Recovery: Proceedings of the NETL Workshop on Carbon Sequestration Science.
- Hare, J.L., Ferguson, J.F., and Aiken, C. L. V., 1999, The 4-D microgravity method for waterflood surveillance: A model study from the Prudhoe Bay reservoir, Alaska: *Geophysics*, **64**, 78-87.
- Hart, D. J., and Wang, H. F., 1995, Laboratory measurements of a complete set of poroelastic moduli for Berea sandstone and Indiana limestone, *Journal of Geophysical Research*, **17**, 741-751
- Hart, D. J., and Wang, H. F., 2010, Variations of unjacketed pore compressibility using Gassmann's equation and an overdetermined set of volumetric poroelastic measurements, *Geophysics*, **75**, N9-N18.
- Hemsing, D. B., 2007, Laboratory determination of seismic anisotropy in sedimentary rock from the Western Canadian Sedimentary Basin: M.Sc. Thesis, University of Alberta.
- Hill, R., 1952, The elastic behaviour of crystalline aggregate: *Proceedings of the Physical Society*, **65**, 349-354.
- Hovem, J. M., and Ingram, G. D., 1979, Viscous attenuation of sound in saturated sand: *Journal of the Acoustical Society of America*, **66**, 1807-1812.
- Hoversten, G. M., Gritto, R., Washbourne, J., and Daley, T., 2003, Pressure and fluid saturation prediction in a multicomponent reservoir using combined seismic and electromagnetic imaging: *Geophysics*, **68**, 1580-1591.
- Hovorka, S.D., Collings, D., Benson, S., Mayer, L., Bryer, C., and Cohen, K., 2005, Update on the Frio Brine Pilot: eight months after injection: National Energy Technology Laboratory Fourth Annual Conference on Carbon Capture and Sequestration, Alexandria, Virginia, May 2-5, 2005. GCCC Digital Publication Series #05-04i, pp. 1-31. retrieved from [http://www.beg.utexas.edu/gccc/bookshelf/Final%20Papers/05-04-Final%20\(NETL%20Papers\)/05-04i-Final.pdf](http://www.beg.utexas.edu/gccc/bookshelf/Final%20Papers/05-04-Final%20(NETL%20Papers)/05-04i-Final.pdf) on December 2010.

- Huang, F. H., Li, M. H, Lee, L. L., Starling, K. E., and Chung F. T. H., 1985, An accurate equation of state for carbon dioxide, *Journal of Chemical Engineering of Japan*, **18**, 490-496.
- IPCC, 2005, In: Metz B., Davidson, O., de Coninck, H.C., Loos, M., and Mayer, L. A. (eds) *IPCC Special Report on CO₂ Capture and Storage*, prepared by Working group III of the International Panel on Climate Change: Cambridge University Press.
- IPCC, 2007, In: Pachauri, R. K., and Reisinger, A., (eds) *Climate Change 2007: Synthesis Report, Contribution of Working Groups I, II and III to the Fourth Assessment Report of the Intergovernmental Panel on Climate Change*, IPCC, Geneva, Switzerland, pp 109. Retrieved from http://www.ipcc.ch/publications_and_data/ar4/syr/en/contents.html, accessed on December 2, 2010.
- Jaya, M. S, Shapiro, S. A., Kristinsdottir, L. H., Bruhn, D., Milsch, H., and Spangenberg, E., 2010, Temperature dependence of seismic properties in geothermal rocks at reservoir conditions, *Geothermics*, **39**, 115-123.
- Johnson, D. L., and Plona, T. J., 1982, Acoustic slow waves and the consolidation transition: *Journal of Acoustical Society of America*, **72**, 556-565.
- Johnston, D. H., and Toksoz, M. N., 1980, Ultrasonic P- and S-waves attenuation in dry and saturated rocks under pressure, *Journal of Geophysical Research*, **85**, 925-936.
- Jones, T., and Nur, A., 1983, Velocity and attenuation in sandstone at elevated temperatures and pressures: *Geophysical Research Letters*, **10**, 140-143.
- Jones, T., 1986, Wave Propagation in Porous Rocks and Models for Crystal Structure: PhD. Thesis, Stanford University, California.
- Kessel'man, P. M., Kotlyarevskii, P. A., and Afanas'ev, M. M., 1965, The equation of state of carbon dioxide in the temperature range 273- 4000 K, for pressures up to $1000 \cdot 10^5$ N/m²: *Journal of Engineering Physics*, **9**, 527-532.
- Kilmer, N. H., Morrow, N. R., and Pitman, J. K, 1987, Pressure sensitivity of low permeability sandstones: *Journal of Petroleum Science and Engineering*, **1**, 65-81.

- Kim, Y., 2007, Equation of State for Carbon Dioxide: Journal of Mechanical Science and Technology, **21**, 799-803.
- Klinkenberg, L. J., 1941, The permeability of porous media to liquids and gases: Drilling and Production Practice, 200-213.
- Kongsjorden, H., Karstad, O., and Torp, T. A., 1998, Saline aquifer storage of carbon dioxide in the Sleipner project: Waste Management, **17**, 303-308
- Lakes, R., 2009, Viscoelastic materials: Cambridge University Press, New York, USA.
- Lay, T., and Wallace, T. C., 1995, Modern Global Seismology *in* International Geophysics Series, Academic Press, San Diego, USA., vol 58.
- Lei, X., and Xue, Z., 2009, Ultrasonic velocity and attenuation during CO₂ injection into water-saturated porous sandstones: Measurements using difference seismic tomography: Physics of the Earth and Planetary Interiors, **176**, 224-234
- Lemmon, E. W., McLinden, M. O., and Friend, D. G., Thermophysical Properties of Fluid Systems in NIST Chemistry WebBook, NIST Standard Reference Database Number 69, Eds. Linstrom, P. J. and Mallard, W. G., National Institute of Standards and Technology, Gaithersburg MD, 20899, <http://webbook.nist.gov>, (retrieved 2008-2011).
- Liang, J., Robertson, E. P., and Raterman, K. T., 2003, A Mechanistic Model for CO₂ sequestration in Tiffany Coal Bed Methane Field: The 2003 International Coal Bed Methane Symposium, USA, May 5-9, 2003.
- Lowrie, W., 1997, Fundamentals of Geophysics: Cambridge University Press
- Mashinkskii, E., 2005, Experimental study of the amplitude effect on wave velocity and attenuation in consolidated rocks under confining pressure: Journal of Geophysics and Engineering, **2**, 199-212.
- Mavko, G. M., and Nur, A., 1979, Wave attenuation in partially saturated rocks, Geophysics, **44**, 161-178.
- Mavko G., Mukerji, T., and Dvorkin, J., 2009, The Rock Physics Handbook: Cambridge University Press.

- McCann, C., and Sothcott, J., 1992, Laboratory measurements of the seismic properties of sedimentary rocks: The Geological Society, London, Special Publications, **65**, 285-297.
- McKavanagh, B., and Stacey, F. D., 1974, Mechanical hysteresis in rocks at low strain amplitudes and seismic frequencies, Physics of the Earth and Planetary Interiors, **8**, 246-250.
- Mobarek, S. A. M., 1971, The effect of temperature on wave velocities in porous rocks: M.Sc. Thesis, University of California.
- Molyneux, J. B., and Schmitt, D. R., 2000, Compressional-wave velocities in attenuating media: A laboratory physical model study: Geophysics, **65**, 1162-1167.
- Murphy, W. F. III, 1982, Effects of partial water saturation on attenuation in Massilon sandstone and Vycor porous glass: Journal of Acoustical Society of America, **71**, 1458-1468.
- New England Research, Inc., Tiny Perm II: Portable Air Permeameter: User's Manual.
- Newmark, R., Ramirez, A., and Daily, W., 2002, Monitoring carbon dioxide sequestration using electrical resistance tomography (ERT): A minimally invasive method: Proceedings of the Sixth International Conference on Greenhouse Gas Control Technologies, 353-358.
- Nooner, S. L., Eiken, O., Hermanrud, C., Sasagawa, G.S., Stenvold, T., and Zumberge, M. A., 2007, Constraints on the in situ density of CO₂ within the Utsira formation from time-lapse seafloor gravity measurements: International Journal of Greenhouse Gas Control, **1**, 198-214.
- Nur, A., 1971, Viscous phases in rocks and the low velocity zone: Journal of Geophysical Research, **76**, 1270-1277.
- Nur, A., and Murphy, W., 1981, Wave velocities and attenuation in porous media with fluids, Proceedings of the 4th International Conference on Continuum models of discrete systems, Stockholm, 311-327

- Nur, A., Mavko, G., Dvorkin, J., and Gal, D., 1995, Critical porosity: the key to relating physical properties to porosity in rocks. In Proceedings of the 65th Annual International Meeting Society of Exploration Geophysics, 878, Tulsa.
- O'Connell, R. J., and Budiansky, B., 1977, Viscoelastic properties of fluid-saturated cracked solids: *Journal of Geophysical Research*, **76**, 2022-2034.
- O'Hara, S. G., 1985, Influence of pressure, temperature, and pore fluid on the frequency-dependent attenuation of elastic waves in Berea sandstone, *Physical Review A*, **32**, 473-488.
- Palmer, I. D., and Traviolia, M. L., 1981, Attenuation by squirt flow in undersaturated gas sands, *Geophysics*, **45**, 1780-1792.
- Park, K. G., Choi, H., Park, Y. C., and Hwang, S., 2009, Ultrasonic laboratory measurements of the seismic velocity changes due to CO₂ injection: EGU General Assembly 2009, Expanded Abstract.
- Pitzer, K. S., and Sterner, S. M., 1994, Equations of state valid continuously from zero to extreme pressures for H₂O and CO₂: *Journal of Chemical Physics*, **101**, 3111-3116.
- Purcell, C., Mur, A., Soong, Y., McLendon, R., Haljasmaa, I. V., and Harbert, W., 2010, Integrating velocity measurements in a reservoir rock sample from the SACROC unit with an AVO proxy for subsurface supercritical CO₂: *The Leading Edge*, **29**, 192-195.
- Qi, X., 2008, Simulation and laboratory measurements of velocity and attenuation in viscoelastic body: A frequency dependent study with respect to viscosities: M.Sc. Thesis, University of Alberta.
- Rackley, S. A., 2010, Carbon Capture and Storage: Elsevier.
- Reuss, A., 1929, Berechnung der fliessgrenze von mischkristallen auf grund der plastizitatbedingung fur einkristalle: *Zeitschrift fur Angewandte Mathematik aus Mechanik*, **9**, 49-58.
- Rickett, J., 2006, Integrated estimation of interval-attenuation profiles: *Geophysics*, **71**, A19-A23.
- Ronstron, B., White, D., Johnson, J., Hawkes, C., Gardner, C., Chalatryk, R., and Whittaker, S., 2009, CO₂ storage monitoring efforts at the Weyburn-

Midale Fields, Canada: AAPG/SEG/SPE Hedberg Conference Expanded abstract, August 16-19.

Saito, H., Nobuoka, D., Azuma, H., Xue, Z., and Tanase, D., 2006, Time-lapse crosswell seismic tomography for monitoring injected CO₂ in an onshore aquifer, Nagaoka, Japan: Exploration Geophysics, **37**, 30-36

Santos, C. A., Urdaneta, V., Jaimes, G., and Trujillo, L., 2009, Ultrasonic Spectral and Complexity Measurements on Brine and Oil Saturated Rocks: Rock Mechanics and Rock Engineering, **43**, 351-359.

Sarma, L. P., and Ravikumar, N., 2000, Q-factor by spectral ratio technique for strata evaluations: Engineering Geology, **57**, 123-132.

Schmitt, D. R., and Zoback, M. D., 1989, Poroelastic effects in the determination of the maximum horizontal principal stress in hydraulic fracturing tests-A proposed breakdown equation employing a modified effective stress relation for tensile failure: International Journal of Rock Mechanics and Mining Sciences & Geomechanics Abstracts, **26**, 499-506.

Seibel, B. A., and Walsh, P. J., 2001, Potential Impacts of CO₂ Injection on Deep Sea Biota: Science, **294**, 319-320

Shankland, T. J., and Johnson, P. A., 1993, Elastic wave attenuation and velocity of Berea sandstone measured in the frequency domain: Geophysical Research Letters, **20**, 391-394

Shi, J., Xue, Z., and Durucan, S., 2007, Seismic monitoring and modelling of supercritical CO₂ injection into a water-saturated sandstone: Interpretation of P-wave velocity data: International Journal of Greenhouse Gas Control, **1**, 473-480.

Spetzler J., Xue, Z., Saito, H., and Nishizawa, O., 2008, Case story: time-lapse seismic crosswell monitoring of CO₂ injected in an onshore sandstone aquifer: Geophys. J. Int, **172**, 214-225.

Springer, D. S., and Loaiciga, H. A., Cullen, S. J., and Everetta, L. G., 1998, Air Permeability of Porous Materials Under Controlled Laboratory Conditions: Ground Water, **36**, 558-565.

- Stein, W. A., 1972, Die Zustandsgleichung für reine fluide Stoffe: Chemical Engineering Science, **27**, 1371-1382.
- Sweatman, R., and McColpin G. R., 2009, Monitoring technology enables long-term CO₂ geosequestration, E &P Magazine, November issue.
- Telford, W. M., Geldart, L. P., and Sheriff, R. E., 1990, Applied Geophysics Second Edition : Cambridge University Press.
- Thurman, E. S., Abousleiman, Y., and Zaman, M., 2002, Acoustical Imaging and Mechanical Properties of Soft Rock and Marine Sediments: Quarterly Technical Progress Report #15302R06
- Timur, A., 1968, Velocity of compressional waves in porous media at permafrost temperatures: Geophysics, **33**, 584-595.
- Timur, A., 1977, Temperature dependence of compressional and shear wave velocities in rocks: Geophysics, **42**, 950-956.
- Toksöz, M. N., and Johnston, D. H., and Timur, A., 1979, Attenuation of seismic waves in dry and saturated rocks, I, Laboratory measurements, Geophysics, **44**, 681-690.
- Tonn, R., 1991, The determination of seismic quality factor Q from VSP data: A comparison of different computational techniques: Geophysical Prospecting, **45**, 87-109.
- Tosaya, C., and Nur, A., 1982, Effects of diagenesis and clays on compressional velocities in rocks: Geophysical Research Letters, **9**, 5-8.
- Tutuncu, A. N., Podio, A. L., and Sharma, M. M., 1994, An experimental investigation of factors influencing compressional-wave and shear wave velocities and attenuations in tight gas sandstones, Geophysics, **59**, 77-86.
- Walsh, J. B., 1966, Seismic wave attenuation in rock due to friction: Journal of Geophysical Research, **71**, 2591-2599.
- Wang, Z., and Nur, A. M., 1989, Effects of CO₂ flooding on wave velocities in rocks with hydrocarbons: Society of Petroleum Engineers. Reservoir Engineering, 3, 429-436.
- Wang, Z., Hirsche, W. K., and Sedgwick, G., 1991, Seismic monitoring of water floods-A petrophysical study: Geophysics, **56**, 1991.

- Wang, Z., Cates, M. E., and Langan, R. T., 1998, Seismic monitoring of a CO₂ flood in a carbonate reservoir: A rock physics study, *Geophysics*, **63**, 1604-1617.\
- Wark, K. Jr., and Richards, D. E., 1999, Thermodynamics: McGraw-Hill.
- Wepfer, W. W., and Christensen, N. I., 1991, Q structure of the Oceanic –Crust: *Marine Geophysical Researches*, **13**, 227-237.
- White, R. E., 1992, The accuracy of estimating *Q* from seismic data: *Geophysics*, **57**, 1508-1511.
- White, D., 2009, Monitoring CO₂ storage during EOR at the Weyburn-Midale field: *The Leading Edge*, **28**, 838-842.
- Wilt, M., 2003, Oil reservoir characterization and CO₂ injection monitoring in the Permian basin with crosswell electromagnetic imaging: Final report DOE Award Number: DE-FC26-00BC15307, retrieved from <http://www.netl.doe.gov/KMD/cds/disk22/G-CO2%20&%20Gas%20Injection/BC15307.pdf> on December 2010.
- Winkler, K., 1979, The effects of pore fluids and frictional sliding on seismic attenuation: PhD. Thesis, Stanford University, California.
- Winkler, K., and Nur, A., 1982, Seismic attenuation: effects of pore fluids and frictional sliding: *Geophysics*, **47**, 1-15.
- Winkler, K., and Plona, T., 1982, Technique for measuring ultrasonic velocity and attenuation spectra in rocks under pressure: *Journal of Geophysical Research*, **87**, 776-780.
- Winkler, K. W., 1985, Dispersion analysis of velocity and attenuation in Berea sandstone: *Journal of Geophysical Research*, **90**, 183
- Wolf, K., 2010, Laboratory Measurements and Reservoir Monitoring of Bitumen Sand Reservoirs: PhD. Thesis, Stanford University, California.
- Wu, Y., Pruess, K., and Persoff, P., 1998, Gas Flow in Porous Media with Klinkenberg Effects: *Transport in Porous Media*, **32**, 117-137.
- Wyllie, M. R. J., Gregory, A. R., and Gardner, G. H. F, 1958, An experimental investigation of factors affecting elastic wave velocities in porous media: *Geophysics*, **23**, 459-493

- Verwer, K., Braaksma, H., and Kenter, J. A. M., 2008, Acoustic properties of carbonates: Effects of rock texture and implications for fluid substitution: *Geophysics*, **73**, B51-B66
- Voigt, W., 1928, Lehrbuch der Kristallphysik: Teubner.
- Xue, Z., Oshumi, T., and Koide, H., 2002, Laboratory measurements of seismic wave velocity by CO₂ injection in two porous sandstones: Proceedings of the Sixth International Conference on Greenhouse Gas Control Technologies, 359-364.
- Xue, Z., and Oshumi, T., 2004, Seismic wave monitoring of CO₂ migration in water-saturated porous sandstone: *Exploration Geophysics*, **35**, 25-332.
- Xue, Z., Oshumi, T., and Koide, H., 2005, An experimental study on seismic monitoring of CO₂ flooding in two sandstones: *Energy*, **30**, 2352-2359.
- Xue, Z., Tanase, D., Saito, H., Nobuoka, D., and Watanabe, J., 2005, Time-lapse crosswell seismic tomography and well logging to monitor the injected CO₂ in an onshore aquifer, Nagaoka, Japan: 75th Annual International Meeting of the Society of Exploration Geophysicists Annual Meeting, Expanded Abstracts 24:1433
- Xue, Z., and Lei, X., 2006, Laboratory study of CO₂ migration in water-saturated anisotropic sandstone, based on P-wave velocity imaging: *Exploration Geophysics*, **37**, 10-18.
- Yin, C. S., Batzle, M. L., and Smith, B. J., 1992, Effects of partial liquid gas saturation on extensional wave attenuation in Berea sandstone: *Geophysical Research Letters*, **19**, 1399-1402.
- Yin, H., 1993, Acoustic velocity and attenuation of rocks, isotropy, intrinsic anisotropy, and stress-induced anisotropy: Ph.D. thesis, Stanford University, California.
- Zadler, B. J., Le Rousseau, J. H. L., Scales, J. A., and Smith, M. L., 2004, Resonant ultrasound spectroscopy: theory and application: *Geophysical Journal International*, **156**, 154-169.

- Zhan, X., Schwartz, L. M., Toksoz, M. N., Smith, W. C., and Morgan, F. D., 2010, Pore-scale modeling of electrical and fluid transport in Berea sandstone: *Geophysics*, **75**, F135.
- Zhang, Z. G., and Duan, Z. H., 2005b, An optimized molecular potential for carbon dioxide; *Journal of Chemical Physics*, **122**, 214507.
- Zhu, X., and Meng, Z. (Schwartz, M. (eds)), 2002, Actuators, piezoelectric ceramic, functional gradient: *Encyclopedia of Smart Material*: John Wiley and Sons.

Appendix A

Observed and Modelled Results

For each sample examined in this study, the samples were measured under dry, CO₂ saturated and water saturated conditions. Here, the full set of normalized P- and S-wave waveforms, the observed wave velocities, modelled Gassmann and Biot's wave velocities from all measurement conditions, and the observed and modelled differential attenuation coefficient under CO₂ saturation are shown including the conditions that were mentioned but not shown in chapter 6 and chapter 7. In addition, the computed amplitude spectra used in determining the differential attenuation coefficients for the CO₂ saturated P-and S-waves are also given here.

A.1 Porous Ceramic Rod

Sample	Mass (g)	Bulk volume (cm ³)	Bulk density (g/cm ³)	Grain volume (cm ³)	Grain density (g/cm ³)	Porosity (%)	Modal Pore size (μm)	Air permeability (mD)	Tortuosity
Porous Ceramic Rod	39.36	25.33	1.55	10.63	3.70	58.4	2.06	96.94	1.73

Table A.1: Petrophysical properties determined of the porous ceramic rod.

A.1.1 Dry Condition Results

The porous ceramic rod under a dry condition (pore space under vacuum), was measured at room temperature, $T = 23^\circ\text{C}$, while confining pressure varied through both pressurization and depressurization. The dry sample was also measured while being heated where a constant confining pressure of 10 MPa was applied. Here, the observed waveforms and the wave velocities from these two dry measurement runs are given.

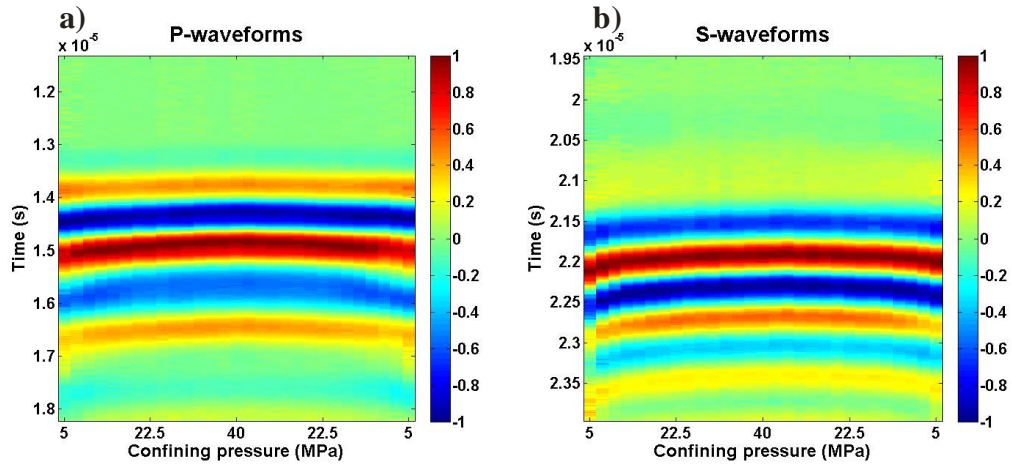


Figure A.1: Normalized (a) P-waves (b) and S-waves waveforms obtained under dry conditions at $T = 23^\circ\text{C}$ plotted as a function of confining pressure displayed as coloured amplitudes for the porous ceramic rod.

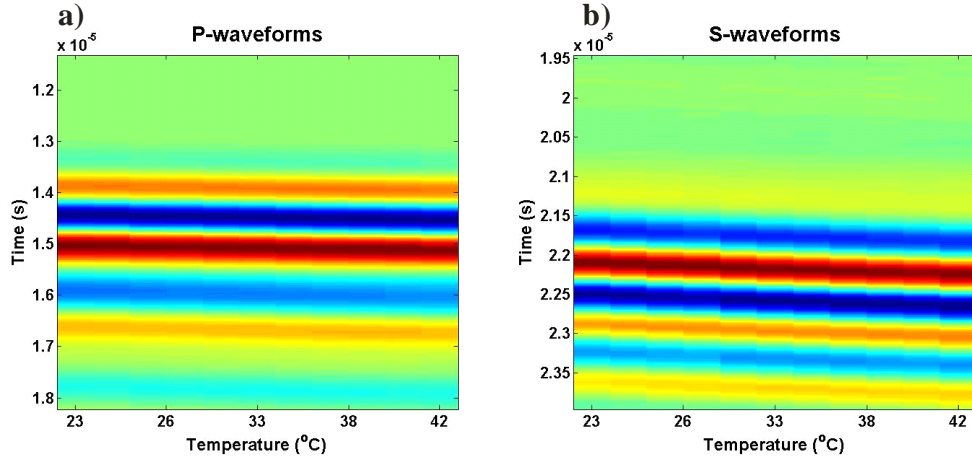


Figure A.2: Normalized (a) P-waves (b) and S-waves waveforms obtained under heated dry conditions at a constant confining pressure of 10 MPa, plotted as a function of temperature and displayed as coloured amplitudes for the porous ceramic rod.

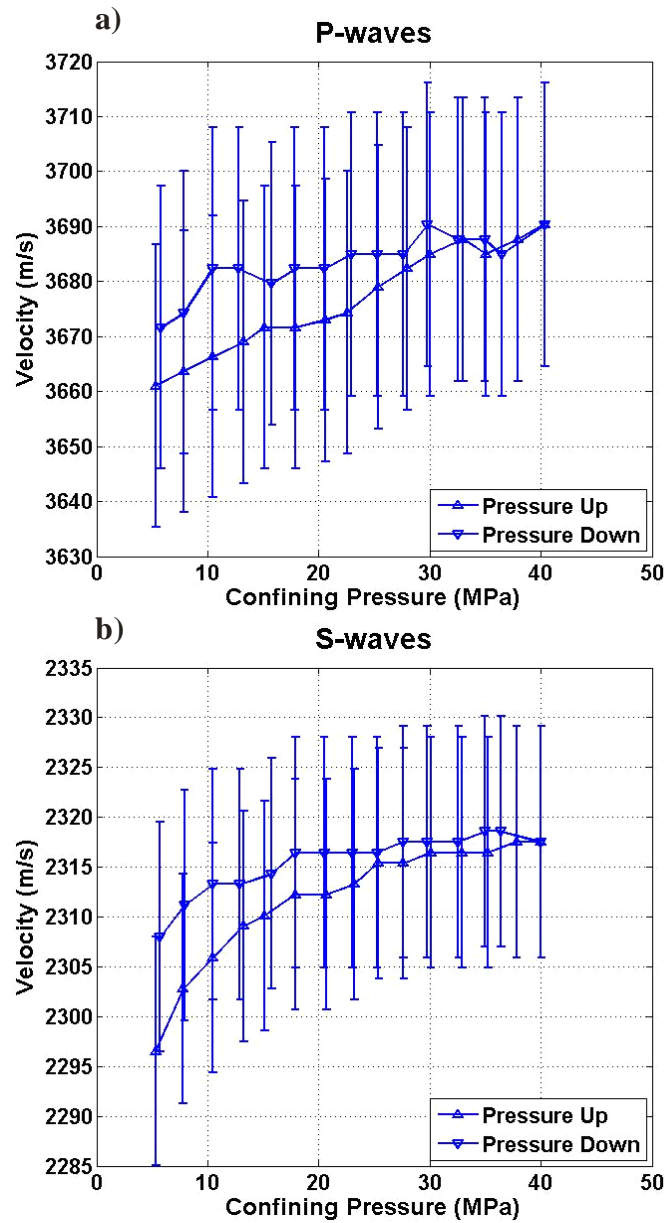


Figure A.3: Dry P-wave (a) and S-wave (b) velocities of the waveforms obtained under dry conditions at $T = 23^\circ\text{C}$ as a function of confining pressure with their respective errors for the porous ceramic rod.

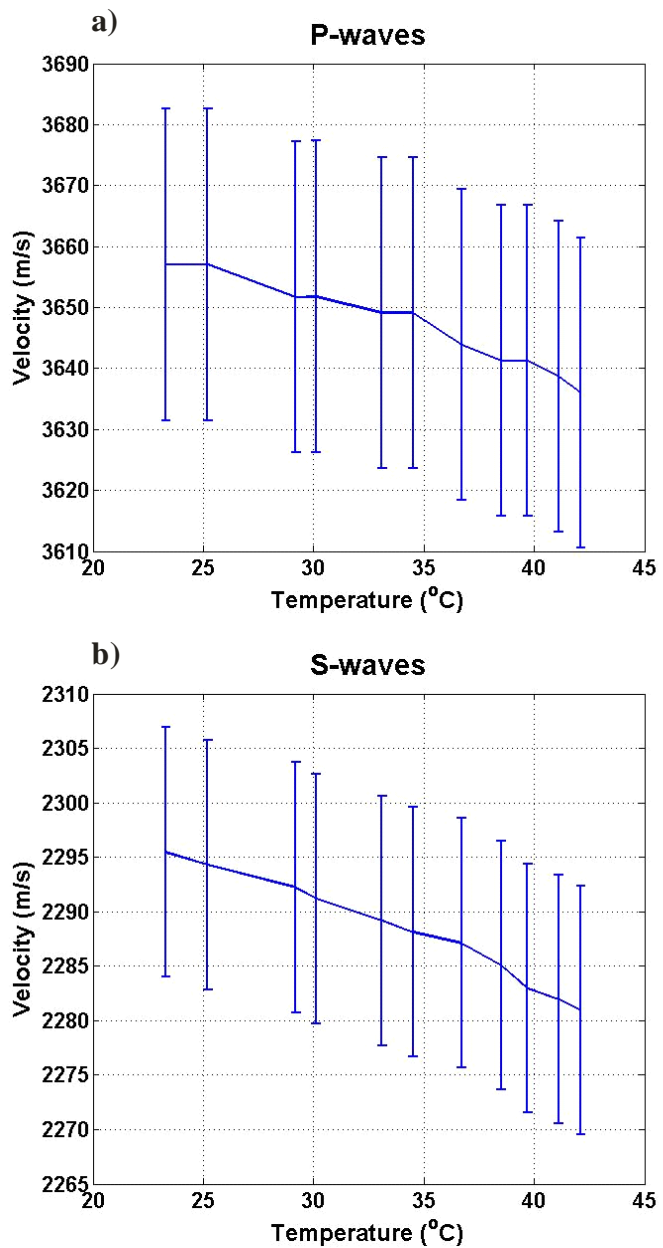


Figure A.4: (a) P-waves (b) and S-wave velocities obtained under heated dry conditions at a constant confining pressure of 10 MPa, plotted as a function of temperature with their respective errors.

T = 23°C						
Confining Pressure (MPa)	Vp (m/s)			Vs (m/s)		
5	3661	±	26	2297	±	11
7.5	3664	±	26	2303	±	12
10	3666	±	26	2306	±	12
12.5	3669	±	26	2309	±	12
15	3672	±	26	2310	±	12
17.5	3672	±	26	2312	±	12
20	3673	±	26	2312	±	12
22.5	3674	±	26	2313	±	12
25	3679	±	26	2315	±	12
27.5	3682	±	26	2315	±	12
30	3685	±	26	2316	±	12
32.5	3688	±	26	2316	±	12
35	3685	±	26	2316	±	12
37.5	3688	±	26	2318	±	12
40	3690	±	26	2318	±	12
37.5	3685	±	26	2319	±	12
35	3688	±	26	2319	±	12
32.5	3688	±	26	2318	±	12
30	3690	±	26	2318	±	12
27.5	3685	±	26	2318	±	12
25	3685	±	26	2316	±	12
22.5	3685	±	26	2316	±	12
20	3682	±	26	2316	±	12
17.5	3682	±	26	2316	±	12
15	3680	±	26	2314	±	12
12.5	3682	±	26	2313	±	12
10	3682	±	26	2313	±	12
7.5	3674	±	26	2311	±	12
5	3672	±	26	2308	±	12

Table A.2: Dry P-and S-wave velocities of the porous ceramic rod at T = 23°C under various confining pressures.

Pc = 10 MPa					
Temperature (°C)	Vp (m/s)		Vs (m/s)		
23.3	3657	± 26	2295	± 11	
25.2	3657	± 26	2294	± 11	
29.2	3652	± 26	2292	± 11	
30.1	3652	± 26	2291	± 11	
33.1	3649	± 26	2289	± 11	
34.5	3649	± 26	2288	± 11	
36.7	3644	± 26	2287	± 11	
38.5	3641	± 25	2285	± 11	
39.7	3641	± 25	2283	± 11	
41.1	3639	± 25	2282	± 11	
42.1	3636	± 25	2281	± 11	

Table A.3: Dry P-and S-wave velocities of the porous ceramic rod at $P_c = 10$ MPa while under various temperatures.

A.1.2 CO₂ saturated Results

In this section, provided are the observed waveforms, the observed wave velocities, Gassmann and Biot's modelled wave velocities, the observed amplitude spectra for all waveforms, the observed differential attenuation coefficient, and the Biot's modelled differential attenuation coefficient for all CO₂ saturated measurements that were conducted in this study for the porous ceramic rod. The observed and modeled results pertaining to the constant temperature runs will be given first, and is followed by the results of the constant pore pressure runs.

Constant Temperature Runs

Constant temperature measurements for the porous ceramic rod were conducted at 23 °C, 28°C, 40°C and 45°C while pore pressure varied.

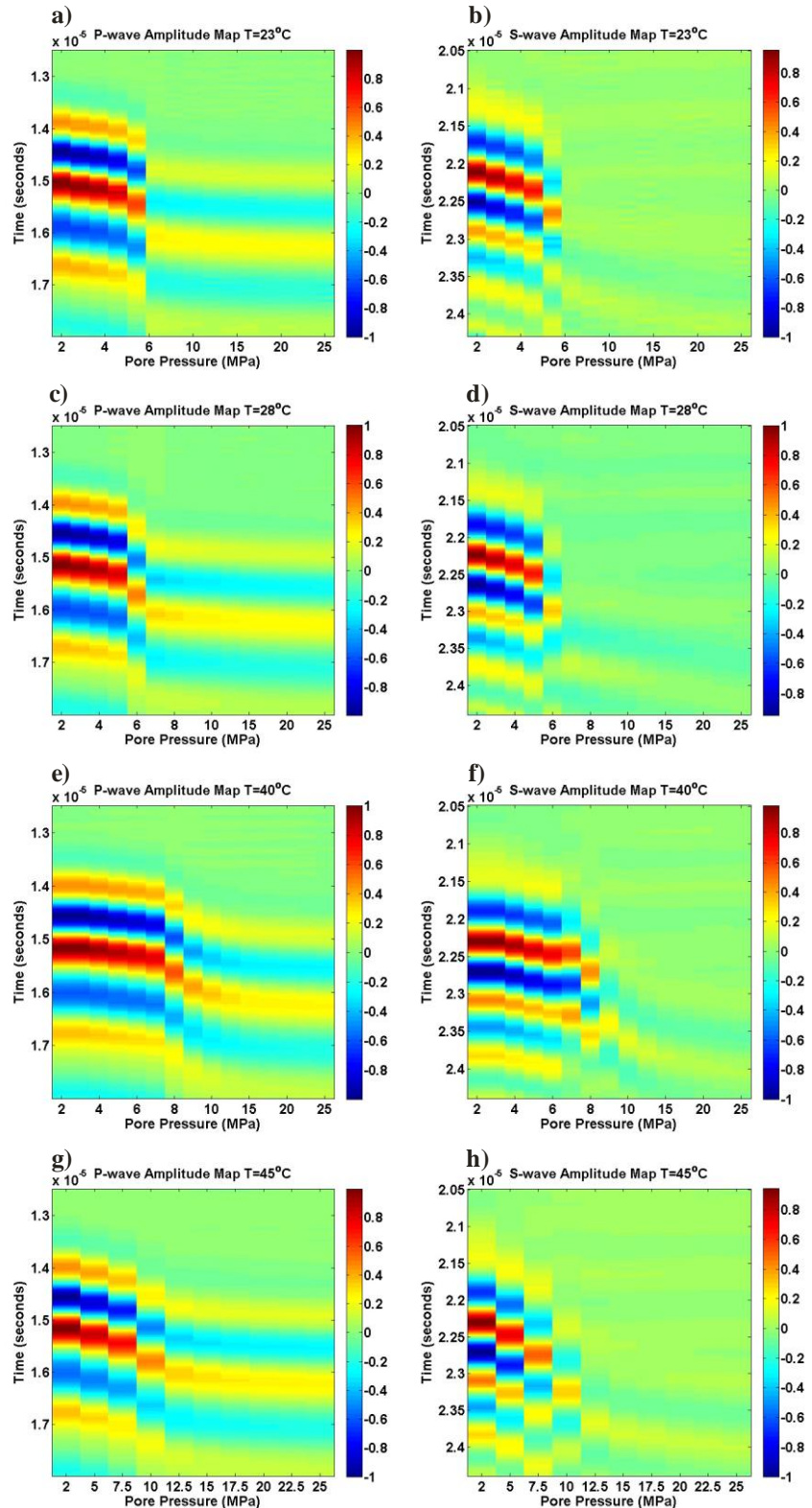


Figure A.5: Normalized P- and S-wave waveforms of the CO_2 saturated porous ceramic rod displayed as a function of pore pressures collected during the constant temperature runs of a) and b) $T = 23^\circ\text{C}$, c) and d) $T = 28^\circ\text{ C}$, e) and f) $T = 40^\circ\text{C}$, and g) and h) $T = 45^\circ\text{C}$. A constant differential pressure of 15 MPa was maintained throughout each measurement run.

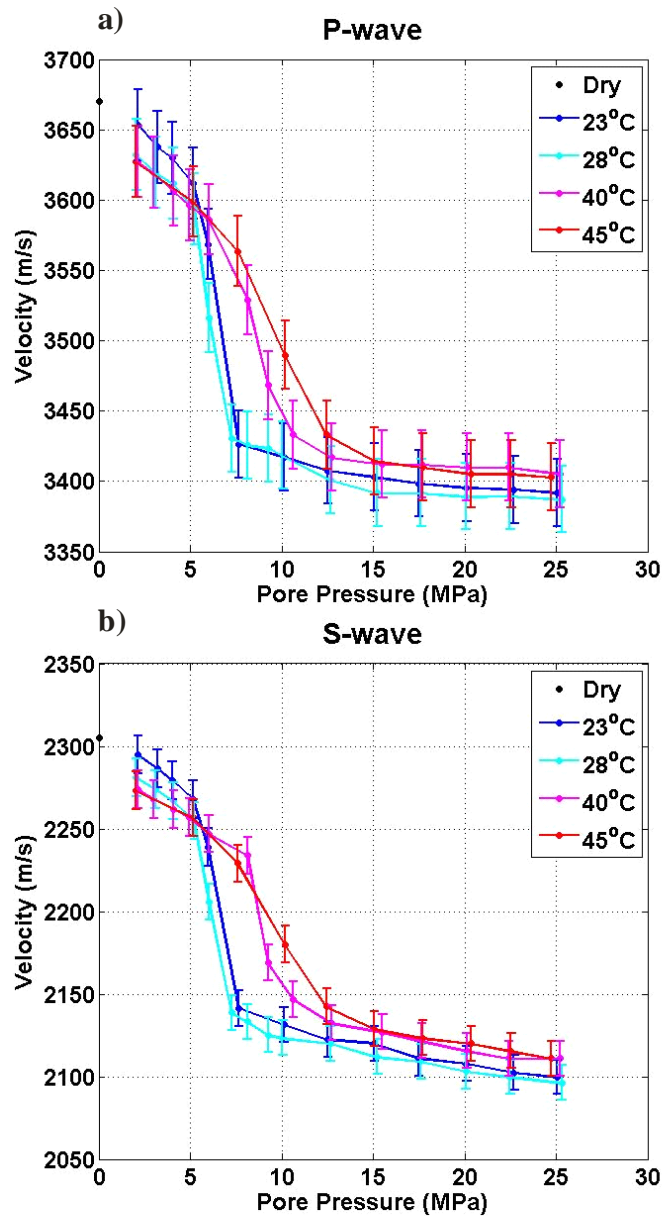


Figure A.6: P-wave (a) and S-wave (b) velocities with their respective errors measured of the porous ceramic rod saturated with CO₂ for all constant temperature runs and when the sample is not saturated (black dot at P_p = 0 MPa).

T = 23 °C						
Pore Pressure (MPa)	Vp (m/s)			Vs (m/s)		
2	3653	±	26	2295	±	11
3	3638	±	25	2286	±	11
4	3630	±	25	2279	±	11
5	3612	±	25	2268	±	11
6	3568	±	25	2239	±	11
7.5	3427	±	24	2141	±	11
10	3417	±	24	2131	±	11
12.5	3408	±	24	2123	±	11
15.05	3403	±	24	2120	±	11
17.5	3398	±	24	2111	±	11
20	3395	±	24	2108	±	11
22.5	3394	±	24	2102	±	11
25	3392	±	24	2100	±	10

Table A.4: CO₂ saturated P-and S-wave velocities of the porous ceramic rod for the T = 23 °C constant temperature run, while under a constant differential pressure of 15 MPa.

T = 28 °C						
Pore Pressure (MPa)	Vp (m/s)			Vs (m/s)		
2	3632	±	25	2281	±	11
3	3619	±	25	2274	±	11
4	3612	±	25	2267	±	11
5	3594	±	25	2255	±	11
6	3516	±	25	2206	±	11
7	3431	±	24	2139	±	11
8	3426	±	24	2133	±	11
9	3424	±	24	2125	±	11
10	3418	±	24	2123	±	11
12.5	3401	±	24	2120	±	11
15	3392	±	24	2112	±	11
17.5	3392	±	24	2109	±	11
20	3389	±	24	2103	±	11
22.5	3389	±	24	2100	±	10
25	3387	±	24	2096	±	10

Table A.5: CO₂ saturated P-and S-wave velocities of the porous ceramic rod for the T = 28 °C constant temperature run, while under a constant differential pressure of 15 MPa.

T = 40 °C						
Pore Pressure (MPa)	Vp (m/s)			Vs (m/s)		
2	3627	±	25	2274	±	11
3	3619	±	25	2268	±	11
4	3606	±	25	2262	±	11
5	3596	±	25	2257	±	11
6	3586	±	25	2247	±	11
8	3529	±	25	2234	±	11
9	3468	±	24	2169	±	11
10	3433	±	24	2147	±	11
12.5	3417	±	24	2132	±	11
15	3412	±	24	2127	±	11
17.5	3412	±	24	2122	±	11
20	3410	±	24	2115	±	11
22.5	3410	±	24	2111	±	11
25	3405	±	24	2111	±	11

Table A.6: CO₂ saturated P-and S-wave velocities of the porous ceramic rod for the T = 40°C constant temperature run, while under a constant differential pressure of 15 MPa.

T = 45 °C						
Pore Pressure (MPa)	Vp (m/s)			Vs (m/s)		
2	3627	±	25	2273	±	11
5	3599	±	25	2257	±	11
7.5	3563	±	25	2229	±	11
10	3490	±	24	2180	±	11
12.5	3433	±	24	2142	±	11
15	3415	±	24	2129	±	11
17.5	3410	±	24	2123	±	11
20	3405	±	24	2120	±	11
22.5	3405	±	24	2115	±	11
25	3403	±	24	2111	±	11

Table A.7: CO₂ saturated P-and S-wave velocities of the porous ceramic rod for the T = 45°C constant temperature run, while under a constant differential pressure of 15 MPa.

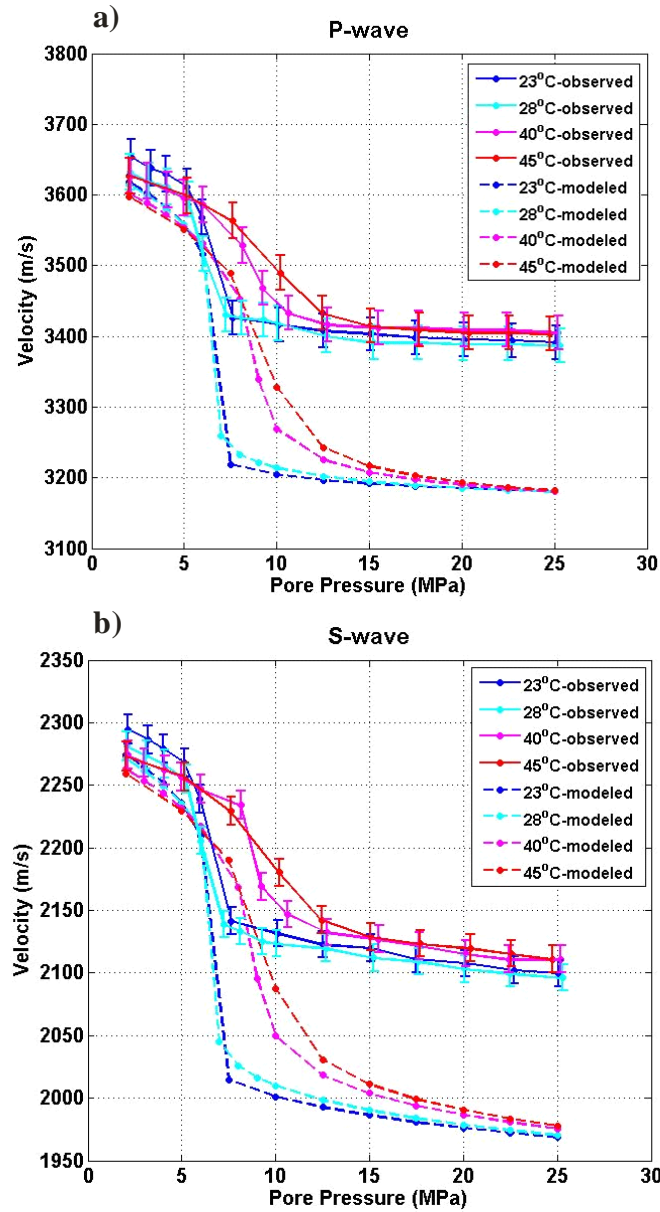


Figure A.7: Observed and Gassmann's modelled P- wave (a) and S-wave (b) CO_2 saturated velocities for $T = 23^\circ\text{C}, 28^\circ\text{C}, 40^\circ\text{C}, 45^\circ\text{C}$ constant temperature runs. The observed wave velocities are shown with their respective errors.

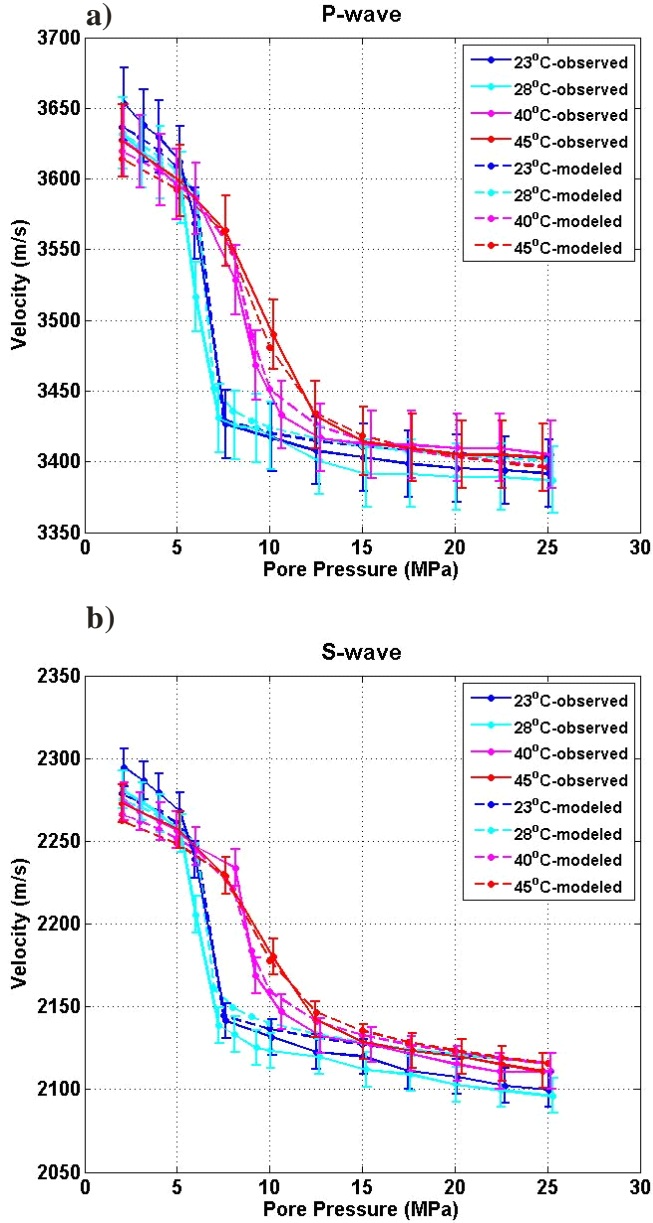


Figure A.8: Observed and Biot's modelled P- wave (a) and S-wave (b) CO₂ saturated velocities for T = 23°C, 28°C, 40°C, 45°C constant temperature runs. The observed wave velocities are shown with their respective errors.

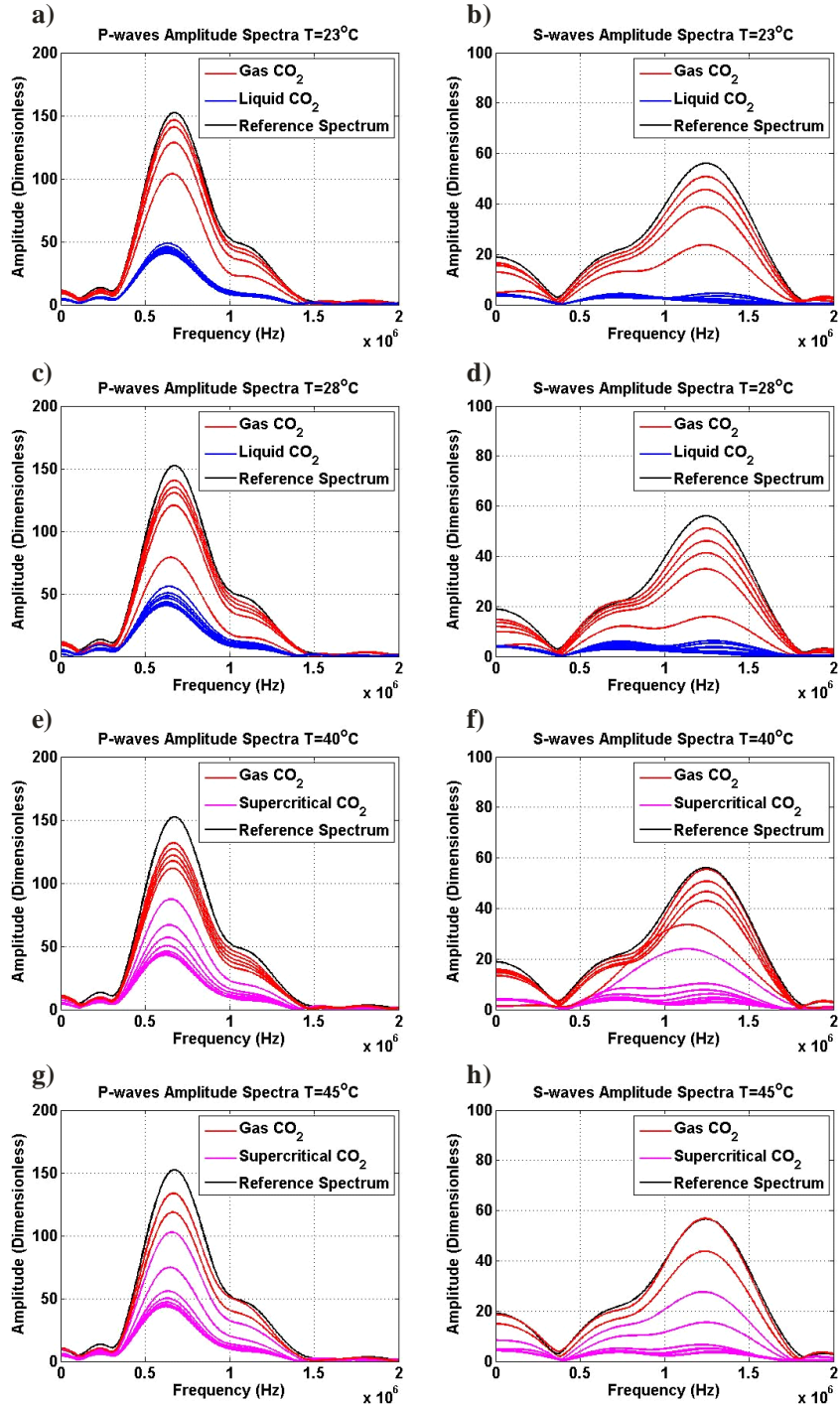


Figure A.9: The amplitude spectra of the collected P- and S-waves of the CO₂ saturated porous ceramic rod for a) and b) T = 23°C, c) and d) T = 28°C, e) and f) T = 40°C, and g) and h) T = 45°C constant temperature runs as a function of frequency. The prevailing CO₂ phase states of the signals are determined from the pressure and temperature conditions applied. The reference spectrum is of the signal collected at T = 23°C and P_p = 2 MPa of CO₂.

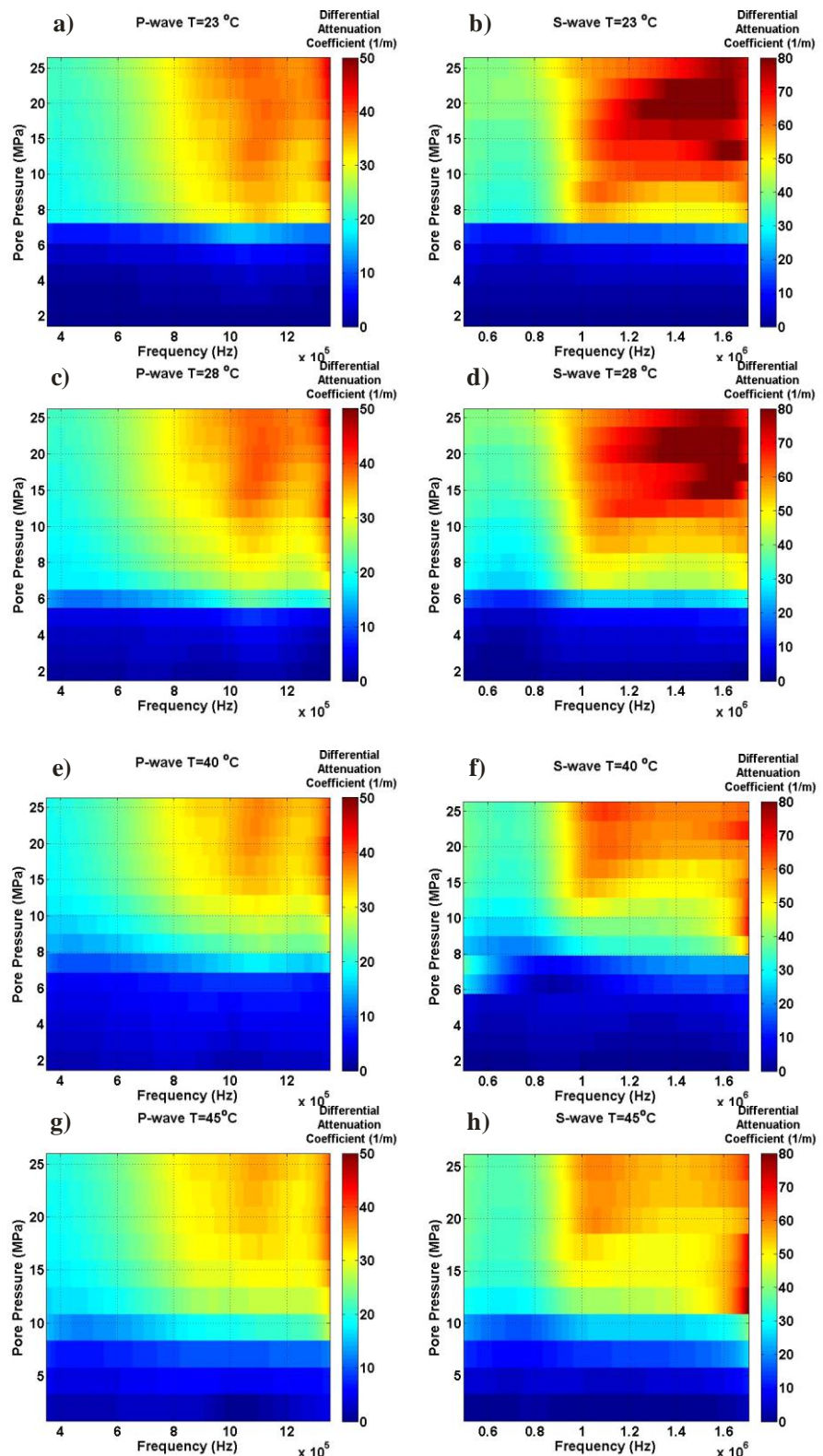


Figure A.10: Measured P- and S-wave differential attenuation coefficient of the CO_2 saturated porous ceramic rod determined for a) and b) $T = 23^\circ\text{C}$, c) and d) $T = 28^\circ\text{C}$, e) and f) $T = 40^\circ\text{C}$, and g) and h) $T = 45^\circ\text{C}$ constant temperature runs as a function of frequency and pore pressure.

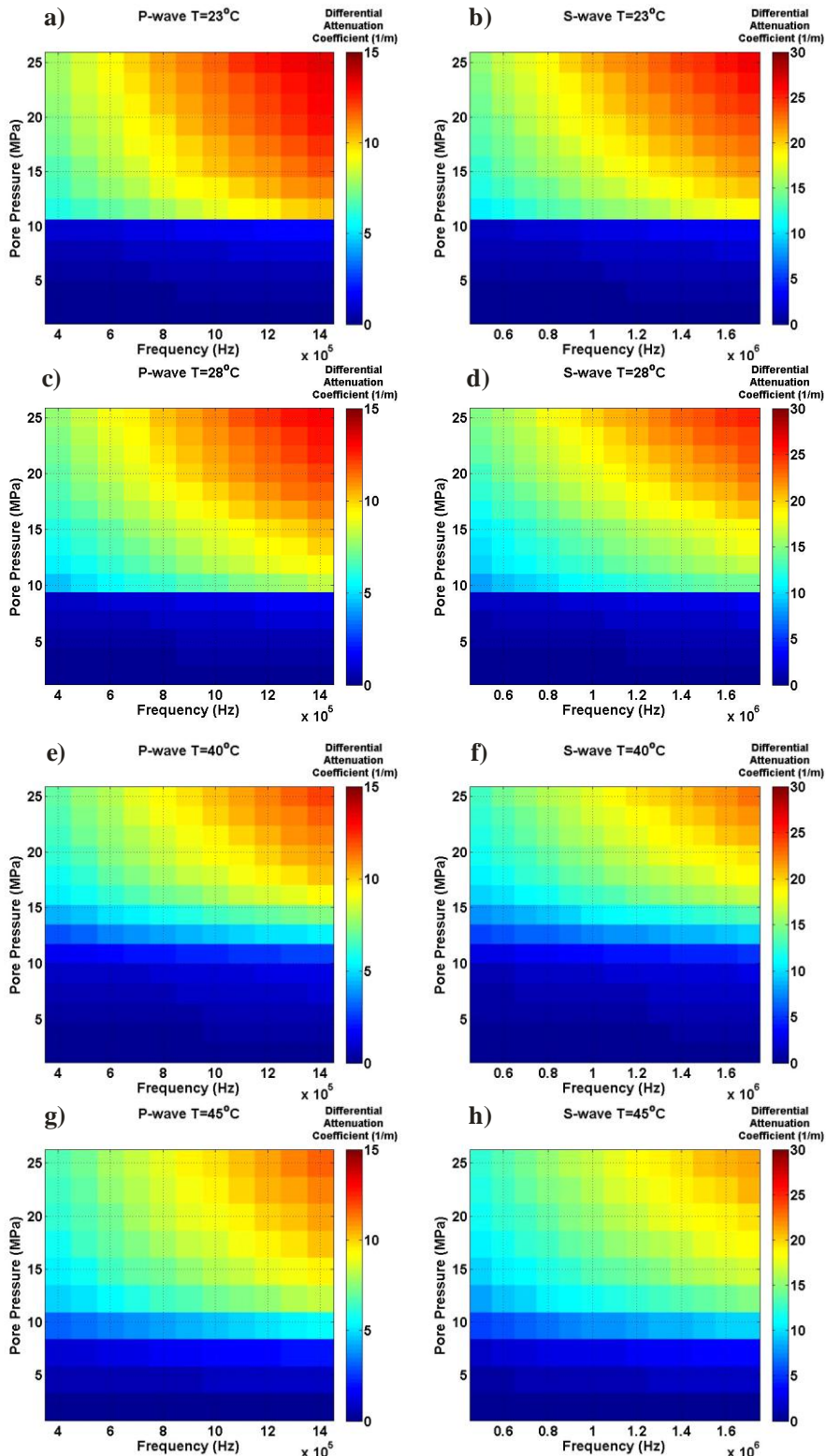


Figure A.11: Biot's modelled P- and S-wave differential attenuation coefficient of the CO_2 saturated porous ceramic rod determined for a) and b) $T = 23^\circ\text{C}$, c) and d) $T = 28^\circ\text{C}$, e) and f) $T = 40^\circ\text{C}$, and g) and h) $T = 45^\circ\text{C}$ constant temperature runs as a function of frequency and pore pressure.

Constant Pore Pressure Runs

Constant pore pressure runs for the porous ceramic rod were conducted at $P_p = 7 \text{ MPa}$, 10 MPa , and 25 MPa while temperature varied.

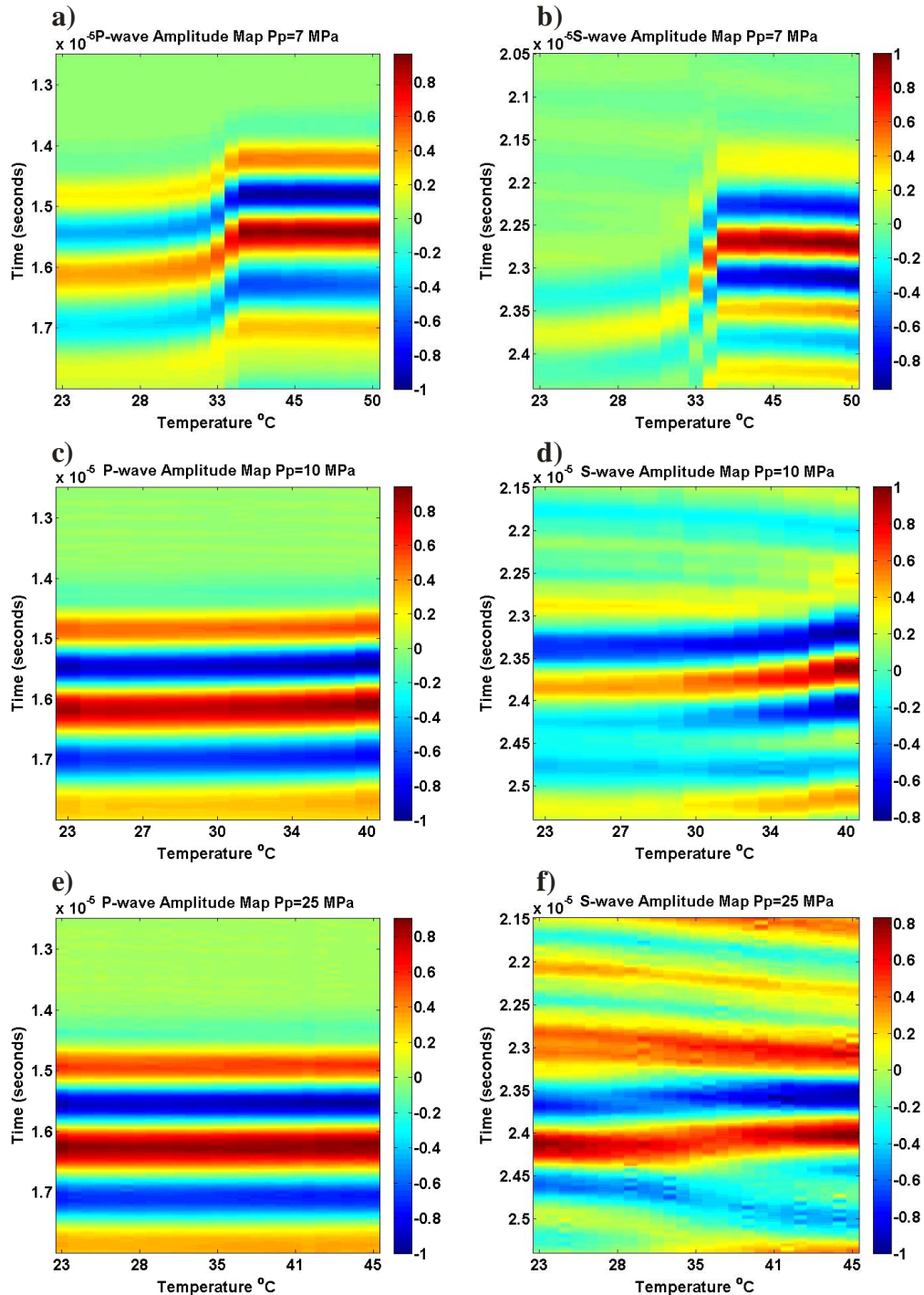


Figure A.12: Normalized P- and S-wave waveforms as a function of temperature collected during the constant pore pressure runs of a) and b) $P_p = 7 \text{ MPa}$, c) and d) $P_p = 10 \text{ MPa}$ and e) and f) $P_p = 25 \text{ MPa}$. A constant differential pressure of 15 MPa was maintained throughout each measurement run.

P_P = 7 MPa					
Temperature (°C)	V_P (m/s)		Temperature (°C)	V_S (m/s)	
22.6	3426	± 24	22.4	2133	± 11
23	3426	± 24	22.9	2133	± 11
23.9	3426	± 24	24.5	2135	± 11
25.2	3426	± 24	25.5	2137	± 11
26.1	3426	± 24	26.4	2139	± 11
27.1	3428	± 24	27.5	2140	± 11
27.8	3431	± 24	28.1	2140	± 11
28.8	3426	± 24	29.2	2142	± 11
30	3435	± 24	29.6	2142	± 11
30.5	3442	± 24	30.8	2154	± 11
32.1	3456	± 24	31.8	2159	± 11
33.3	3490	± 24	33.7	2190	± 11
35.6	3551	± 25	35.2	2216	± 11
37.3	3568	± 25	37.6	2236	± 11
37.9	3568	± 25	39.3	2236	± 11
39.1	3566	± 25	41.2	2236	± 11
41.5	3563	± 25	43	2237	± 11
42.8	3568	± 25	44.4	2237	± 11
44.5	3568	± 25	45.8	2236	± 11
45.6	3568	± 25	47.2	2235	± 11
47.3	3566	± 25	48.9	2235	± 11
48.8	3571	± 25	50.8	2235	± 11
50.9	3566	± 25	-	-	-

Table A.8: CO₂ saturated P-and S-wave velocities of the porous ceramic rod for the P_P = 7 MPa constant pore pressure run, while under a constant differential pressure of 15 MPa.

P_p = 10 MPa							
Temperature (°C)	Vp (m/s)		Temperature (°C)	Vs (m/s)			
24.3	3421	±	24	24	2126	±	11
25.1	3421	±	24	24.8	2126	±	11
25.8	3421	±	24	26.3	2126	±	11
26.7	3421	±	24	27.2	2127	±	11
27.7	3424	±	24	28.2	2128	±	11
28.8	3424	±	24	29.3	2130	±	11
29.8	3421	±	24	30.4	2130	±	11
30.9	3424	±	24	31.4	2130	±	11
32.2	3424	±	24	32.6	2131	±	11
33.3	3424	±	24	33.8	2135	±	11
34.3	3421	±	24	35.7	2135	±	11
35.1	3424	±	24	37	2136	±	11
37.1	3424	±	24	37.7	2143	±	11
37.7	3428	±	24	40.3	2146	±	11
40.3	3433	±	24	-	-	-	-

Table A.9: CO₂ saturated P-and S-wave velocities of the porous ceramic rod for the P_p = 10 MPa constant pore pressure run, while under a constant differential pressure of 15 MPa.

P_p = 25 MPa					
Temperature (°C)	V_p (m/s)		Temperature (°C)	V_s (m/s)	
22.3	3398	± 24	22.3	2101	± 11
23	3394	± 24	22.7	2099	± 10
23.4	3394	± 24	23.8	2100	± 10
24.4	3394	± 24	24.9	2098	± 10
25.5	3394	± 24	26.1	2098	± 10
26.6	3392	± 24	27.1	2098	± 10
27.5	3392	± 24	28	2099	± 10
28.6	3394	± 24	29.1	2100	± 10
29.7	3389	± 24	30.3	2101	± 11
31	3389	± 24	31.7	2101	± 11
32.2	3394	± 24	32.9	2100	± 10
33.4	3398	± 24	33.9	2100	± 10
34.5	3398	± 24	35.2	2103	± 11
35.7	3401	± 24	36.4	2104	± 11
36.8	3401	± 24	37.4	2105	± 11
37.9	3398	± 24	38.5	2108	± 11
39	3401	± 24	39.5	2111	± 11
39.9	3398	± 24	40.4	2110	± 11
40.9	3398	± 24	41.4	2110	± 11
41.8	3405	± 24	42.1	2111	± 11
42.5	3401	± 24	42.9	2110	± 11
43.3	3405	± 24	43.6	2111	± 11
44	3403	± 24	44.3	2110	± 11
44.6	3405	± 24	44.9	2110	± 11
45.2	3403	± 24	45.5	2109	± 11

Table A.10: CO₂ saturated P-and S-wave velocities of the porous ceramic rod for the P_p = 25 MPa constant pore pressure run, while under a constant differential pressure of 15 MPa.

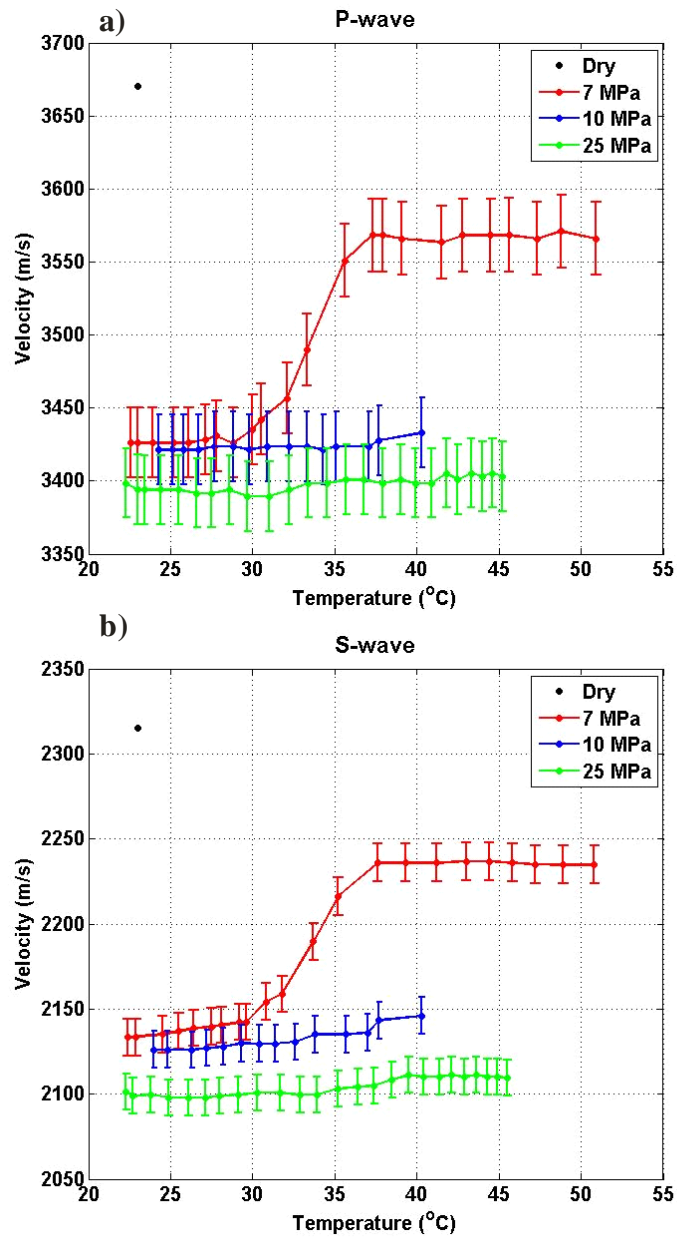


Figure A.13: P- wave (a) and S-wave (b) velocities with their respective errors measured of the sample saturated with CO₂ for all constant pore pressure runs and when the sample is not saturated (black dot at P_p = 0 MPa).

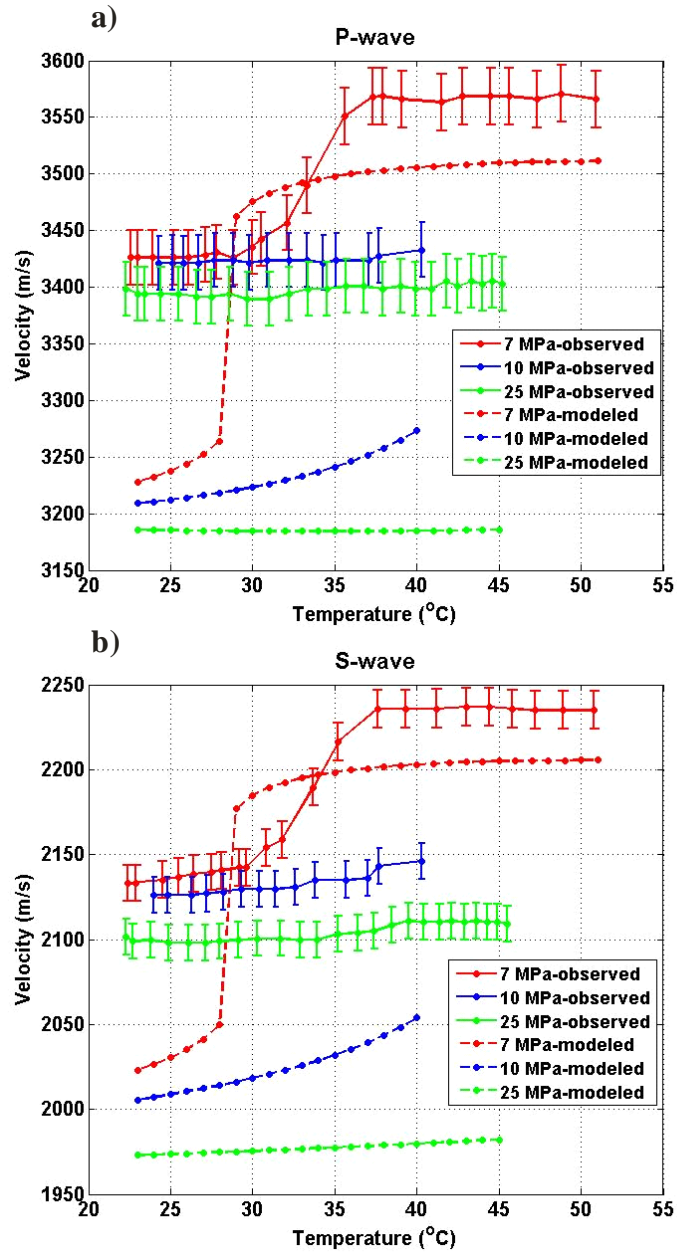


Figure A.14: Observed and Gassmann's modelled (a) P-wave and (b) S-wave CO_2 saturated velocities for $P_p = 7 \text{ MPa}$, $P_p = 10 \text{ MPa}$, and $P_p = 25 \text{ MPa}$ constant pore pressure runs. The observed wave velocities are shown with their respective errors.

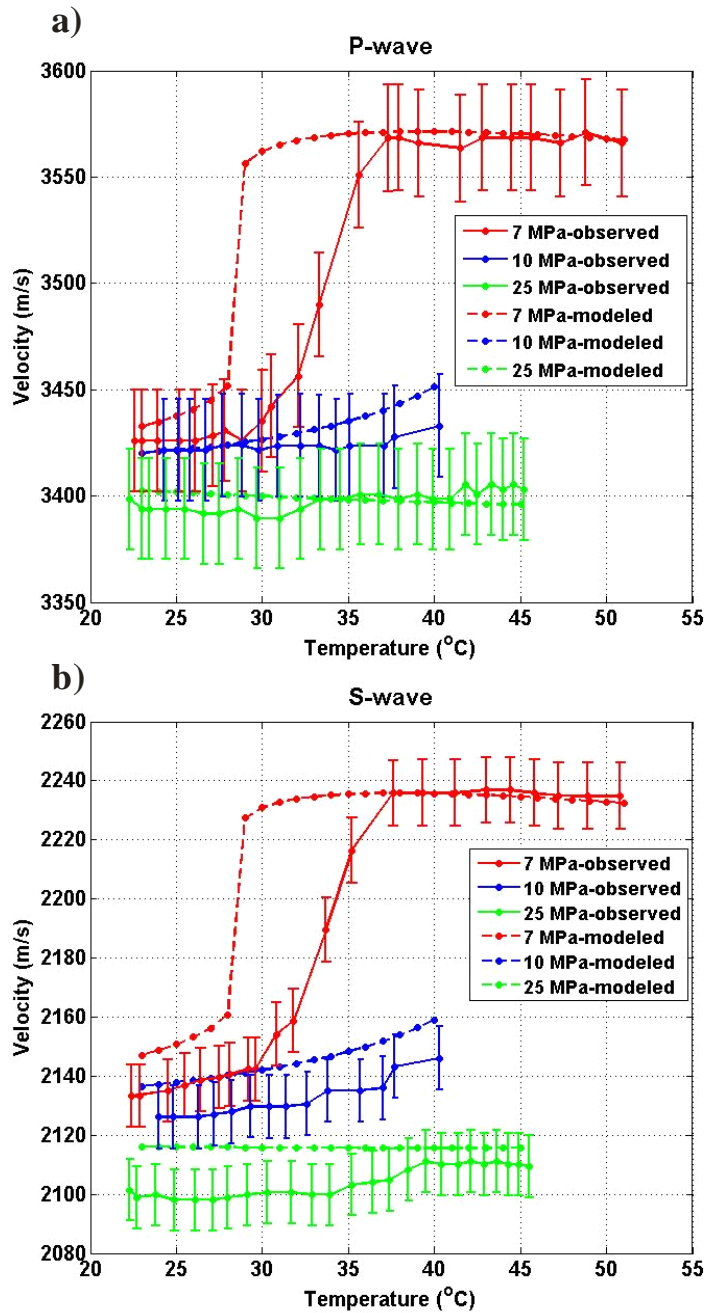


Figure A.15: Observed and Biot's modelled (a) P-wave and (b) S-wave CO_2 saturated velocities for $P_p = 7 \text{ MPa}$, $P_p = 10 \text{ MPa}$, and $P_p = 25 \text{ MPa}$ constant pore pressure runs. The observed wave velocities are shown with their respective errors.

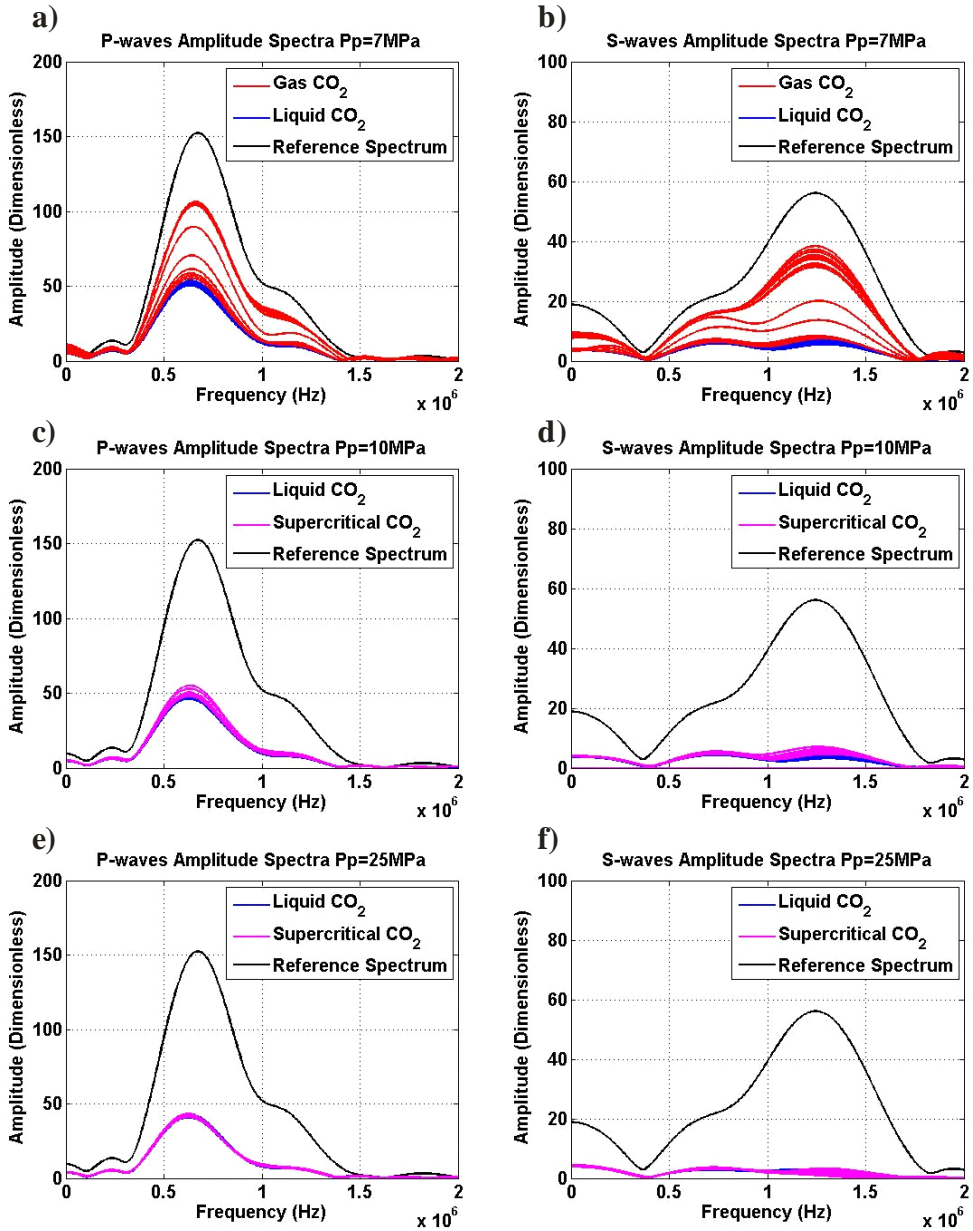


Figure A.16: The computed amplitude spectra of the collected P- and S-wave of the CO_2 saturated porous ceramic rod for a) and b) $P_p=7\text{ MPa}$, c) and d) $P_p=10\text{ MPa}$, and e) and f) $P_p=25\text{ MPa}$ constant temperature runs as a function of frequency. The prevailing CO_2 phase states of the signals are determined from the pressure and temperature conditions applied. The reference spectrum is of the signal collected at $T = 23^\circ\text{C}$ and $P_p = 2\text{ MPa}$ of CO_2 .

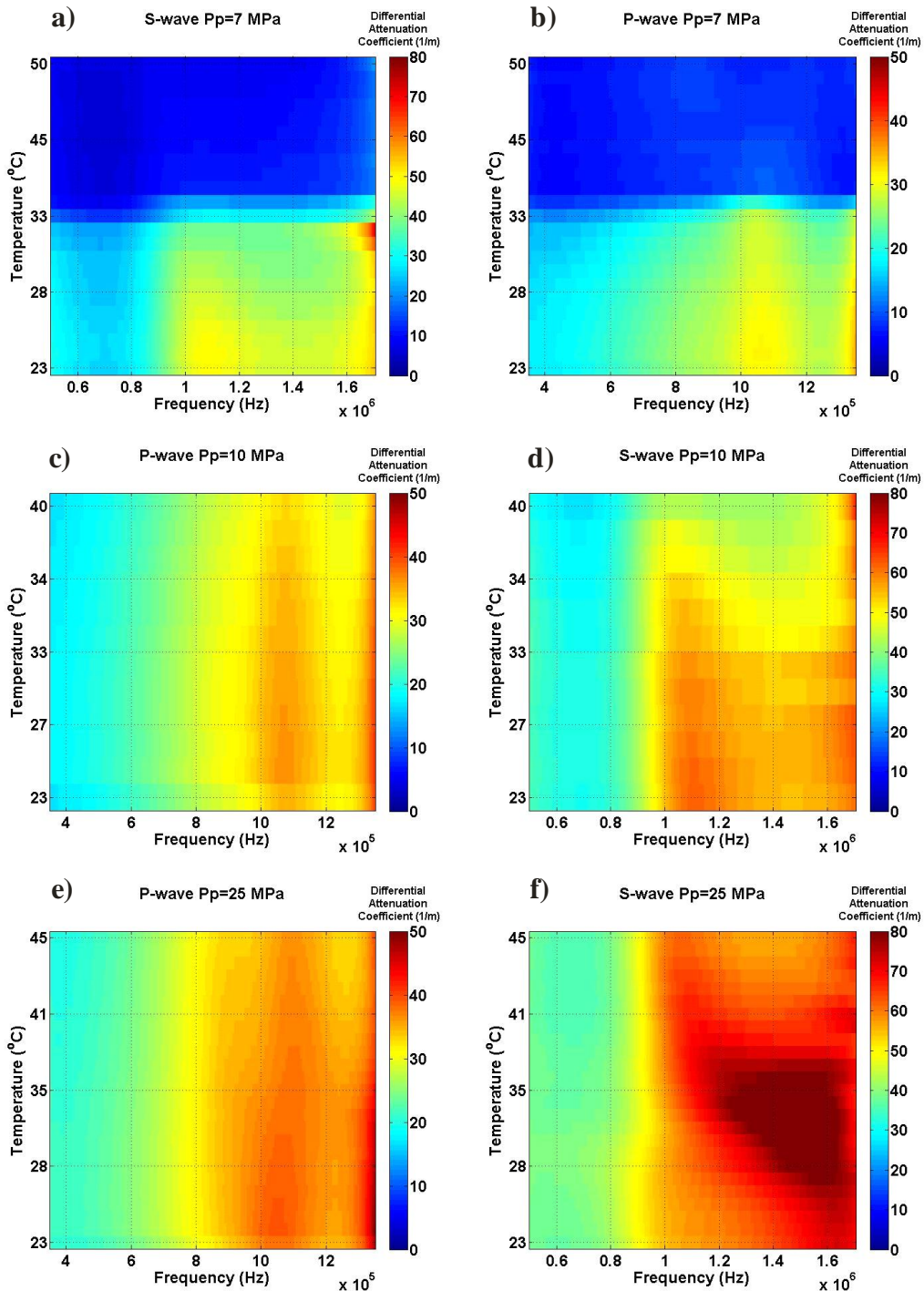


Figure A.17: Measured P- and S-wave differential attenuation coefficient of the CO_2 saturated porous ceramic rod determined for a) and b) $P_p = 7 \text{ MPa}$, c) and d) $P_p = 10 \text{ MPa}$, and e) and f) $P_p = 25 \text{ MPa}$ constant temperature runs as a function of frequency and pore pressure.

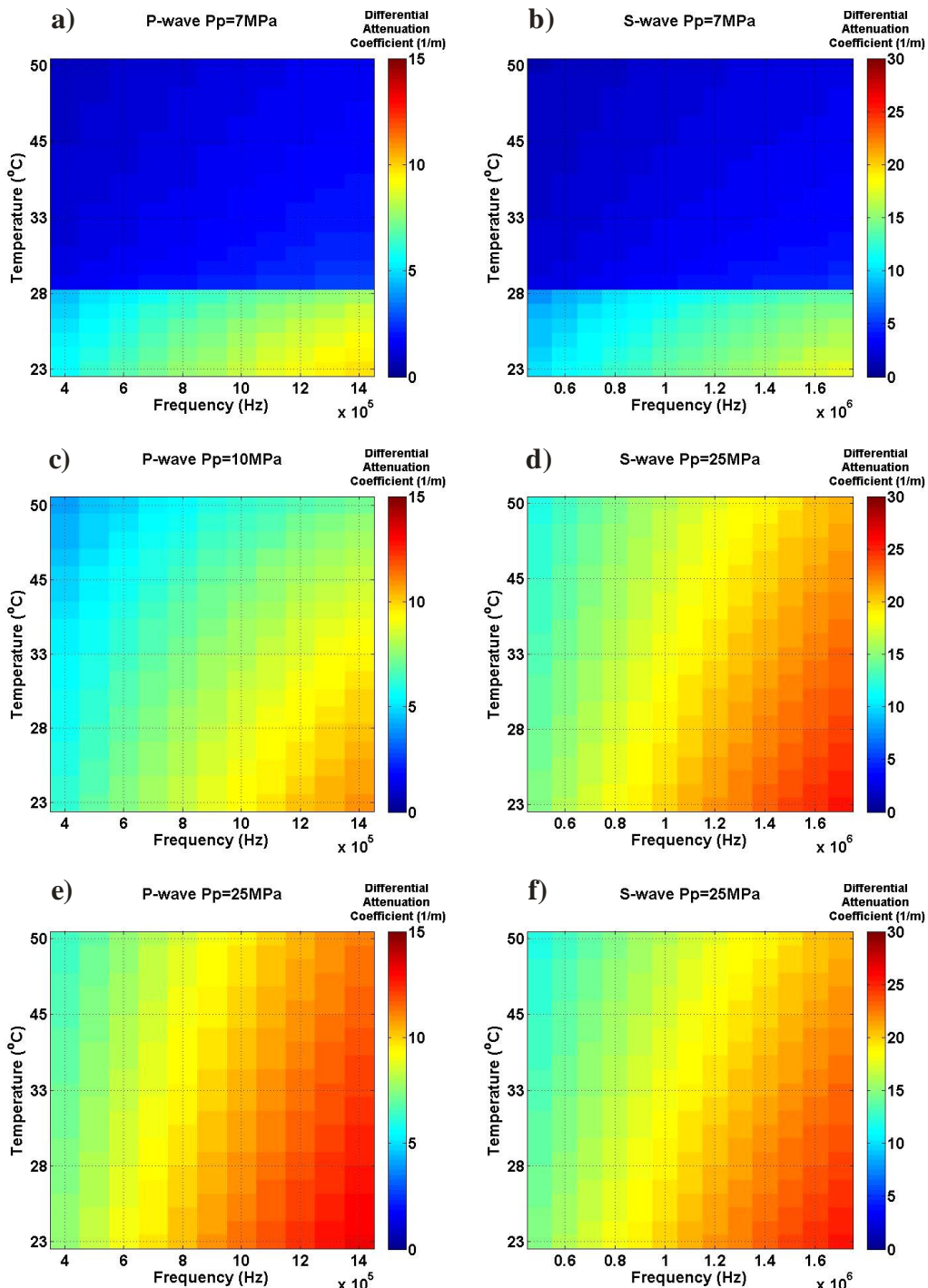


Figure A.18: Biot's modelled P- and S-wave differential attenuation coefficient of the CO_2 saturated porous ceramic rod determined for a) and b) $P_p = 7 \text{ MPa}$, c) and d) $P_p = 10 \text{ MPa}$, and e) and f) $P_p = 25 \text{ MPa}$ constant temperature runs as a function of frequency and pore pressure.

A.1.3 Water Saturated Results

The water saturated porous ceramic rod was only measured at $T = 23^\circ\text{C}$ as a function of pore pressure while under a constant differential pressure of 5 MPa. The resulting observed waveforms and the wave velocities are provided here.

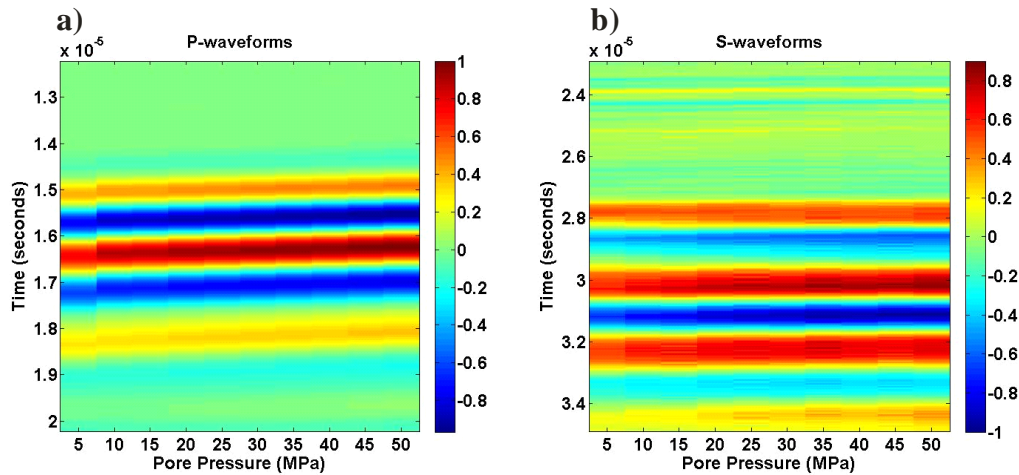


Figure A.19: Normalized P- (a) and S-wave (b) water saturated waveforms as a function of pore pressure of the porous ceramic rod. A constant differential pressure of 5 MPa was maintained throughout the measurement run.

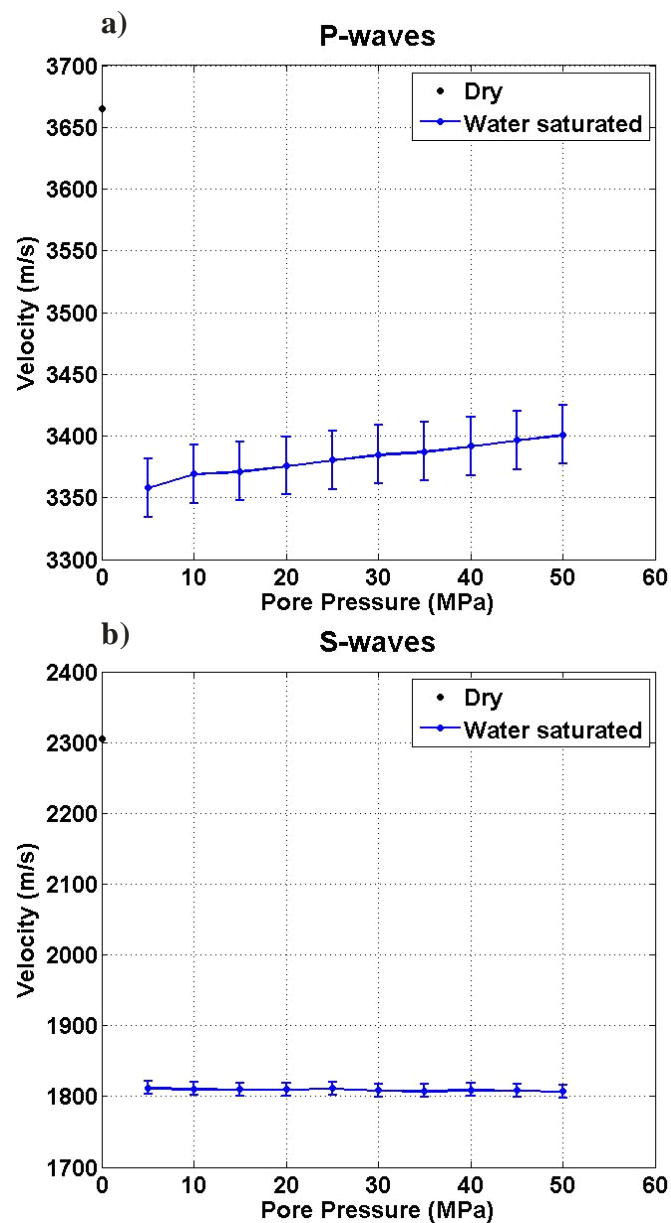


Figure A.20: P- (a) and S-wave (b) velocities with their respective errors measured of the water saturated porous ceramic rod under various pore pressures at $T = 23^\circ\text{C}$ and when the sample is not saturated (black dot at $P_p = 0 \text{ MPa}$).

Pore Pressure (MPa)	Vp (m/s)			Vs (m/s)		
5	3358	±	24	1812	±	9
10	3369	±	24	1811	±	9
15	3371	±	24	1810	±	9
20	3376	±	24	1810	±	9
25	3381	±	24	1811	±	9
30	3385	±	24	1809	±	9
35	3387	±	24	1808	±	9
40	3392	±	24	1810	±	9
45	3396	±	24	1809	±	9
50	3401	±	24	1807	±	9

Table A.11: Water saturated P-and S-wave velocities of the porous ceramic rod at T = 23°C for varying pore pressures, while under a constant differential pressure of 5 MPa.

A.2 Berea Sandstone

Sample	Mass (g)	Bulk volume (cm ³)	Bulk density (g/cm ³)	Grain volume (cm ³)	Grain density (g/cm ³)	Porosity (%)	Modal Pore size (μm)	Air permeability (mD)	Tortuosity
Berea Sandstone	43.24	22.02	2.15	17.79	2.45	19.0	11.33	237.65	3.9 ^a

Table A.12: Petrophysical properties determined of the Berea sandstone. ^a tortuosity value taken from Garrouch et al (2001)

A.2.1 Dry Condition Results

The Berea sandstone under a dry condition (pore space under vacuum), was measured twice at room temperature, T = 23°C, while confining pressure varied through both pressurization and depressurization. Here, the observed waveforms and the wave velocities from these two dry measurement runs are given.

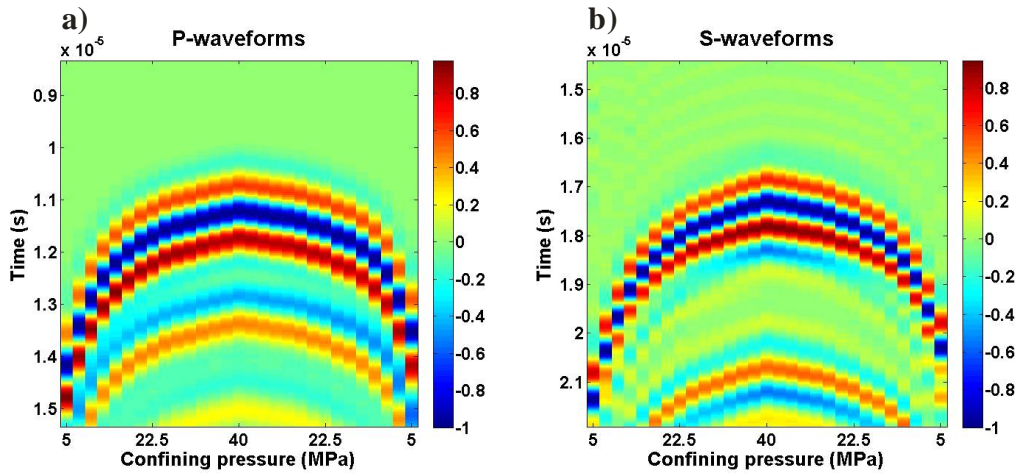


Figure A.21: Normalized (a) P- wave and (b) S-wave waveforms obtained under dry conditions at $T = 23^{\circ}\text{C}$ plotted as a function of confining pressure displayed as coloured amplitudes for the Berea sandstone. This is the first dry measurement run and was obtained prior to running the series of CO_2 measurements.

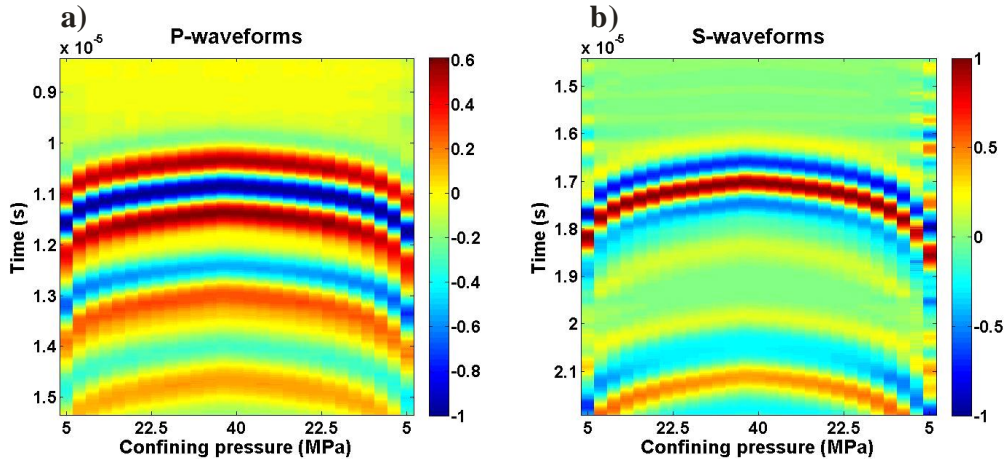


Figure A.22: Normalized (a) P- wave and (b) S-wave waveforms obtained under dry conditions at $T = 23^{\circ}\text{C}$ plotted as a function of confining pressure displayed as coloured amplitudes for the Berea sandstone. This is the second dry measurement run and was obtained after the running the series of CO_2 measurements.

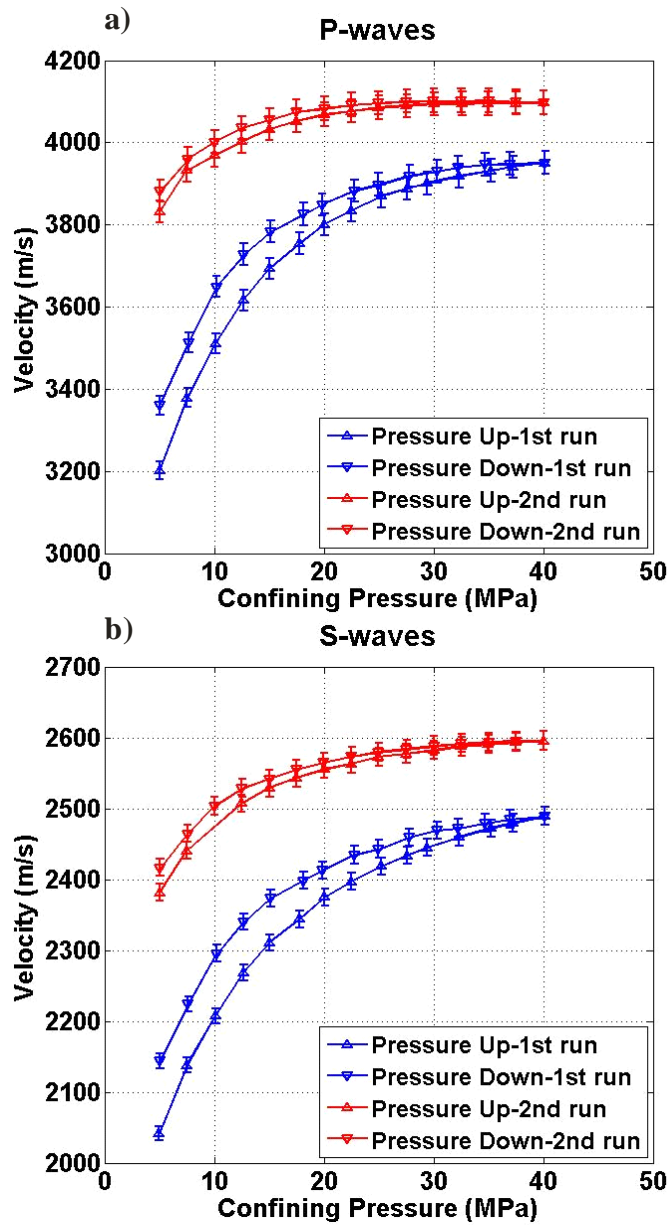


Figure A.23: Dry P-wave (a) and S-wave (b) velocities of the waveforms obtained under dry conditions at $T = 23^\circ\text{C}$ as a function of confining pressure with their respective errors of the two runs conducted for the Berea sandstone.

T = 23°C First run						
Confining Pressure (MPa)	Vp (m/s)			Vs (m/s)		
5	3202	±	22	2041	±	10
7.5	3379	±	24	2138	±	11
10	3510	±	25	2207	±	11
12.5	3616	±	25	2268	±	11
15	3693	±	26	2310	±	12
17.5	3754	±	26	2344	±	12
20	3801	±	27	2375	±	12
22.5	3835	±	27	2397	±	12
25	3870	±	27	2418	±	12
27.5	3888	±	27	2433	±	12
30	3901	±	27	2445	±	12
32.5	3918	±	27	2460	±	12
35	3931	±	28	2472	±	12
37.5	3941	±	28	2479	±	12
40	3951	±	28	2489	±	12
37.5	3948	±	28	2485	±	12
35	3947	±	28	2479	±	12
32.5	3939	±	28	2472	±	12
30	3930	±	28	2469	±	12
27.5	3919	±	27	2459	±	12
25	3898	±	27	2443	±	12
22.5	3883	±	27	2435	±	12
20	3849	±	27	2413	±	12
17.5	3826	±	27	2398	±	12
15	3783	±	26	2373	±	12
12.5	3727	±	26	2340	±	12
10	3649	±	26	2296	±	11
7.5	3512	±	25	2224	±	11
5	3360	±	24	2144	±	11

Table A.13: Dry P-and S-wave velocities of the Berea sandstone at T = 23°C under various confining pressures of the first measurement run.

T = 23°C Second run						
Confining Pressure (MPa)	Vp (m/s)			Vs (m/s)		
5	3832	±	27	2381	±	12
7.5	3932	±	28	2441	±	12
10	3969	±	28		±	
12.5	4003	±	28	2507	±	13
15	4033	±	28	2529	±	13
17.5	4052	±	28	2544	±	13
20	4068	±	28	2555	±	13
22.5	4076	±	29	2563	±	13
25	4085	±	29	2573	±	13
27.5	4089	±	29	2577	±	13
30	4094	±	29	2582	±	13
32.5	4094	±	29	2587	±	13
35	4095	±	29	2591	±	13
37.5	4096	±	29	2593	±	13
40	4097	±	29	2596	±	13
37.5	4100	±	29	2595	±	13
35	4103	±	29	2594	±	13
32.5	4102	±	29	2592	±	13
30	4102	±	29	2589	±	13
27.5	4101	±	29	2584	±	13
25	4096	±	29	2580	±	13
22.5	4092	±	29	2573	±	13
20	4083	±	29	2565	±	13
17.5	4075	±	29	2555	±	13
15	4055	±	28	2542	±	13
12.5	4036	±	28	2529	±	13
10	4002	±	28	2504	±	13
7.5	3961	±	28	2465	±	12
5	3882	±	27	2417	±	12

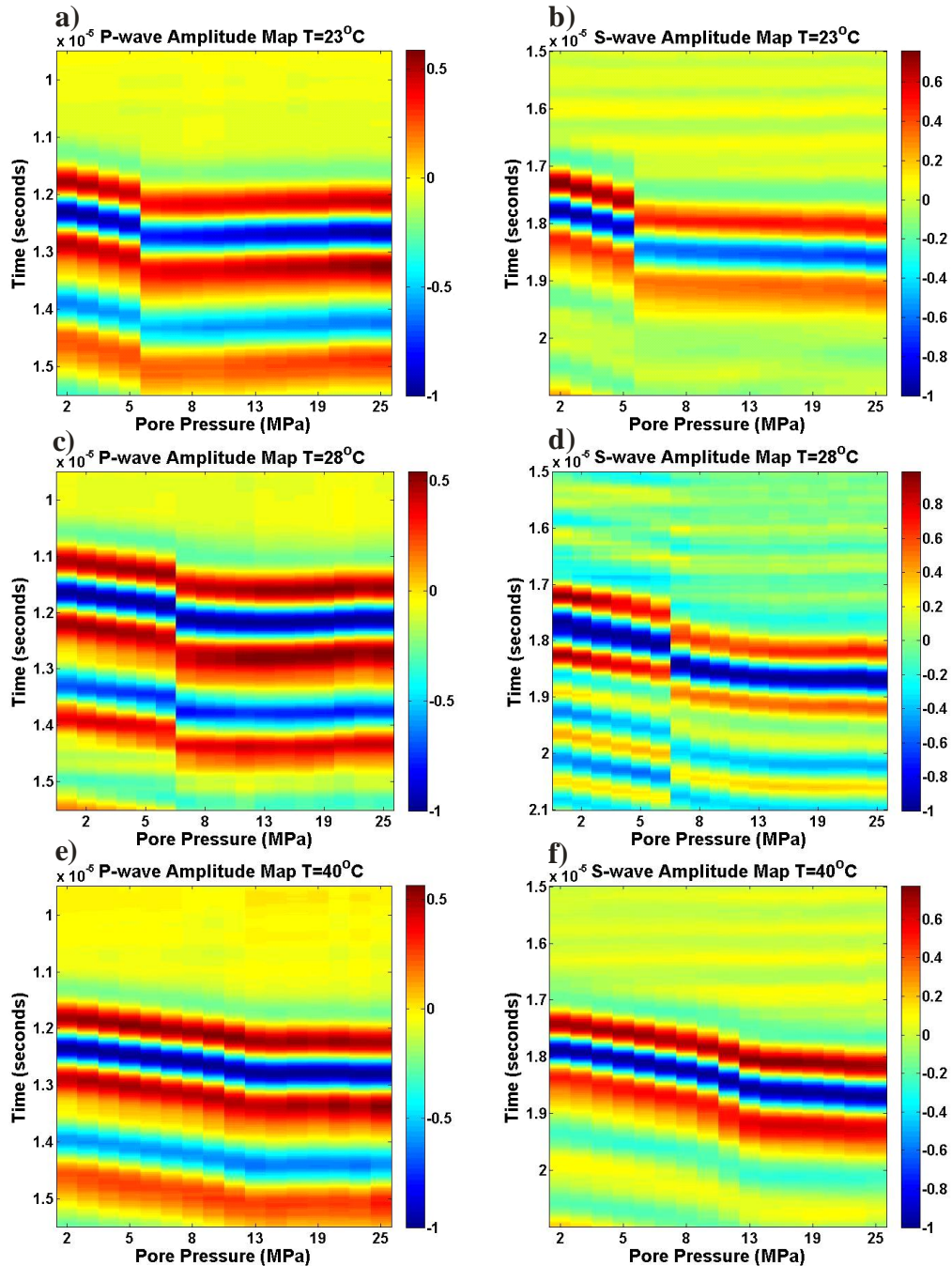
Table A.14: Dry P-and S-wave velocities of the Berea sandstone at T = 23°C under various confining pressures of the second measurement run.

A.2.2 CO₂ Saturated Results

The set of observed and modeled CO₂ saturated results that were provided in section A.1.2 for the porous ceramic rod, will be provided here for the Berea sandstone. Again, the observed and modeled results pertaining to the constant temperature runs will be given first, and is followed by the results of the constant pore pressure runs.

Constant Temperature Runs

Constant temperature measurements for the Berea sandstone were conducted at 23 °C, 28°C, 40°C, 45°C, and 55°C while pore pressure varied.



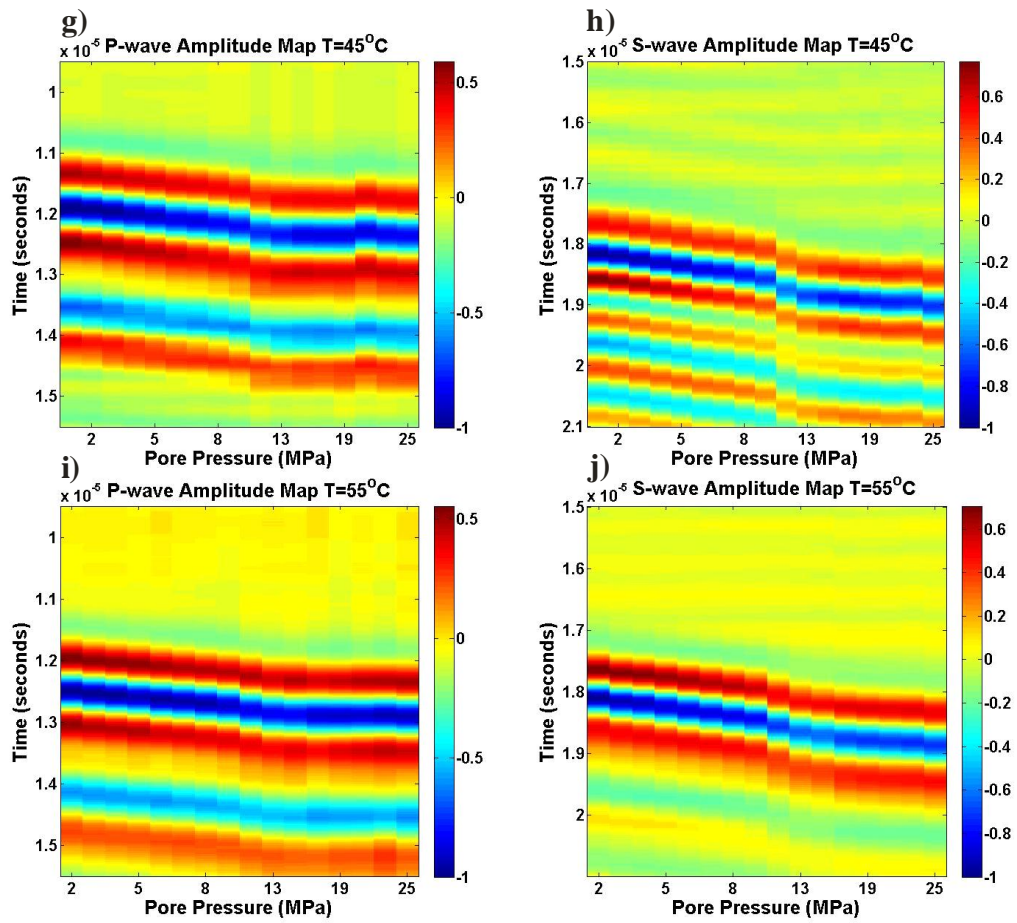


Figure A.24: Normalized P- and S-wave waveforms of the CO_2 saturated Berea sandstone displayed as a function of pore pressures collected during the constant temperature runs of a) and b) $T = 23^\circ\text{C}$, c) and d) $T = 28^\circ\text{C}$, e) and f) $T = 40^\circ\text{C}$, g) and h) $T = 45^\circ\text{C}$, and i) and j) $T = 55^\circ\text{C}$. A constant differential pressure of 15 MPa was maintained throughout each measurement run.

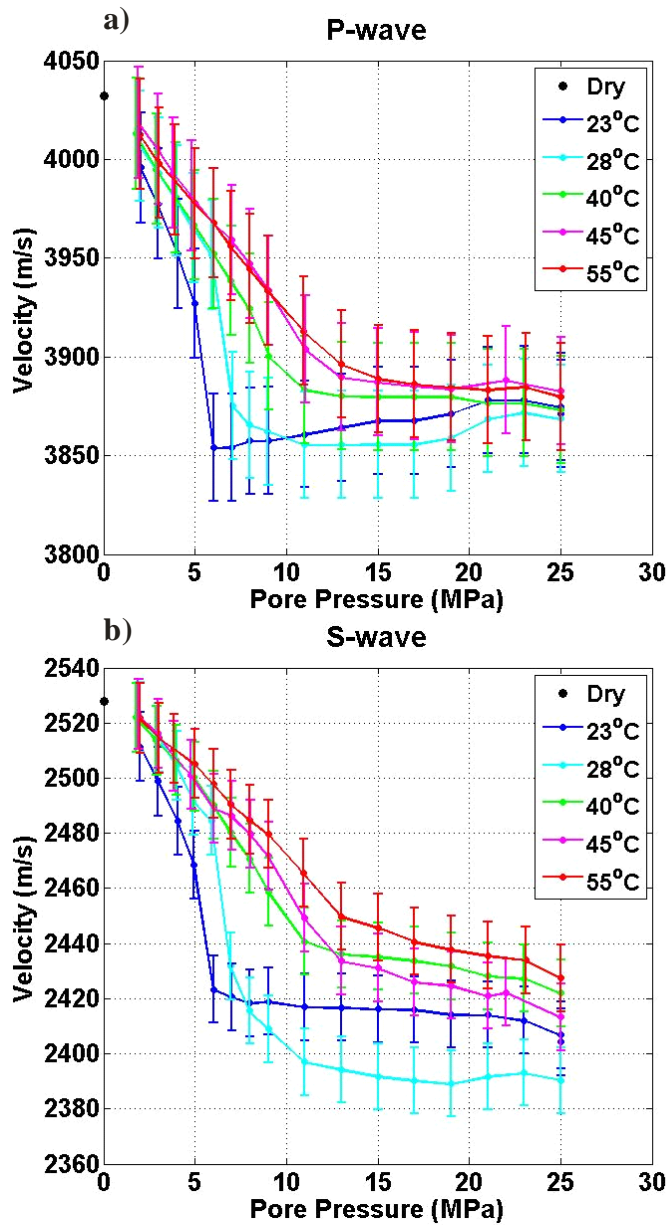


Figure A.25: Corrected P-wave (a) and S-wave (b) velocities with their respective errors measured of the Berea sandstone saturated with CO₂ for all constant temperature runs and when the sample is not saturated from the second dry measurement run (black dot at P_p = 0 MPa).

T = 23 °C						
Pore Pressure (MPa)	Vp (m/s)			Vs (m/s)		
2	3996	±	28	2511	±	13
3	3977	±	28	2499	±	12
4	3952	±	28	2484	±	12
5	3927	±	27	2468	±	12
6	3854	±	27	2423	±	12
7	3854	±	27	2421	±	12
8	3857	±	27	2418	±	12
9	3858	±	27	2419	±	12
11	3861	±	27	2417	±	12
13	3864	±	27	2417	±	12
15	3868	±	27	2416	±	12
17	3868	±	27	2416	±	12
19	3871	±	27	2414	±	12
21	3878	±	27	2414	±	12
23	3878	±	27	2412	±	12
25	3875	±	27	2407	±	12

Table A.15: CO₂ saturated P-and S-wave velocities of the Berea sandstone for the T = 23°C constant temperature run, while under a constant differential pressure of 15 MPa.

T = 28 °C						
Pore Pressure (MPa)	Vp (m/s)			Vs (m/s)		
2	4007	±	28	2522	±	13
3	3993	±	28	2515	±	13
4	3979	±	28	2505	±	13
5	3965	±	28	2492	±	12
6	3952	±	28	2484	±	12
7	3875	±	27	2432	±	12
8	3865	±	27	2416	±	12
9	3862	±	27	2409	±	12
11	3855	±	27	2397	±	12
13	3856	±	27	2394	±	12
15	3856	±	27	2392	±	12
17	3856	±	27	2390	±	12
19	3859	±	27	2389	±	12
21	3869	±	27	2392	±	12
23	3872	±	27	2393	±	12
25	3869	±	27	2390	±	12

Table A.16: CO₂ saturated P-and S-wave velocities of the Berea sandstone for the T = 28°C constant temperature run, while under a constant differential pressure of 15 MPa.

T = 40 °C						
Pore Pressure (MPa)	Vp (m/s)			Vs (m/s)		
2	4013	±	28	2522	±	13
3	3995	±	28	2514	±	13
4	3981	±	28	2506	±	13
5	3967	±	28	2500	±	13
6	3952	±	28	2490	±	12
7	3938	±	28	2480	±	12
8	3924	±	27	2471	±	12
9	3900	±	27	2459	±	12
11	3883	±	27	2441	±	12
13	3880	±	27	2436	±	12
15	3880	±	27	2435	±	12
17	3880	±	27	2434	±	12
19	3880	±	27	2432	±	12
21	3877	±	27	2428	±	12
23	3877	±	27	2427	±	12
25	3873	±	27	2422	±	12

Table A.17: CO₂ saturated P-and S-wave velocities of the Berea sandstone for the T = 40°C constant temperature run, while under a constant differential pressure of 15 MPa.

T = 45 °C						
Pore Pressure (MPa)	Vp (m/s)			Vs (m/s)		
2	4018	±	28	2523	±	13
3	4005	±	28	2516	±	13
4	3993	±	28	2508	±	13
5	3981	±	28	2501	±	13
6	3968	±	28	2489	±	12
7	3959	±	28	2486	±	12
8	3947	±	28	2480	±	12
9	3934	±	28	2472	±	12
11	3904	±	27	2449	±	12
13	3890	±	27	2434	±	12
15	3887	±	27	2431	±	12
17	3885	±	27	2426	±	12
19	3884	±	27	2425	±	12
-	-	-	-	2421	±	12
22	3888	±	27	2422	±	12
25	3883	±	27	2413	±	12

Table A.18: CO₂ saturated P-and S-wave velocities of the Berea sandstone for the T = 45°C constant temperature run, while under a constant differential pressure of 15 MPa.

T = 55 °C						
Pore Pressure (MPa)	Vp (m/s)			Vs (m/s)		
2	4013	±	28	2522	±	13
3	3998	±	28	2514	±	13
4	3990	±	28	2511	±	13
5	3978	±	28	2505	±	13
6	3968	±	28	2498	±	12
7	3956	±	28	2490	±	12
8	3945	±	28	2485	±	12
9	3933	±	28	2480	±	12
11	3913	±	27	2466	±	12
13	3896	±	27	2450	±	12
15	3889	±	27	2446	±	12
17	3886	±	27	2441	±	12
19	3885	±	27	2438	±	12
21	3883	±	27	2436	±	12
23	3885	±	27	2434	±	12
25	3880	±	27	2428	±	12

Table A.19: CO₂ saturated P-and S-wave velocities of the Berea sandstone for the T = 55°C constant temperature run, while under a constant differential pressure of 15 MPa.

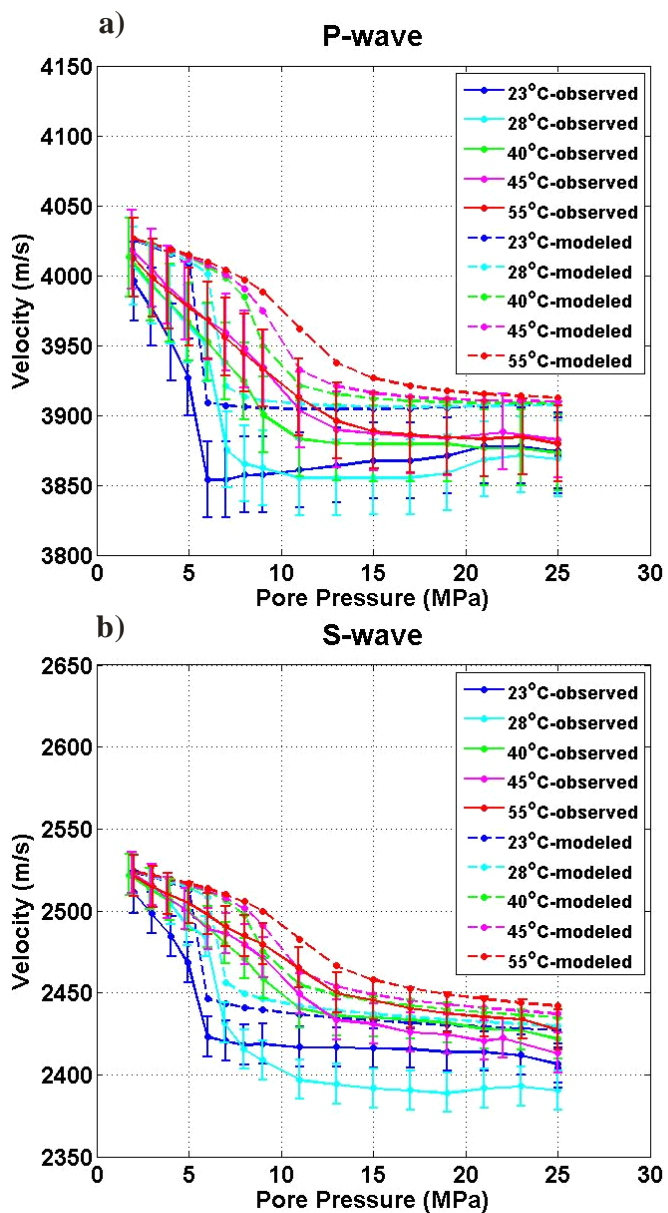


Figure A.26: Observed and Gassmann's modelled P- wave (a) and S-wave (b) CO₂ saturated velocities for T=23°C, 28°C, 40°C, 45°C, 55°C constant temperature runs. The observed wave velocities are shown with their respective errors.

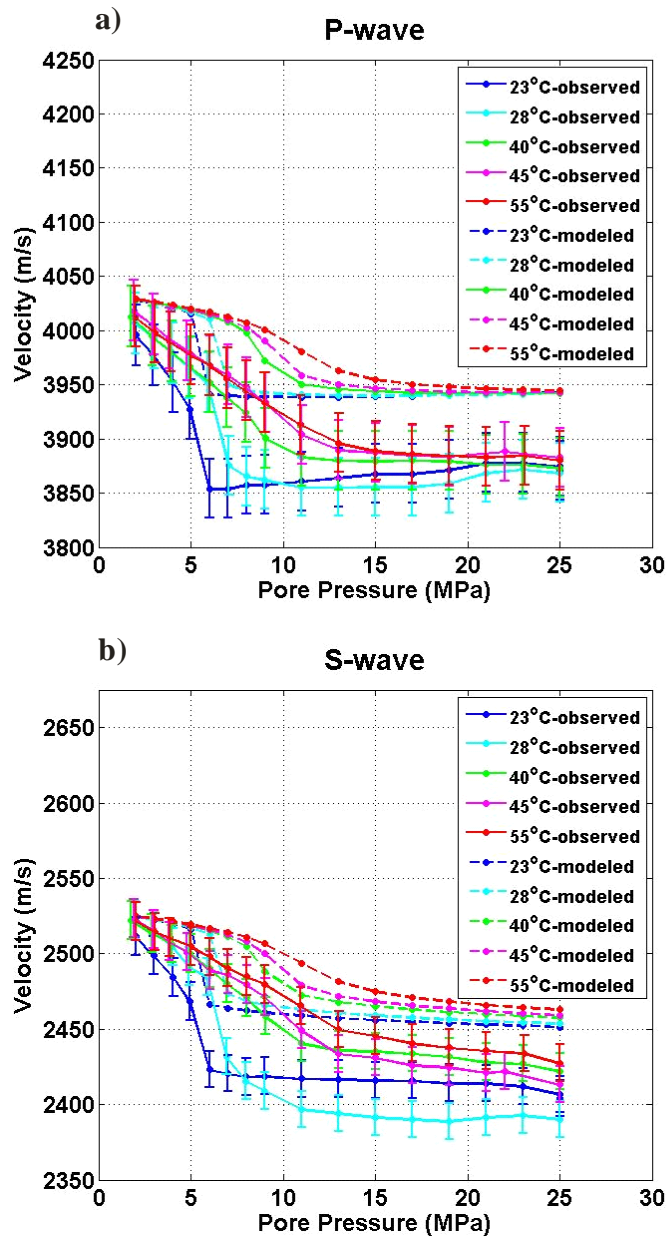
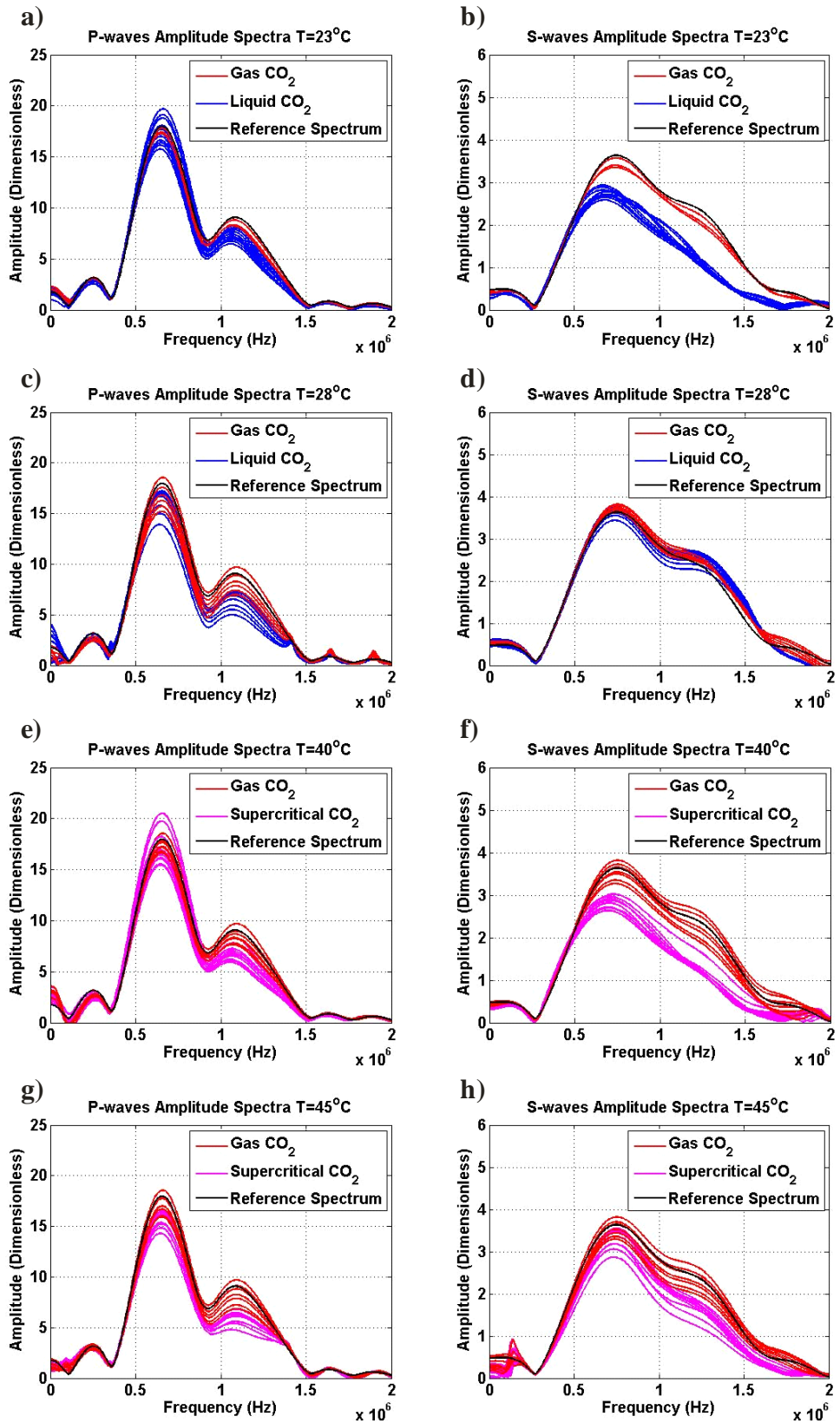


Figure A.27: Observed and Biot's modelled P- wave (a) and S-wave (b) CO_2 saturated velocities for $T = 23^\circ\text{C}$, 28°C , 40°C , 45°C , 55°C constant temperature runs. The observed wave velocities are shown with their respective errors.



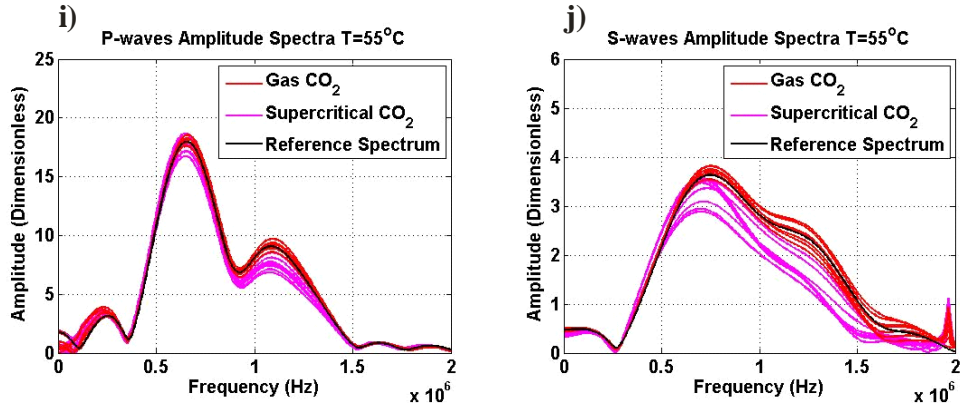
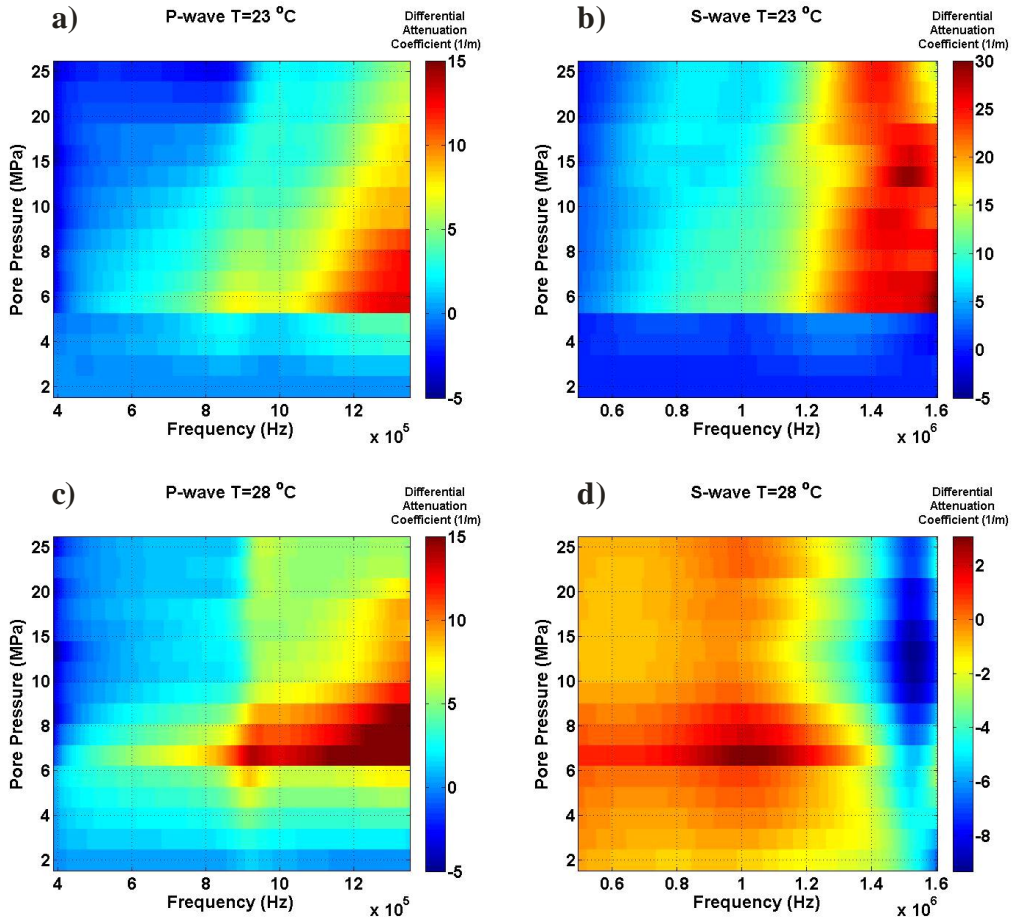


Figure A.28: The computed amplitude spectra of the collected P- and S-wave of the CO_2 saturated Berea sandstone for a) and b) $T = 23^\circ\text{C}$, c) and d) $T = 28^\circ\text{C}$, e) and f) $T = 40^\circ\text{C}$, g) and h) $T = 45^\circ\text{C}$, and i) and j) $T = 55^\circ\text{C}$ constant temperature runs as a function of frequency. The prevailing CO_2 phase states of the signals are determined from the pressure and temperature conditions applied. The reference spectrum is of the signal collected at $T = 23^\circ\text{C}$ and $P_p = 2 \text{ MPa}$ of CO_2 .



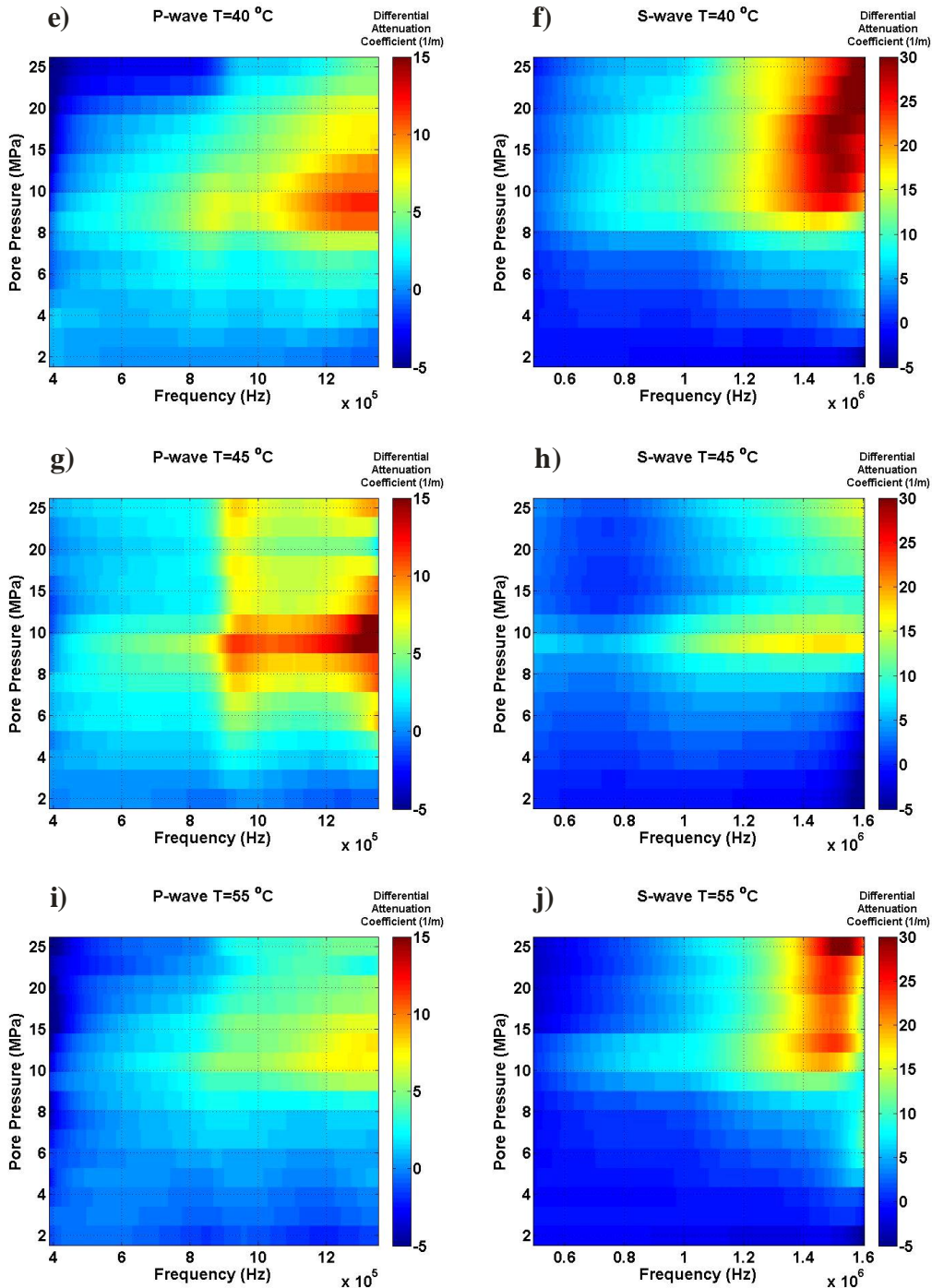
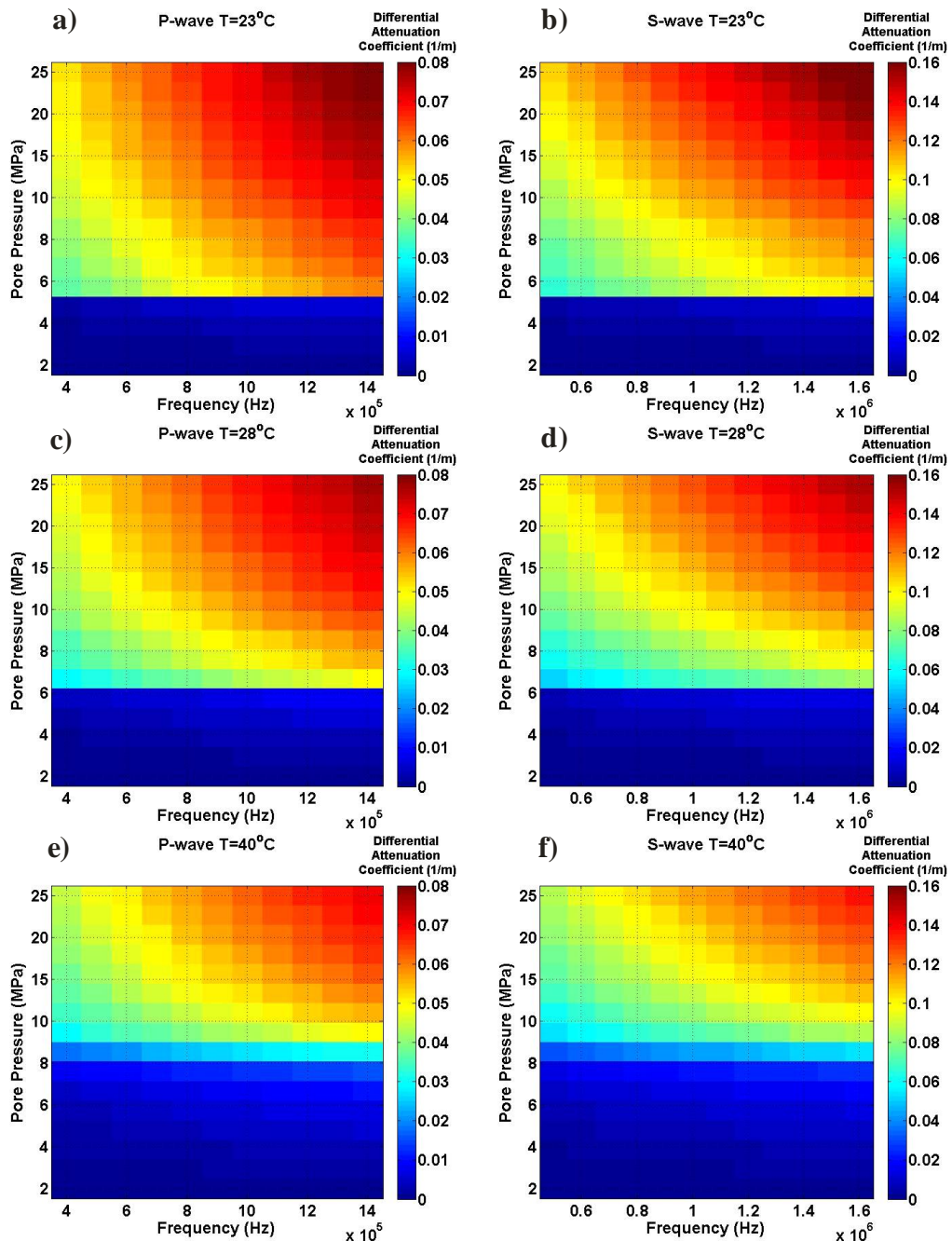


Figure A.29: Measured P- and S-wave differential attenuation coefficient of the CO₂ saturated Berea sandstone determined for a) and b) T = 23°C, c) and d) T = 28°C, e) and f) T = 40°C, g) and h) T = 45°C, i) and j) T = 55°C constant temperature runs as a function of frequency and pore pressure. The T = 28°C S-wave display and index is quite different than the other S-wave plots and this is attributed to the deterioration of the transducer used during the run.



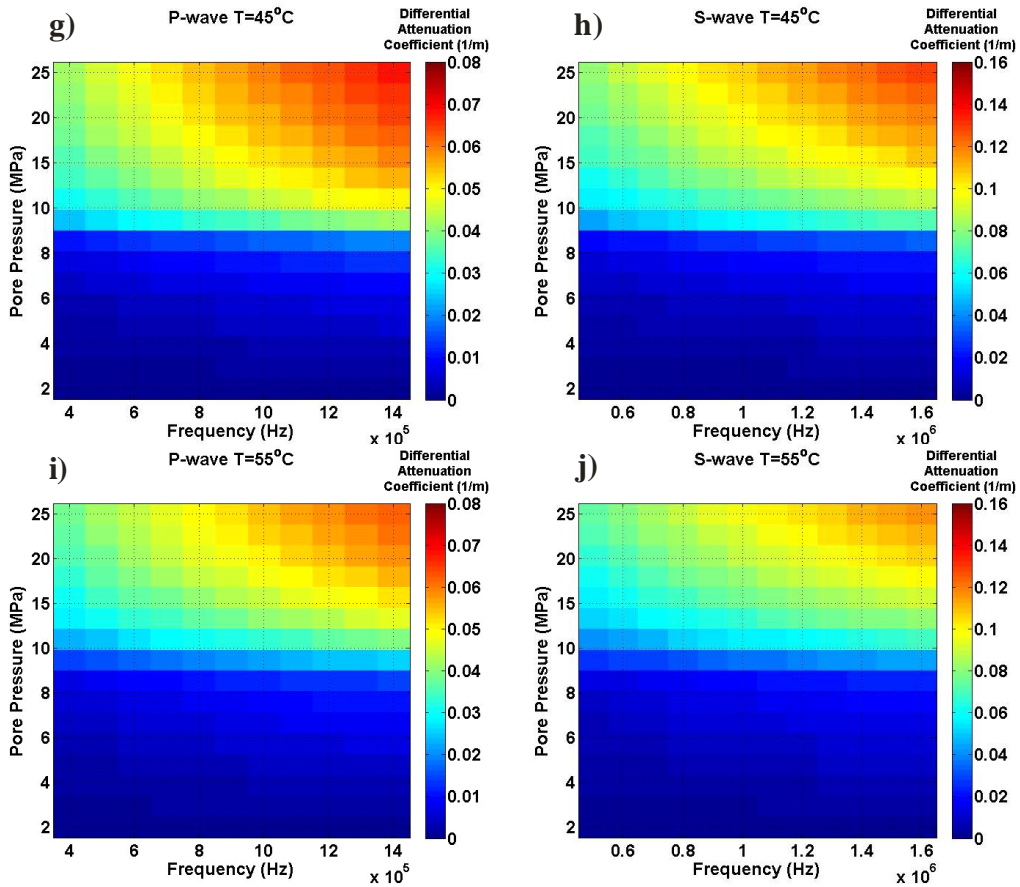


Figure A.30: Biot's modelled P- and S-wave differential attenuation coefficient of the CO_2 saturated Berea sandstone determined for a) and b) $T = 23^{\circ}\text{C}$, c) and d) $T = 28^{\circ}\text{C}$, e) and f) $T = 40^{\circ}\text{C}$, g) and h) $T = 45^{\circ}\text{C}$, and i) and j) $T = 55^{\circ}\text{C}$ constant temperature runs as a function of frequency and pore pressure.

Constant Pore Pressure

Constant pore pressure measurements for the Berea sandstone were conducted at $P_p = 7 \text{ MPa}$, 10 MPa , and 25 MPa while temperature varied.

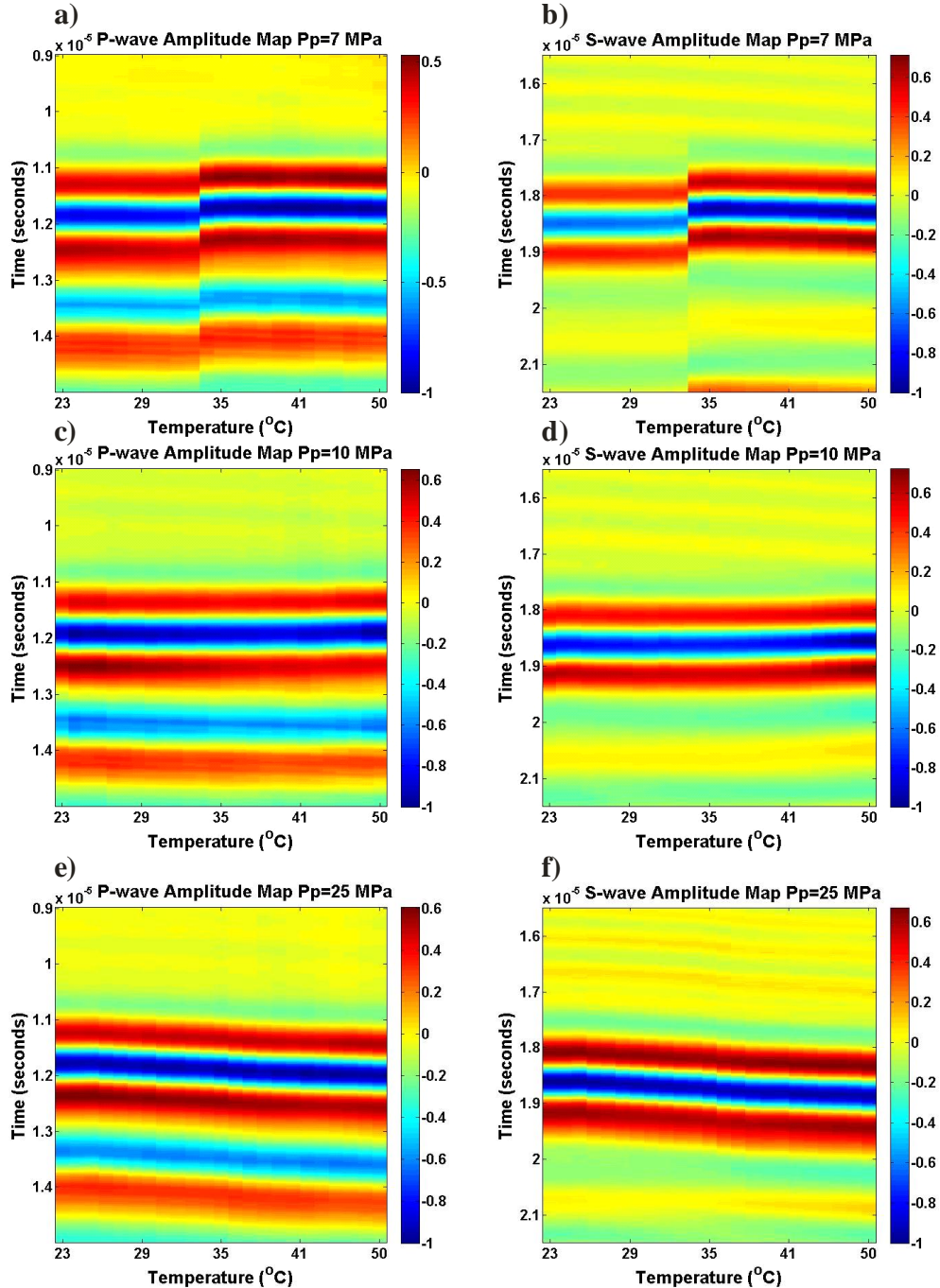


Figure A.31: Normalized P- and S-wave waveforms as a function of temperature collected during the constant pore pressure runs of a) and b) $P_p = 7 \text{ MPa}$, c) and d) $P_p = 10 \text{ MPa}$ and e) and f) $P_p = 25 \text{ MPa}$. A constant differential pressure of 15 MPa was maintained throughout each measurement run.

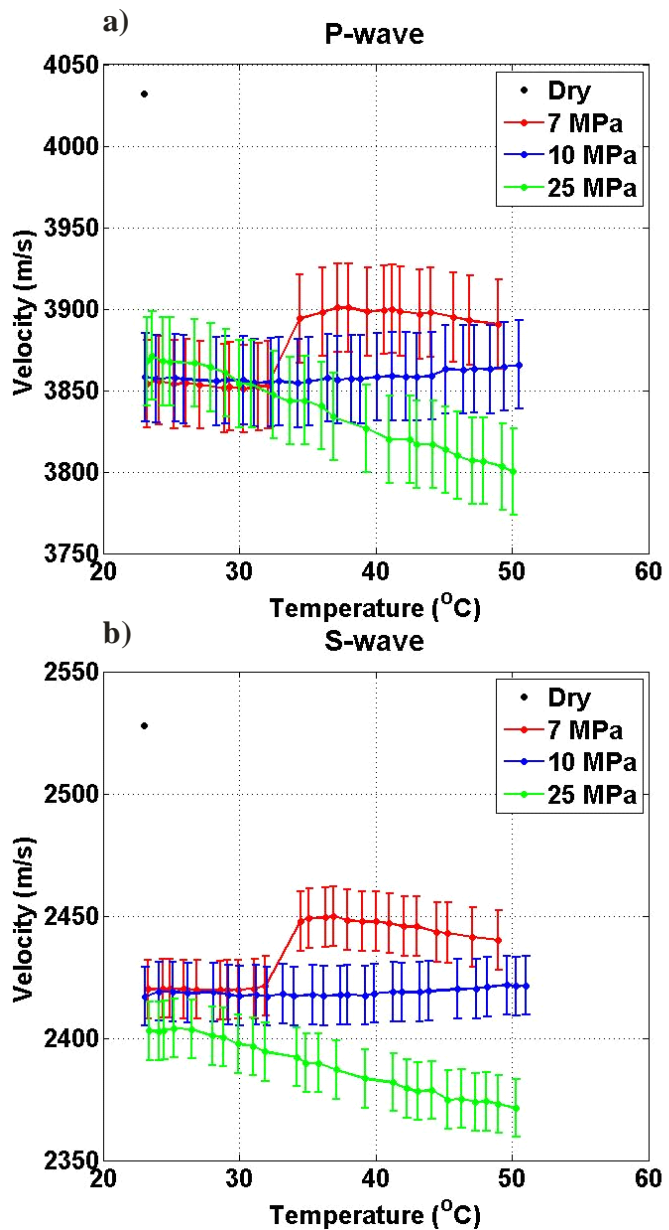


Figure A.32: Corrected P- wave (a) and S-wave (b) velocities with their respective errors measured of the Berea sandstone saturated with CO₂ for all constant pore pressure runs and when the sample is not saturated from the second dry measurement run (black dot at P_p = 0 MPa).

P_P = 7 MPa					
Temperature (°C)	Vp (m/s)		Temperature (°C)	Vs (m/s)	
23.2	3854	±	27	23.3	2420 ± 12
24.1	3856	±	27	24.4	2420 ± 12
25.2	3854	±	27	24.9	2420 ± 12
26.1	3854	±	27	25.9	2420 ± 12
27.1	3853	±	27	26.9	2420 ± 12
28.9	3851	±	27	28.6	2420 ± 12
29.3	3852	±	27	29.1	2420 ± 12
30.3	3851	±	27	29.9	2420 ± 12
31.4	3852	±	27	31.1	2420 ± 12
32.1	3853	±	27	31.9	2421 ± 12
34.4	3894	±	27	34.5	2448 ± 12
36.1	3898	±	27	35.1	2449 ± 12
37.2	3901	±	27	36.3	2449 ± 12
38	3901	±	27	36.9	2450 ± 12
39.4	3898	±	27	37.9	2448 ± 12
40.6	3899	±	27	39	2448 ± 12
41.2	3900	±	27	40	2448 ± 12
41.8	3899	±	27	41	2447 ± 12
43.2	3897	±	27	42.1	2446 ± 12
44	3898	±	27	43	2446 ± 12
45.7	3895	±	27	44.5	2443 ± 12
46.9	3893	±	27	45.3	2443 ± 12
49	3891	±	27	47.1	2441 ± 12
-	-	-	-	49	2440 ± 12

Table A.20: CO₂ saturated P-and S-wave velocities of the Berea sandstone for the P_P = 7 MPa constant pore pressure run, while under a constant differential pressure of 15 MPa.

P_p = 10 MPa					
Temperature (°C)	V_p (m/s)		Temperature (°C)	V_s (m/s)	
23.1	3858	± 27	23.1	2417	± 12
23.9	3857	± 27	24.1	2419	± 12
25.3	3858	± 27	25.1	2419	± 12
25.9	3857	± 27	26.2	2418	± 12
28.3	3856	± 27	28.1	2419	± 12
29	3856	± 27	29.2	2418	± 12
30.3	3856	± 27	30	2417	± 12
31.1	3855	± 27	31.2	2418	± 12
32.3	3855	± 27	32	2417	± 12
32.9	3856	± 27	33.2	2418	± 12
34.3	3854	± 27	34	2417	± 12
35.1	3855	± 27	35.4	2418	± 12
36.5	3857	± 27	36.2	2417	± 12
37.2	3856	± 27	37.4	2417	± 12
38.2	3857	± 27	37.9	2418	± 12
38.9	3857	± 27	39.2	2417	± 12
40.1	3858	± 27	39.9	2418	± 12
41.2	3859	± 27	41.3	2419	± 12
42.2	3858	± 27	41.9	2419	± 12
43	3858	± 27	43.2	2419	± 12
44.1	3859	± 27	43.9	2419	± 12
45.1	3863	± 27	46	2420	± 12
46.4	3863	± 27	47.4	2420	± 12
47.2	3863	± 27	48.2	2421	± 12
48.4	3863	± 27	49.6	2422	± 12
49.4	3865	± 27	50.3	2421	± 12
50.5	3866	± 27	51	2422	± 12

Table A.21: CO₂ saturated P-and S-wave velocities of the Berea sandstone for the P_p = 10 MPa constant pore pressure run, while under a constant differential pressure of 15 MPa.

P_p = 25 MPa					
Temperature (°C)	V_p (m/s)		Temperature (°C)	V_s (m/s)	
23.2	3868	± 27	24.1	2403	± 12
23.6	3871	± 27	23.4	2403	± 12
24.4	3868	± 27	24.5	2403	± 12
24.9	3868	± 27	25.2	2404	± 12
26.7	3867	± 27	26.5	2404	± 12
27.9	3864	± 27	28	2401	± 12
29	3861	± 27	28.8	2400	± 12
30	3854	± 27	29.9	2398	± 12
30.9	3854	± 27	31	2397	± 12
32.5	3847	± 27	31.9	2394	± 12
33.7	3844	± 27	34.2	2392	± 12
34.8	3844	± 27	34.9	2390	± 12
36	3840	± 27	35.8	2390	± 12
36.9	3834	± 27	37.1	2387	± 12
39.3	3827	± 27	39.2	2383	± 12
41	3820	± 27	41.3	2382	± 12
42.5	3820	± 27	42.3	2379	± 12
43	3817	± 27	43.1	2378	± 12
44.2	3817	± 27	44.1	2379	± 12
45.1	3813	± 27	45.3	2375	± 12
46	3810	± 27	46.3	2375	± 12
47.1	3807	± 27	47.3	2374	± 12
47.9	3807	± 27	48.1	2374	± 12
49.3	3803	± 27	49	2373	± 12
50.1	3800	± 27	50.3	2371	± 12

Table A.22: CO₂ saturated P-and S-wave velocities of the Berea sandstone for the P_p = 25 MPa constant pore pressure run, while under a constant differential pressure of 15 MPa.

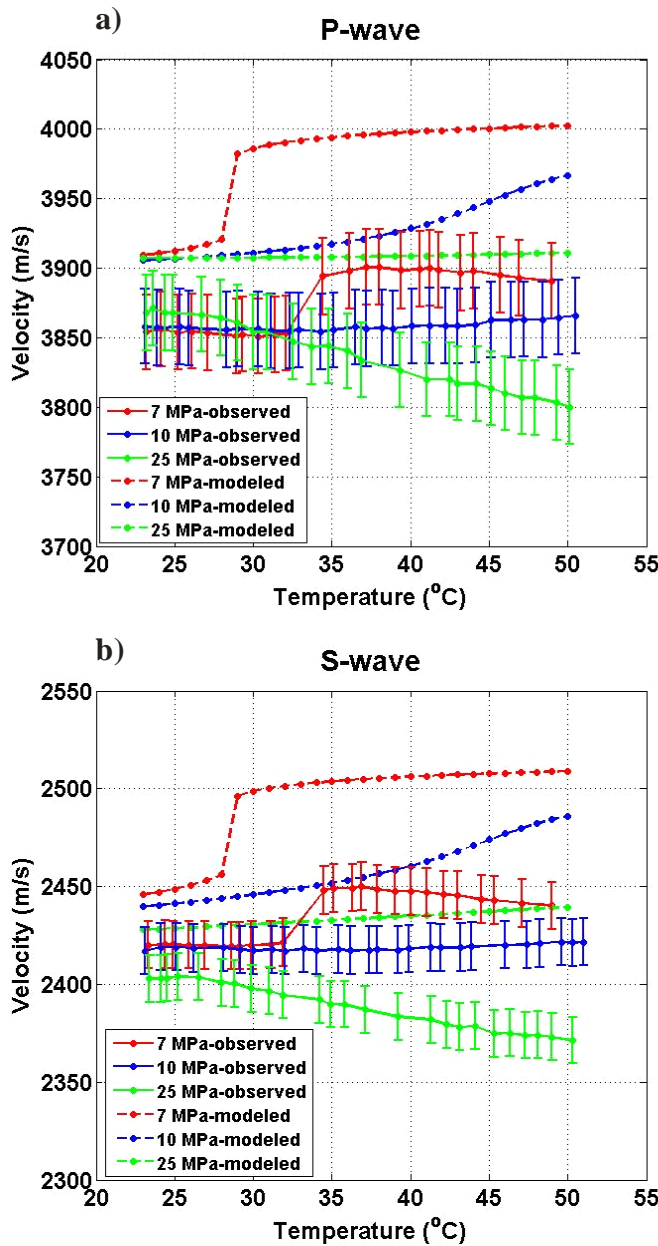


Figure A.33: Observed and Gassmann's modeled (a) P-wave and (b) S-wave CO_2 saturated velocities for $P_p=7 \text{ MPa}$, $P_p=10 \text{ MPa}$, and $P_p=25 \text{ MPa}$ constant pore pressure runs. The observed wave velocities are shown with their respective errors.

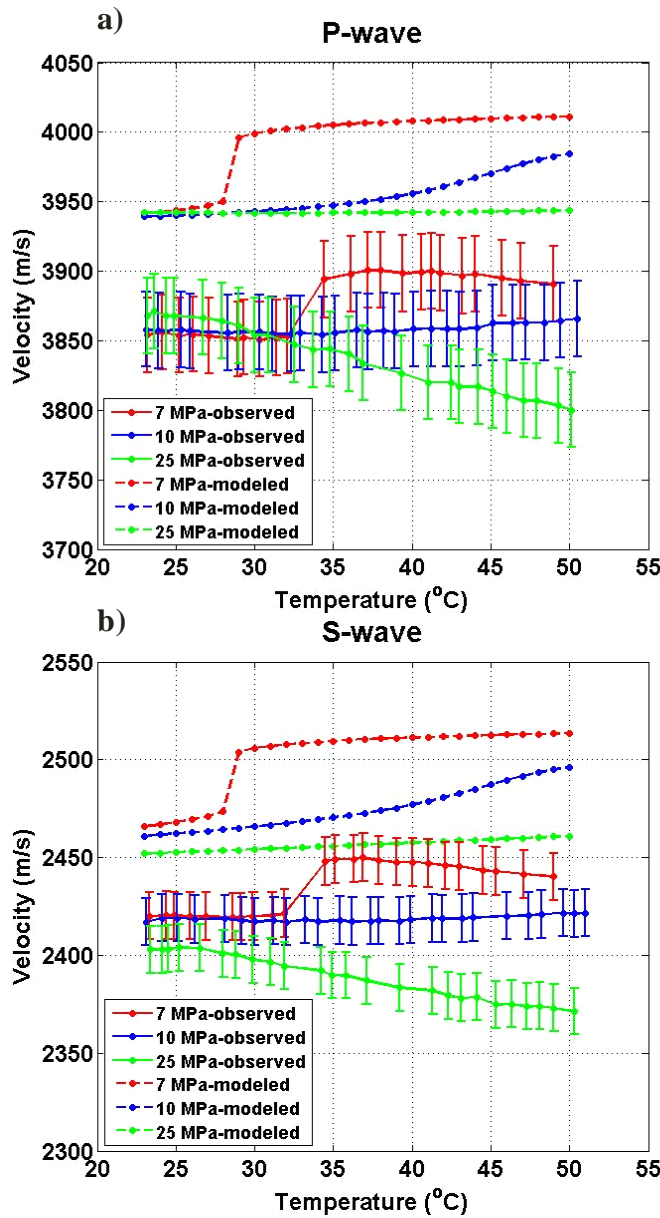


Figure A.34: Observed and Biot's modelled (a) P-wave and (b) S-wave CO_2 saturated velocities for $P_p = 7 \text{ MPa}$, $P_p = 10 \text{ MPa}$, and $P_p = 25 \text{ MPa}$ constant pore pressure runs. The observed wave velocities are shown with their respective errors.

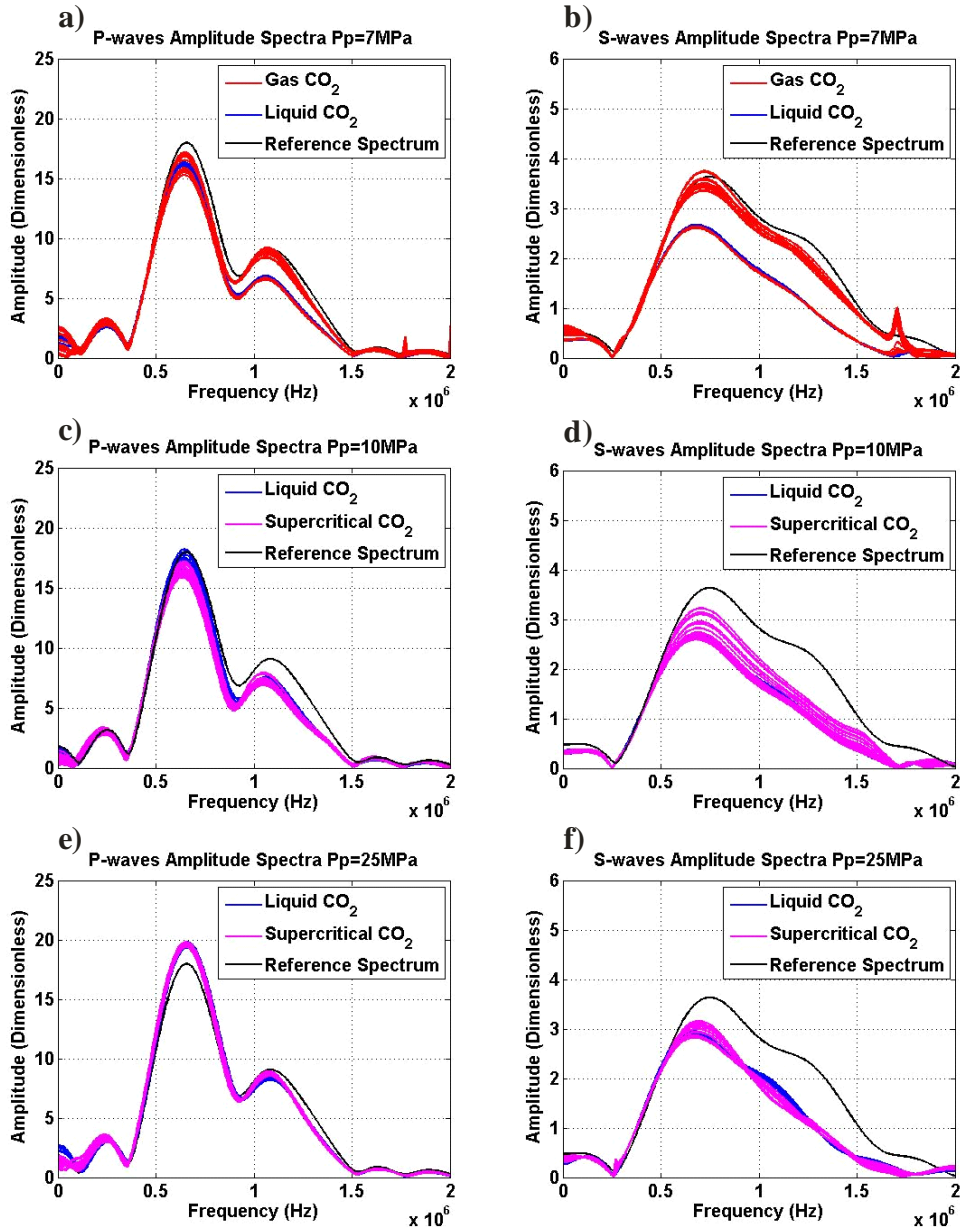


Figure A.35: The computed amplitude spectra of the collected P- and S-wave of the CO₂ saturated Berea sandstone for a) and b) $P_p = 7\text{ MPa}$, c) and d) $P_p = 10\text{ MPa}$, and e) and f) $P_p = 25\text{ MPa}$ constant temperature runs as a function of frequency. The prevailing CO₂ phase states of the signals are determined from the pressure and temperature conditions applied. The reference spectrum is of the signal collected at $T = 23^\circ\text{C}$ and $P_p = 2\text{ MPa}$ of CO₂.

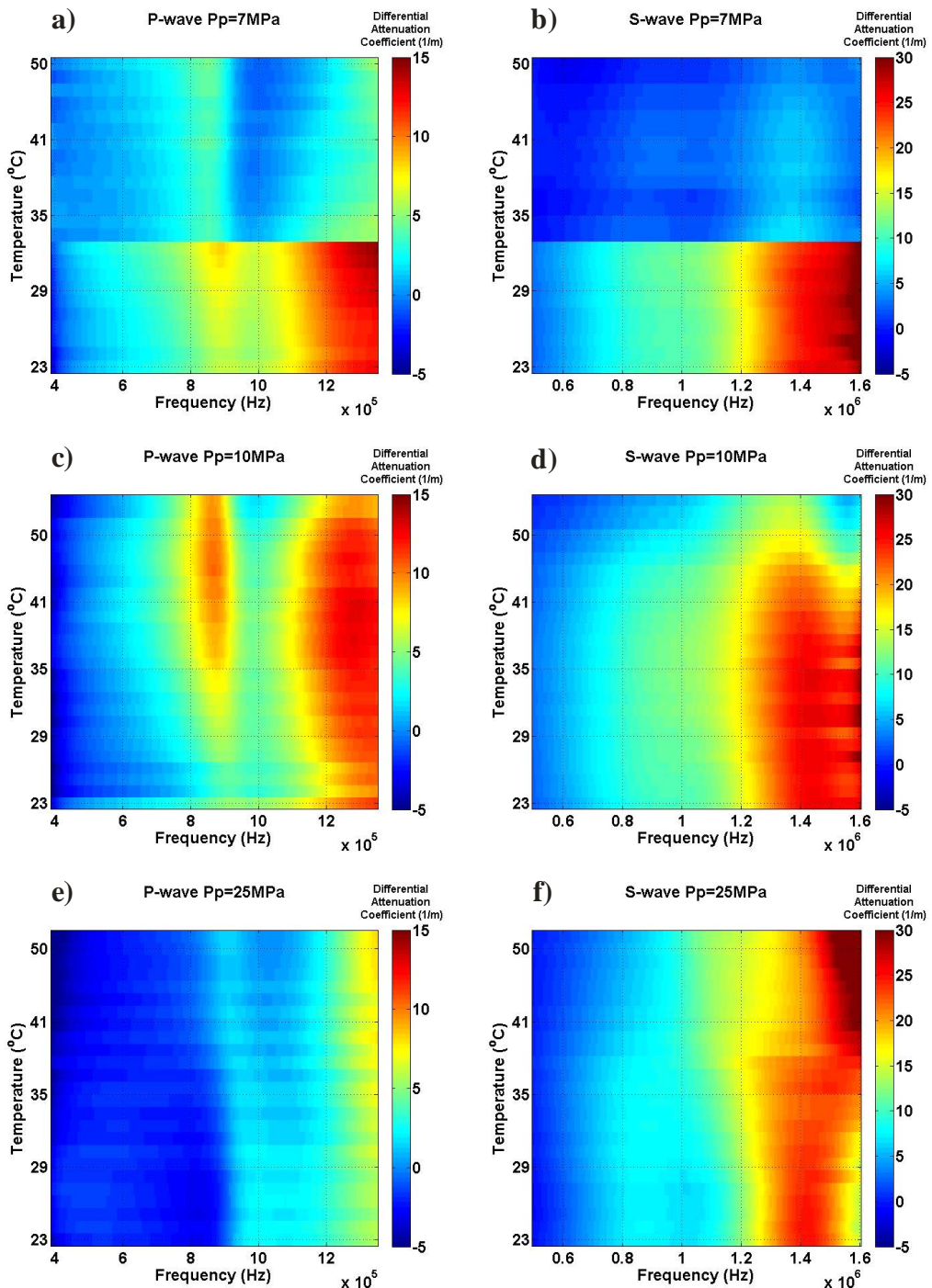


Figure A.36: Measured P- and S-wave differential attenuation coefficient of the CO_2 saturated Berea sandstone determined for a) and b) $P_p = 7\text{ MPa}$, c) and d) $P_p = 10\text{ MPa}$, and e) and f) $P_p = 25\text{ MPa}$ constant temperature runs as a function of frequency and pore pressure.

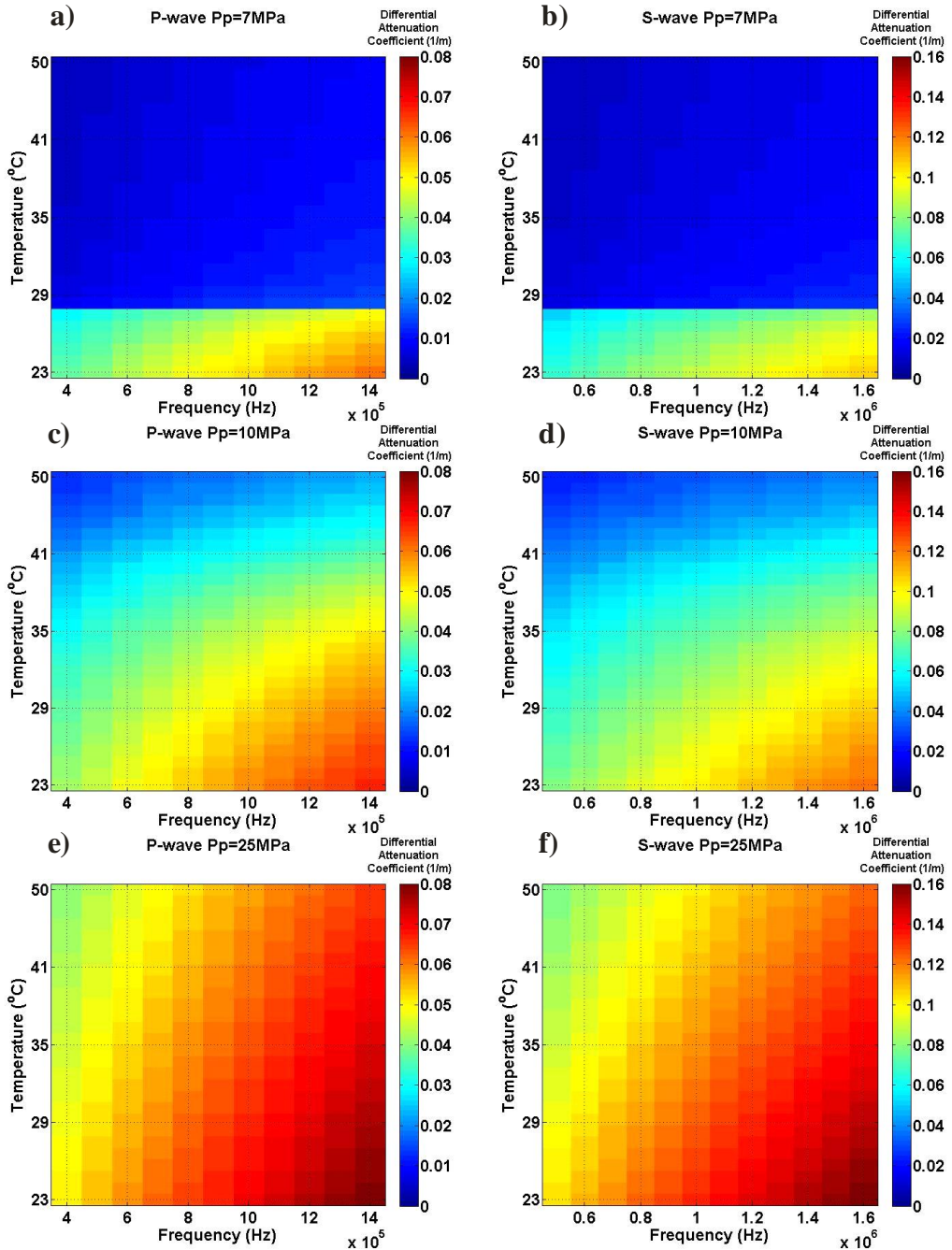


Figure A.37: Biot's modelled P- and S-wave differential attenuation coefficient of the CO_2 saturated Berea sandstone for a) and b) $P_p = 7 \text{ MPa}$, c) and d) $P_p = 10 \text{ MPa}$, and e) and f) $P_p = 25 \text{ MPa}$ constant temperature runs as a function of frequency and pore pressure.

A.2.3 Water Saturated Results

The water saturated Berea sandstone was only measured at $T = 23^{\circ}\text{C}$ as a function of pore pressure while under a constant differential pressure of 15 MPa. The resulting observed waveforms and the wave velocities are provided here.

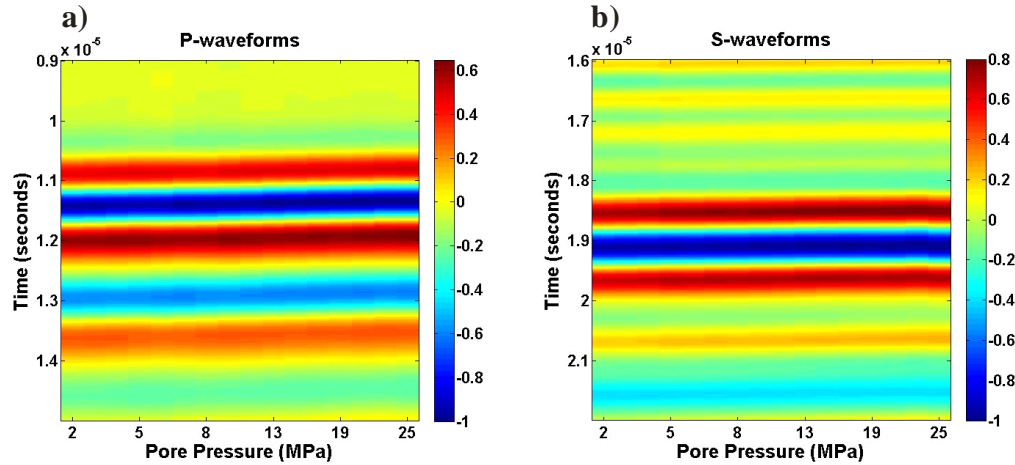


Figure A.38: Normalized P- (a) and S-wave (b) water saturated waveforms as a function of pore pressure of the Berea sandstone. A constant differential pressure of 15 MPa was maintained throughout the measurement run.

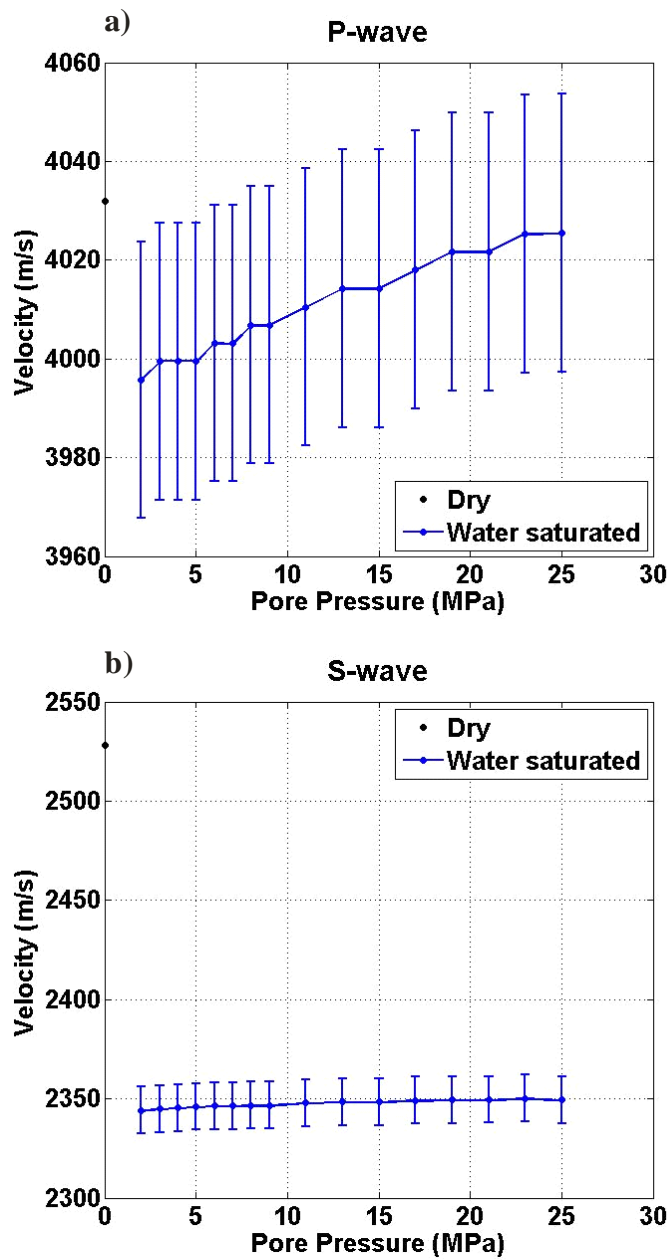


Figure A.39: P- (a) and S-wave (b) velocities with their respective errors measured of the water saturated Berea sandstone under various pore pressures at $T = 23^\circ\text{C}$ and when the sample is not saturated (black dot at $P_p = 0 \text{ MPa}$).

Pore Pressure (MPa)	Vp (m/s)			Vs (m/s)		
2	3996	±	28	2344	±	12
3	3999	±	28	2345	±	12
4	3999	±	28	2345	±	12
5	3999	±	28	2346	±	12
6	4003	±	28	2346	±	12
7	4003	±	28	2346	±	12
8	4007	±	28	2347	±	12
9	4007	±	28	2347	±	12
11	4010	±	28	2348	±	12
13	4014	±	28	2348	±	12
15	4014	±	28	2348	±	12
17	4018	±	28	2349	±	12
19	4022	±	28	2349	±	12
21	4022	±	28	2350	±	12
23	4025	±	28	2350	±	12
25	4025	±	28	2349	±	12

Table A.23: Water saturated P-and S-wave velocities of the Berea sandstone at T = 23°C for varying pore pressures, while under a constant differential pressure of 15 MPa.